ABSTRACT

Title of Document: PLASMA-SURFACE INTERACTIONS OF MODEL POLYMERS FOR ADVANCED PHOTORESIST SYSTEMS

Sebastian Ulrich Engelmann,
Doctor of Philosophy, 2008

Directed By: Professor Gottlieb S. Oehrlein, Department of Material Science and Engineering

Plasma processing of advanced photoresist (PR) materials is a critical step in nano-manufacturing. We have studied the interactions of PRs and polymers in fluorocarbon/Ar discharges. The effects of process time, PR material, bias and source power, pressure and gas chemistry (C_4F_8/Ar, CF_4/Ar and CF_4/H_2/Ar) were studied by ellipsometry, atomic force microscopy and x-ray photoelectron spectroscopy. Additionally, patterned structures of 193nm PR were examined using scanning electron microscopy. Polymer destruction in the top surface, oxygen and hydrogen loss along with fluorination were observed for all materials initially, which was followed by steady state etch conditions. A strong dependence of plasma-induced

surface chemical and morphological changes on polymer structure was observed. In particular, the adamantane group of 193 nm PR showed poor stability. Two linked mechanisms for the roughening behavior of the films during processing were identified: A physical pattern transfer mechanism enhances initial roughness by non-uniform removal. Additional to that, roughness formation occurred linear to the energy density deposited during processing. For adamantyl polymers, a higher roughening constant was found. Additionally, fluorocarbon (FC) deposition on the damaged PR affected roughening in two opposing ways: Ion-induced mixing with the damaged PR increased roughening, whereas for simple FC precursor deposition a reduction of roughness was seen. Fluorination of the PR surfaces using plasma increased etching yields, which were found to improve the roughness of 193nm PR after etch. The fluorination of the PR prevented the formation of characteristic small scale roughness features at the cost of large scale roughness introduction. Use of low energy density processes suppressed the roughness growth by ion-induced transfer. Examining 3-dimensional trenches and contact holes patterned in PR showed that the sidewall roughness changed with process parameters similar to that seen for blanket films. The close correlation suggested that our model of polymer surface roughening also applies to resist sidewall evolution during etch. All process conditions can be combined in the energy density roughening model. Even for various feedgas chemistries adamantyl containing polymers show enhanced roughening rates, suggesting that the instability of the adamantyl structure used in 193nm PR polymers is the performance limiting factor for processing PR materials.

PLASMA-SURFACE INTERACTIONS OF MODEL POLYMERS FOR ADVANCED PHOTORESIST SYSTEMS

By

Sebastian Ulrich Engelmann

Dissertation submitted to the Faculty of the Graduate School of the
University of Maryland, College Park, in partial fulfillment
of the requirements for the degree of
Doctor of Philosophy
2008

Advisory Committee:
Professor Gottlieb S. Oehrlein, Chair
Professor Raymond J. Phaneuf
Professor Robert M. Briber
Professor Martin Peckerar
Dr. Eric A. Hudson

© Copyright by

Sebastian Ulrich Engelmann

2008

Dedication

This dissertation is dedicated in memory of my grandfather:

Josef Schubert

You showed me how important it is to have faith, in people and in yourself.

Your love for family and thirst for knowledge continue to inspire me today.

Acknowledgements

I would like to begin by thanking Prof. Oehrlein for all the effort and time he spent while working with me. His critical thinking and approach to problems have taught me a lot during my years in Maryland. I am also very thankful for all the freedom I had while working with him, the trust he put in me, the financial support he has provided me with during all these years and the chances and opportunities I received due to his efforts. Thank you very much for everything.

I would like to thank all members of my committee for their efforts on my behalf: Professor Briber, Professor Peckerar, Professor Phaneuf and Dr. Hudson.

I would like to thank the National Science Foundation (NSF) and Lam Research for financial support. I would like to express special thanks to Dr. Eric Hudson from Lam Research, who hosted me for two summer long internships in Fremont, CA. During these times I gained invaluable insights without which this thesis wouldn't have been possible. I also would like to thank Dr. Cecily Andes from Rohm and Haas Electronic Materials for her support of the GOALI project. Our interactions and discussions were also very crucial to understand different aspects of this work. I like to thank all my outside collaborators and colleagues who all had contributions to this thesis: Dr. Maryam Moravej, Dr. Alexi Marakhtanov, Sun-Hyung Kim (Lam Research), Dustin Nest, Dr. Joe Vegh, Dr. Erwine Pargon, Prof. David Graves (University of California, Berkeley), Paolo Lazzeri, Erica Iacob, Prof. Mariano Anderle (ITC-Irst, Povo, Italy), Taesoon Kwon, Prof. Phaneuf, (UMD). I like to thank everyone else, who I interacted with during my four years. Even though

no accountable results emerged from these interactions, they were still very important in driving my overall progress.

I like to thank my colleagues in the plasma processing group for spending parts of my four years with me: Xuefeng Hua, Li Ling, Bryan Orf, Guido Stueber, Brian Smith, Michel Figueroa, Deuk-Yeon Lee, Ming-Shu Kuo, Robert Bruce, Magda Benavides, Yilin Liu, Masahiro Sumiya, Arup Pal, Rajendra Deshmukh and Florian Weilnboeck. I always had a lot of fun working with you and will definitely miss our time together and the lab and its special atmosphere in the future.

I also don't want to miss thanking all my friends back in old Europe and here in America for all the good and fun times we had together. My "American family", the Dusens, and certainly all my friends here in College Park all make me appreciate how good it is to spend time with your friends when away from your family. Your friendship means so much to me and I am so happy to have you.

Lastly of course, I like to thank my family for unbelievable support during all my years here. I was very happy to see my godfather Dr. Ulrich Schubert visit me here in Maryland and learn about the things I do here. I am very happy to have my brother Martin and my two sisters Franziska and Claudia to keep my spirits up. I am very grateful to my parents, Monika and Ekkehard Engelmann, and my grandparents, Ursula Schubert, Steffi and Klaus Engelmann, for occasional financial help and all other support. Because of your efforts I had the best conditions possible and never had to worry about anything else. Thank you very much!

Finally, there's only one word left to say:

EJÖ!!

Table of Contents

Dedication ii

Acknowledgements iii

Table of Contents v

List of Tables viii

List of Figures ix

Chapter 1: *Introduction* 1
1.1 Material properties of photoresist materials 3
1.1.1 Photolithography for nanoscale fabrication 3
1.1.2 Historic developments in photolithography 5
1.1.3 Chemically amplified photoresists 7
1.2 Plasma processing of advanced electronic materials 11
1.3 Experimental setup 14
1.3.1 Plasma Processing 14
1.3.1.1 Inductive plasma sources 15
1.3.1.2 Capacitive plasma sources 17
1.3.2 Surface Analysis 19
1.4 Experimental Approach 22
1.4.1 Laboratory for plasma processing of materials (UMD) 23
1.4.2 Other laboratories 25
1.5 Outline of thesis 26

Chapter 2: *"Plasma-surface interactions of model polymers for advanced photoresists using C_4F_8/Ar discharges and energetic ion beams"* 28
2.1 Introduction 30
2.2 Experiment 32
2.2.1 Description of materials 32
2.2.2 Plasma processing 37
2.2.3 Surface characterization 39
2.3 Results 41
2.3.1 Structural and morphological changes upon plasma exposure 41
2.3.2 Qualitative evaluation of structural and morphological changes 51
2.3.3 Influence of energetic ion beams 63
2.4 Discussion 66
2.5 Conclusions 71

Chapter 3: *"Dependence of polymer surface roughening rate on deposited energy density during plasma processing"* 73

Chapter 4: *"Plasma-Surface Interactions of Advanced Photoresists Using C_4F_8/Ar Discharges: Plasma Parameter Dependencies"* 83
4.1 Introduction 85
4.2 Experimental 87
4.2.1 Description of materials 87
4.2.2 Plasma processing 89
4.2.3 Characterization 91
4.3 Results 93
4.3.1 Effect operating parameters on process results 93
4.3.1.1 Bias power 93
4.3.1.2 Pressure 98
4.3.1.3 Source power 102
4.3.2 Role of surface fluorine in roughening of PR materials 112
4.3.3 Impact of plasma radicals 116
4.3.3.1 Interactions with sidewalls 116
4.3.3.2 Interactions of radicals with nanoscale geometries 118
4.4 Discussion 120
4.4.1 Dependence of surface roughness on deposited energy density 120
4.4.2 Are line edge roughness and surface roughness correlated? 127
4.4.3 Influence of plasma species 130
4.5 Conclusions 133

Chapter 5: *"Adjusting surface energy density by feedgas composition: Comparison of C_4F_8- and CF_4-based discharges"* 136
5.1 Introduction 138
5.2 Experimental 140
5.2.1. Description of materials 140
5.2.2. Plasma processing 141
5.2.3. Post process characterization 142
5.3 Results 143
5.3.1. Polymer modifications for five fluorocarbon discharge conditions 143
5.3.2. Effect of fluorocarbon gas addition to Ar discharges 151
5.3.2.1. C_4F_8/Ar discharges 151
5.3.2.2. CF_4/Ar discharges 156
5.3.3. Surface compositional analysis by XPS 161
5.4 Discussion 167
5.4.1. Influence of surface composition on polymer removal 167

5.4.2. Influence of surface composition on surface energy density and roughening 176
5.4.3. Correlation of surface and sidewall roughness 186
5.5 Conclusions 187

Chapter 6: *Overall conclusions* 189

Chapter 7: *Future work and directions* 196

References 202

List of Tables

Table 1.1: *Overview of groups and tasks in the GOALI project.*

Table 4.1: *Process matrix for exposing 193nm PR, p-MAMA and 248nm PR in C_4F_8/90% Ar discharges.*

Table 5.1: *Sampling depths of Al Kα source in [nm] (from D. Briggs)*[5.35]

List of Figures

Chapter 1:

Fig. 1.1: *Cross section schematic of a typical integrated circuit and its interconnect levels.*[1.5]

Fig. 1.2: *Production scheme for patterning of one interconnect layer.*

Fig. 1.3: *Optical absorption of 248nm PR (SU-8; A) and two traditional PR materials (RISTON© T-168; B and Novolak resist; C)*[1.11]

Fig. 1.4: *Polymer modifications during the lithographic exposure step for 248nm PR a) and 193nm PR b).*[1.29]

Fig. 1.5: *248nm PR (a) and 193nm PR (b) after processing in identical process conditions.*[1.17]

Fig. 1.6: *Schematic of typical surfaces involved in pattern transfer plasmas.*

Fig. 1.7: *Schematic of inductively coupled plasma reactor used in this work.*

Fig. 1.8: *Schematic of the capacitively coupled plasma reactor used in this work.*

Fig. 1.9: *Schematic Overview of LPPM.*

Chapter 2:

Figure 2.1: *Molecular structure of the MAMA/GBLMA/RAMA reference compound.*

Figure 2.2: *Molecular structures of (a) EAMA/GBLMA/RAMA, (b) MAMA/GBLMA/RADA, (c) Full Formulated 193nm Photoresist, (d) p-MAMA and (e)Full Formulated 248nm Photoresist.*

Figure 2.3: *Time evolution of resist etch rate(a) and refractive index change (b) during C_4F_8/90% Ar plasma etching for RADA compound. The discharges were generated using 1000W source power, a pressure of 10 mTorr, 50sccm total gas flow and a fixed self bias voltage of -125 V. The lines (a) are inserted as a guide for the eye.*

Figure 2.4: *High resolution XPS C1s spectra of MAMA compound before (a) and after (b) 60 sec. exposure to a C_4F_8/90% Ar discharge. The discharges were generated using 800W source power, a pressure of 10 mTorr, 50sccm total gas flow and a fixed self bias voltage of -100 V.*

Figure 2.5: *High resolution O1s XPS spectra of MAMA compound before and after processing in a C_4F_8/90% Ar discharge. The discharges were generated using 800W source power, a pressure of 10 mTorr, 50sccm total gas flow and a fixed self bias voltage of -100 V.*

Figure 2.6: *Time evolution of calculated F/C (a) and O/C (b) ratios of MAMA compound in C_4F_8/90% Ar discharge. The discharges were generated using 800W source power, a pressure of 10 mTorr, 50sccm total gas flow and a fixed self bias voltage of -100 V.*

Figure 2.7: *RMS roughness along with AFM micrographs of the MAMA compound as a function of exposure time in a C_4F_8/90% Ar discharge. The discharges were generated using 1000W source power, a pressure of 10 mTorr, 50sccm total gas flow and a fixed self bias voltage of -125 V.*

Figure 2.8: *Etch rates for different materials vs. effective carbon content obtained after 60 sec processing in a C_4F_8/90% Ar discharge. The discharges were generated using 800W source power, a pressure of 10 mTorr, 50sccm total gas flow and a fixed self bias voltage of -100 V. The line has been inserted as a guide for the eye.*

Figure 2.9: *Time evolution of the change in refractive index for EAMA, MAMA, RADA, 193nm PR (a) and MAMA, p-MAMA, 193nm PR, 248nm PR (b) during exposure to a C_4F_8/90% Ar discharge. The discharges were generated using 800W source power, a pressure of 10 mTorr, 50sccm total gas flow and a fixed self bias voltage of -100 V. The refractive index changes were averaged over the total remaining photoresist or polymer thickness.*

Figure 2.10: *High resolution XPS C1s spectra of MAMA (a) and p-MAMA (b) before and after 60 sec. exposure to a C_4F_8/90% Ar discharge. The discharges were generated using 800W source power, a pressure of 10 mTorr, 50sccm total gas flow and a fixed self bias voltage of -100 V.*

Figure 2.11: *RMS roughness (a) and roughening rate (b) of the 4 model compounds as a function of exposure time in a C_4F_8/90% Ar discharge. The discharges were generated using 1000W source power, a pressure of 10 mTorr, 50sccm total gas flow and a fixed self bias voltage of -125 V.*

Figure 2.12: *Measured RMS roughness as a function of calculated F/C ratio (20° deg) for the tested materials after 60 sec exposure to a C_4F_8/90% Ar discharge. The discharges were generated using 800W source power, a pressure of 10 mTorr, 50sccm total gas flow and a fixed self bias voltage of -100 V.*

Figure 2.13: *Roughening rates for plasma exposures (as shown in Fig. 11b) and ion beam exposures of the four 193nm model compounds.*

Figure 2.14: *Temporal overview of PR modifications during exposure to a C_4F_8/90% Ar plasma based on data presented in this article. The AFM micrographs are for exposure of MAMA to C_4F_8/90% Ar plasma with a fixed self bias voltage of -125V.*

Chapter 3:

Figure 3.1: *Molecular structures of 193nm PR (a)), 248nm PR (b)) and p-MAMA (c)) employed in this work.*

Figure 3.2: *Etch rate and RMS roughness vs. energy density for 193nm PR, 248nm PR and p-MAMA for different processing conditions.*

Figure 3.3: *Roughening rate vs. energy density for 193nm PR, 248nm PR and p-MAMA for different processing conditions.*

Figure 3.4: *LER vs. RMS roughness for patterned 193nm PR for etch conditions with different inductive power.*

Chapter 4:

Figure 4.1: *Molecular structures of 193nm PR (a)), p-MAMA (b)) and 248nm PR (c)) employed in this work.*

Figure 4.2: *Etch rates, RMS roughness and F/C ratios as a function of self bias voltage in a C_4F_8/90% Ar plasma.*

Figure 4.3: *SEM micrographs of unexposed (a)) and exposed trench structures after processing in a C_4F_8/90% Ar plasma with a self bias voltage of -50V (b)), -100V (c)) and -150V (d)).*

Figure 4.4: *CD measurements (a)) and LER/LWR values (b)) of trenches before and after plasma etch as a function of the self bias voltage.*

Figure 4.5: *Etch rates, RMS roughness and F/C ratios as a function of pressure in a C_4F_8/90% Ar plasma.*

Figure 4.6: *SEM micrographs of unexposed (a)) and exposed trench structures after processing in a C_4F_8/90% Ar plasma with at a pressure of 10 mTorr (b)), 45 mTorr (c)) and 80 mTorr (d)).*

Figure 4.7: *CD measurements (a)) and LER/LWR values (b)) of trenches before and after plasma etch as a function of pressure.*

Figure 4.8: *Etch rates, RMS roughness and F/C ratios as a function of source power in a C_4F_8/90% Ar plasma.*

Figure 4.9: *Etch Yields and RMS roughness as a function of % C_4F_8 addition to an Ar discharge.*

Figure 4.10: *F/C ratio (a) and F(2s)/F(1s) ratio(b) as a function of % C_4F_8 addition to an Ar discharge.*

Figure 4.11: *SEM micrographs of unexposed (a)) and exposed trench structures after processing in a C_4F_8/90% Ar plasma with for a source power of 400W (b)), 800W (c)) and 1200W (d)).*

Figure 4.12: *CD measurements (a)) and LER/LWR values (b)) of trenches before and after plasma etch as a function of source power.*

Figure 4.13: *Roughness as a function of the F/C ratio for C_4F_8/90% Ar exposures.*

Figure 4.14: *Roughening rates of 248nm PR, RADA, EAMA and 193nm PR for pure Ar and C_4F_8/Ar mixtures.*

Figure 4.15: *Evolution of contact hole samples as exposed to different source power levels.*

Figure 4.16: *Evolution of contact hole samples(a) and trenches (b) as exposed to the same discharge condition (C_4F_8/90% Ar).*

Figure 4.17: *Schematic surface conditions for etching at low or high energy densities during processing. For processing at high energy densities, more energy is transferred into the deeper regions of the surface leading to characteristic roughening of the surface.*

Figure 4.18: *Roughening rate vs. energy density for C_4F_8/90% Ar exposures.*

Figure 4.19: *LER and LWR roughness as a function of the RMS roughness for different source power levels (a)) and different ion energies (b)).*

Figure 4.20: *Etch Yield vs. F/C ratio for C_4F_8/90% Ar exposures*

Chapter 5:

Figure 5.1: *Etch rates (a)), RMS roughness (b)) and F/C ratio (c)) after processing for five plasma process conditions.*

Figure 5.2: *SEM micrographs of trench samples before (a)) and after plasma processing using C_4F_8/90% Ar (b)), CF_4/90% Ar (c)), CF_4 (d)), CF_4/40% H_2 (e)) and CF_4/40% H_2/40% Ar (f)).*

Figure 5.3: *CD measurements (a)) and LER/LWR values of trenches (b)) before and after plasma etching using five discharge conditions.*

Figure 5.4: *Profile evolution of contact hole samples after plasma etching using five typical discharge conditions.*

Figure 5.5: *Etch rates (a)) and RMS roughness (b)) as a function of C_4F_8/Ar percentage.*

Figure 5.6: *SEM micrographs of trench sample before (a)) and after processing in pure Ar (b)), C_4F_8/90% Ar (c)), C_4F_8/80% Ar (d)), C_4F_8/60% Ar (e)) and C_4F_8/40% Ar (f)).*

Figure 5.7: *CD measurements (a)) and LER/LWR values of trenches (b)) before and after processing as a function of C_4F_8/Ar percentage.*

Figure 5.8: *Etch rates (a)) and RMS roughness (b)) as a function of CF_4 percentage in an Ar discharge.*

Figure 5.9: *SEM micrographs of trench sample before (a)) and after processing in pure Ar (b)), CF_4/90% Ar (c)), CF_4/80% Ar (d)), CF_4/40% Ar (e)) and CF_4 (f)).*

Figure 5.10: *CD measurements (a)) and LER/LWR values of trenches (b)) before and after processing as a function of CF_4/Ar percentage.*

Figure 5.11: *F/C ratio vs. F/C ratio measured in the C1s spectrum for C_4F_8/90% Ar, CF_4/90% Ar and CF_4/40% H_2 (a)) and all conditions tested in CF_4/Ar discharges at 90 deg emission angle (b)).*

Figure 5.12: *F/C ratios after processing as a function of Ar percentage in a C_4F_8 discharge (a)) and F/C ratio obtained from the C1s spectrum as a function of percent CF_4 in an Ar discharge (b)).*

Figure 5.13: *Deposition rate vs. percentage of Ar in CF_4 and C_4F_8 discharges.*

Figure 5.14: *Etching yields vs. neutral coverage of PR materials in pure Ar and C_4F_8/Ar discharges (a)). The data for C_4F_8/Ar are compared with data obtained in C_4F_8/90% Ar at different operating pressures(b)). (From[5.7])*

Figure 5.15: *Etching yields vs. neutral coverage of PR materials in pure Ar and CF_4/Ar discharges (a)). CF_4/Ar, CF_4/H_2 and CF_4/H_2/Ar conditions are compared in (b)).*

Figure 5.16: *Amplitude vs. spatial frequency of FT-AFM line scans for C_4F_8/ 90% Ar (a)), CF_4/80% Ar (b)) and 193nm PR in CF_4/Ar discharges (c)).*

Figure 5.17: *Roughening rate vs. energy density as shown in[5.7] and for C_4F_8/Ar (a)) and for CF_4/Ar, CF_4/H_2 and CF4/Ar/H_2 discharge conditions (b)).*

Figure 5.18: *Sidewall roughness vs. surface roughness in CF_4/Ar discharge conditions.*

Chapter 1:

Introduction

Starting with its invention by Bardeen and Shockley in 1947, the transistor has revolutionized every-day life.[1.1] Computers and semiconducting devices make life much easier due to very fast computational abilities. This was started by the first integrated circuit in 1961 and has been further improved ever since.[1.2] Miniaturization of the integrated structures has led to faster devices on a pace never seen before. This is usually referred to as Moore's law, which states that the complexity, e.g. number of transistors per chip, doubles every 18 months.[1.3] The semiconductor industry has been able to advance at this fast pace by using so a called "top down" approach,[1.2] which means a solid state body is changed into an array of structures with nanoscale dimensions by a patterning procedure. By patterning layer by layer, complex structures, such as microprocessors or others, can be generated. The cheapest and fastest way for manufacturing these structures in mass production was found to be optical lithography of photoresist (PR) materials followed by a pattern transfer using plasma. Both technologies offer the advantage of producing large numbers of devices simultaneously, making typical processing time very short and keeping production costs low. At this time, a couple tens of millions of transistors are packed on one typical chip.[1.4] Smaller devices and chip sizes in turn increase the number of chips per wafer, reducing the cost of the very expensive lithography and etch processes even further.

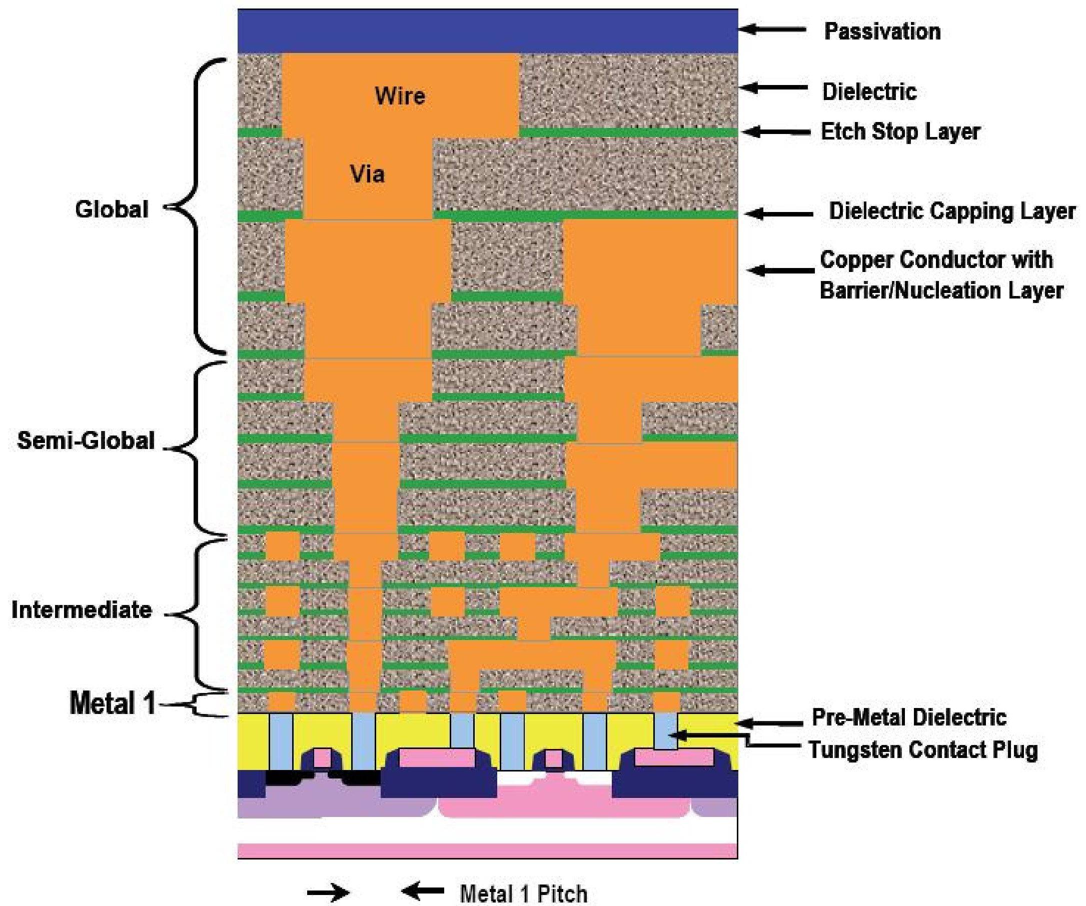

Fig. 1.1: *Cross section schematic of a typical integrated circuit and its interconnect levels.*[1.5]

To build devices on a nanoscale, very high precision has to be maintained during fabrication and so complex production schemes have to be used. Besides manufacturing of the actual transistors, which perform the computational work, increased attention also has to be directed towards the complex architecture of the interconnect levels, which control and address the individual transistors and with that affect the speed of the overall IC device. Fig. 1.1 shows a typical cross section of an

integrated circuit (IC). After the dielectric is grown onto the substrate, the vias (and wires) are generated by lithography and plasma pattern transfer.

In nanoscale devices, a number of significant changes also have been achieved by integration of new materials. The interconnect/insulator material combination of Al and SiO_2 has been replaced by Cu and low-k dielectric materials.[1.6,1.7] High-k gate dielectrics replace SiO_2 on the transistor level to increase the gate capacitance and reduce the leakage currents.[1.5] The dimensions of the interconnect levels shrink as one gets to the transistor level. Both techniques will be reviewed briefly to give an overview of the mechanisms and pathways leading to problems due to plasma surface interactions on a nanoscale level.

1.1 Material properties of photoresist materials

1.1.1. Photolithography for nanoscale fabrication

A typical process scheme to generate patterned structures using lithography and plasma transfer is shown in *Fig. 1.2*. A layer of PR material (light) is spun on the material to be patterned (black; in the case of microelectronic processing this would be an insulating oxide, e.g. SiO_2). By exposing the PR to light using an exposure mask, the exposed portions of the PR (darker) undergo a chemical change and can then be removed from the layer stack by an aqueous solution. Using a transfer plasma, the open area of the PR material is transferred into the underlying substrate (positive image). After the pattern transfer-plasma, a second, less damaging plasma discharge (plasma ash) is used to remove the residual PR material from the layer

stack. The generated trench is then filled with Cu to complete the process. By patterning several layers in the same fashion, highly complex memory, storage or computing units can be manufactured. The schematic in Fig. 1.2 is of course a simplified approach. Patterning of multiple layers usually requires additional separation layers, which also prevent damage of the underlying material (e.g. bottom anti-reflection coatings). Also, the patterning usually occurs two layers at a time, using the so called "dual damascene" process.[1.8, 1.9]

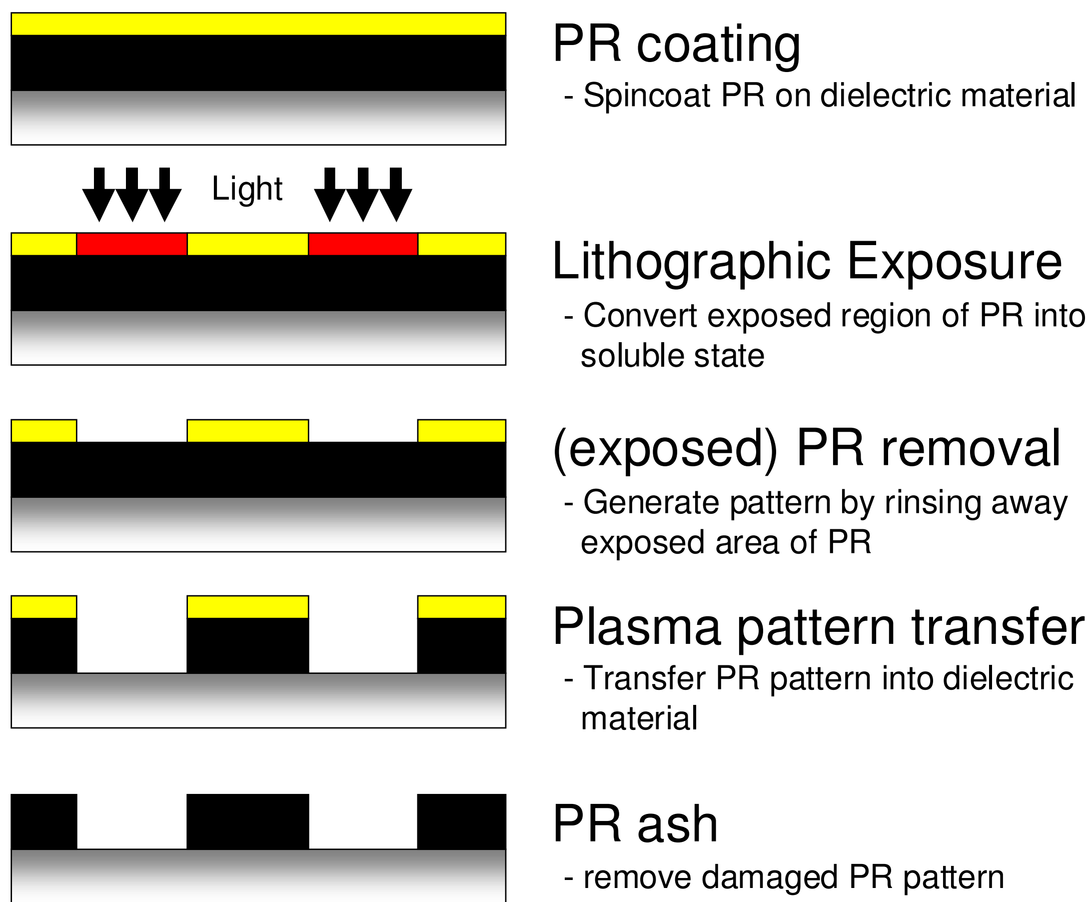

Fig. 1.2: *Production scheme for patterning of one interconnect layer.*

1.1.2. Historic developments in photolithography

The choice of the PR material is of great importance, since its performance can ultimately determine the resolution of manufacturable device features. The PR needs to be designed so that it can meet the demands for both technologies, lithography and plasma etching. The very basic features that all PR materials have in common is that they can be switched from an aqueous base insoluble to an aqueous base soluble state and are significantly more etch resistant than the substrate material.[1.10] This is ideally achieved through (1) sufficient transparency of the PR material at the exposure radiation wavelength, (2) a solubility switch mechanism based on this light exposure, (3) high etch resistance and (4) smooth surfaces and sidewalls after both litho- and etch processes.

The exposure of the PR material to light initiates a chemical reaction which changes the chemical state of the PR material. By making the exposed areas more soluble, a positive image of the exposure mask can be generated. A complete exposure of the whole PR film also requires the film to be optically transparent at the exposure radiation wavelength. The ultimate resolution of the critical dimension (CD) for the patterned features obeys a modified Raleigh equation

$$\textbf{Ultimate resolution} = k_1\lambda/NA \tag{1}$$

where k_1 is an experimental parameter that depends on the resist material, λ the exposure wavelength and NA the numerical aperture of the system.[1.2] The preferred method to decrease the critical dimension (CD) to date has been the reduction of the exposure wavelength since it is the most easily accessible parameter. This imposes

new challenges on the PR material design, as certain polymer moieties absorb energy differently as a function of wavelength. The difference in absorbance of different PR materials is shown in Fig. 1.3.[1.11] The materials typically used for exposure at 436nm and 365nm (B and C) and 248nm (A) show very high absorption at wavelengths shorter than the exposure wavelength. Paradoxically, too high absorption means higher exposure doses need to be used to complete the exposure or the film doesn't change its state over its entire thickness. High absorption generates an imperfect pattern in the PR material or in the case of higher exposure doses the PR material is damaged easily leading to increased roughness and related effects.

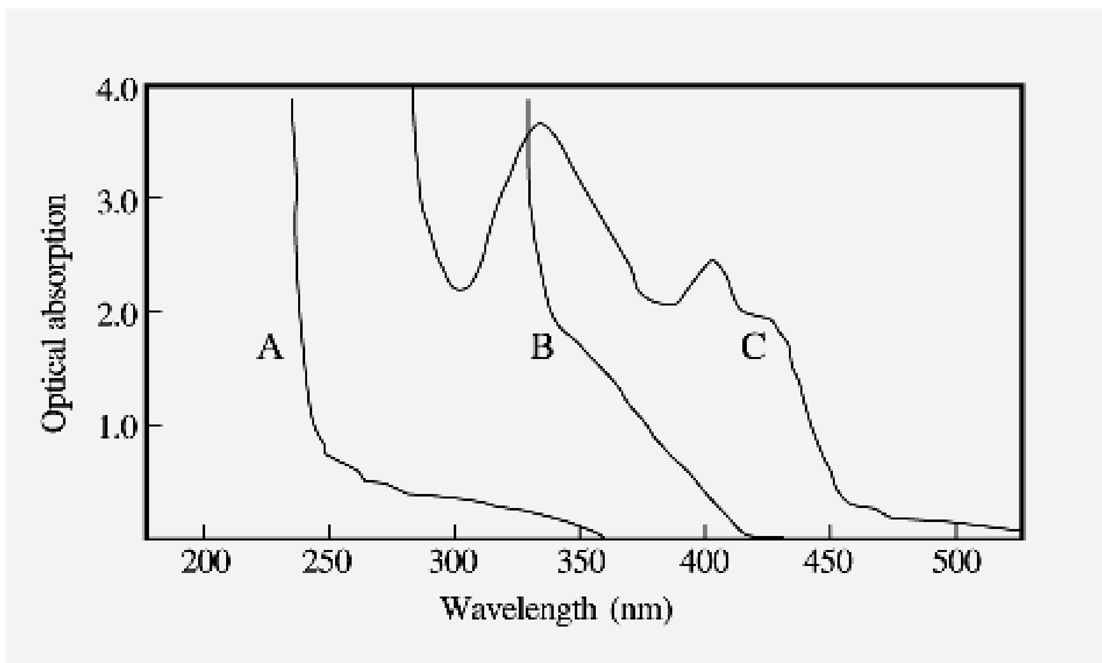

Fig. 1.3: *Optical absorption of 248nm PR (SU-8; A) and two other PR materials (RISTON© T-168; B and Novolak resist; C)*[1.11]

1.1.3. Chemically amplified photoresists

While traditional Novolak resins at exposure wavelengths of 436nm (G-line) or 365nm (I-line) have been able to define patterns in the range from 1μm to 0.2μm, a slightly different approach had to be taken to resolve features below 200nm. Starting with 248nm (KrF) photolithography, the concept of "chemically amplified" (CA) resists was introduced.[1.10,1.12,1.13] In addition to the polymer matrix, low molecular weight polymers were added to make the exposure more effective. One of those additives is called PhotoAcid Generator (PAG), which releases H^+ upon exposure to light. This proton attacks a specific polymer sidegroup, leading to cleavage of this specific group. A product of this second reaction is also H^+, making the overall reaction self multiplying. In addition to this, a base additive is used to limit the diffusion of the PAG, defining the image. The name chemically amplified resist reflects this self multiplying chain reaction (regeneration of H^+) upon exposure.

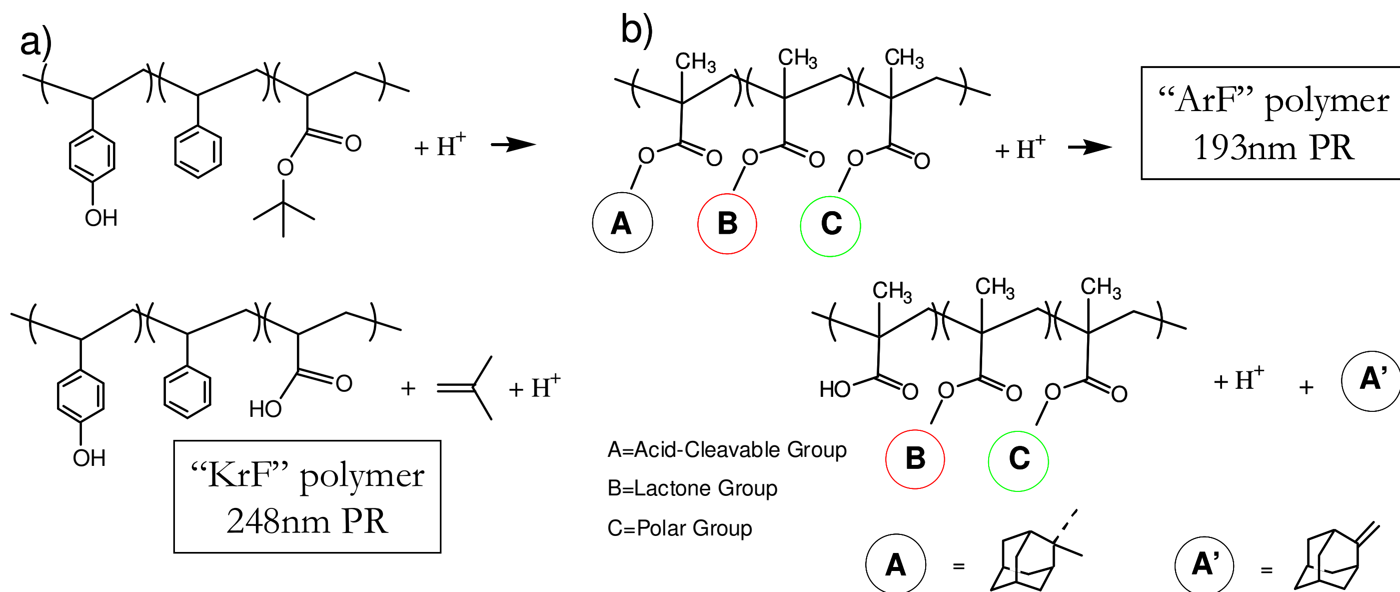

Fig. 1.4: *Polymer modifications during the lithographic exposure step for 248nm PR a) and 193nm PR b).*[1.29]

The acid (H^+) attacks the weakest bond in the polymer matrix. The PR materials are designed in a way that a C-O linkage is broken and an –OH endgroup forms. This switches the PR from a water-insoluble state to a water-soluble state. A soft bake at moderate temperatures (~100ºC) is usually performed to accelerate this reaction. As shown in Fig. 1.4, the basic principle remains the same when switching from 248nm PR to 193nm PR's, however the polymeric structures have changed significantly. This is mostly due to the strong absorbance of the conjugated C-C bonds at 193nm.[1.11,1.14] For 193nm lithography the aromatic ring structure has therefore been replaced by a more cage-like carbon arrangement, called adamantyl. Other differences include the use of a methacrylate main chain, motivated by details of the polymer synthesis.[1.14-1.16]

Whereas lithographic exposures of adamantyl-based PR at 193nm have been successfully used to switch the water-solubility, other PR requirements are less well met. The etch resistance in the plasma as well as roughness evolution during lithographic or plasma exposure caused problems in the integration of 193nm PR into manufacturing.[1.17] Since 193nm PRs contain more oxygen per monomer, high removal rates are found for these materials. This affects the selectivity of the etch process to the underlying substrate and with that the manufacturable aspect ratios. An improvement in etch resistance was achieved by introduction of more carbon into the polymer matrix.[1.18,1.19]

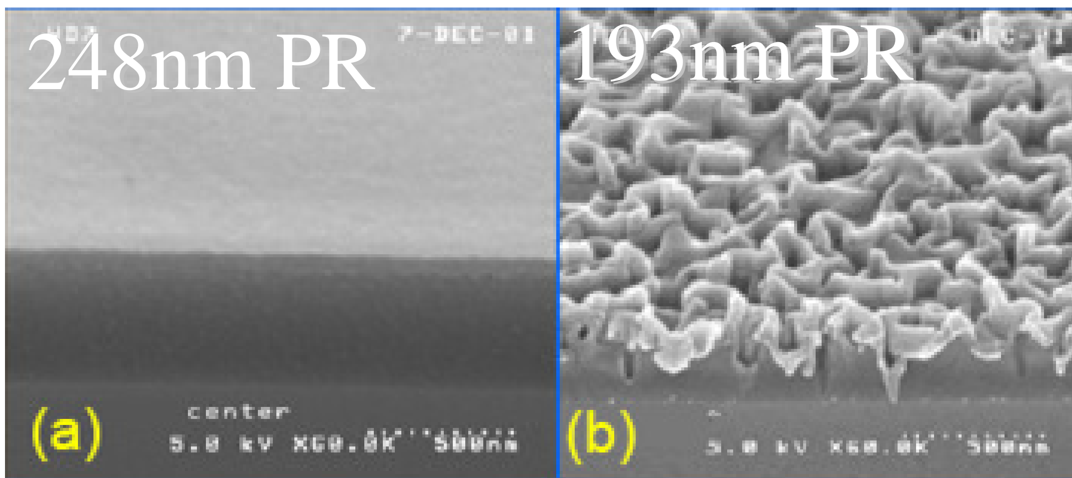

Fig. 1.5: *248nm PR (a) and 193nm PR (b) after processing in identical process conditions.*[1.17]

Previous work has shown that fluorine-based plasma pattern transfer processes which are successful for 248nm PR can introduce problems for 193nm PR that include high etch rates, “pinholing” and formation of surface/line edge roughness (see Fig. 1.5).[1.17,1.20-1.21] The roughness that is generated on the PR surfaces and

sidewalls can be transferred into the underlying substrate. This may lead to pattern degradation, charge scattering during device operation and ultimately device failure. The typical size of a PR molecule (i.e. radius of gyration) used in 193nm lithography is 3-5nm.[1.22] A 50nm wide line therefore corresponds to 10-15 molecules, with the typical thickness of the PR as spun-on corresponds to about 20 molecules. The minimal extent due to plasma modifications by neutrals and ions (~100eV) in a typical plasma-pattern transfer process also corresponds to 3-5nm, similar to one molecule size. For successful pattern transfer, a molecular control of the plasma-surface interactions is needed.

1.2 Plasma processing of advanced electronic materials

A schematic of a F-containing plasma-based pattern transfer process is shown in Fig. 1.6. A successful pattern transfer requires optimal management of the species fluxes involved in the plasma-surface interactions. We will therefore briefly review the known plasma-surface interactions leading to the characteristics of a typical transfer etch process.

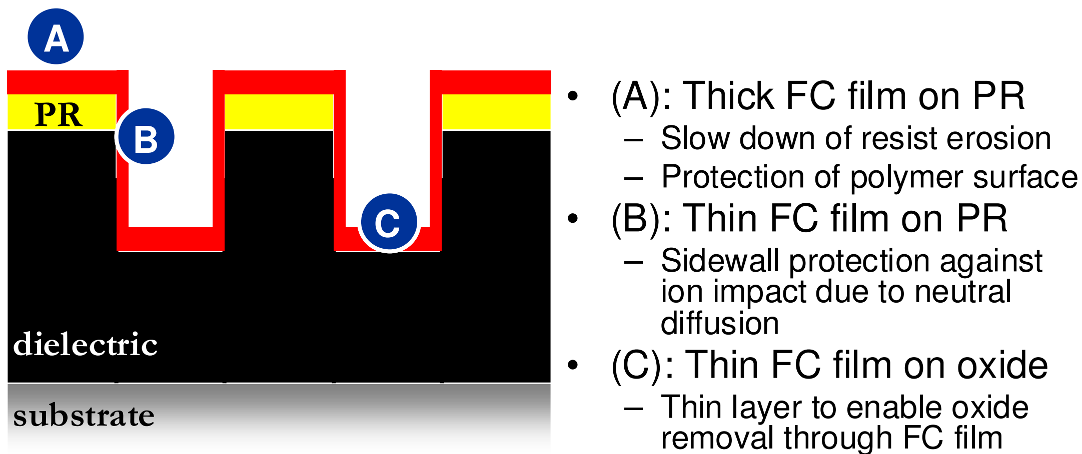

Fig. 1.6: *Schematic of typical surfaces involved in pattern transfer plasmas.*

The ion bombardment during processing plays a very important role in the plasma surface interactions. Most frequently, argon glow discharges are used to provide high energy ion bombardment and provide a physical sputtering environment for the surfaces A and C in Fig. 1.6. Additionally, synergetic effects due to an increased reaction probability of neutral atoms and/or radicals with the surface being etched are generated by a molecular gas flow that forms volatile compounds upon reactions in the surface. The classical experiment for this behavior was performed by

Coburn and Winters[1.23], in which the removal rate for reactive neutral beam and ion bombardment simultaneously was found to be significantly larger than the sum for the removal for the individual components. Molecular gases in the plasma have important implications on the polymerization during the plasma discharge. High selectivity discharges (i.e. higher dielectric material removal relative to the resist removal) are preferred during pattern transfer. By polymerization of an added molecular gas, a competing mechanism with the etching is initiated in the plasma. Based on whether surfaces are subject to ion bombardment or not, polymer deposition can occur.[1.24,1.25] Typical fluorocarbon gases used in plasma processing show deposition for low-ion energy conditions, but etching under higher energy bombardment conditions.[1.24,1.25] Since ion bombardment in a typical plasma discharge geometry always occurs perpendicular to the surface, highly anisotropic etching is possible in plasma processing. Surfaces A and C (see Fig. 1.6) are subject to high ion bombardment and are therefore in the etching regime. Ions arriving perpendicular to the average surface cannot reach the sidewalls B (see Fig. 1.6); the sidewalls are thus not subject to high ion bombardment, and a thin FC film can be deposited. This sidewall deposit protects the resist and dielectric material sidewalls against chemical attack or erosion and so highly anisotropic etch profiles can be generated. The deposition flux by the added FC gas can also reduce the net etching rate of the resist (A in Fig. 1.6) while the dielectric etch rate (B) may remain nearly unaffected. For certain resist/dielectric material combinations, nearly infinite selectivity process conditions were found.[1.26,1.27] The involved etch rates can be fine-tuned by a careful

selection of gases involved in the plasma process. A detailed review of the mechanisms can be found elsewhere.[1.28]

The plasma-surface interactions with polymeric materials are a lot less well defined. The etch rates of polymers are usually reported in etch studies, since they are directly correlated to what process selectivity is possible. Many models have been developed to describe the etch behavior of different polymers in a plasma environment. The fist model was developed by Ohninshi et al.[1.19], which proposed a dependence of the sputter resistance on the effective carbon content, i.e. number of carbon atoms per monomer. Even though this model wasn't proven to be valid in plasma environments, it was consistently developed further by many groups. Most models are based on the basic idea that a higher C-content per monomer leads to a lower removal rate in a plasma environment.[1.29]

A detailed understanding on the molecular level as well as the impact of the plasma condition on the etch rates has mostly not been addressed. The impact of the change in fluorination due to plasma processing[1.30] on the resist etch results remains unclear. Material modifications of polymers during radiation processing are well established,[1.31,1.32] however very little is known about the impact of UV radiation on polymers present in typical plasma discharges.[1.33] Novel phenomena due to reduced dimensions of nanoscale structures might have additional impacts on the plasma-surface interactions. In particular, the roughening behavior of surfaces has usually not been addressed in any model of plasma-surface interactions, since it has only become important as device dimensions shrunk significantly.

1.3 Experimental setup

1.3.1 Plasma processing

Plasmas perform the transfer of the image generated with the PR material into the substrate. This "dry etching" has the advantage of displaying highly anisotropic etch profiles, enabling the production of very high aspect ratio features.[1.34] A plasma is a partially ionized gas containing an equal number of positive and negative ions in addition to neutral and other species. Typical plasmas used in microelectronics manufacturing are weakly ionized plasma discharges, meaning that only a small fraction of the species in the discharge are actually ionized.[1.35] Typical ranges for plasma discharges are electron temperatures of a few electron volts (eV) ($k_bT_e \approx 1$-10 eV) and plasma densities in the range of $n \approx 10^8$-10^{13} cm^{-3}. [1.35-1.37] Related techniques extensively used in semiconductor manufacturing include applications such as plasma enhanced chemical vapor deposition or plasma enhanced ion implantation.[1.37-1.40]

Many different reactor configurations have been developed for processing of materials involved in semiconductor industry. Starting from reactive ion etching (RIE) to helicon or electron cyclotron sources, intensive research and development has lead to an increased understanding of plasma physics and the impact of the reactor geometry.[1.34,1.35,1.41,1.42] Since the focus of this work is the plasma-surface interactions rather than the physics of the plasma reactors itself, we limit ourselves to a short introduction of the two technologically most important reactor configurations, inductively and capacitively coupled sources. The desired properties of a plasma reactor are that there are two separate power inputs, where one input controls the

plasma density, whereas the other power input controls the ion energy of the discharge.

1.3.1.1 Inductive plasma sources

A schematic of the inductively coupled plasma (ICP) reactor used in this work is shown in *Fig. 1.7.* A planar coil is placed on top of a quartz window. By applying a RF current through the coil, an electromagnetic field is coupled into the vacuum below the window. Due to the low mass, the electrons are able to follow the varying electromagnetic fields at 13.56 MHz. The highly energetic electrons then lose their energy by ionizing collisions with gas atoms or molecules, generating a plasma. The heavy ions on the other hand, are not able to follow the RF field and so the applied inductive power is directly related to the plasma density. The electrons are heated by the electromagnetic fields, their direction is randomized due to collisions with neutrals. Characteristic electron temperatures of 3 to 5 eV and ion/neutral temperatures of 0.05 eV result. Electrons diffuse readily from the plasma generation area throughout the whole reactor vessel.

During the initial plasma ignition period, fast electrons charge the chamber walls and generate an electric field, which accelerates the ions but slows down the electrons. A space charge separation builds up on all surfaces of the plasma reactor; this is usually referred to as the plasma sheath. In our reactor configuration, the sheath thickness is of the order of 1mm. For all other areas within the plasma, the discharges can be considered quasi neutral. The potential difference over the sheath is usually 10-30 V, accelerating ions entering the sheath towards the negatively charged surface.

For the desired decoupling of ion energy and density, a second, capacitively coupled source is applied to the substrate electrode. By adjusting the average potential of the substrate to a more negative value, a net increase of the ion energy reaching the substrate can be achieved. Due to their very low contamination levels and high throughput, high density ICP sources are mostly used in front end of line (FEOL) applications.

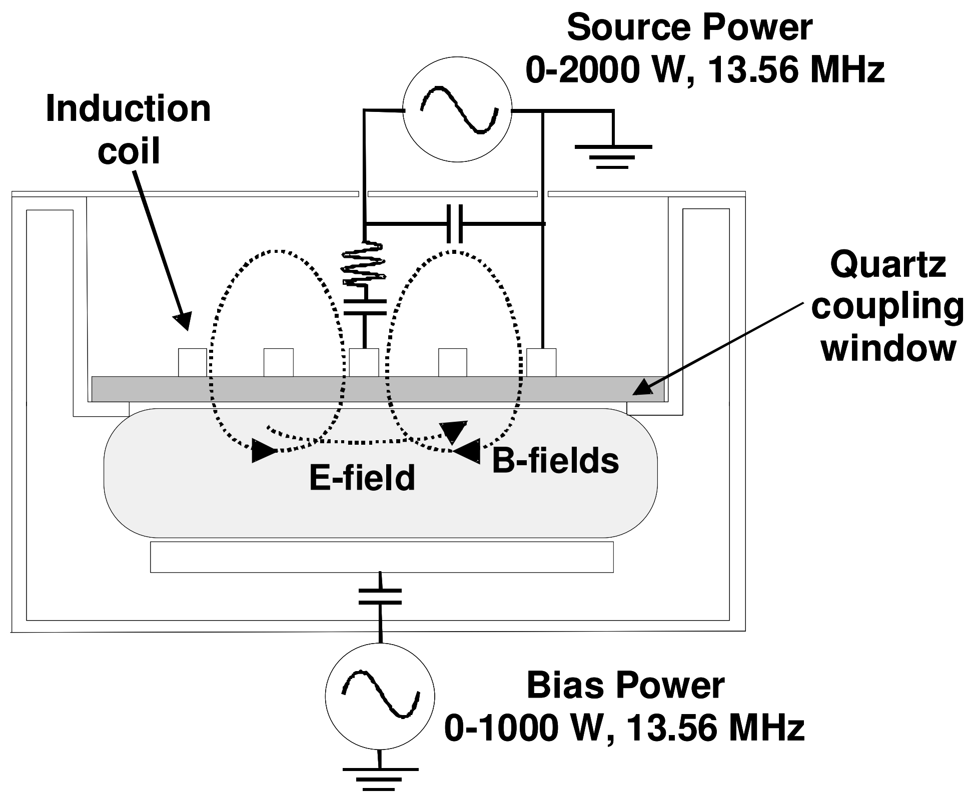

Fig. 1.7: *Schematic of the inductively coupled plasma reactor used in this work.*[1.43]

The ICP reactor in this work has been described in details before.[1.43] A RF current at 13.56 MHz, driven through the coil on top of a 1” thick quartz window, is coupled into the reactor vessel evacuated by a turbomolecular pump. A 300mm

bottom electrode is used for material processing, which is additionally capacitively coupled to a 13.56 MHz power supply for biasing. The bias electrode and the quartz window are separated by a gap of ~8cm, while the plasma generation is confined to 2-3cm below the window.[1.43] The chamber walls are maintained at 50°C during operation and a mesh around the electrodes at equilibrium temperature ensure stable discharge conditions and prevent extensive contamination by the chamber walls.[1.43] The process gas (50sccm) is injected from left side of the reactor, then passes through the vessel and is finally pumped out by the vacuum pump at the right side of the system. The bias electrode is cooled to 10°C to avoid temperature gradients in the samples due to plasma heating. A thermal paste was applied to the backside of the scribed wafer pieces. This procedure provided enough thermal contact to keep the sample close to the temperature set for the bias electrode.

1.3.1.2 Capacitive plasma sources

Parallel plate or capacitively coupled reactors have slightly different mechanisms of plasma generation. A high RF frequency is applied to control the plasma density. The electrons in the bulk plasma are accelerated by the applied RF field until they lose their energy due to collisions with other particles. In addition to this, secondary electrons are generated by bombardment of the substrates. These electrons are then accelerated into the plasma by the sheath. Another mechanism for plasma generation is that a stochastically moving sheath can increase the plasma density. Typically densities of 10^{9}-10^{11} cm^{-3} can be generated at pressures from 20-300

mTorr, which are slightly higher operating pressures than in inductively coupled plasmas. For the selection of the ion energy, a second, low frequency power supply is added to accelerate the ions. Because of their large mass, ions are not able to follow the rapidly changing excitation at the high frequency used for plasma density control. The low frequency RF power is able to increase the potential of the powered electrode, similar to the case for the inductively coupled reactor. Plasma and floating potentials in capacitively coupled plasmas can be very high, ranging from a couple tens to a couple hundreds of eV. This becomes an important factor when controlling contamination within the discharge. Medium density capacitive sources have shown better control of the chemical reactions in the plasma discharges and enable better sidewall control. The high aspect ratio Back end-of-line (BEOL) interconnect levels are mostly generated using capacitive sources.

The CCP reactor used for our photoresist studies was a Lam 2300 Exelan® dielectric etch system, which uses a high RF frequency at 27 MHz to excite electrons and a low RF frequency at 2 MHz to accelerate ions (see Fig. 1.8). The electrodes were 300mm in size and the gap between the electrodes was 2.3cm. A confinement ring around the electrodes (not shown) ensured stable plasma operation and reduced chamber contamination. The process gases were injected through a "showerhead" aperture array in the top electrode and pumped out using a turbomolecular pump at the bottom of the chamber vessel. The wafer substrate is clamped by an electrostatic chuck and 20 Torr Helium applied to wafer backside to ensure efficient heat transfer and to reduce thermal gradients in the samples.[1.8,1.42] The bottom electrode was cooled to 10°C. Significant differences to the ICP reactor used in this work include very high

gas flow rates, much larger peak and average ion energies during processing and significantly higher RF power density during processing leading to faster processing speed and a greater versatility of the reactor.

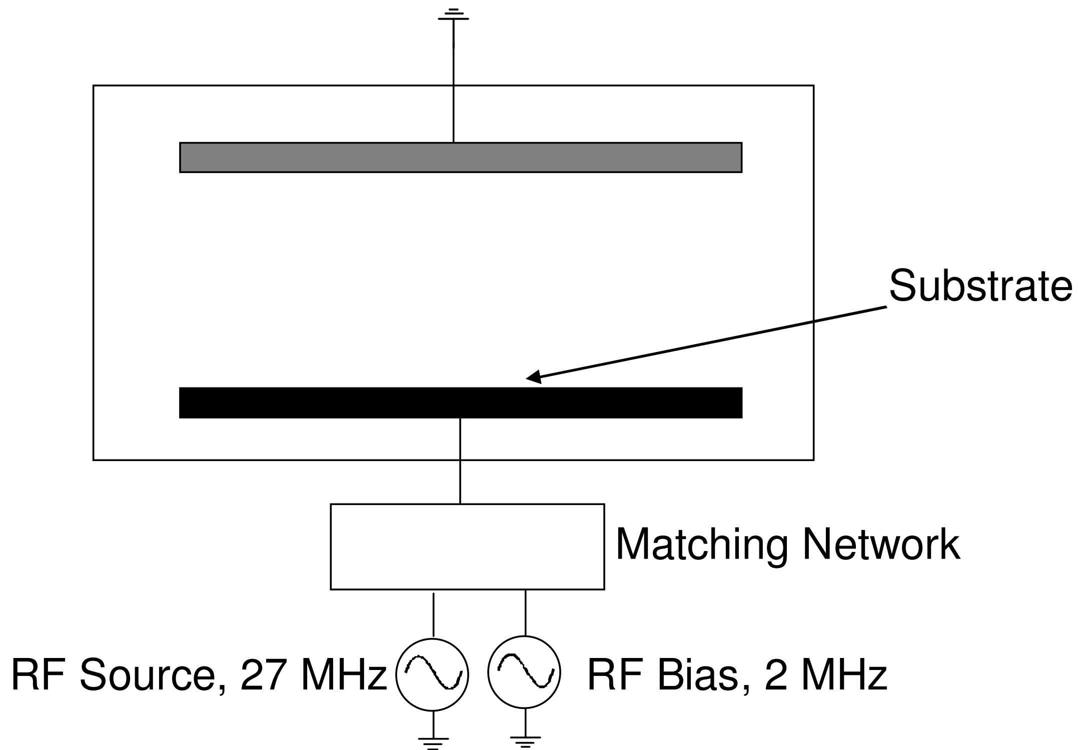

Fig. 1.8: *Schematic of the capacitively coupled plasma reactor used in this work.*

1.3.2 Surface analysis

After processing, the PR materials were analyzed using many surface analysis techniques. Requirements for these techniques are (1) that they be highly sensitive to thin films, (2) high spatial resolution and (3) that they be non destructive, due to the fragility of the polymeric materials.

Very high precision measurements of the film thickness are required during plasma processing. Furthermore, the thickness measurement has to be fast and should not interfere with the electrical properties of the plasma discharge. For measuring etch and deposition rates during processing, ellipsometry was applied to monitor film thickness and index. By measuring the change in polarization of light as it is reflected from a sample, refractive indices and thickness values of unknown thin films on a known substrates can be determined.[1.44]

The change in the near-surface (3-5nm) composition which is most affected during plasma processing is of great interest. In particular, incorporated fluorine detection is a critical issue for plasma processing. X-ray photoelectron spectroscopy (XPS) was used as a non-damaging technique to determine the elemental composition and chemical bonding of the PR films before and after processing. X- ray irradiation of materials leads to the emission of electrons from core orbitals ranging from depths of up to 10nm, and allows the composition of this part of the sample to be analyzed. The emitted electrons carry characteristic information, in the form of their energy spectrum, which identifies their environmental origin.[1.40,1.45-1.47]

The roughening of polymer films due to plasma processing became a critical issue in manufacturing when the semiconductor roadmap for technology began to call for producing features of nanoscale size. A highly resolving technology to measure and quantify this surface degradation was therefore needed. The surface morphology in this work was analyzed using an atomic force microscope (AFM).[1.2,1.40] By rastering a tip with very high spatial resolution over the surface, high resolution

images of the processed PR samples were obtained and numerically analyzed according to their height-variations (i.e. roughness).

AFM scanning of 3D structures is usually very time consuming and additionally specially manufactured tips are needed to reduce convolution-based artifacts in the measured data. Secondary electron microscopy (SEM) was used to image the topographic transformations of nanoscale patterned 3d structures. A focused beam of electrons is directed onto the specimen depositing the energy in a certain volume of the sample upon contact. The energy exchange between the electrons and the sample results in the emission of electrons and electromagnetic radiation each of which can be used to produce an image. By rastering the electron beam over a selected area, a high resolution image can be achieved[1.47]. Variations of patterned 193nm PR structures were examined by this technique. The acquired images were numerically analyzed using image software programs.

The stability of polymer structures in a plasma environment was monitored as a function of time by time of flight secondary ion mass spectroscopy (ToF-SIMS).[1.40,1.45] A highly collimated beam of ions is directed towards the sample. The surface then emits material through a sputtering process. The ion masses are usually detected at very high resolution and are therefore characteristic of their molecular structure and are ideal to measure compositional changes in the PR materials.

1.4 Experimental approach

The results presented here build the core of the collaborative efforts of PI Prof. Gottlieb Oehrlein and Co-PI's Prof. David Graves and Dr. Eric Hudson under NSF grant # DMR 0406120 entitled "GOALI (Grant Opportunity for Academic Liaison with Industry) Interactions of Plasmas/Energetic Beams with Organic Masking Materials".

Project member	Group	Tool	Task
UMD	Oehrlein	ICP reactor Ellipsometry XPS (in UHV)	• Plasma processing • Etch/deposition rates • Chemical information
	Phaneuf	AFM	• Surface morphology
UCB	Graves	Ion beam reactor AFM	• Beam processing • Surface morphology
Lam Research	Hudson	CCP reactor AFM	• Commercial processing • Surface morphology • State of the art materials processing
RHEM	Andes	PR spin coating Lithographic scanner SEM	• Material synthesis • State of the art resist knowledge • 3D sample topography
ITC-Irst	Anderle	ToF-SIMS	• Chemical information

Table 1.1: *Overview of groups and tasks in the GOALI project.*

To examine the novel effects of plasma-polymer interactions, we examined a broad set of PR materials under a wide range of plasma conditions at the University of Maryland. Through exposure in well modeled and characterized etch reactors at

the laboratory for plasma processing of materials (LPPM), molecular understanding of the plasma-polymer surface interactions could be obtained. We obtained additional insights through exposures in complementary ion and/or radical beams as well as UV radiation exposures at the laboratories of Prof. Graves at the University of California in Berkeley. The results of ion and neutral beam exposure, photon radiation and synergistic effects of these fluxes can be found in a separate publication.[1.48] Exposures of the PR materials under similar plasma conditions in commercial etch reactors at Lam Research ensured that our findings are generally applicable and not dependent on reactor configuration or geometry. A complete overview of the groups and tasks involved in this work is shown in Table 1.1.

1.4.1 Laboratory for plasma processing of materials (UMD)

Most experiments were performed in the laboratory for plasma processing of materials (LPPM) at the University of Maryland in College Park. The plasma exposures were performed in an inductively coupled plasma reactor, which is connected to a cluster system. After processing, the samples were either exposed to atmosphere to perform ex-situ analyses, including ellipsometry, AFM, SEM or ToF-SIMS. Alternativly, they were transferred in-vacuum to a VG ESCA Analysis Chamber for XPS analysis. A schematic overview of the lab setup is given in Fig. 1.9.[1.49] The chamber conditions were routinely checked using complementary measurements.[1.50]

In addition to the experimental methods described, a modified exposure mode in the ICP chamber was used for highly controlled time-dependent experiments. Stabilization periods for conventional plasma discharges might typically take up to 30s. This is well past the time resolution required to study polymer interactions. A special experimental technique, the shutter approach[1.51] was used to overcome this problem and shed light on those early transformations. Previous studies showed that the perturbation of the plasma sheath due to the shutter setup were negligible. Surfaces covered by the shutter received a flux of about one monolayer of neutrals due to diffusion of the plasma species under the shutter during the stabilization period.

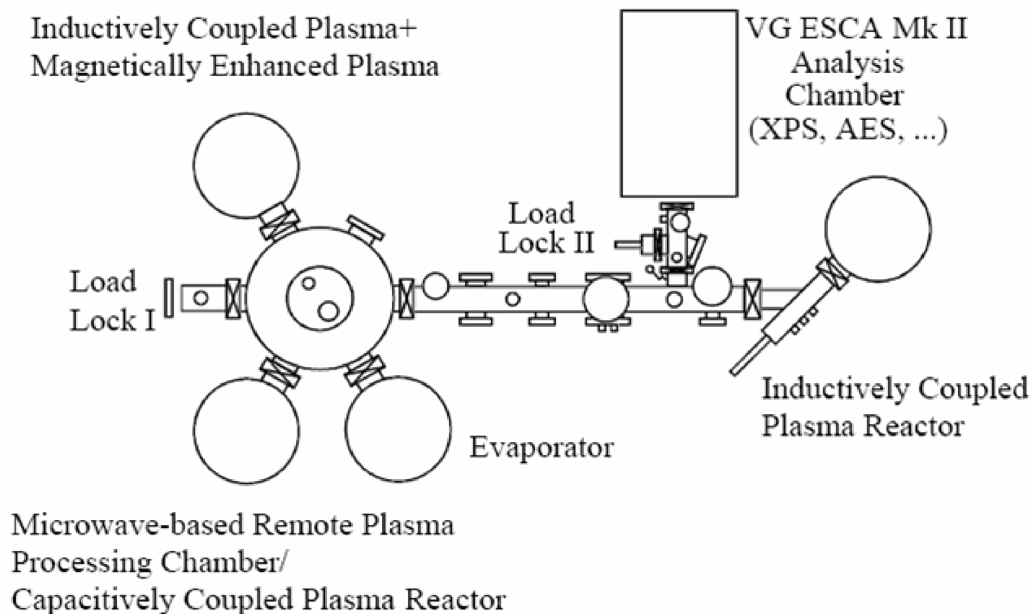

Fig. 1.9: *Schematic Overview of LPPM.*[1.49]

1.4.2 Other Laboratories

As shown in Table 1.1, the surface characterization by AFM was performed in several different locations involved in this project. The consistency of the measurements between each other was experimentally confirmed.

The ion beam exposures reported in Chapter 2 were performed in the lab of Prof. Graves by Dustin Nest at the University of California-Berkeley. ToF-SIMS experiments were performed at ITC-IRST in Italy by Paolo Lazzeri. The SEM imaging of the plasma processed samples was supervised by Dr. Cecily Andes at RHEM in Marlborough, MA. She also provided us with the already spin coated PR wafers used for our studies in College Park, Berkeley and Fremont.

Additionally, selected experiments have been performed at Lam Research using a Lam 2300 Exelan© dielectric etch system. Experiments similar to the findings in chapters 2,4 and 5 were chosen to complement the studies performed in LPPM and compare our results to findings in an industrial setting. Even though significantly higher power densities were used during commercial processing, the process result trends using the Lam Exelan® chamber were very similar to our findings reported in chapters 2,4, and 5, leading to the conclusion that our findings are broadly applicable and not reactor or discharge-specific. No significant new insights were obtained in these experiments and they are therefore omitted in this thesis.

1.5 Outline of thesis

The studies of plasma-surface interactions in plasma reactors were approached systematically. The findings were divided into four chapters: Chapter 2 describes the plasma-surface interactions as a function of processing time as well as polymer material. Chapter 3 is a short communication of the roughening model developed to describe the photoresist-plasma interactions. Chapter 4 describes the plasma surface interactions for different processing parameters and chapter 5 discusses the influence of different plasma chemistries on the plasma-surface interactions.

General modifications seen for all polymeric materials due to plasma exposure are described in chapter 2. Selective loss of O and H during the first seconds of exposure coincides with an increased introduction of roughness. Steady-state conditions for later processing times are characterized by low roughening and removal rates. The damage for different polymer materials is based on stoichiometry as well as the behavior under radiation from the plasma. A characteristic relation of the surface fluorination introduced to the introduced roughness could be observed. Equivalent exposure of polymers to ion beams only generated no damage, indicating that ions, fluorination and radiation are responsible for plasma damage.

The roughening model for polymers in plasma processing is discussed in chapter 3. Based on the polymer specific roughening rates and discharge and polymer specific etch yields, characteristic roughness forms on the polymer surface, which can also be related to sidewall roughness evolution.

Chapter 4 examines the impact of the plasma properties on the observed results. The damage due to ion bombardment and plasma fluorination could clearly be identified. A roughening model based on the energy density required to remove a unit volume of material was developed. Results obtained over a widely varying plasma parameter space the surface roughening behavior could be described by a simple universal relationship and only depended on one material-dependent parameter, suggesting that the molecular structure of the PR material plays an overriding role in plasma-induced PR modifications.

Chapter 5 extends the study to that of the impact of different discharge chemistries. The different plasma chemistries affected the removal and roughening characteristics greatly. Due to changes in the surface chemistry, different etch mechanisms were observed, which were consistent with the roughness model presented in chapter 4. An increase in ion-induced removal seen for very reactive plasma chemistries was accompanied with smoother surfaces due to much smaller energy densities possible for those conditions which yielded very high etching yields.

Finally, chapter 6 summarizes the main conclusions of this thesis.

Chapter 2:

Plasma-Surface Interactions of Model Polymers for Advanced Photoresists Using C_4F_8/Ar Discharges and Energetic Ion Beams

J. Vac. Sci. Technol. B, 25, 1353 (2007)

S. Engelmann, R. L. Bruce, T. Kwon, R. Phaneuf, G. S. Oehrlein, Y. C. Bae, C. Andes, D. Graves, D. Nest, E. A. Hudson, P. Lazzeri, E. Iacob and M. Anderle

ABSTRACT

Plasma based transfer of photoresist (PR) patterns into underlying films and substrates is basic to micro- and nano-fabrication, but can suffer from excessive surface and line edge roughness in the photoresist and resulting features. We have studied the interaction of a set of adamantyl methacrylate-based model polymers with fluorocarbon/Ar discharges and energetic Ar^+ ion beams. Through systematic variation of the polymer structure, we were able to clarify the contributions of several critical polymer components on the chemical and morphological modifications in the plasma environment. Etching rates and surface chemical and morphological changes for the model polymers and fully formulated 193 nm and 248 nm photoresists were determined by ellipsometry, atomic force microscopy, time-of-flight static secondary ion mass spectrometry and x-ray photoelectron spectroscopy.

The polymer structure in the near-surface region (~10 nm) of all materials is destroyed within the first seconds of exposure to a fluorocarbon/Ar plasma. The plasma induced changes include destruction of polymeric structure in the near surface

region, oxygen and hydrogen loss along with fluorination. For the 193nm PR material, the initial densification of the near-surface region was followed by introduction of pronounced surface roughness. This change was not seen for 248 nm PR processed under identical conditions. When comparing the responses of different polymer materials, we observed a strong dependence of plasma-induced surface chemical and morphological changes on polymer structure. In particular, the adamantane group of 193nm PR showed poor stability under plasma exposure. On the other hand, the plasma induced changes for polymer resins with or without the low molecular weight chemicals required to make the photoresist system photoactive did not differ significantly.

The behavior of the same materials during energetic argon ion beam bombardment was also investigated. No significant differences in etch yield and surface roughness evolution for the different materials was seen in that case.

2.1 INTRODUCTION

In order to shrink semiconductor device dimensions to the nanoscale, shorter lithographic exposure wavelengths are required for photolithographic patterning. Since the size of the resin molecules used in photoresist materials is about 3-5 nm, critical dimensions of 50 nm and below requires molecular level control of photolithographic and follow-on processes, e.g. plasma based pattern transfer[2.1]. The design of photoresist (PR) materials becomes of critical importance for achieving controlled nanoscale patterning. Until recently, 248nm photolithography has been the workhorse for micro and nanopatterning of materials in advanced semiconductor fabrication[2.2]. While PR materials used for 248nm photolithography employ etch resistant aromatic ring structures, these can not be used for 193nm lithography due to the strong optical absorption of the carbon double bonds and conjugated bonds[2.3,2.4].

Previous work has shown that fluorine based pattern transfer[2.5-2.7] processes which are successful for 248nm PR can introduce problems for 193nm PR that include high etch rates, "pinholing" and formation of surface/line edge roughness[2.8-2.10]. Several material platforms have been tested for 193nm lithography, and methacrylate-based materials have been the most promising candidates[2.2,2.3,2.11]. Further improvements have been achieved by introducing etch resistant groups into the overall polymer structure, e.g. adamantyl[2.12,2.13]. Other issues investigated for advanced photoresist materials are the difference in dissolution behavior[2.14] and the increased exposure dose required at shorter wavelength[2.15]. Studies have been performed to link chemical properties, (e.g. carbon/hydrogen content, cross-

linking/chain scission (G)[2.16] values) to properties observed as a result of plasma exposure[2.17].

Still, the fundamental mechanisms causing photoresist degradation remain unclear. One of the contributing factors is that for conventional plasma processing conditions, the stabilization period of the discharge can take up to 30 s[2.5], well past the required time resolution to study polymer modifications. In this work we used a shutter approach[2.18] which allows a minimum controlled exposure time of about 1 s to overcome this problem.

The present study is an effort at laying the groundwork for understanding the role of specific polymer components in controlling the response of the PR material when interacting with fluorocarbon plasmas used for pattern transfer. We initially present a review of the design of 193nm PR materials and critical elements of plasma discharges used for pattern transfer. This knowledge is required to understand the approach of the current study, and helpful in the interpretation of the observed results. Our results are presented in three sections, where each section has been designed to answer specific questions.

The goals of our studies were the following:

a) Establishing the modifications of the chemical composition and roughness of the polymer surface region in a C_4F_8/90% Ar plasma as a function of time,
b) Clarifying the influence of different polymer structures on the above modifications,
c) Comparing the behavior of the same materials when exposed only to Ar^+ ion bombardment.

2.2 EXPERIMENTAL

2.2.1 Description of Materials

In 193nm lithography, light exposure causes an acid-catalyzed reaction in chemically amplified photoresist materials by converting ester groups into carboxylic acids. This renders the exposed areas aqueous base-soluble[2.19]. One concern is that the high strength acid required to remove the ester groups[2.20] might cause additional problems in the etch properties of the photoresist[2.21]. The *leaving group* in the polymer contains the acid sensitive constituent that enables the conversion of the photoresist from aqueous base-insoluble to aqueous base-soluble. The challenge in materials selection is to identify polymers capable of acid-catalyzed switching of solubility while being transparent to an exposure wavelength of 193 nm.

Various polymers used in 193 nm photoresists were provided by Rohm & Haas Electronic Materials for the present study. Three model polymers similar to those used in advanced photoresist materials were studied, along with fully formulated 193nm and 248 nm photoresist systems. Additionally, one core homopolymer was used. By interacting well characterized plasmas with the model compounds[2.22], and fully formulated photoresist systems derived from the model compounds, we were able to provide a number of basic insights on plasma-photoresist interactions.

The model compounds tested contain a *ter*-polymer structure, consisting of three basic components used for methacrylate photoresist polymers (see Fig. 2.1)

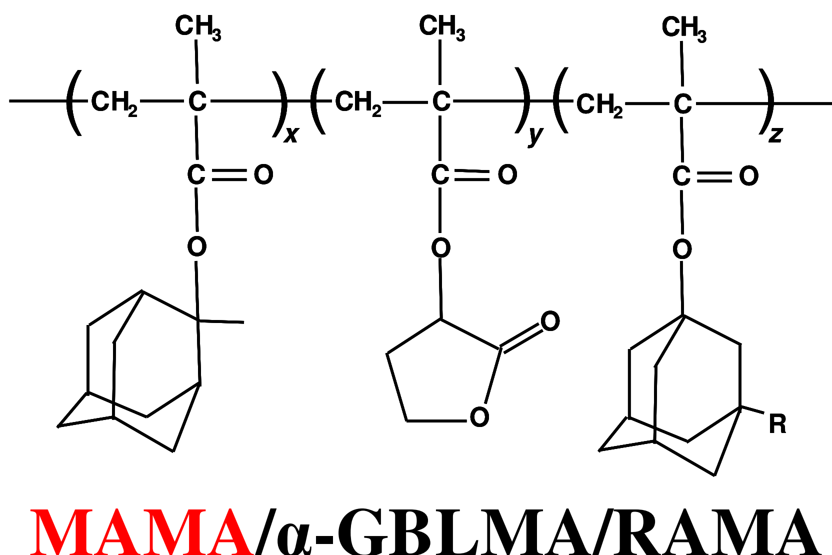

Figure 2.1: *Molecular structure of the MAMA/GBLMA/RAMA reference compound.*

The *leaving group polymer* provides the ability to switch the photoresist polarity from an insoluble state into an aqueous base-soluble. Due to the reaction with the photo-generated acid, the adamantyl group is removed resulting in deprotection and conversion of the ester into carboxylic acid. The *lactone group* in the polymer improves the solubility of the photoresist after exposure. However, the high oxygen content of the lactone group can reduce plasma etch resistance[2.21]. The *polar group* consists of a R-functionalized adamantane structure and improves the base solubility of the photoresist. The final ingredients of 193 nm photoresists are the *photoacid generator (PAG)* and the *base*. UV photon bombardment of the PAG generates acid, which diffuses through the polymer and attacks the leaving group during post-

exposure bake. The base limits diffusion of the acid throughout the film and thus controls the amount of acid that reacts with the polymer to prevent deprotection of the polymer beyond regions defined by the original photoimage[2.21].

The reference compound which serves as the basis of the materials tested in the present work is shown in Fig. 2.1. It consists of a methyl adamantyl methacrylate in the leaving group (MAMA), an α-gamma butyrolactone methacrylate in the lactone group (GBLMA) and R-functionalized adamantyl methacrylate in the polar group (RAMA)[2.22]. This polymer structure is typical of common 193nm PR materials. In this article we refer to this model compound as *MAMA*.

The first modification of the reference compound MAMA is to change the leaving group to ethyl adamantyl methacrylate (EAMA) and is shown in Fig. 2.2(a). As discussed before, the leaving group in the 193nm PR material acts like a "switch" for the photoresist upon exposure. By changing the structure of the leaving group, the sensitivity of the polymer to the photogenerated acid can be manipulated. The compound shown in Fig. 2.2(a) is referred to as *EAMA*.

The second modification is aimed at studying the effect of replacing a methacrylate with an acrylate group in the MAMA reference compound. In order to keep the change in the chemistry as small as possible, only the polar group was changed into an acrylate. This is shown in Fig 2.2(b). Heat treatment was found to crosslink this polymer, whereas the methacrylate compounds exhibited chain scission[2.11,2.22]. 248nm PR showed slight crosslinking behavior after UV-exposure[2.15], and improvement of the etch characteristics for this compound might be expected. We will refer to this compound as *RADA* (Fig. 2.2(b)).

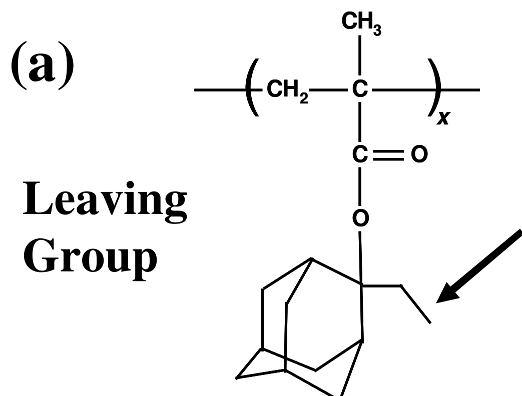

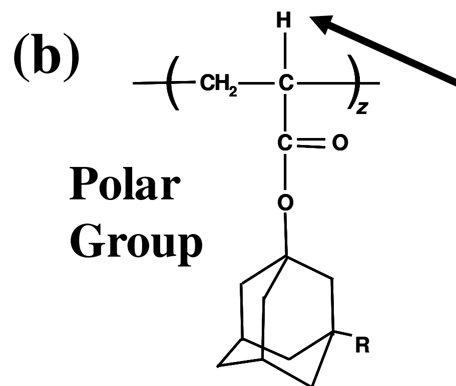

EAMA/α-GBLMA/RAMA **MAMA/α-GBLMA/RADA**

(c)

1.) 96.8 wt%:
MAMA/α-GBLMA/RAMA
2.) 3 wt%:
TPS-PFBS (PAG)
3.) 0.2 wt%:
TOA (Base)

Full Formulation

193nm PR

(d)

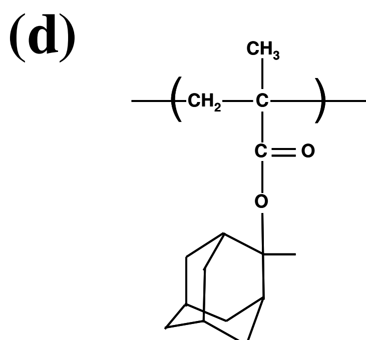

p-MAMA

(e)

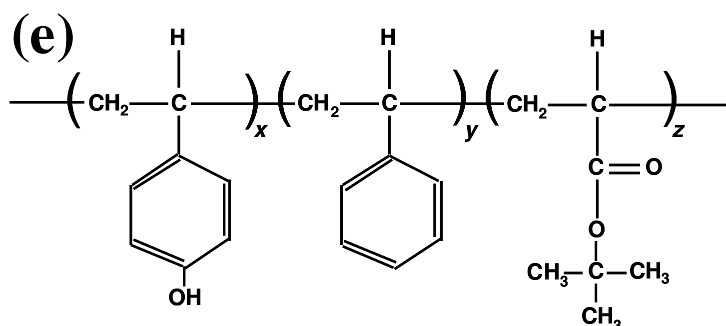

PHOST/PS/TBA

Full Formulation

248nm PR

Figure 2.2: *Molecular structures of (a) EAMA/GBLMA/RAMA, (b) MAMA/GBLMA/RADA, (c) Full Formulated 193nm Photoresist, (d) p-MAMA and (e)Full Formulated 248nm Photoresist.*

The model compounds shown in Figs. 2.1 and 2.2 (a) and (b) are not actual photoresists since they lack PAG and a base. The material specified in Fig. 2.2(c) was used to explore the effect of additives used in full photoresist formulations on plasma etch performance. The polymer used for this fully formulated chemically amplified photoresist is identical to the reference *MAMA* shown in Fig. 2.1. The additional chemistry present for the full formation are the photo acid generator and base (Fig. 2.2(c)). The PAG (triphenyl sulfonium perfluorobutylsulfonate) has a higher absorption at 193 nm due to its aromatic structure. However, since it is only present in small quantity (<5 wt %), it is compatible with good overall lithographic performance. The base polymer is trioctyl amine (TOA). The material specified in Fig. 2.2(c) will be referred to as *193nm PR*.

To further investigate the effect of the adamantyl structure on the actual etch performance, we also studied poly-methyladamantylmethacrylate (p-MAMA) – see Fig. 2.2(d) - for comparison with the other materials. It may be expected that the resulting modifications of this homopolymer during plasma etching could play an important role in plasma etch performance of the model compounds, since it is used as one of the key groups in the resin formulation. This material will be referred to as *p-MAMA*.

To compare the behavior of the above model compounds with a well established photoresist material, we also used a fully formulated 248 nm photoresist in this study (Fig. 2.2(e)). The 248 nm PR contains three functional groups, including highly etch resistant hydroxystyrene, styrene and t-butylacrylate. The photoresist switch employed in this compound is t-butylactrylate, and ester elimination converts

it to aqueous base soluble. Just like the 193 nm PR, this resin also has small chemical additions in form of a PAG and a base to generate a photoresist system. This material will be referred to as *248 nm PR*.

"Blanket" films of all materials were coated on Si wafers with a resulting thickness of 400 nm. This was followed by a 1 min soft bake at 120˚C to drive off solvents from the materials.

2.2.2 Plasma Processing

The inductively coupled plasma reactor used in this study has been described in previous publications of this group[2.23]. A planar coil is placed on top of a quartz window and powered through an L-type matching network at 13.56 MHz with a power supply (0-2000W). Ion bombardment of a 300 mm diameter substrate can be independently controlled using another 13.56 MHz source (0-1000W). The temperature of the electrode was fixed at 10°C using a cooling liquid. The total gas flow rate was maintained at 50 sccm. 10 mTorr operating pressure was achieved through an automatic throttle valve in the exhaust line. Before each experiment, the chamber was dry cleaned using an O_2 plasma followed by one-minute chamber seasoning applying the conditions for the next experiment. A thin metal mesh around the discharge region was used to ensure stable process conditions. The temperature of the chamber walls was set to 50°C using heating straps. For time resolved studies, we used a shutter approach in the gradient exposure mode described previously[2.10,2.18].

All materials were exposed to argon/fluorocarbon discharges (C_4F_8/90%Ar), which is close to standard industrial processes used for pattern transfer and has been

well characterized for dielectric etch processing [2.13,2.24,2.25]. For commercial oxide etch processes based on mixtures of fluorocarbon gases and Ar, Ar^+ ion bombardment provides an effective material removal rate, while a small amount of fluorocarbon gas like C_4F_8 is added to passivate the sidewalls and enable etching selectivity[2.26]. Together, they make possible high selectivity etch processes typically used for high-aspect ratio or contact hole etch[2.27,2.28]. In this work we have used discharges fed with C_4F_8/Ar gas mixtures in an ICP reactor using process conditions that have been thoroughly characterized and modeled[2.29-2.32]. Based on laser-diode IR laser absorption work, compositional and energy resolved analysis of the ion flux and calibration of the mass spectrometer data using a Langmuir probe, absolute data on the important radical (CF, CF_2 and COF_2) and ion fluxes are available in this system as a function of processing conditions. The C_4F_8/Ar system allows us to vary the surface flux conditions from neutral-dominated conditions (e.g. the CF_2/ion flux ratio can be greater than 70 in pure C_4F_8) to ion-dominated surface flux conditions (for C_4F_8/90% Ar, 70% of the total ion flux is Ar+, and the ion/neutral flux ratio is greater than 1). The latter process conditions were used here[2.29,2.30,2.33]. Although commercial pattern transfer discharges typically contain oxygen for sidewall control, this component was omitted in our studies to examine the modifications of the oxygen in the photoresist itself. The source power applied was typically 800 W, and the RF bias power was adjusted to achieve a DC self bias voltage of -100 V. These conditions remain the same for sections 2.3.1 and 2.3.2 unless otherwise noted, and will be referred to as "standard" conditions. Changes in the inductive power from 800 W to 1000 W yielded near-identical results.

The ion beam experiments have been performed where the vacuum chamber is maintained at a base pressure of $5x10^{-8}$ Torr pumped by a 2000 Ls-1 turbomolecular pump (Seiko Seiki STP H2000C). Argon is introduced into a differentially pressured commercial ion gun (PHI 04191) raising the pressure of the main chamber to $5x10^{-7}$ Torr. The four resists were bombarded with 500 eV Ar+ at normal incidence with a beam flux of ~4.0 $\mu A.cm^{-2}$. The spot size of the ion beam was about 5x5mm. The ion flux onto the sample was measured by a Faraday cup. After processing the samples, they were measured to determine the thickness loss due to the ion exposure. The results have then been normalized to the received ion dose to determine an average etch yield assuming a polymer density ρ of ~ $1 g/cm^3$.

The ion beam experiments have been performed in comparison to the C_4F_8/90% Ar discharges, where the majority of the ion flux (>70%) are Ar+ ions[2.34]. Furthermore, plasma species contain reactive ions, FC radicals, metastables, etch products and trace oxygen from the quartz window. Other differences include the shape of the ion energy distribution and the interaction of the etch chemistry with ion activation at the surface. The ion beam experiments allow isolating the effects due to the argon ion bombardment and are therefore able to provide further important details.

2.2.3 Surface Characterization

After processing, the materials were analyzed using various surface characterization techniques.

Single wavelength ellipsometry using a 632.8 nm He/Ne laser with a rotating compensator in the polarizer-compensator-sample-analyzer (PCSA) configuration was used to determine thin film etch rates as well as refractive indices. The change of the refractive index is used as a measure of a broad number of polymer surface and materials modifications introduced by the plasma exposure.

The thickness loss of the ion beam exposed samples was measured with a Nanometrics Nanospec/AFT Model #010-0180, which was used to calculate the average etch yield.

X-ray Photoelectron Spectroscopy (XPS) analysis was performed at 90° and 20° electron take-off angle relative to the surface using a non-monochromatized Al-Kα x-ray source (1486.5 eV). The etched samples were transferred in ultra high vacuum into a Vacuum Generators ESCA Mk II surface analysis chamber, where the pass energy of the hemispherical analyzer was set to 20 eV. The charging of the samples was compensated by setting the position of the C-C/C-H peak to 285.00 eV and adjusting all other binding energies with a fixed charge correction. Intensities were obtained by least-square fits of Gaussian peaks after background correction using a Shirley background and the full width half maximum (FWHM) of fitted individual carbon species was fixed at 2eV. Elemental ratios were obtained by using cross sections and mean electron escape depths of specific elements[2.35]. The spectra shown in the figures below were obtained at a 90-degree detector angle with respect to the sample surface.

Atomic Force Microscopy (AFM) measurements were performed on both gradient and homogenously plasma etched samples as well as ion beam-exposed

samples. The scan size for all measurements was fixed at 2x2 μm^2. The surface roughness values reported were calculated from the root mean square (RMS) of the surface profile after the measurement.

Time of Flight Static Secondary Ion Mass Spectroscopy (ToF-SSIMS) was performed using a pulsed 15keV Ga^+ beam scanning an area of 300x300 μm^2 on selected gradient plasma etched samples.

2.3 RESULTS

Section 2.3.1 describes the temporal evolution of the material modifications in the C_4F_8/90% Ar discharge, whereas section 2.3.2 describes the effects of exposing different polymer structures to the same discharge. Finally, section 2.3.3 reports about the results of energetic ion beams onto the resists under pure Ar^+ ion bombardment.

2.3.1 Structural and morphological changes upon plasma exposure

To test the macroscopic response inside the plasma, ellipsometry measurements have been applied to monitor the etch resistance as well as the index of the photoresist materials using a single layer interpretation of the measured psi/delta values. Figure 3 displays the etching rate (a) and the change of the refractive index (b) of the RADA polymer as a function of plasma processing time. The behavior seen for the RADA polymer, with acrylate incorporation, agrees well with previous studies[2.9,2.10], with regard to both etch rate and refractive index evolution with exposure time. The etch rate starts out at an initially higher value and drops within the

first 10-20 s of plasma exposure to reach a steady state value. The behavior displayed in Fig. 2.3(a) is a characteristic response of the resist material to constant plasma etch conditions. These results suggest that a modified layer forms on the photoresist due to the plasma surface interactions. Figure 2.3(b) displays the change in refractive index with time and is characteristic of 193nm PR materials[2.9,2.10]. The refractive index of the RADA material initially increases. This is seen for all polymers studied, and also observed for the 248nm PR. A possible interpretation of the refractive index increase is densification of the polymer due to hydrogen and oxygen depletion caused by plasma attack. After this initial index increase, the refractive index for 193nm PR materials drops. Compositional physical changes that could explain this are fluorination of the polymer and introduction of severe surface roughness.

The time scale of materials modifications is short relative to the total time required for a typical plasma etching step. Combining the capability of temporal "printing" using the shutter approach with the high spatial resolution of ToF-SSIMS, allows the examination of PR chemical modifications for plasma exposure timescales never tested before. Because of its limited probing depth, this method is an excellent technique to study the evolution of the near surface chemistry, where the interaction of plasma particles with the photoresist material is expected to be highest. Using ToF-SSIMS we monitored selected ions representative of the different functional groups in 193nm PR materials for the first 30 sec of plasma exposure. For instance, the leaving group (MAMA), the lactone group (GBLMA) and the PAG (PFBS) all exhibit severe changes at the sample surface due to the interaction with the plasma.

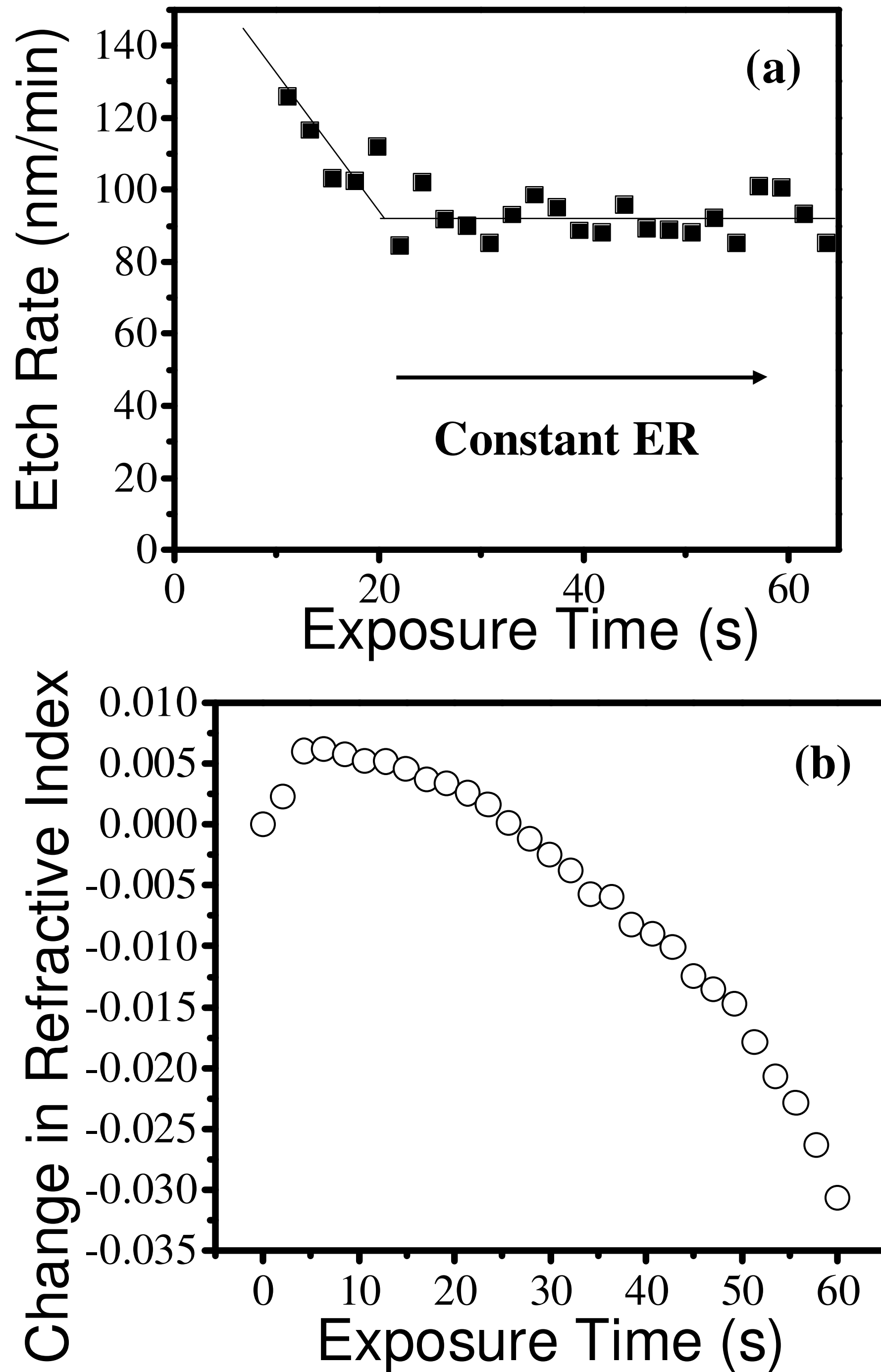

Figure 2.3: *Time evolution of resist etch rate(a) and refractive index change (b) during C_4F_8/90% Ar plasma etching for RADA compound. The discharges were generated using 1000W source power, a pressure of 10 mTorr, 50sccm total gas flow and a fixed self bias voltage of -125 V. The lines (a) are inserted as a guide for the eye.*

All PR characteristic ion intensities drop immediately after exposure of the PR material to the plasma and reach background values within several seconds and can no longer be detected for the modified PR surface. All materials studied showed a similar behavior as a function of plasma exposure time.

The chemical evolution of the photoresist materials was also analyzed using x-ray photoelectron spectroscopy (XPS). Just as for the ToF-SSIMS technique, XPS is characterized by a limited probing depth. Due to ultra high vacuum transfer of the plasma-exposed PR specimens from the plasma processing chamber into the UHV analysis chamber we can be confident about the surface chemical evolution seen in these studies, since secondary modifications, e.g. due to air exposure, can be neglected. Also, the ability to examine the fluorination of the materials in detail yields new insights. Figure 2.4 shows typical C 1s photoemission high resolution spectra of the MAMA polymer obtained by x-ray photoelectron spectroscopy. The unexposed material is displayed in Figure 2.4 (a). The major peak at 285.00 eV can be identified as C-C/C-H bonding. Two further peaks are required to account for the chemical shifts introduced by C-O-C bonding (at 286.5 eV) and O-C=O (at 289 eV). The same polymer after exposure to a C_4F_8/90% Ar plasma is shown in Fig. 2.4 (b). The initial C-C/C-H peak intensity has dropped and the carbon-oxygen peak intensities are diminished relative to the as received materials. Additional peaks were required to fit the data, and account for formation of CF_n groups due to plasma-induced fluorination of the material. The position of the C-CF_x peak was set to 286.6 eV, whereas the position for C-F, C-F_2 and C-F_3 were fixed at 287.9eV, 290.3 and 292.65 eV, respectively. These spectra indicate that the carbon bonds rearrange due to fluorine

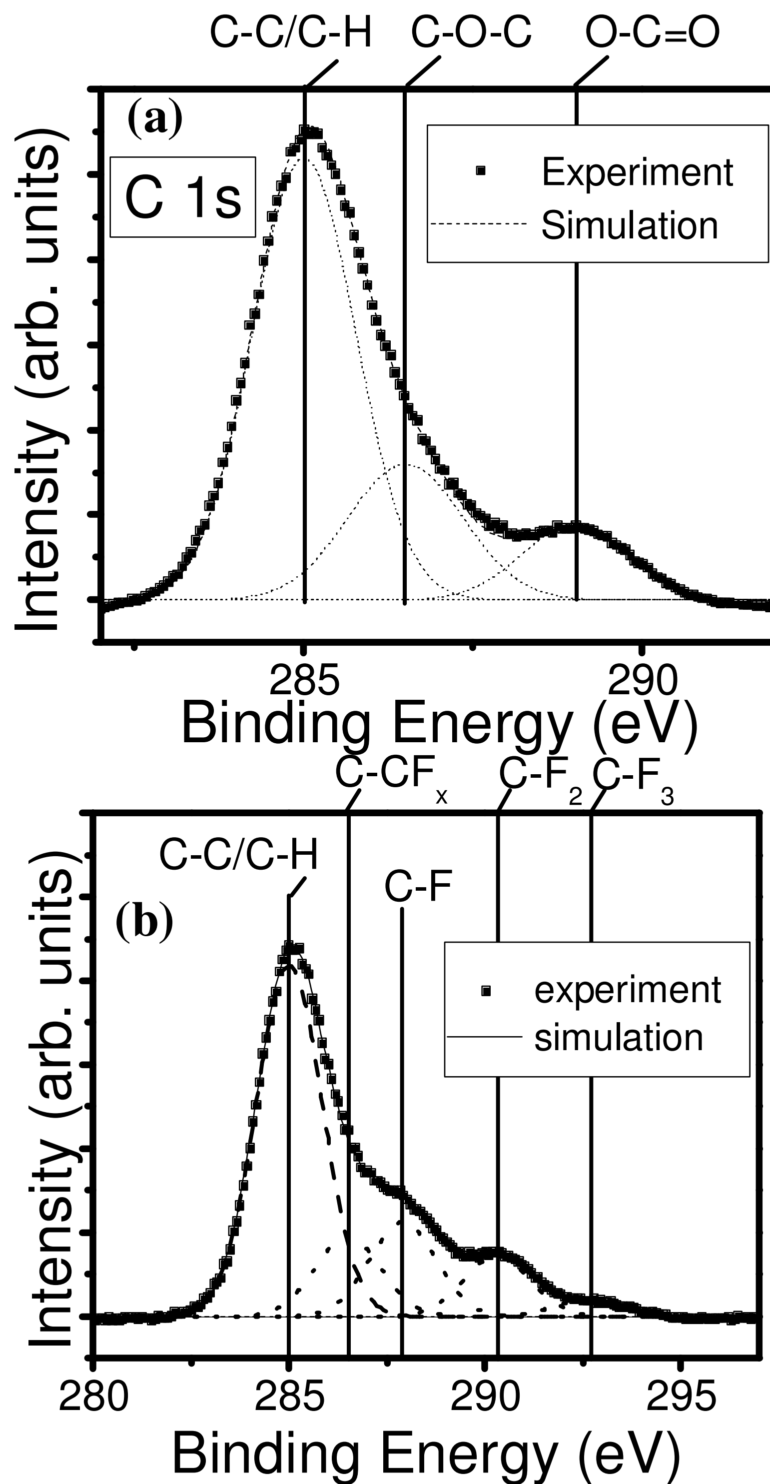

Figure 2.4: *High resolution XPS C1s spectra of MAMA compound before (a) and after (b) 60 sec. exposure to a C_4F_8/90% Ar discharge. The discharges were generated using 800W source power, a pressure of 10 mTorr, 50sccm total gas flow and a fixed self bias voltage of -100 V.*

and ion attack, forming a fluorinated carbon layer on top of possibly unmodified material. No significant difference in the appearance of the C 1s spectra was observed for different plasma exposure times of 15 s and longer. It should be noted that the intensities for both the O 1s spectrum and the carbon-oxygen moieties within the C 1s spectrum indicated that the oxygen content of the exposed compound dropped significantly upon plasma treatment.

Estimating the oxygen content from peak-fitting the C 1s spectrum introduces some uncertainty due to the fluorine penetration of the material and the overlap of the oxygen-carbon peaks and the fluorine-carbon related peaks. Examination of the corresponding oxygen 1s spectrum yields valuable insights. Figure 2.5 shows the evolution of the O 1s spectrum for the same samples used in Fig. 2.4. The O 1s spectrum has been peak-fitted in the same fashion as performed by Ben Amor et al.[2.36] for PMMA. The peak fits account for the carbonyl group (C=O) at 532.3 eV, bridging ether oxygen, -OH or plasma-related oxygen at 532.7 eV, and the singly bonded carboxylic oxygen (C-O-C) at 533.8 eV. A clear decrease in all intensities can be observed. Just like the C1s spectra, the O 1s spectra also did not show further significant changes for exposure times greater than 15 s. The results obtained from both, ToF-SSIMS and XPS indicate a significant transformation of the surface region has occurred in the photoresist material as a result of plasma exposure.

Additional information about the magnitude of the effects seen in Figs. 2.4 and 2.5 could be extracted from the elemental ratios as determined by the XPS measurements. Figure 2.6 displays the calculated F/C and O/C ratios of the model compound after plasma exposures for different times.

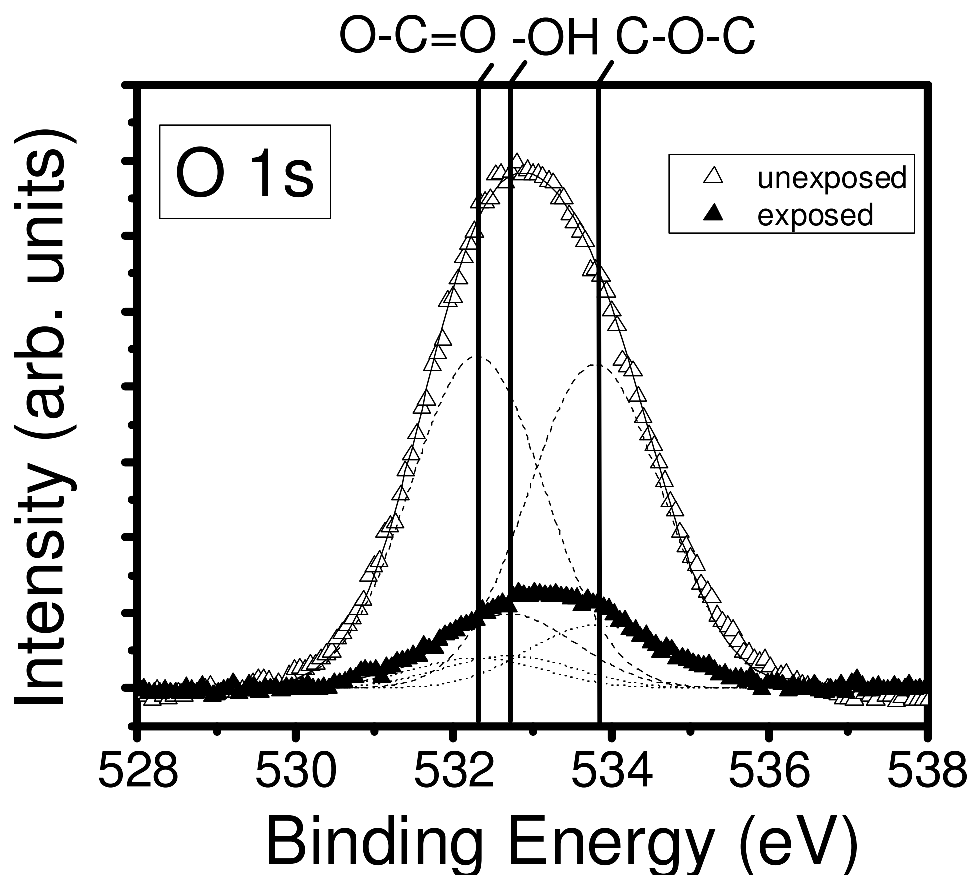

Figure 2.5: *High resolution O1s XPS spectra of MAMA compound before and after processing in a C_4F_8/90% Ar discharge. The discharges were generated using 800W source power, a pressure of 10 mTorr, 50sccm total gas flow and a fixed self bias voltage of -100 V.*

By comparing the two emission angles of the electron analyzer, one can modify the probing depth of the measurements where a 90˚ detector angle corresponds to the maximum probing depth. Comparing the two emission angles, one can see that the fluorinated layer is predominantly present very near the surface, which is plausible since the fluorine originated from the plasma species. No further evolution occurs after the initial transformation (see Fig. 2.6(a)).

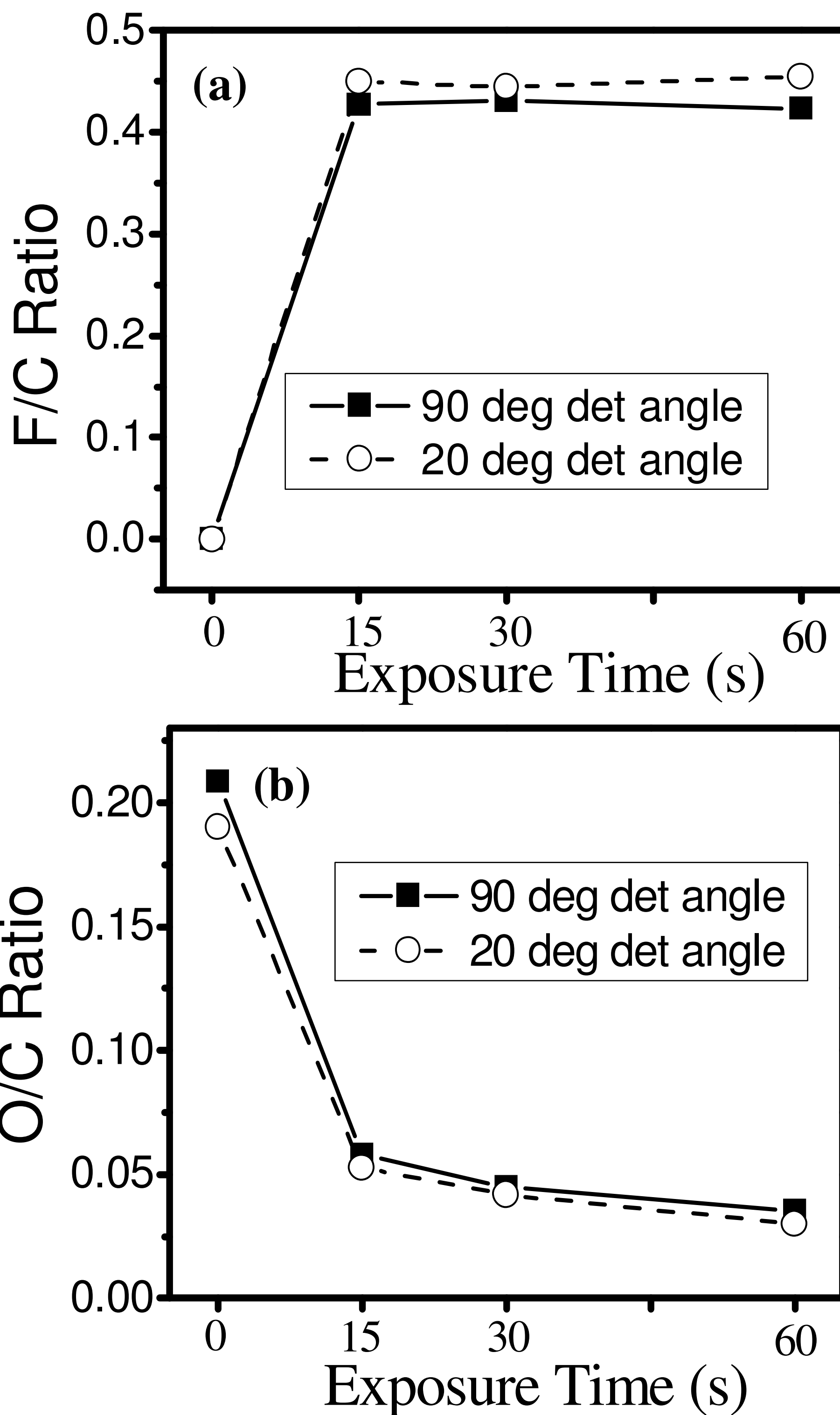

Figure 2.6: *Time evolution of calculated F/C (a) and O/C (b) ratios of MAMA compound in C_4F_8/90% Ar discharge. The discharges were generated using 800W source power, a pressure of 10 mTorr, 50sccm total gas flow and a fixed self bias voltage of -100 V.*

The oxygen content of the plasma-exposed photoresist has dropped significantly compared to the as-received material (see Fig. 2.6(b)). Further analysis has shown that the oxygen signal remaining after processing of our samples originates from SiO_2 that is redeposited on our materials and due to ion-induced erosion of the quartz coupling window of the ICP apparatus by ion attack. Assuming all oxygen and silicon found in the sample after processing is due to this contamination, an atomic percentage of less than 4% was measured. The oxygen loss of the photoresist materials has been observed previously and has been attributed to the photoresist modification[2.9,2.10]. It can thus be argued that nearly all oxygen has been depleted from the photoresist surface region by the interaction with the plasma. Both results suggest the model that the material has undergone a transformation into a surface-modified version of the original compound, which then displays the steady state etching conditions seen in dry etch processes for longer exposure times.

To complement the surface chemical studies of changes of the photoresist materials due to the plasma exposure, we employed atomic force microscopy (AFM) to obtain information on the morphological evolution of the photoresist materials. The roughness evolution as a function of plasma exposure time of the photoresist is shown in Fig. 2.7. In addition, actual AFM micrographs of the surface at particular times are shown, demonstrating the formation of increasingly rougher features. The surface roughness of the polymer is expressed as RMS height variation and shows a dramatic increase with plasma exposure time. The material undergoes severe roughening within the first seconds of exposure, whereas for later times a decreased roughening rate is seen. This behavior was found to be similar to other 193nm PR materials tested

before[2.9,2.10]. The micrographs show that the roughness starts as single rough spots, which grow with time, evolving into what is commonly referred to as PR wiggling[2.8,2.27].

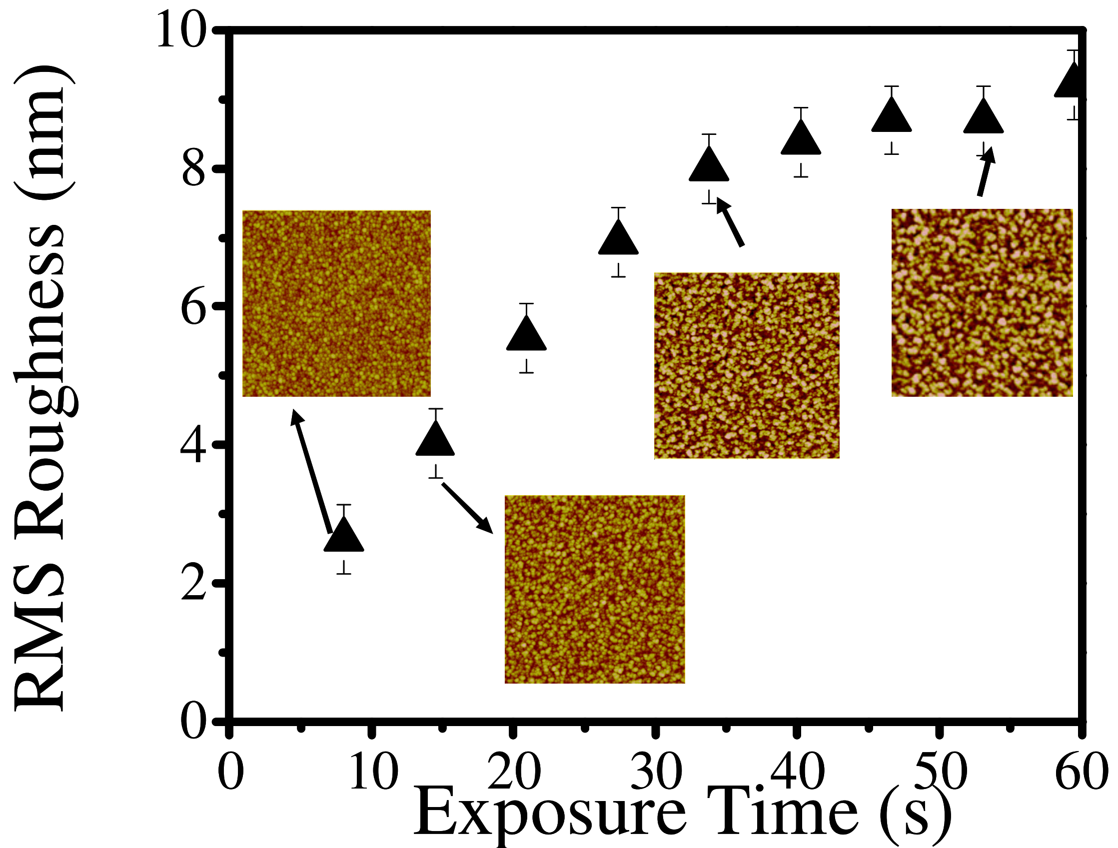

Figure 2.7: *RMS roughness along with AFM micrographs of the MAMA compound as a function of exposure time in a C_4F_8/90% Ar discharge. The discharges were generated using 1000W source power, a pressure of 10 mTorr, 50sccm total gas flow and a fixed self bias voltage of -125 V.*

2.3.2 *Qualitative Evaluation Of Structural And Morphological Changes*

Gokan et al.[2.37] proposed a model which states that the etch rate under ion-beam exposure is inversely proportional to the "effective carbon content" of a PR material, also sometimes called the Ohnishi parameter. This is usually referred to as the "Ohnishi" model and it is based on the observation that materials containing a high concentration of C-O and C=O groups exhibit much higher sputter yields than pure carbon materials[2.37]. The "effective carbon content" ($N/(N_c-N_o)$) is defined as the number of carbon atoms minus the number of oxygen atoms normalized to the total number of atoms in the monomer. Based on the Ohnishi model one would expect polymers that have a high alicyclic content to approach the performance of aromatic resins in plasma environments. Unfortunately, it was found that although increasing the alicyclic carbon content improved etch resistance, it worsened lithographic performance[2.21]. Also, the presence of oxygen groups in PR cannot be avoided, since they are needed to improve the aqueous base solubility of photoresists[2.21]. Even though the Ohnishi model did not prove to hold true in a plasma environment[2.37], we present the comparison of the responses of the 193 nm PR material and its model polymers, the 248nm PR, and p-MAMA polymer using this parameter due to its simplicity and wide-spread use.

Figure 2.8 displays the etch rate of the different materials for our "standard" process conditions. Clear differences can be observed for the 248nm PR and p-MAMA which reveal the lowest etch rates. These materials have the lowest relative oxygen content before plasma etch which may explain the low removal rates.

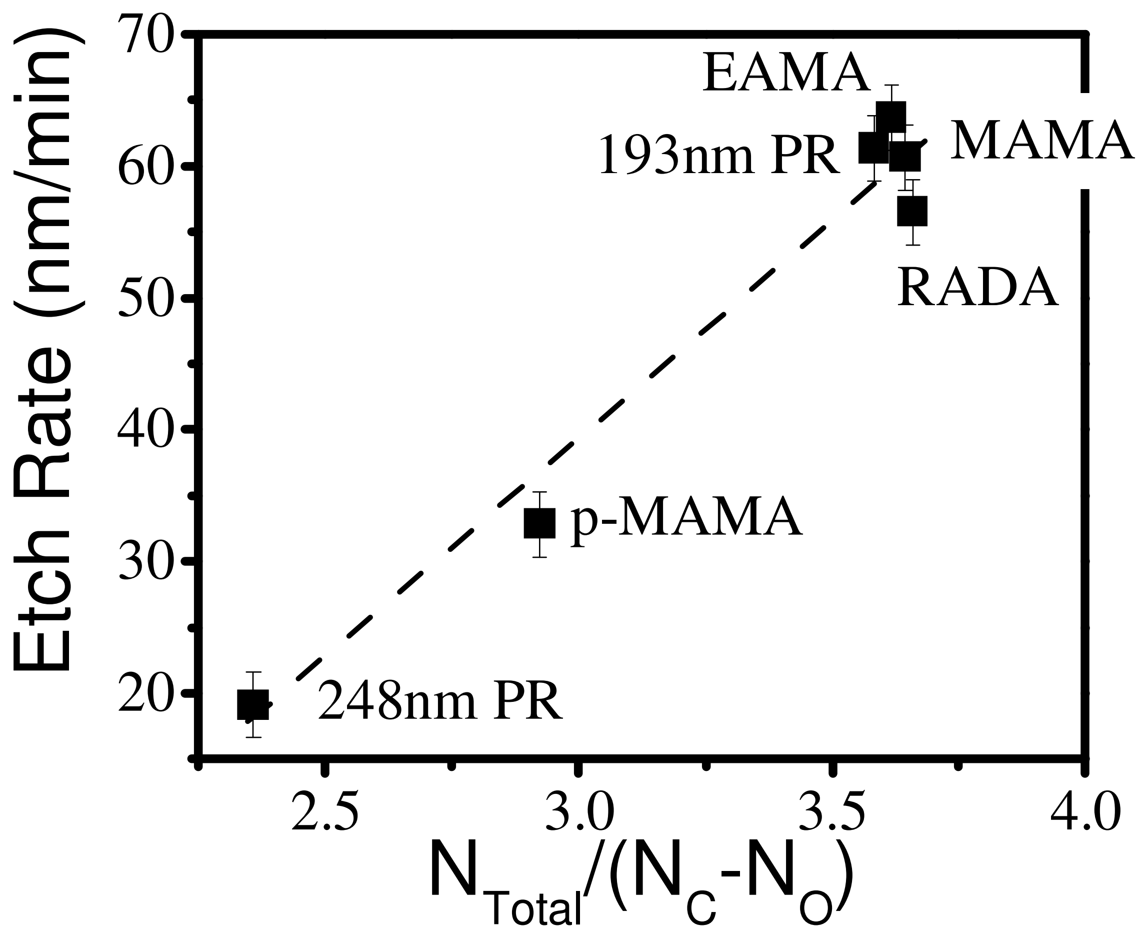

Figure 2.8: *Etch rates for different materials vs. effective carbon content obtained after 60 sec processing in a C_4F_8/90% Ar discharge. The discharges were generated using 800W source power, a pressure of 10 mTorr, 50sccm total gas flow and a fixed self bias voltage of -100 V. The line has been inserted as a guide for the eye.*

It is well known that oxygen content strongly influences the etching resistance of polymers[2.3,2.21,2.38]. In addition, carbon and hydrogen content also affect the etch rate. The four model compounds all have very similar initial contents of carbon, hydrogen and oxygen, but their responses to the plasma environment are different. A partially cross-linked overlayer may reduce etching of the RADA material relative to

the MAMA compound. Comparisons of the fully formulated 193nm PR and the corresponding MAMA polymer show that the additives required to produce a full photoresist system have no measurable effect on etch rate. The EAMA sample tends to have slightly higher etch rates, which may be due to additional hydrogen available from the ethyl group. Figure 2.8 shows that while the Onishi model[2.37] provides a rough description of the overall behavior of polymers due to major differences in oxygen content of the photoresist materials, it cannot account for systematic and significant differences for materials for which the oxygen content is comparable. This is likely due to the fact that the Ohnishi model does not explicitly account for the effect of hydrogen content within a material by distinguishing between hydrogen atoms in the main chain or in the functional groups. For the four model compounds studied in this work, the Ohnishi model predicts nearly the same etch rates, which is not consistent with the observations.

An insight into the different evolution of the optical properties of the photoresist materials has been obtained by determining the effective refractive indices of the materials based on interpretation of the ellipsometric data. The refractive index of the polymer is sensitive to a number of physical and chemical changes of the materials induced by the plasma exposure. Using these characteristics, the ellipsometric data can also be used as a quick indication of the microscopic responses seen by other techniques, e.g. AFM. The refractive index change at 632.8 nm vs. exposure time for the different materials is shown in Fig.2.9, and is averaged over the total remaining layer thickness. We divided the materials into two groups which are displayed in Figs. 2.9(a) and (b), respectively.

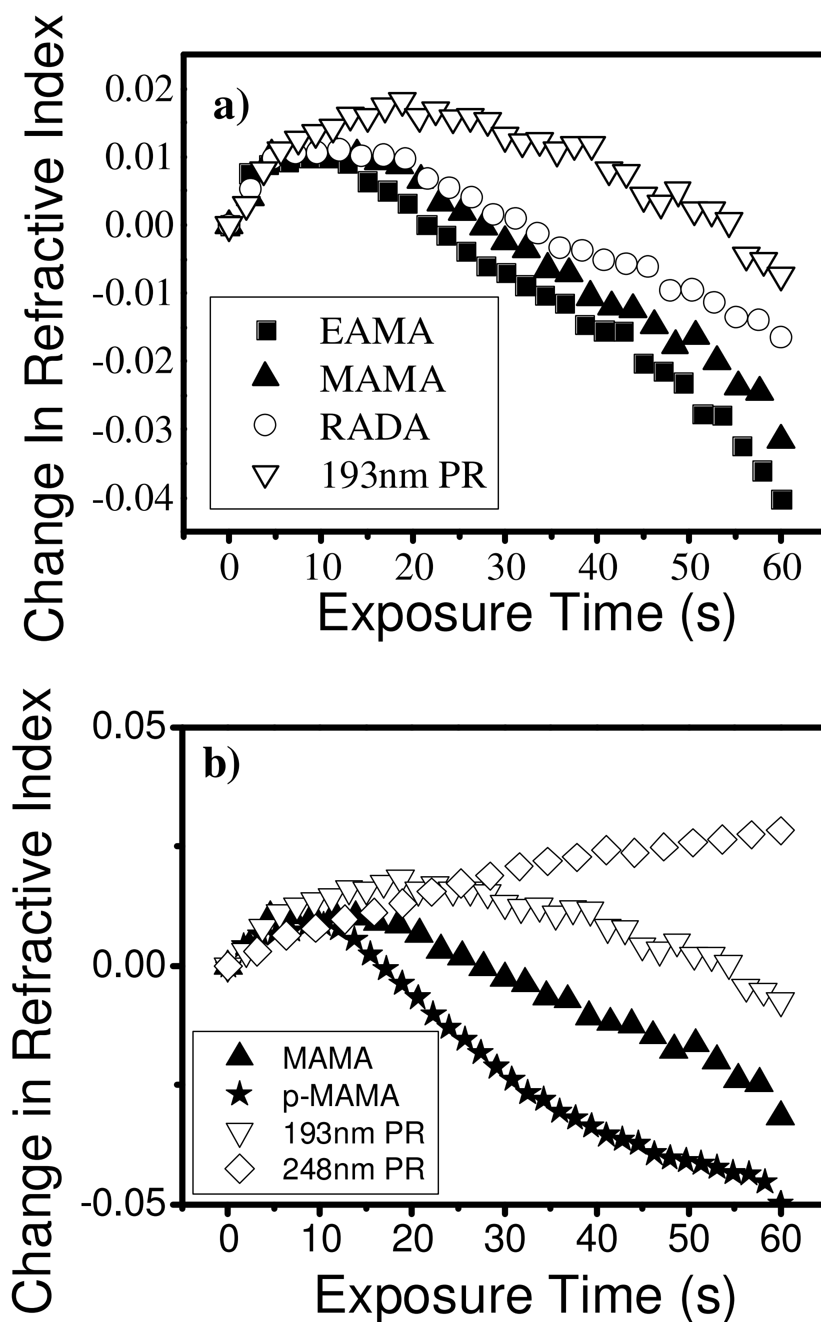

Figure 2.9: *Time evolution of the change in refractive index for EAMA, MAMA, RADA, 193nm PR (a) and MAMA, p-MAMA, 193nm PR, 248nm PR (b) during exposure to a C_4F_8/90% Ar discharge. The discharges were generated using 800W source power, a pressure of 10 mTorr, 50sccm total gas flow and a fixed self bias voltage of -100 V. The refractive index changes were averaged over the total remaining photoresist or polymer thickness.*

The refractive index change of the materials shown in Fig. 2.9(a) follows the pattern seen in Fig. 2.3(b) for MAMA, i.e. an initial refractive index increase is followed by a refractive index decrease. Both the changes of the refractive indices of RADA and EAMA relative to MAMA may be interpreted in the following way: the refractive index decrease seen for plasma exposure times longer than ~15 s is due to the introduction of surface roughness. The RADA compound shows less of a refractive index decrease and less surface roughness introduction than MAMA, respectively, whereas exactly the opposite trends are seen for the refractive index of the EAMA sample. The evolution of the refractive index for the 193nm full photoresist and the MAMA polymer used for its synthesis are different. Since the etching rates and surface roughness of MAMA and 193 nm PR are the same (this is shown in Figs. 2.8 and 2.12), the difference is in the optical properties of the remaining layers. Since by design of the PR material, the whole film should be exposed to photon radiation during the plasma process, one possible explanation is a difference in the responses of MAMA and 193 nm PR to UV photon irradiation from the plasma, where the 193nm PR is able to initiate the PAG process, whereas the MAMA compound remains fairly inactive. If the observed difference in the evolution of refractive indices of MAMA and 193 nm PR is indeed due to this, this would imply that changes in optical properties of plasma exposed 193 nm PR and MAMA do not necessarily translate into observable differences in etch performance and surface roughness.

Figure 2.9(b) shows the refractive index changes with exposure time for 248nm PR and 193nm PR along with MAMA and p-MAMA. The p-MAMA sample

shows the same characteristic index increase followed by an index decrease. However the rate of decrease is much larger than for the MAMA compound. It can therefore be expected that this material shows a high surface roughness (and is indeed observed, see Fig. 2.12). The 248nm PR shows only a refractive index increase. This is consistent with previous observations[2.10] and can be attributed to the fact that for 248nm PR severe surface roughening is not observed.

The chemical evolution for different materials was examined using XPS. Figure 2.10 displays high resolution C 1s XPS spectra for both as-received and plasma etched MAMA compound (Fig. 2.10(a)) and p-MAMA (Fig. 2.10(b)), respectively. These two materials have been selected since p-MAMA is a core polymer backbone of the MAMA compound, but its surface morphological evolution after plasma exposure is quite different. The C 1s spectra obtained with as-received materials show high C-C/C-H signals, whereas after exposure to C_4F_8/90% Ar plasmas both materials show decreased C-C/C-H signals and similar degree of fluorination as indicated by the C-F_x peaks. The C-C/C-H peak for the p-MAMA sample dropped off more significantly compared to MAMA. Since the p-MAMA monomer supplies the leaving group of the MAMA compound, this comparison may indicate that the decrease of the C-C/C-H peak measured for the plasma etched MAMA sample is mainly due to the instability of the adamantyl in the leaving group.

Differences in surface morphology evolution were measured using AFM. We begin with a discussion of the temporal evolution of the surface roughness for the four model compounds. Figure 2.11(a) shows the corresponding roughness evolution with plasma exposure time for the four model compounds.

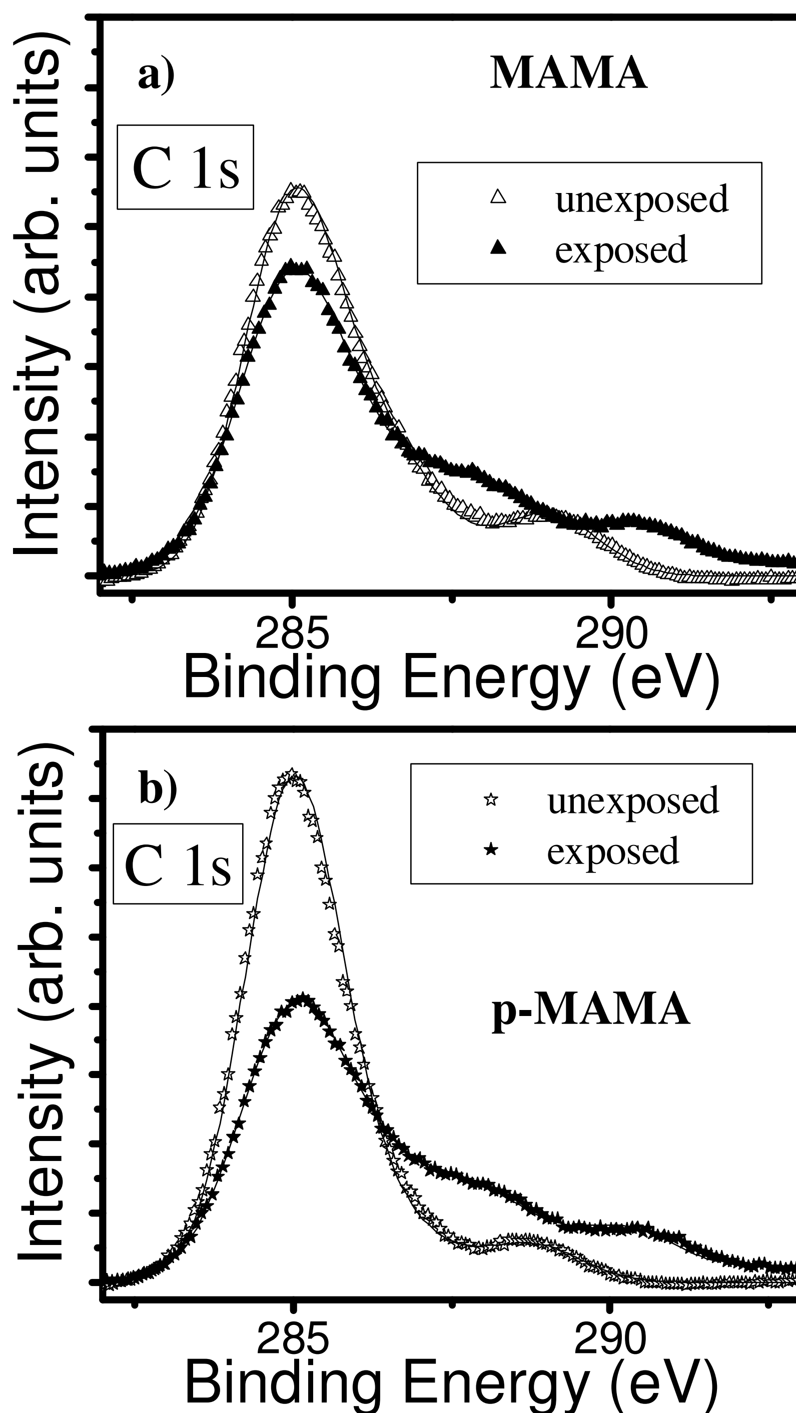

Figure 2.10: *High resolution XPS C1s spectra of MAMA (a) and p-MAMA (b) before and after 60 sec. exposure to a C_4F_8/90% Ar discharge. The discharges were generated using 800W source power, a pressure of 10 mTorr, 50sccm total gas flow and a fixed self bias voltage of -100 V.*

All materials show a strong roughness increase within the first 20 seconds, followed by much slower surface roughening. This characteristic behavior was found to be true for all 193nm PR materials. We discuss all comparisons with respect to the reference compound MAMA. It can be seen that EAMA develops more surface roughness than MAMA for a given plasma exposure time. A reasonable explanation may be the plasma etch properties of the ethyladamantyl group employed in this compound, which provides an additional degree of freedom for radical and ion attack from the plasma, and leads to increased surface roughness. The RADA sample shows the opposite trend. The initial rapid roughness increase is followed by a strong slow-down of the overall roughening rate, leading to smaller surface roughness. An explanation for the difference could be that the acrylate content of this material causes the plasma influence on the polymer to favor cross linking over chain scission and thus creates a thin, more etch resistant top layer[2.39]. This modified layer could reduce the etch rate of the material and lower surface roughness introduction for similar exposure times relative to the MAMA compound due to an improved plasma resistance. Finally the effect of the photoresist additives is given by comparing 193nm PR with MAMA. Figure 2.11(a) shows that both materials for which the polymer structure is identical, display comparable surface roughness evolution differences. We conclude from this that the photoresist additives do not have a major influence on surface roughening, consistent with a prior study[2.28].

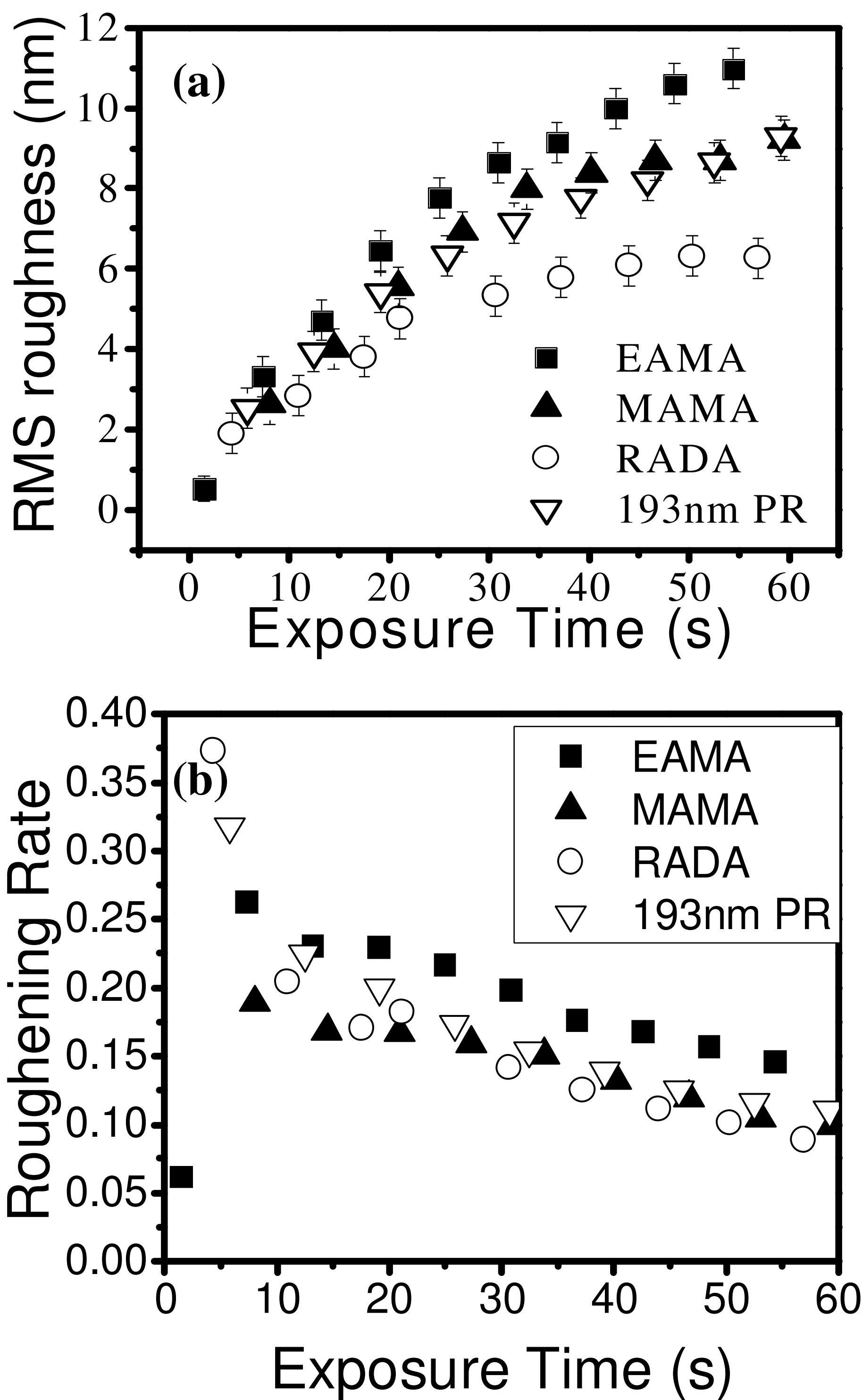

Figure 2.11: *RMS roughness (a) and roughening rate (b) of the 4 model compounds as a function of exposure time in a C_4F_8/90% Ar discharge. The discharges were generated using 1000W source power, a pressure of 10 mTorr, 50sccm total gas flow and a fixed self bias voltage of -125 V.*

To correlate the roughness trends to the etch resistance trends, we defined a normalized roughness which was defined as the RMS roughness introduced during a time interval divided by the film thickness removed during the same time interval. This normalization also tests if the observed differences in roughness are indeed caused by different roughening mechanisms or only by different removal rates. It can be seen in Fig 2.11(b) that all 4 compounds show a higher roughening rates for the first 10-20 s. We suspect that this initial roughness increase is a basic characteristic of the methacrylate based adamantyl polymers resulting from the substantial modifications due to rapid hydrogen and oxygen loss. After these initial high roughening introduction rate values, all values decrease with time. Three of the compounds show similar values while a higher roughening rate is found for the EAMA compound. This suggests that the differences seen in the surface roughness for EAMA are caused by a different roughening mechanism, possibly due to the additional radical attack on the ethyladamantyl group, whereas the improvement in the resist roughening of the RADA sample may possibly be due to a decreased etch rate associated with the incorporation of acrylate into the main chain. This again shows the importance of distinguishing ethyl and/or methyl groups originating from the main chain (in RADA) and from the functional groups (in EAMA).

Figure 2.12 contains the calculated F/C ratios for all materials after processing. EAMA shows a higher degree of fluorination than MAMA, whereas for RADA the fluorination is reduced relative to MAMA. The 193nm PR shows essentially the same F/C ratio as MAMA. The p-MAMA material shows the highest level of fluorination of all materials examined, whereas the 248nm PR shows the

lowest degree of fluorination of all materials studied. One may expect that the measured F/C ratio depends on the overall degree of cross linking for the polymer materials, i.e. as the degree of cross linking increases, the fluorination of the materials (and the measured F/C ratio) will be reduced[2.40].

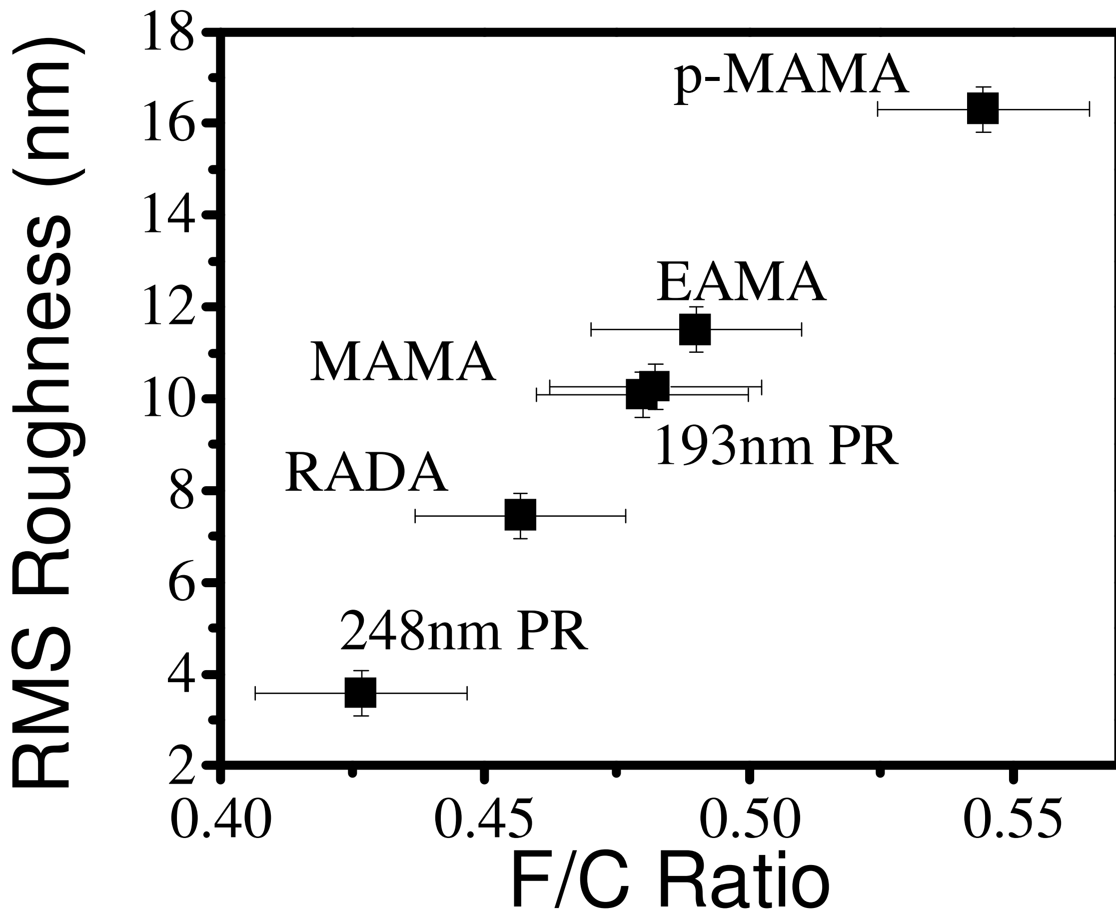

Figure 2.12: *Measured RMS roughness as a function of calculated F/C ratio (20° deg) for the tested materials after 60 sec exposure to a C_4F_8/90% Ar discharge. The discharges were generated using 800W source power, a pressure of 10 mTorr, 50sccm total gas flow and a fixed self bias voltage of -100 V.*

Figure 2.12 also shows the RMS roughness values obtained with samples processed for 60 sec using standard conditions. The results are consistent with trends seen for the intensity of materials modifications determined by other characterization techniques. EAMA shows an increased roughness, whereas RADA shows improved etch resistance due to acrylate incorporation. 193nm PR does not show a significant difference relative to its corresponding MAMA polymer. The 248nm PR material shows much lower surface roughness. The p-MAMA homopolymer shows the highest surface roughness, indicating that the adamantyl structure is more susceptible to plasma attack, and possibly pointing to one key factor for the surface roughness effects seen for all the 193nm polymer materials examined in this work. Relating the observed results to the effective carbon content fails completely. This confirms a picture where surface roughness introduction correlates with the complex polymer functionality employed for 193nm PR materials, including the moiety location within the monomer and interactions with neighboring groups, rather than simply polymer stoichiometry.

Correlation of AFM results with XPS data

A comparison of the removal rates, the fluorination and the roughening of the samples suggests that there may be an underlying reason for the similarity of the observed relationships. For instance, p-MAMA displays a relatively low removal rate, but at the same time exhibits the highest amount of surface roughening. This means that material removal and the roughening behavior of the materials are not correlated.

One may expect that surface chemical changes may be related to surface roughness evolution. In Fig. 2.12 we plot the measured RMS roughness values for the model compounds versus the measured F/C ratio after plasma etching. There appears to be a correlation between the two measurements, i.e. the lower the F/C ratio, the lower the surface roughness. One possible explanation of this observation may be that a lower F/C ratio indicates a higher degree of cross-linking of the surface region, with better etching resistance and greater morphological stability. Another possible explanation is that fluorine replaces hydrogen within the photoresist structure and causes roughening. Care must be taken not to over-interpret the correlation seen in Fig. 2.12. The correlation displayed in Fig. 2.12 applies for the exposure times shown (after 60 sec processing). As shown in Fig. 2.6(a), the F/C ratio is essentially constant for all plasma exposure times studied here, whereas the surface roughness changes continuously as a function of plasma exposure time (see Fig. 2.11(a)). This can be explained by the limited probing depth of the XPS technique, where the modification depth of the sample due to the plasma exposure exceeds the probing depth of the XPS after short processing times. Still, even though this correlation is based on combining results of two completely different characterization techniques, repeated testing for different plasma exposure times has shown it to remain true when comparing different materials.

2.3.3 Influence of Energetic Ion Beams

To clarify the role of ion bombardment in the transformation of the materials reported above, we also processed these materials in an UHV ion beam system.

Previous ion beam studies on other photoresist materials showed similar results to plasma exposures, i.e. hydrogen and oxygen loss of the resist resulting in a graphitization of the material[2.41-2.43]. The effect of the ion energy on the material loss has been well established, where higher ion energies result in higher removal rates[2.44,2.45].

Samples processed with an Ar^+ ion beam also show increased removal rates at early exposure times, similar to observed behavior in plasmas (Fig. 2.3(a)). However, ion beam exposures show increased etch yields[2.46] for fluences less than ~ $1x10^{17}$ ions/cm^2, whereas the etch rates for plasma exposures reach a steady state value at higher fluence (~ $1x10^{18}$ ions/cm^2), possibly because the plasma-induced fluorination of the material delays this effect. All ion-beam processed samples however are in this steady state regime. A detailed report about these findings can be found in the corresponding publication[2.46].

The exposure of the four model compounds to the Ar^+ ions has resulted in very similar etch yields, where the small differences in etch yields between materials can be attributed to the experimental error. The corresponding RMS roughness values did not display significant differences between the materials either.

It should be noted that even with the removed thickness being comparable for the ion beam and the plasma exposures, the induced roughness is more than six times higher for the plasma condition. Fig. 2.13 illustrates this by comparing the roughening rates for the plasma vs. the ion beam exposure. This plot shows two important insights into the roughness evolution of the PR materials examined: The presence of the plasma species creates a significant amount of roughness for plasma

exposures, whereas the roughening seen under argon ion bombardment is almost negligible. It appears from this that the simultaneous presence of reactive fluorocarbon radicals and strong surface chemical changes, multiple ionic species and UV for the plasma exposure may result in strongly increased surface roughness. In addition, the important and consistent differences seen between the four model compounds for the plasma processes were not observed under argon ion bombardment conditions.

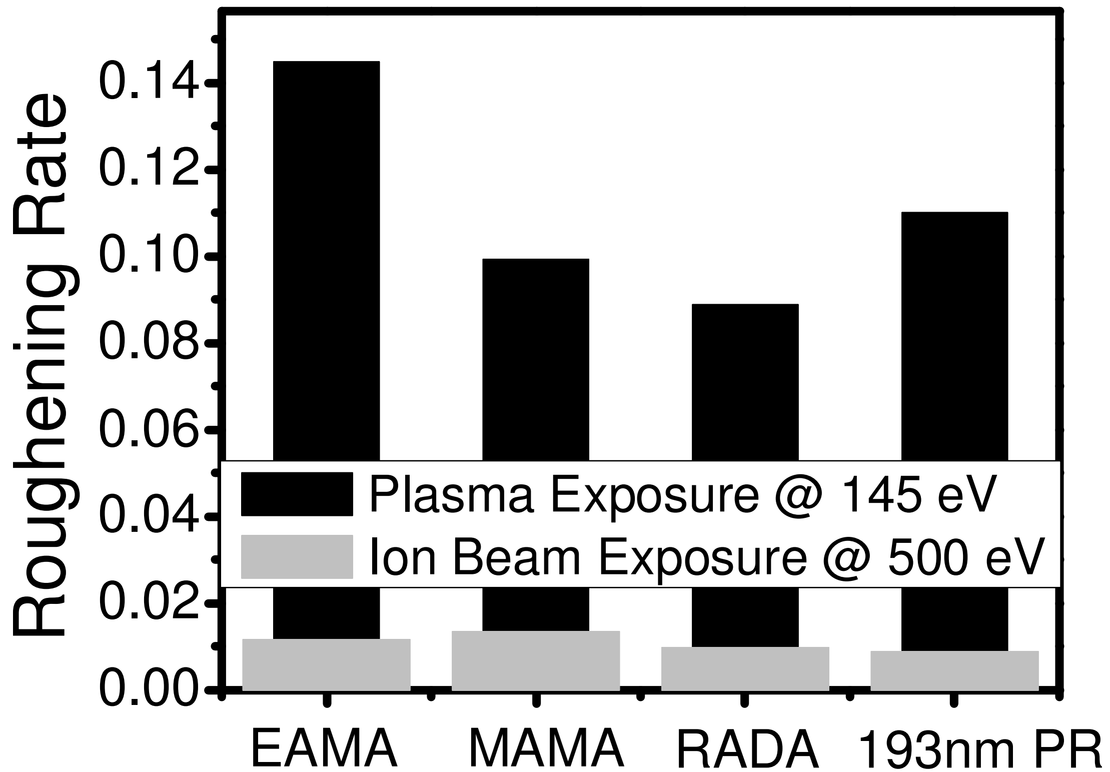

Figure 2.13: *Roughening rates for plasma exposures (as shown in Fig. 2.11b) and ion beam exposures of the four 193nm model compounds.*

Ion energy may play an important role in the observed effects, with qualitative evidence that energies below 500 eV show some extent of roughening[2.46]. Due to the reactor configuration, ion energies in the plasma exposures are limited to a certain range and may be difficult to control independent of other factors. In this comparison the ion energies for plasma exposure were much lower than the ion beam energies. However ion beam exposures offer the possibility to explore energy-related effects in more detail. The effect of ion energy, ion mass, and substrate temperature for ion beam exposures onto photoresist materials will be discussed in more detail elsewhere[2.46].

2.4 DISCUSSION

In Fig. 2.14 we present an overview of surface modifications that take place as a function of exposure time during plasma processing of photoresist polymers. Typical AFM micrographs of the PR surface are displayed for different times. The surface modifications are characteristic for the exposure of 193 nm PR materials using fluorocarbon etching processes comparable to those presented in section 2.3.1. Nevertheless, the picture of Fig. 2.14 should apply for polymer materials that are similar in structure and composition when exposed plasma process conditions for which the main plasma characteristics are comparable.

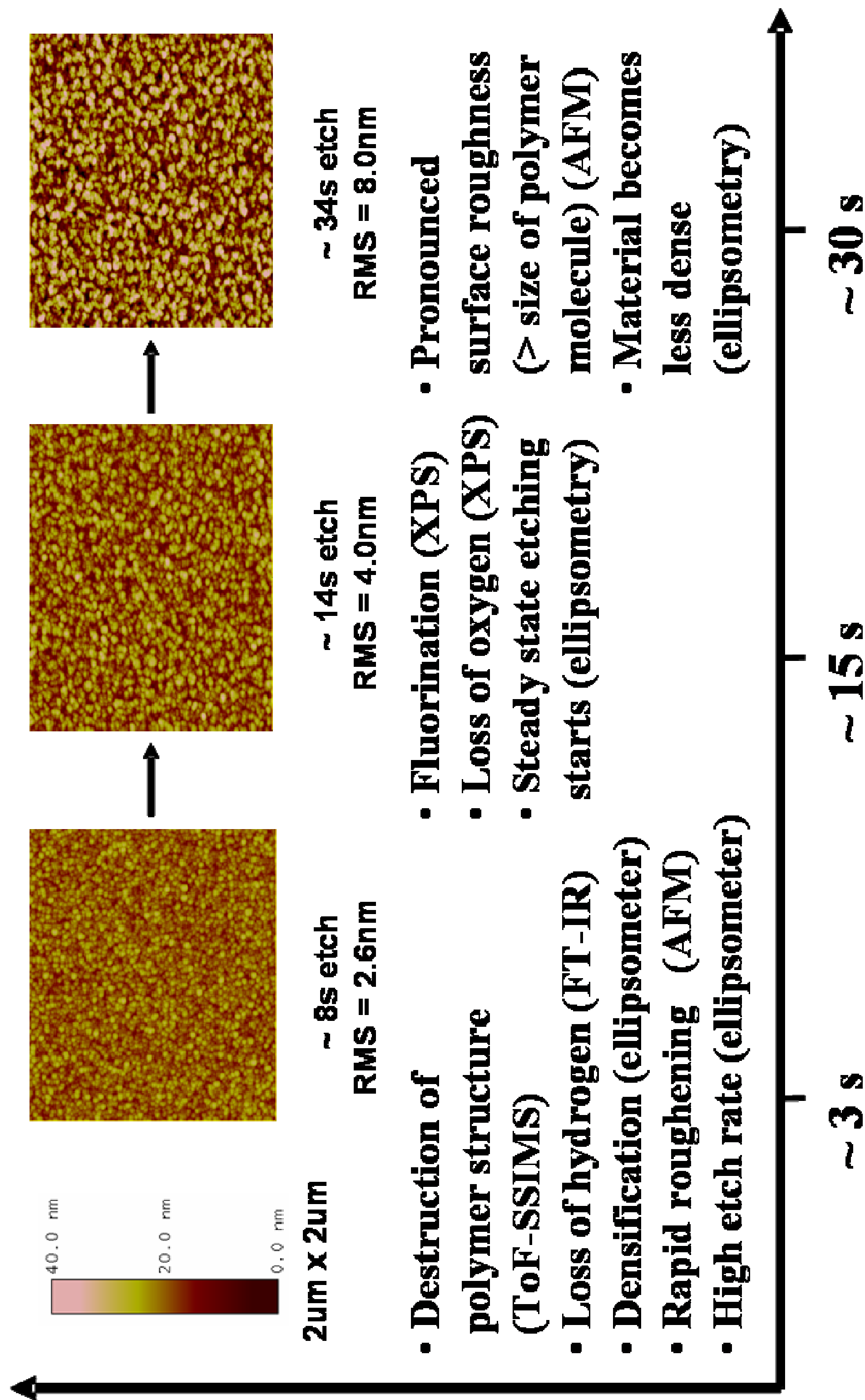

Figure 2.14: *Temporal overview of PR modifications during exposure to a C_4F_8/90% Ar plasma based on data presented in this article. The AFM micrographs are for exposure of MAMA to C_4F_8/90% Ar plasma with a fixed self bias voltage of -125V.*

The initial photoresist modification regime occurs within the first few seconds of plasma exposure. During this period the destruction of the polymer structure at the surface of the material takes place. This is evident by the vanishing of the photoresist fingerprints in the ToF-SSIMS data. Additionally, hydrogen and oxygen loss in the resist causes a transformation in the top surface layers, accompanied by densification of the material. These significant changes in composition are consistent with the observation of the high initial etch rates. High surface roughening rates are also measured for these times.

Following this regime is an intermediate time regime, where the fluorination and oxygen loss at the surface of the material reaches steady state, and steady state etching rates are established.

Finally after about 30 s plasma exposure, the photoresist surface exhibits pronounced surface roughness. The RMS roughness is greater than the average size of a polymer molecule of about 3-5nm. This is the limit of control needed for successful pattern transfer using 193nm PR in conventional lithography and indicates that the plasma process used here would be inadequate. Along with this phenomenon goes the decrease in the refractive index which can be regarded as the material on average becoming optically less dense (we assume that the decrease of the refractive index is due to both increasing fluorination and reduced density).

Our experiments show that the polymer structure has a very important influence on the evolution of these materials, and indicate the need for a trade-off in materials design for meeting both lithographic etch process objectives.

We also found that acrylate addition reduces etch rate and surface roughness. The acrylate created a possibly higher degree of cross-linking in the polymer material forming an etching resistant modified over layer.

Furthermore, our work showed that the addition of small quantities of different functional groups to the main polymer required for full photoresist formulation did not change the plasma etch performance relative to the polymer employed. This is consistent with the fact that the PAG and base additives are also used in the 248nm PR based polymer, which showed significantly better plasma etch performance compared to all 193nm PR materials and model compounds.

Our p-MAMA polymer result suggests that the adamantyl methacrylate group, a key monomer in typical 193nm *ter*-polymers, plays an important role in surface roughening. With the etch rates for p-MAMA being smaller than the corresponding compounds, one can conclude that the oxygen incorporation of the *ter*-polymers, especially in the lactone group tends to increase the material's etch rate. This underlines the fact that the adamantyl structures have been incorporated into the photoresist systems to improve the etch resistance[2.12,2.13]. On the other hand this incorporation causes roughening of the PR materials, as can be seen by the poor surface stability of the p-MAMA homopolymer.

We also demonstrated that the effective carbon content as expressed in the Ohnishi parameter does not allow one to predict the structural and morphological changes of polymer materials during plasma exposure. Instead, a description of the factors that control plasma modifications of polymers must consider additional factors,

including hydrogen content, arrangement of specific groups relative to the main chain, and neighbor-neighbor interactions.

Comparisons of C_4F_8/90%Ar plasma and Ar^+ ion beam exposures have shown important differences for these materials. It is possible that this is simply due to the presence of reactive fluorocarbon species, even though the fluxes of those species are considerable less than that of the dominant Ar^+ ion[2.33,2.34]. For the ion beam exposures, the different model compounds yielded no significant difference in etch yield or surface roughness in addition to significantly lower roughening rates. Strong surface chemical changes in the plasma environment, multiple ionic species and UV for the plasma exposure may also be responsible for the strongly increased surface roughness. In particular, the former of these is suggested as an important effect by the relationship of RMS roughness and the fluorine/carbon ratio of the modified polymer surface shown in Fig. 2.12.

2.5 CONCLUSIONS

We studied the consequences of plasma exposures of carefully selected, well-characterized polymers to gain insights into the role of molecular structure on plasma etching behavior and surface morphological and chemical evolution during plasma etching. The focus has been photoresist materials suited for 193nm photolithography. We found that the hydrogen and oxygen content of the materials plays an important role in the evolution of photoresist etch rate. The labile structure of the adamantyl polymer appears to have a significant role in the introduction of surface roughness. Changes in polymer structures have shown the potential to influence the outcome of plasma-polymer interactions. A protecting group based on ethyl instead of methyl, has shown worse plasma etch properties. On the other hand, acrylate content improves the plasma etch properties. The addition of small quantities of low molecular weight chemicals to the polymer required to produce a fully formulated photoresist has shown no measurable effect on the photoresist performance.

Exposing the same materials to energetic argon ion beams, in the absence of any fluorocarbon or reactive species results in identical process results for all four photoresist materials as well as much less roughness than in the plasma exposures. It was furthermore demonstrated that the roughness evolution of photoresist materials is caused by a strong chemical interaction of the fluorine species with the fragile adamantyl structure, which was intentionally introduced into the resin to reduce the etch rate. This demonstrates the difficult task to design a material suited for both low plasma etch rates and high morphological plasma stability.

Alternative routes in adjusting PR etch performance have shown potential for improving the characteristics for 193nm photoresists. These include fluoroalcohol introduction in the methacrylate resists[2.14], the incorporation of the carbon ring structures directly into the main chain[2.3,2.11], electron beam curing of the resist before processing[2.47] or modifications of the plasma processes using different chemistries[2.27].

ACKNOWLEDGEMENTS

The authors gratefully acknowledge financial support of this work by the National Science Foundation under award No. DMR-0406120. We thank Brian Smith, Magda Benavides, Michael Figueroa and Sun Hyung Kim for support in parts of this work. L. Ling, X. Hua B. Orf, M.-S. Kuo, G. Stueber and D. Lee are thanked for collaboration and discussions of parts of this work.

Chapter 3:

Dependence of polymer surface roughening rate on deposited energy density during plasma processing

To be submitted to Appl. Phys. Lett., 2008

S. Engelmann, R. L. Bruce, G. S. Oehrlein, C. Andes, D. Graves, D. Nest and E. A. Hudson

ABSTRACT

Roughening behavior of three basic photoresist polymers (aromatic, adamantyl, adamantyl + lactone) was examined for fluorocarbon/argon plasma etch conditions. The roughening rate (RR), defined as surface roughness (SR) introduced per depth of material etched, scales linearly with energy density (eV/nm^3) deposited by the ions at the surface during processing, regardless of plasma process details. RR after etch is uniquely determined by polymer structure and energy density. Adamantyl groups cause higher RR. Addition of lactone groups increases removal rates, but leaves the RR at given energy density unaffected. We also show that sidewall roughness of etched nanostructures directly correlates to SR.

The introduction of line edge roughness (LER) and surface roughness (SR) of etched features as a result of plasma processing during pattern transfer imposes limitations on the size of manufacturable structures[3.1,3.2]. Roughness of the photoresist (PR) material and features can be introduced during lithographic exposure as well as plasma etch (PE), and is subsequently transferred into the underlying material layers[3.3-3.5]. Roughness formation during lithographic exposure has been related to unstable resist formulations, and/or due to phase separation of unexposed and exposed polymer at the image definition area[3.6-3.7]. The mechanism of PE induced roughness is much less understood since some PE conditions produce smoothing of rough sidewalls[3.4]. Plasma etch related roughness studies typically examined the role of discharge chemistries[3.1,3.2] or PR materials[3.8] in isolation, and it was not well understood if the polymer material or the PE conditions were the performance limiting factors. In our work we have examined SR and LER introduction during realistic plasma etching for a broad set of PR materials, model polymers and plasma etch process conditions[3.9-3.11], complemented by additional ion beam experiments and molecular dynamics simulations[3.12,3.13]. Here we present several remarkable observations on the dependence of nanoscale photoresist/polymer surface roughening rates on deposited energy density during plasma processing, clarifying the respective roles of both polymer structure and plasma etch process parameters.

A detailed description of the polymer materials of this study has been presented elsewhere[3.9]. Briefly, the *193nm* and *248nm* PR materials frequently used in nanoscale manufacturing differ significantly in their polymer structure (Fig. 3.1).

Importantly, *193nm PR* has a higher oxygen content due to presence of lactone than *248nm PR* and additionally, their polymer structures differ (adamantyl vs. aromatic). We showed previously that functional photoresist additives play no role in surface roughening, which is instead determined by the polymer resin[3.9]. The additives are therefore not shown in Fig. 3.1. To clarify the role of oxygen, *p-MAMA* was also studied. It has the same amount of oxygen as *248nm PR* (5%), but is based on a similar polymer structure as *193nm PR*.

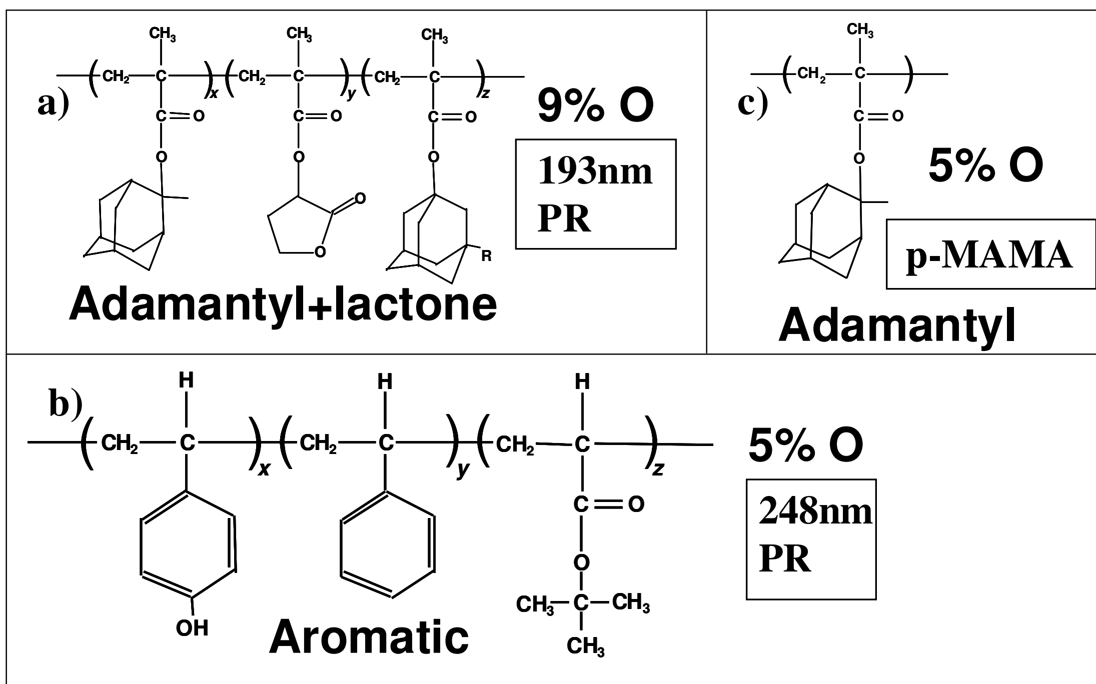

Figure 3.1: *Molecular structures of 193nm PR (a)), 248nm PR (b)) and p-MAMA (c)) employed in this work.*

A detailed description of the experimental procedures employed for plasma processing of polymer materials in our inductively coupled plasma reactor can be found in related publications[3.9-3.11], and only a brief summary is presented here. The PE processes were based on typical fluorocarbon processes (C_4F_8/Ar) employed for

PR pattern transfer into dielectric materials. We systematically varied self bias voltage (-50 to -150 V_{dc} by adjusting bias power), pressure (10-80 mTorr) and inductive power (0.4-1.2 kW) of the C_4F_8/90% Ar PE process to evaluate the impact of these parameters on SR and LER introduction. Etch rates were determined by ellipsometry and surface roughness by atomic force microscopy (AFM). The root mean square (RMS) of the surface profile is reported as measure of the SR of the samples. All data were acquired during the steady state etch period, so that initial transient effects were minimized[3.9,3.14]. We also etched nanoscale patterned *193nm PR* samples to study the impact of PE process parameters on feature sidewalls using scanning electron microscopy (SEM).

We correlated etch rates and roughness data for all processed samples with the energy density ε deposited at the polymer surface during the etching process:[3.10]

$$\varepsilon = \frac{E_i}{v_i EY} \tag{1}$$

Here ε (eV/nm^3) is the energy density deposited by the plasma per unit volume removed, E_i (eV) is the average ion energy of the bombarding ions, v_i (nm^3) is the volume of substrate material removed per etch-inducing ion and EY is the etch yield of the material for the particular discharge conditions. A detailed introduction of the energy density model can be found in[3.10].

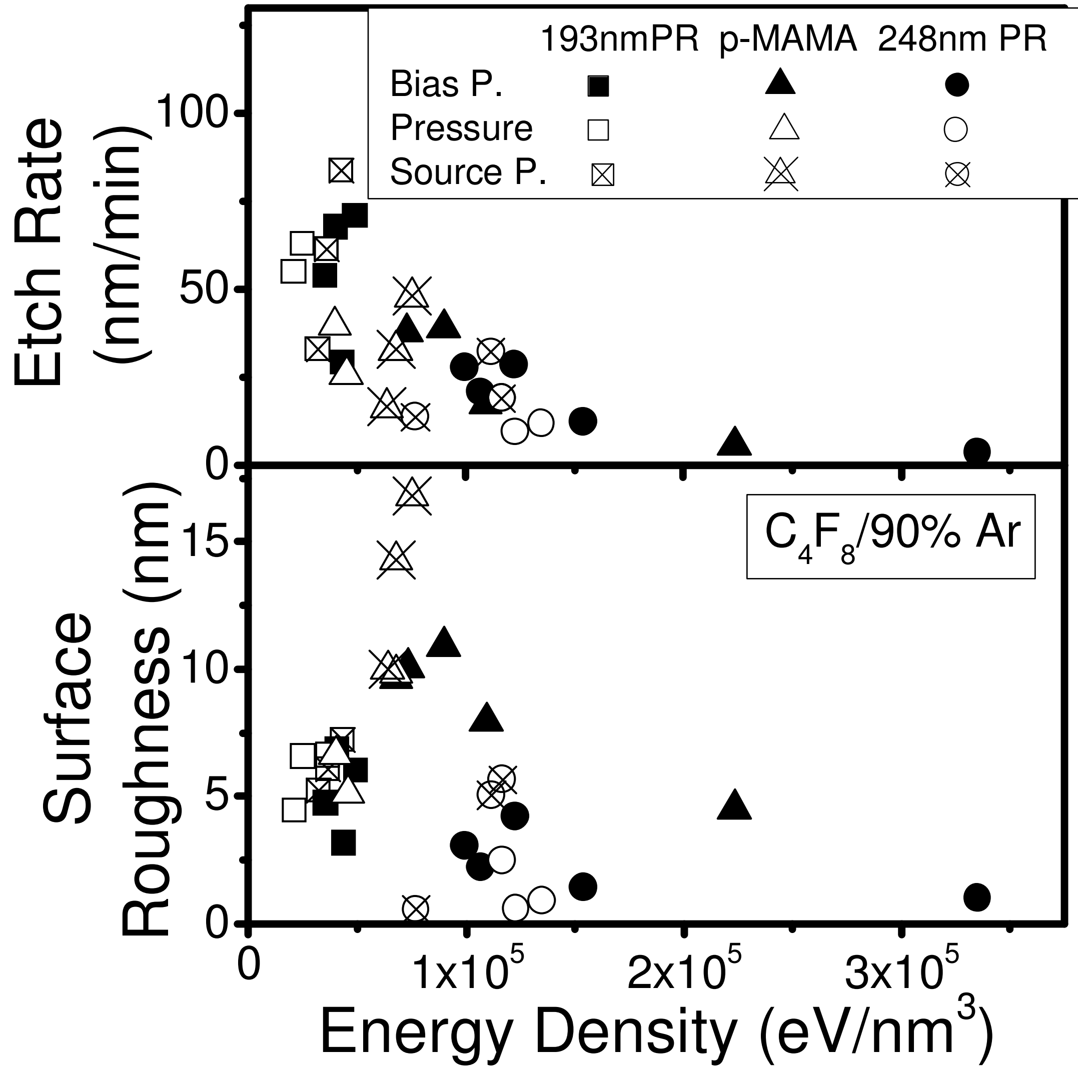

Figure 3.2: *Etch rate and RMS roughness vs. energy density for 193nm PR, 248nm PR and p-MAMA for different processing conditions.*

Etch rates and SR results after plasma etching of the three materials are shown in Fig. 3.2 as a function of ε. Etch rates are roughly proportional to $1/\varepsilon$. On the other hand, SR shows no simple dependence on the energy density.

We define the dimensionless roughening rate *RR* as the roughness introduced per depth of material etched for our conditions, i.e. *RR* equals RMS roughness (nm)

introduced during etch divided by the total etch depth (nm) during the same time period (and related to time-averaged ER shown in Fig. 3.2).

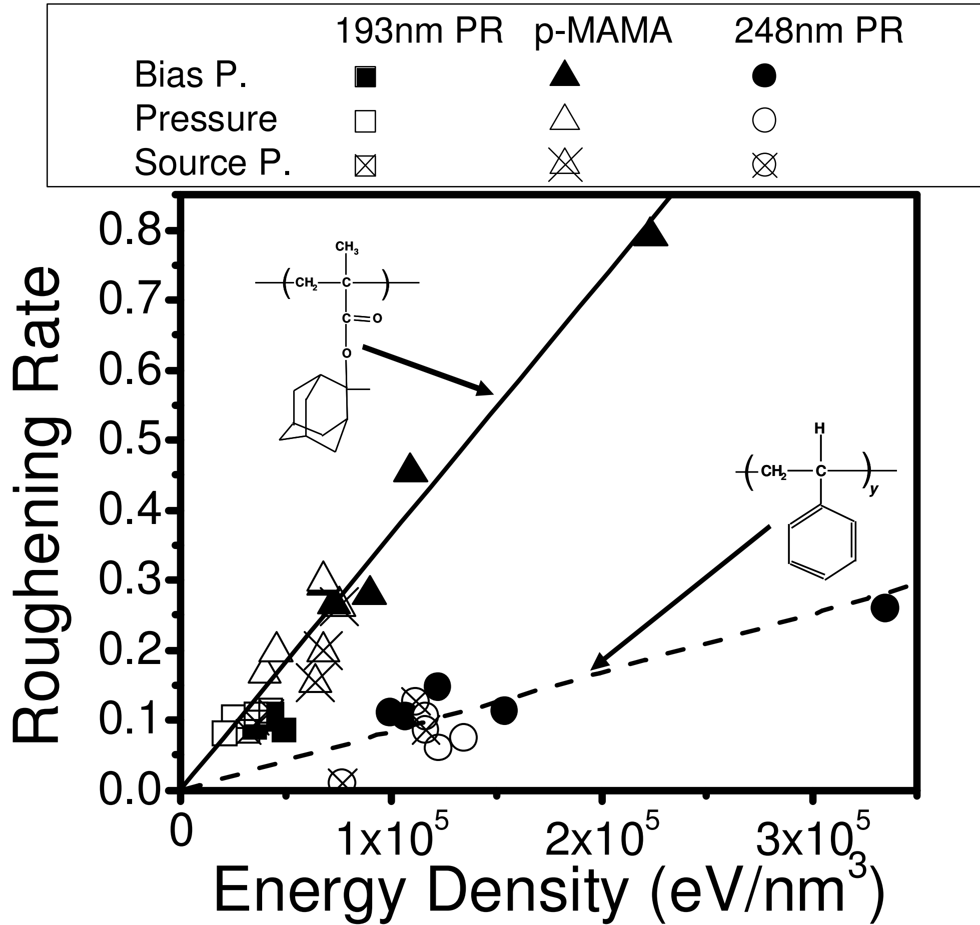

Figure 3.3: *Roughening rate vs. energy density for 193nm PR, 248nm PR and p-MAMA for different processing conditions.*

Figure 3.3 shows that, for each material, RR is proportional to energy density. This relationship between *RR* and energy density ε at the polymer surface during PE may be expressed as:

$$RR_m(\varepsilon) = C_m \varepsilon(E_i, v_i, EY)\,. \qquad [2]$$

The materials constant C_m (nm^3/eV) reflects the molecular structure of the polymer and is a measure of how effectively the deposited energy is converted into surface roughness. Polymer rearrangement due to energy input is prevented if etching takes place instead. Whereas the 248nm PR polymer with the aromatic ring structure shows a small C_m, the adamantyl polymer has substantially higher C_m. Due to a high etch yield (related to O-content), energy densities for *193nm PR* remain below $5x10^4$ eV/nm^3, whereas ε values for the polymers with lower O content cover a wider range. Similar to the presence of O atoms in the polymer, the addition of F through F-rich surface conditions decreased the energy densities ε seen for CF_4/Ar chemistries[3.11]. Surface fluorine was found to increase etch yields similar to a mechanism studied by Schaepkens et al. for Si_3N_4[3.16].

The observations of Fig. 3.3 indicate that PE conditions having high etch yields, i.e. lower energy density ε, show reduced *RR*. A competition for energy dissipation during processing can be identified, where high etch yields result in low roughening rates and vice versa. A possible interpretation of this observation is, that spatial rearrangement of the polymer structure damaged during plasma processing controls the resulting SR measured after etch. A portion of the deposited energy induces material removal (etching). Any remaining energy is dissipated in the near-surface region and may induce polymer rearrangements which contribute to the observed surface roughening. Sumiya et al.[3.15] reported that one mechanism of roughness formation during plasma etch is a transfer mechanism based on etch rate non-uniformity at the surface. The contribution of surface roughness evolution due to

selective removal was eliminated by using the normalized roughening rate in the prior analysis.

The high oxygen content of 193nm PR causes high etch yields, which prevents the material from being exposed to high energy densities during PE and limits *RR*. Since material-dependent surface roughness SR_m is given by

$$SR_m = RR_m(\varepsilon) ER_m t \, , \qquad [3]$$

the high etch rate of the 193nm PR material during the process increases its absolute surface roughness for given process conditions. The high surface roughness values seen for 193nm PR are caused by a high etch rate in conjunction with $RR_m(\varepsilon)$ values that have the same materials constant C_m as p-MAMA. Roughening of 248nm PR takes place at lower $RR_m(\varepsilon)$ values, which in conjunction with very low etch rates result in overall low roughness values for 248nm PR. The high $RR_m(\varepsilon)$ values measured for p-MAMA in conjunction with the low etch rates seen for this material are an expression of the fragility of the adamantyl structure in the plasma environment. In our data there is no evidence that $RR_m(\varepsilon)$ saturates for higher energy densities.

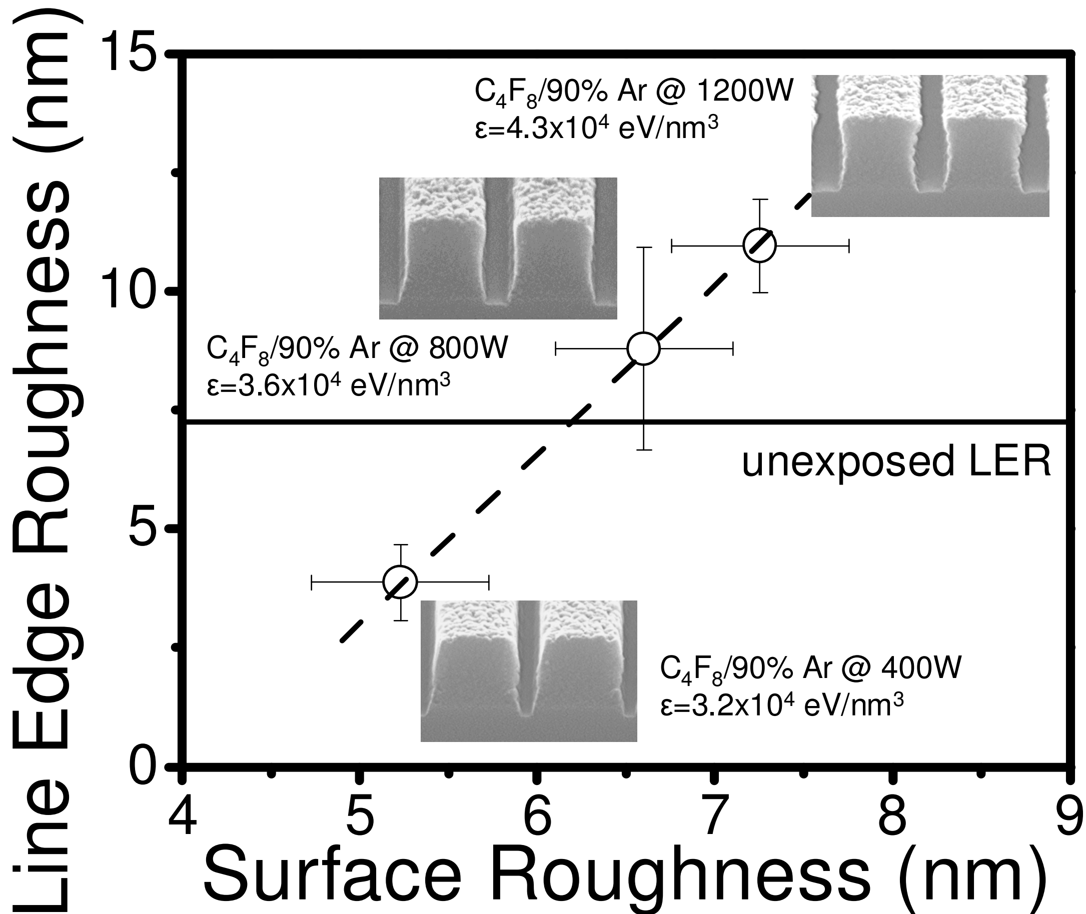

Figure 3.4: *LER vs. RMS roughness for patterned 193nm PR for etch conditions with different inductive power.*

The extension of this work to nanoscale structure fabrication was examined. The impact of different energy densities on nanoscale structures processed by PE is shown in Fig. 3.4. Etching at different inductive power levels corresponds to different energy densities, while the etch yields are very similar for the three conditions. Very smooth surfaces and sidewalls were obtained for lower energy densities. For higher energy density processing, both surfaces and sidewalls roughen extensively. As will be reported elsewhere[3.10], for all process conditions examined, we observed a similar correlation between SR and LER.

In summary, the surface roughening behavior of representative PR materials and polymers in an extensive survey of plasma process operating conditions and chemistries can be described by a model where polymer surface roughening rate scales linearly with deposited energy density. The polymer molecular structure in conjunction with deposited energy density determines the surface roughening behavior for the polymeric materials examined. For materials with a low surface roughening rate $RR_m(\varepsilon)$, resulting surface roughness can still be high if the polymer ER is high, e.g. due to the presence of lactone in *193nm PR*.

This work was supported by NSF DMR-0406120 and DMR-0705953.

Chapter 4:

Plasma-Surface Interactions of Advanced Photoresists With C_4F_8/Ar Discharges: Plasma Parameter Dependencies

To be submitted to J. Vac. Sci. Technol. B, (2008)

S. Engelmann, R. L. Bruce, M. Sumiya, T. Kwon, R. Phaneuf, G. S. Oehrlein, C. Andes, D. Graves, D. Nest and E. A. Hudson

ABSTRACT

One recurring problem in nanoscale processing is roughening of photoresist (PR) materials during plasma etch. We studied the plasma etch behavior of 248nm PR, 193nm PR and poly methyladamantyl methacrylate (p-MAMA) while changing the source power level (400-1200W), adjusting the bias power to change the self bias voltage V_{dc} (-50 to -150V), varying the pressure (10-80 mTorr) and the amount of fluorocarbon gas-additive to the Ar discharge (0-10% c-C_4F_8 in Ar). We found that the PR removal is dominated by the ion energy and fluence. Surface fluorination enhanced the removal rates. Two linked mechanisms for the roughening behavior of the films during processing were identified. Changes of PR top surface roughening behavior in response to variations of bias power and pressure could be interpreted by a model of roughness formation which is dominated by a physical pattern transfer mechanism, i.e. roughness amplification through selective ion-induced transfer. When the plasma source power was varied, we observed that roughness formation was linked to the surface energy density deposited during processing. As the energy

required to volatilize a volume element from the surface increased, the surface roughening rates grew proportionally. This conversion of excess energy into roughening was found to depend on the molecular structure of the polymer, with adamantyl polymers having a very high roughening constant. Additional effects on the etch behavior arise from fluorination of the samples, as quantified by XPS. High F 2s/F 1s intensity ratios, indicated deeper fluorination, were measured for rough surface conditions. Smaller F 2s/F 1s ratios indicate near-surface fluorination, and correspond to smoother top surfaces and feature sidewalls. Molecular compounds showed roughening behavior relative to the respective cross linking behavior even when processed in pure Ar discharges, suggesting that the measured surface fluorination mirrors surface morphology. When plasma etching 3-dimensional trenches and contact holes patterned in PR, we found that the sidewall roughness changed with process parameters in a fashion similar to that seen for blanket surface roughness introduction using the same etch conditions. A close correlation between the surface and sidewall roughness results was obtained, suggesting that our model of polymer surface roughening also applies to resist sidewall evolution during plasma etch.

4.1 INTRODUCTION

One basic problem in manufacturing of nanoscale electronics is roughening of photoresist (PR) surfaces and sidewalls during pattern etch transfer. In an effort to discover key molecular factors responsible for plasma durability of PR materials in plasmas, investigations of plasma-induced transformations of selected model compound photoresist materials and systems with process time in a standard fluorocarbon plasma were discussed in an earlier publication.[4.1] Our time resolved studies revealed that all polymeric materials undergo an initial transformation period, ~ 15 s for our conditions, where selective loss of O- and H- groups in the polymer surface region sustain high etching rates. A O- and H-deficient surface layer is formed, and steady-state etching at a much lower rate takes place subsequently. In a similar fashion, increased roughness introduction is observed during the initial transformation period, possibly linked to the O and H loss during this phase. For longer process times, the rate of roughness introduction was reduced. 193nm PR based on adamantyl and lactone monomers usually showed much higher roughness than 248nm PR based on aromatic polymer. We found that roughness introduction depended on both the molecular structure of the specific polymers and the etching rate during the process. When actual trench or contact hole features were processed, we observed that surface roughness at feature edges is transferred into sidewalls by an ion-induced pattern transfer mechanism.[4.2,4.3] For plasma processed samples we also observed that surface roughness varied linearly with surface fluorination of all materials examined. The different PR materials consistently displayed characteristic

process results relative to each other. Our work left unanswered how much of these differences between photoresist materials were the result of the particular plasma discharge conditions chosen, and to what extent these results may be modified by adjusting discharge parameters. The focus of the current study is the influence of plasma process parameters on photoresist plasma durability for an inductively coupled plasma source.

We examined the variations in etch rate, surface and line edge roughness introduction as a result of changing self bias voltage, plasma density (source power) and discharge pressure. After this, we examined the role of fluorine in a plasma process on the etching response of polymers and introduction of surface roughness. This is followed by a short discussion of the impact of the plasma radicals on the observed etch profiles. We then present our roughening model, and test it using the results of all measurements performed in this work for different plasma operating conditions. We continue with a brief discussion of the implications of this surface model on profile evolution of 3-dimensional nanostructures and compare them with the results obtained in this work. Our results show that the degree of feedgas breakdown has a strong impact on etching rate, surface roughness and etched profile results. A second publication addressing the effects of different discharge chemistries has been prepared as well.[4.4]

4.2 EXPERIMENTAL

4.2.1 Description of Materials

The photoresist (PR) materials used in this study were provided by Rohm and Haas Electronic Materials and their properties, along with those of additional model polymers, were presented in a previous publication.[4.1] In the present work we focused on a reduced set of materials, i.e. 193nm PR, 248nm PR and p-MAMA polymers (see Fig. 4.1), since our previous work had shown that this set of materials captures the full range of the roughness behavior as well as the etch resistance response seen for the more expanded set of materials.

For advanced photolithography applications, 193nm PR, a methacrylate based adamantyl ter-polymer, is widely used in industry. 248nm PR is an earlier photoresist material, and based on a different polymer. One key difference of these materials is that 193nm PR contains the single-bonded cage-like adamantyl groups, whereas 248nm PR consists mainly of the aromatic ring structure in the polymer side chain. Furthermore, as a derivative material from polymethyl methacrylate (PMMA), 193nm PR tends to undergo chain scission upon UV irradiation. 248nm PR consists mainly of the styrene polymer, which tends to cross link as a result of plasma exposure.[4.5] We also employed p-MAMA to study the behavior of the adamantyl structure for a material having a similar oxygen content as 248nm PR.

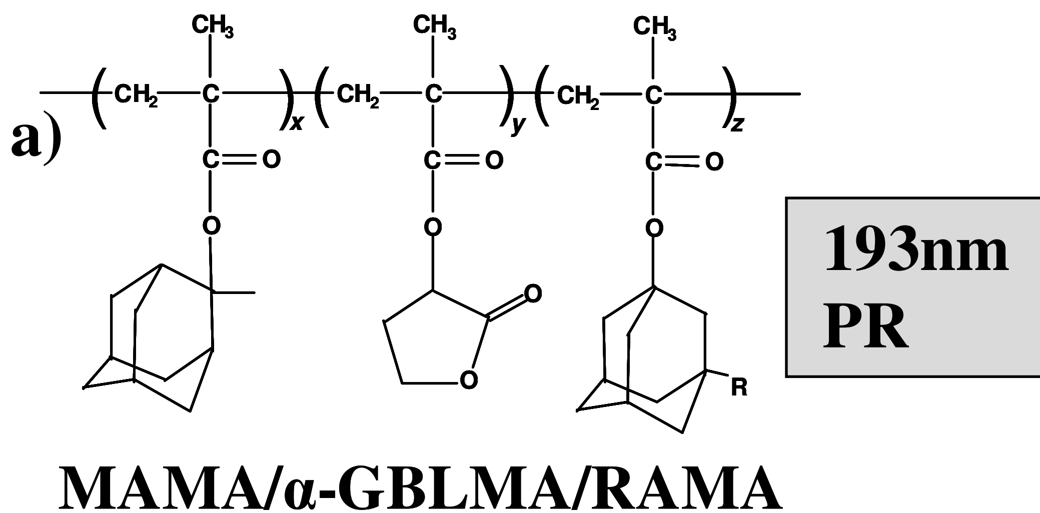

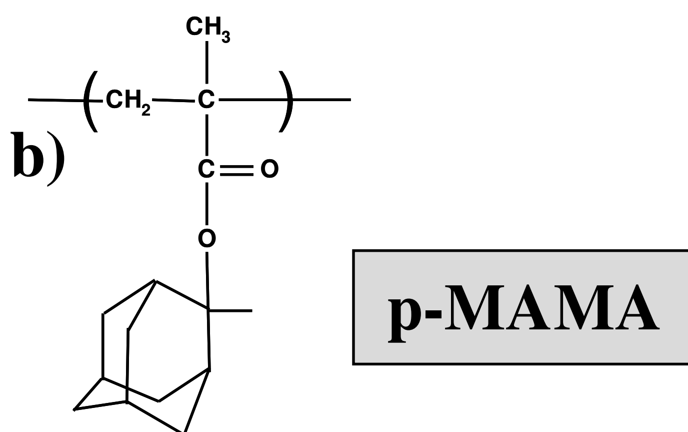

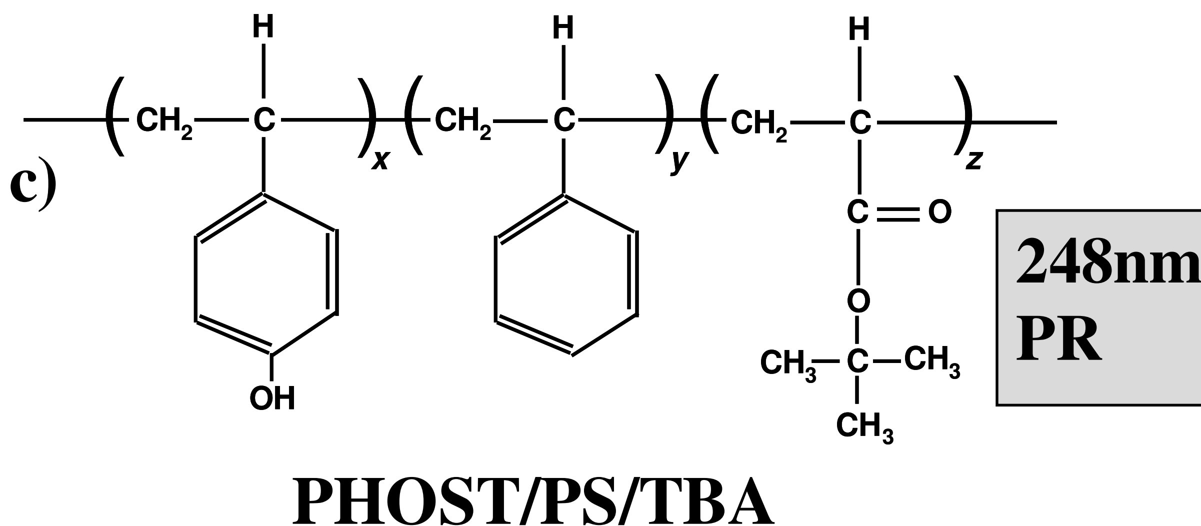

Figure 4.1: *Molecular structures of 193nm PR (a)), p-MAMA (b)) and 248nm PR (c)) employed in this work.*

Blanket films of the above mentioned materials were spin coated on Si-wafers with a resulting thickness of 400nm. A 1 min bake at 120°C was performed to drive off solvents. After plasma processing, we measured the etch rate by ellipsometry, surface roughness by atomic force microscopy (AFM) and surface composition by x-ray photoelectron spectroscopy (XPS). In addition, we also processed patterned 193nm PR materials using the same process conditions and studied the impact on 3-dimensional nanostructures. In order to generate the patterns, 193nm PR resist films on Si were exposed at Rohm and Haas Electronic Materials using an ArF scanner (ASML 1100 (0.75NA)) to produce 150nm wide trenches at a pitch of 450nm and contact holes of 150nm diameter at a pitch of 650nm. A post apply bake (PAB) at 125°C for 60 seconds and a post exposure bake (PEB) at 110°C for 90 seconds were performed to complete the exposure. Due to the missing bottom anti-reflection coating (BARC layer), standing wave patterns could be observed on the resist sidewalls before plasma etch. Plasma etch studies were performed with 1"x1" squares cut from the lithographically exposed wafers. The plasma process parameters for patterned and blanket films were identical.

4.2.2 Plasma Processing

The PR and polymer samples were processed in an inductively coupled plasma (ICP) system described in a previous publication.[4.6] As a discharge chemistry we selected C_4F_8/Ar gas mixtures. The supply of 13.56 MHz RF power (0-2kW) to the planar coil on top of a quartz window is decoupled from a second capacitively

coupled 13.56 MHz RF power supply (0-1kW) to provide independent control of plasma density and ion bombardment energies. The electrode temperature was maintained at 10°C using a chiller, while the chamber walls were maintained at 50°C using heating straps. The gas flow into the chamber was fixed at 50 sccm and the operating pressure was maintained by a throttle valve in the exhaust line. Before each plasma etching process, an O_2 plasma was used to remove residual chamber contaminants, followed by one minute seasoning of the chamber using the process conditions of the following run. These procedures ensured a high repeatability of the process results. For additional experimental details, the reader is referred to prior articles from our group.[4.7-4.11]

The standard plasma etch conditions were source power of 800W, an RF bias power adjusted to achieve a constant self bias voltage of -100V and a pressure of 10mTorr. The standard plasma etch time was 1 min. We varied the RF bias power to examine self bias voltage in the range of -50V to -150V, corresponding to ion energies from ~70 eV to 170 eV. The pressure was raised from 10mTorr to 80 mTorr to examine the effect of different ion/neutral ratios. We changed the plasma source power from 400W to 1200W to study the impact of the FC deposition on the PR substrate. An overview of the plasma conditions examined can be found in Table 4.1.

	RF Bias Power	Source Power	Pressure
V_{DC}	-50 to -150 V	-100V	-100V
Source Power	800W	400-1200 W	800W
Pressure	10mTorr	10mTorr	10-80 mTorr

Table 4.1: *Process matrix for exposing 193nm PR, p-MAMA and 248nm PR in C_4F_8/90% Ar discharges.*

4.2.3 Characterization

After plasma processing, the PR samples were analyzed using multiple techniques:

Single wavelength ellipsometry (632.8 nm) in a rotating compensator, polarizer-compensator-sample-analyzer (PCSA) configuration was used to determine thickness changes of the blanket polymer films as a function of operating conditions. For simplicity, we assumed a one layer model for the polymer materials to interpret changes in the measured Ψ/Δ values in terms of layer thickness changes. Etch yields (amu per ion) were obtained by averaging the ion current over the substrate area ($300mm^2$) and assuming a polymer density of $1g/cm^3$. The applied bias power was used to calculate the ion current assuming a decoupling of source and bias power.

Atomic force microscopy (AFM) measurements were performed by fixing the scan size for all measurements at 2x2 μm^2. The root mean square deviation from the average surface height was used to characterize the roughness of the plasma processed samples. The root mean square (*RMS*) roughness for unprocessed PR

samples was measured as 0.3nm, but all processed samples showed higher values. The dimensionless roughening rates (*RR*) were determined by normalizing the process-induced increase of the RMS surface roughness by the thickness of polymer material removed (RMS roughness increase [nm]/thickness of material removed [nm]).

After processing, the patterned samples were gold-coated for cross sectional imaging with an AMRAY scanning electron microscope (SEM). Critical dimension (CD) analysis was performed on both trenches and contact holes using CDM, an image analysis program. The line edge roughness (LER) and the line width roughness (LWR) measurements of the trench samples were analyzed using SuMMIT, where the cross-sectional images were cropped to show only the top down parts of the original images.

XPS analysis was performed at 90˚ and 20˚ electron take-off angle relative to the surface using a non-monochromatized Al-Kα x-ray source (1486.5 eV). The etched samples were transferred in ultra high vacuum into a Vacuum Generators ESCA Mk II surface analysis chamber. The pass energy of the hemispherical analyzer was set to 20 eV. The charging of the samples was compensated by setting the position of the C-C/C-H peak to 285.00 eV and adjusting all other binding energies with a fixed charge correction. The interpretation of the measured high-resolution spectra was performed according to the protocol described in an earlier publication[4.1].

4.3 RESULTS

Our previous results had shown that PR etching and roughening is influenced by ions, neutrals, radicals and photon radiation from the plasma.[4.1] Material properties also influenced the results:[4.1] 248nm PR exhibited small removal rates and smooth surfaces, whereas p-MAMA showed small removal rates but very high roughness after plasma processing. 193nm PR, showed high removal rates and very rough surfaces as a result of plasma processing. The first section discusses the effect of different plasma operating parameters on the etch results. Since our results indicated a special role of fluorine in etching, the subsequent section specifically addresses F effects. The final part addresses effects of different radicals produced in the plasma when interacting with nanoscale structures.

4.3.1 Effect of operating parameters on process results

4.3.1.1 Bias power

As shown in previous publications,[4.12,4.13] significantly different modifications of the PR materials can be expected when ion energy is changed. We examined the influence of ion energies in the range of 70-170eV (by varying V_{dc} from -50 to -150V) for given plasma densities. Figure 4.2 shows a clear etch rate increase at higher self bias voltages (higher ion energies). For all conditions, 248nm PR was the most etch resistant, followed by p-MAMA. 193nm PR showed the highest etching rates for all conditions. At -50V, 248nm PR and p-MAMA show very low removal

rates, whereas 193nm PR exhibits significant erosion. The high oxygen content of 193nm PR is likely responsible for this difference.

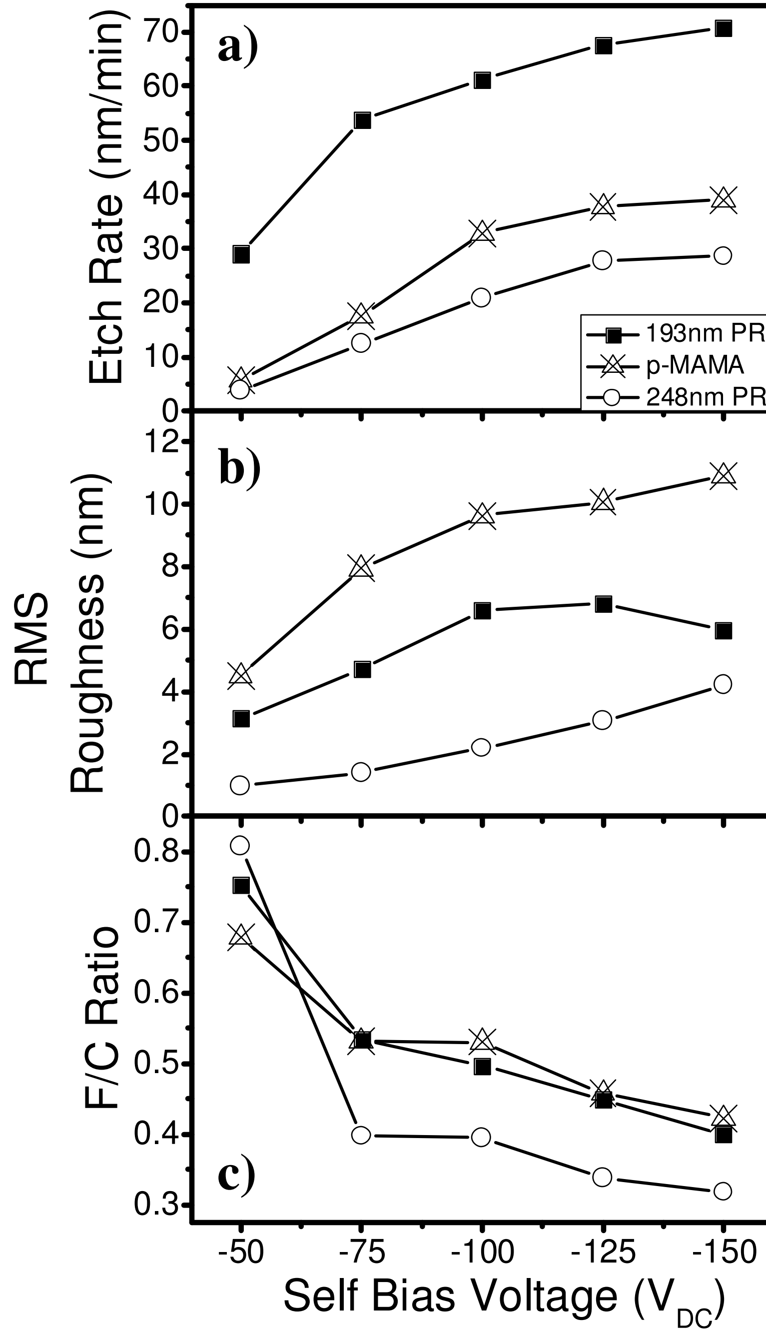

Figure 4.2: *Etch rates, RMS roughness and F/C ratios as a function of self bias voltage in a C_4F_8/90%Ar plasma.*

A clear increase in surface roughness can be observed as the self bias voltage is increased (Fig. 4.2b)). We find that p-MAMA roughens most, followed by 193nm PR and 248nm PR. Figure 4.2c) shows results of XPS measurements. The polymer surfaces are fluorinated after the plasma process, and the degree of fluorination can be expressed by the measured F/C ratio. Surface fluorination decreases as self bias voltage increases,[4.14] consistent with previous observations where a more mixed-layer character for increased self bias voltages is formed and F is driven into the substrate. The highest roughness is seen for conditions for which F/C ratio is the smallest. The inverted material trend for the -50V condition might be a result of the damage in the molecular structure of the polymers as a result of processing. This behavior will be discussed in detail later (see section 4.4.3).

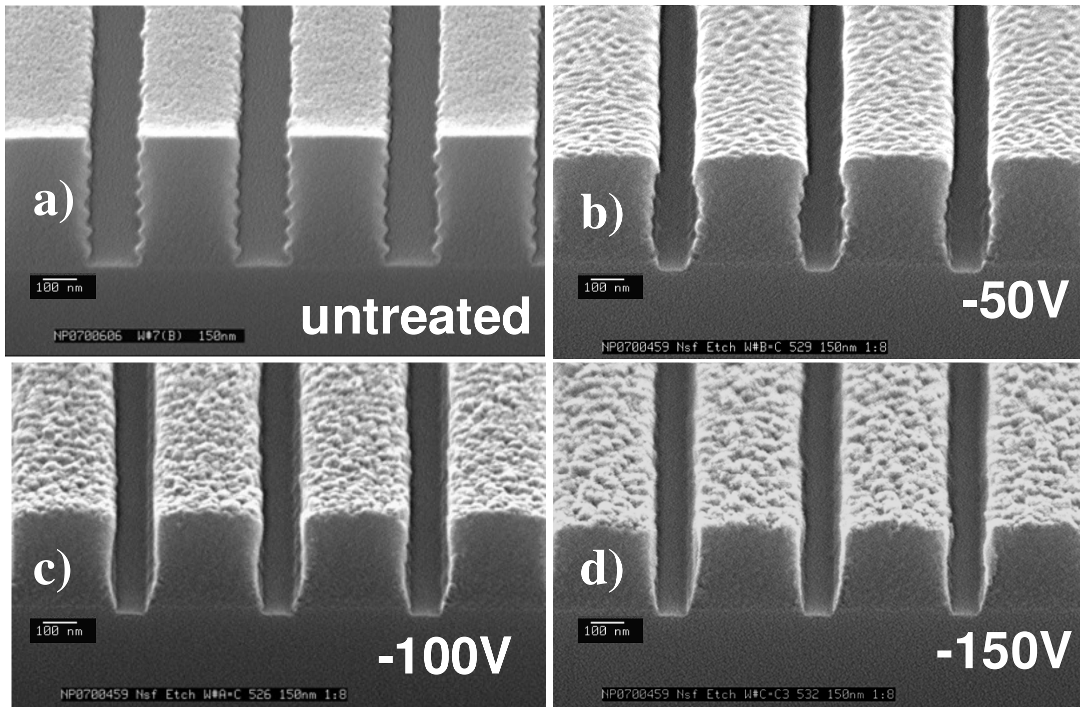

Figure 4.3: *SEM micrographs of unexposed (a)) and exposed trench structures after processing in a C_4F_8/90% Ar plasma with a self bias voltage of -50V (b)), -100V (c)) and -150V (d)).*

Figure 4.3 shows SEM images of PR trenches after plasma processing employing various bias voltages. Use of higher self bias voltages lead to straighter feature sidewalls. Figure 4.4 presents the corresponding numerical analysis of the SEM images. Critical Dimensions (CD) of the trench width were measured at the top, the middle and the bottom of the trench. The sample plasma etched at -50 V shows a significant reduction of the top CD due to fluorocarbon deposition (Fig. 4.4a)), while the underlying mid-section of the trench shows almost no FC film growth. This statement is based on the observation of standing wave patterns at the feature sidewalls that were introduced by the lithographic exposure and are still visible after -50V etching. On the bottom of the trench, ions can reach the sidewalls leading to FC film growth and CD reduction. As the self bias voltage is raised, the top CD increases (less FC deposition), and slightly increased growth of the protective FC film in the middle of the trench sidewall occurs. Additionally, we can see that for -50V plasma etch, the LER and LWR values remain similar to the original values. This could be due to the fairly thick steady state FC layer seen on the top of the trench for this condition (Fig. 4.4b)). Applying higher self bias voltages increased the LER and LWR values after etch. This indicates mostly ion induced erosion for high ion energy plasma etches. A tradeoff for adjusting the process parameters can be noticed, where low energy ion bombardment results in smooth surfaces, but worse profile shapes, whereas high ion energy bombardment results in anisotropic, straight profiles with rougher surfaces and sidewalls.

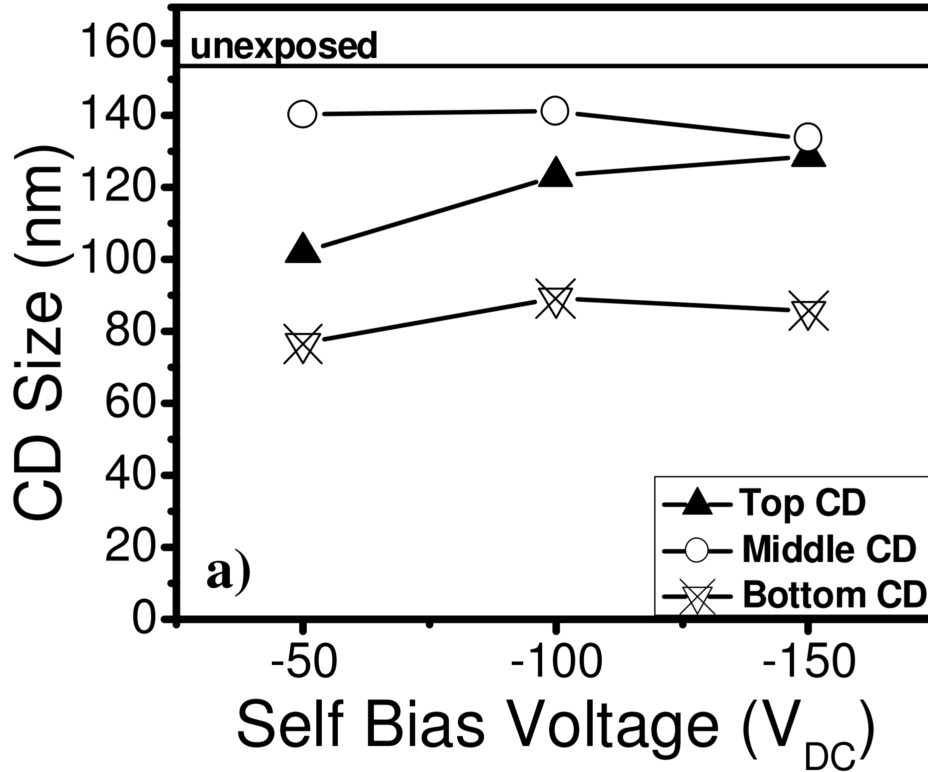

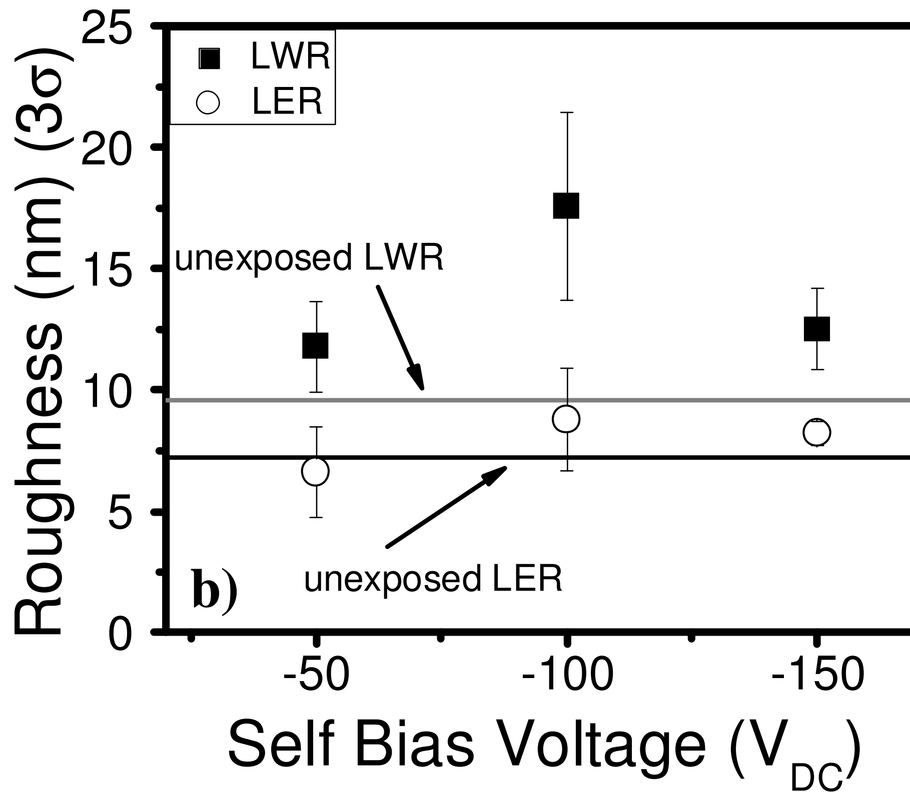

Figure 4.4: *CD measurements (a)) and LER/LWR values (b)) of trenches before and after plasma etch as a function of the self bias voltage.*

4.3.1.2 Pressure

The relative importance of discharge-generated ions versus neutrals on polymer modifications can to some extent be examined by changing the operating pressure from 10-80 mTorr.[4.15] Whereas at 10mTorr a collisionless sheath can be assumed, ion-neutral collisions in the sheath play an increasing role for 45 mTorr and 80 mTorr pressure. The plasma density also decreases slightly for increasing pressure. We converted etch rates to etch yields, and find that etch yields increase with pressure (Fig. 4.5). This effect is stronger for 193nm PR and p-MAMA than for 248nm PR, since for the latter etch yields change little with pressure. All polymers show decreasing roughness with increasing pressure. The difference in roughness between 193nm PR and p-MAMA vanishes at higher pressures. 248nm PR shows the lowest roughness for all conditions. Increased surface fluorination may play an important role in this behavior, since the measured F/C ratio of all materials increases with pressure. This will be discussed further in section 4.4.3.

Figure 4.6 (SEM images) and Fig. 4.7 (SEM image analysis) show the evolution of PR structures for plasma etching at different pressures. Fairly straight sidewall profiles at low pressure change to increasingly bowed profiles for plasma etching at higher pressure. Surface roughness is reduced at higher pressure consistent with the data of Fig. 4.5. The top CD of the trenches continuously decreases as the pressure increases (see Fig. 4.7a)). This is consistent with the idea that at higher pressure a lower ion/neutral ratio leads to increased FC deposition at the top of the trench. It is also consistent with the observed LER and LWR evolution, where the

increased FC deposition causes lower LER and LWR values (Fig. 4.7b)). The increasing ion-neutral collisions in the sheath at higher pressures might contribute to the bowed profiles.

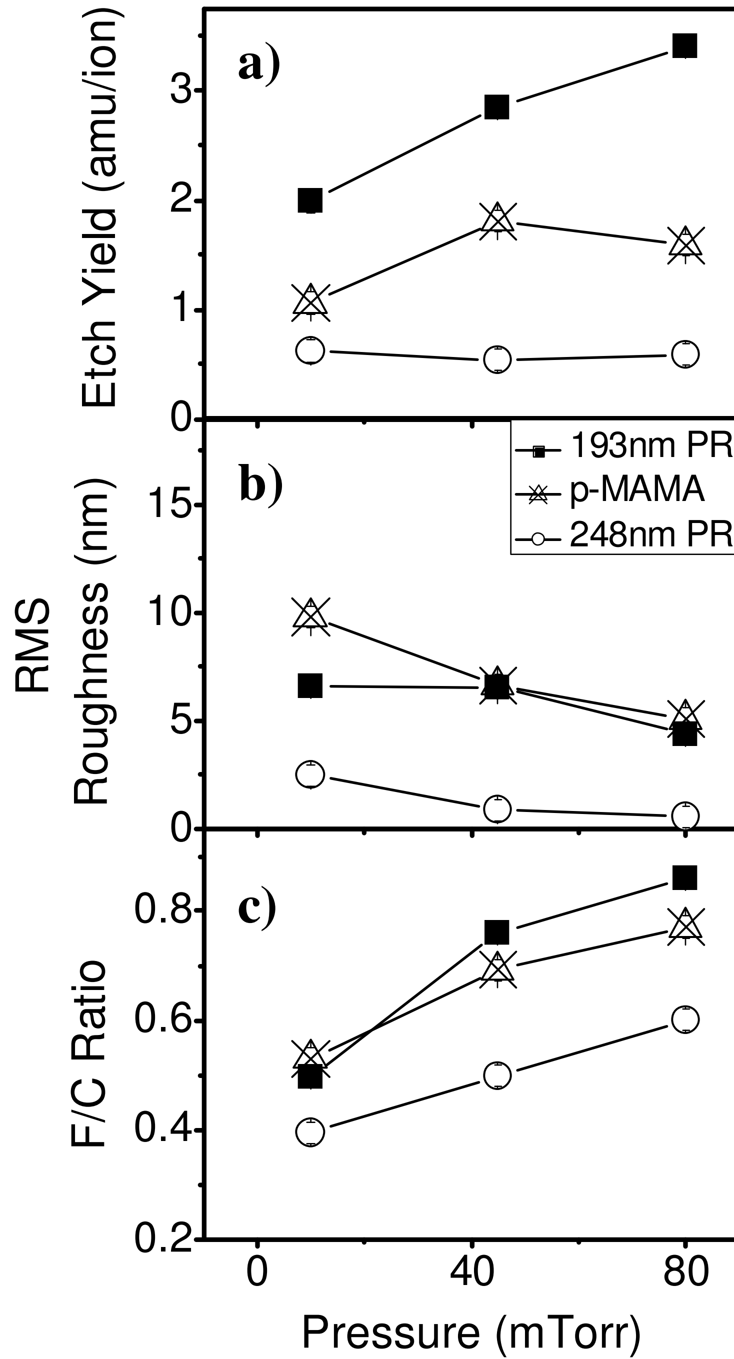

Figure 4.5: *Etch rates, RMS roughness and F/C ratios as a function of pressure in a C_4F_8/90% Ar plasma.*

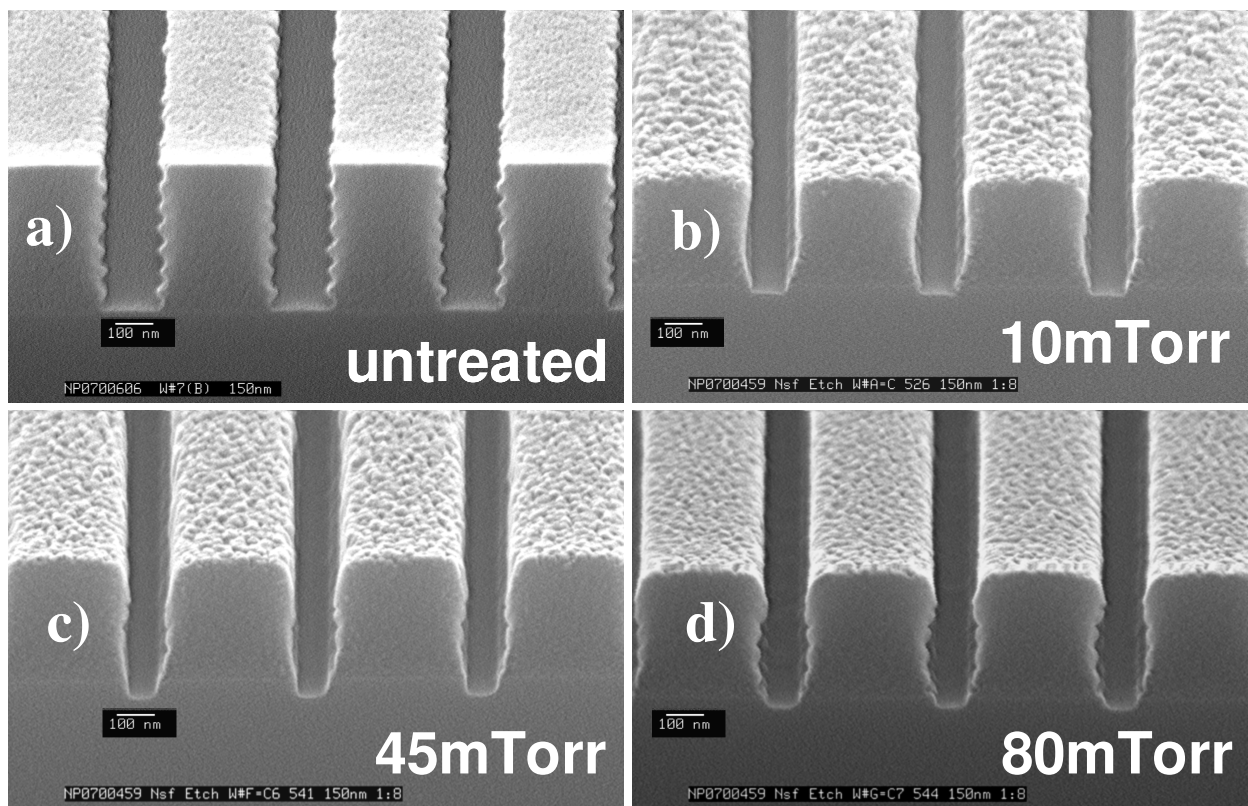

Figure 4.6: *SEM micrographs of unexposed (a)) and exposed trench structures after processing in a C_4F_8/90%Ar plasma with at a pressure of 10 mTorr (b)), 45 mTorr (c)) and 80 mTorr (d)).*

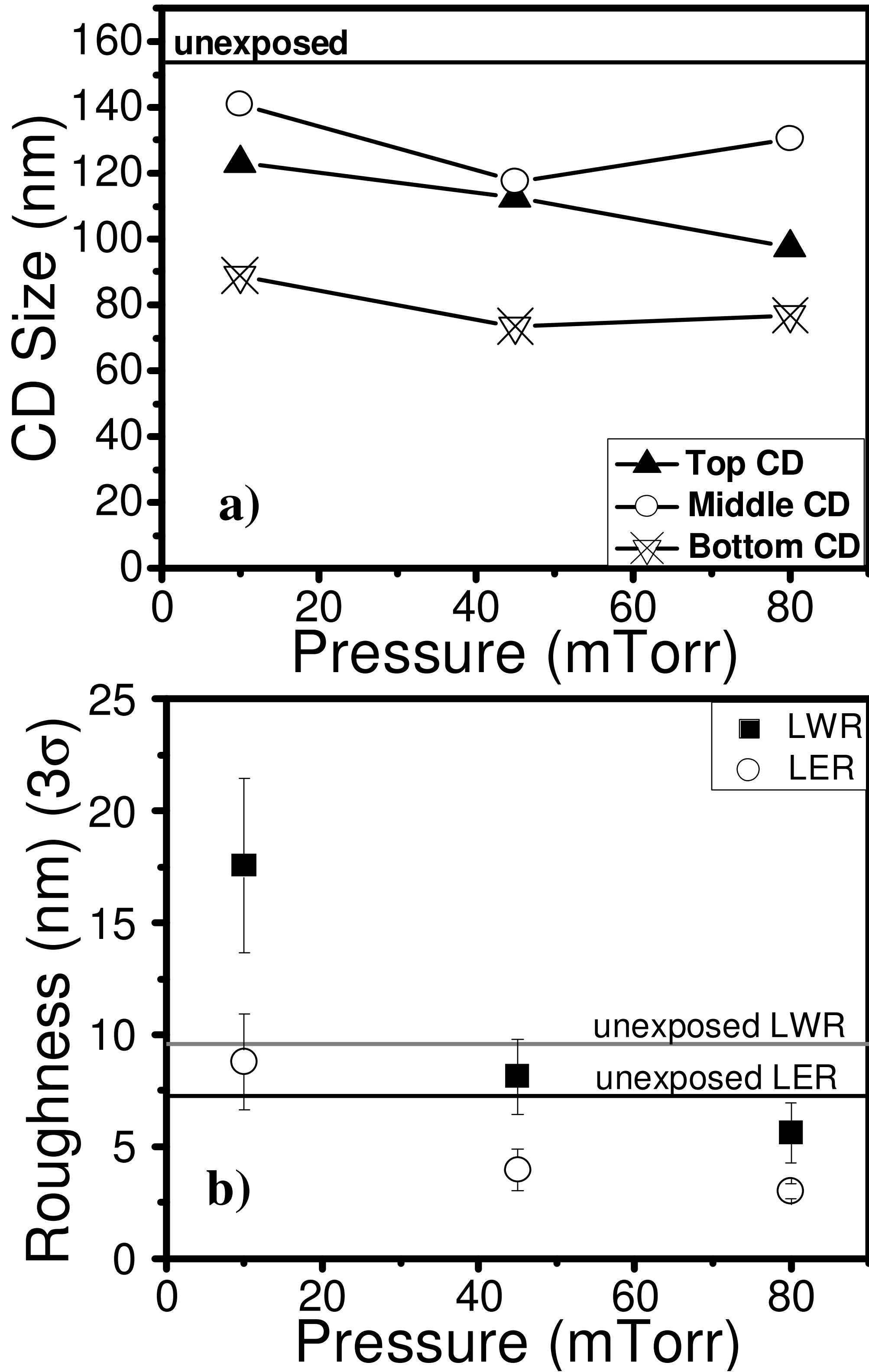

Figure 4.7: *CD measurements (a)) and LER/LWR values (b)) of trenches before and after plasma etch as a function of pressure.*

4.3.1.3 Source power

Varying source power generates plasmas of different plasma densities. For etching at different source power levels material modification is determined mainly by the ion fluence at the substrate rather than the etch time. Additional effects due to changes in surface polymerization induced by C_4F_8 were found. Previous publications showed both experimentally and by computer simulations that an increase in the source power leads to generation of smaller fluorocarbon (FC) radicals.[4.9,4.10] Separate experiments using Si substrates showed that an increase in source power led to a) a significant increase in the steady-state FC film thickness through which etching takes place, and b) a decrease of the F/C ratio of the steady state FC film present on an etching substrate.[4.16] The interaction of F-rich and F-deficient FC films with the polymer materials could therefore be examined in more detail by changing the source power of the plasma discharge.

Results for different source power levels obtained with the three PR materials are shown in Fig. 4.8. Etch yield decreases with source power for all materials, with 193nm PR having the highest etching yield, followed by p-MAMA and 248nm PR. When processing at low source power, thin FC layers formed on top of the PR material. When raising source power, thicker FC films formed on top of the PR material and reduced the effective bombardment of the PR material. For these conditions reduced etch yields were measured. Since the removed thickness of a PR or polymer film influences the measured surface roughness after plasma etch, the same amount of material was etched at different source power levels. The film thicknesses removed for all conditions shown was ~60nm (±5nm), and achieved by

adjusting etching times. Previous studies had shown that variations of ~10nm for this etch depth resulted in a variation of RMS values of at most 1nm.[4.1]

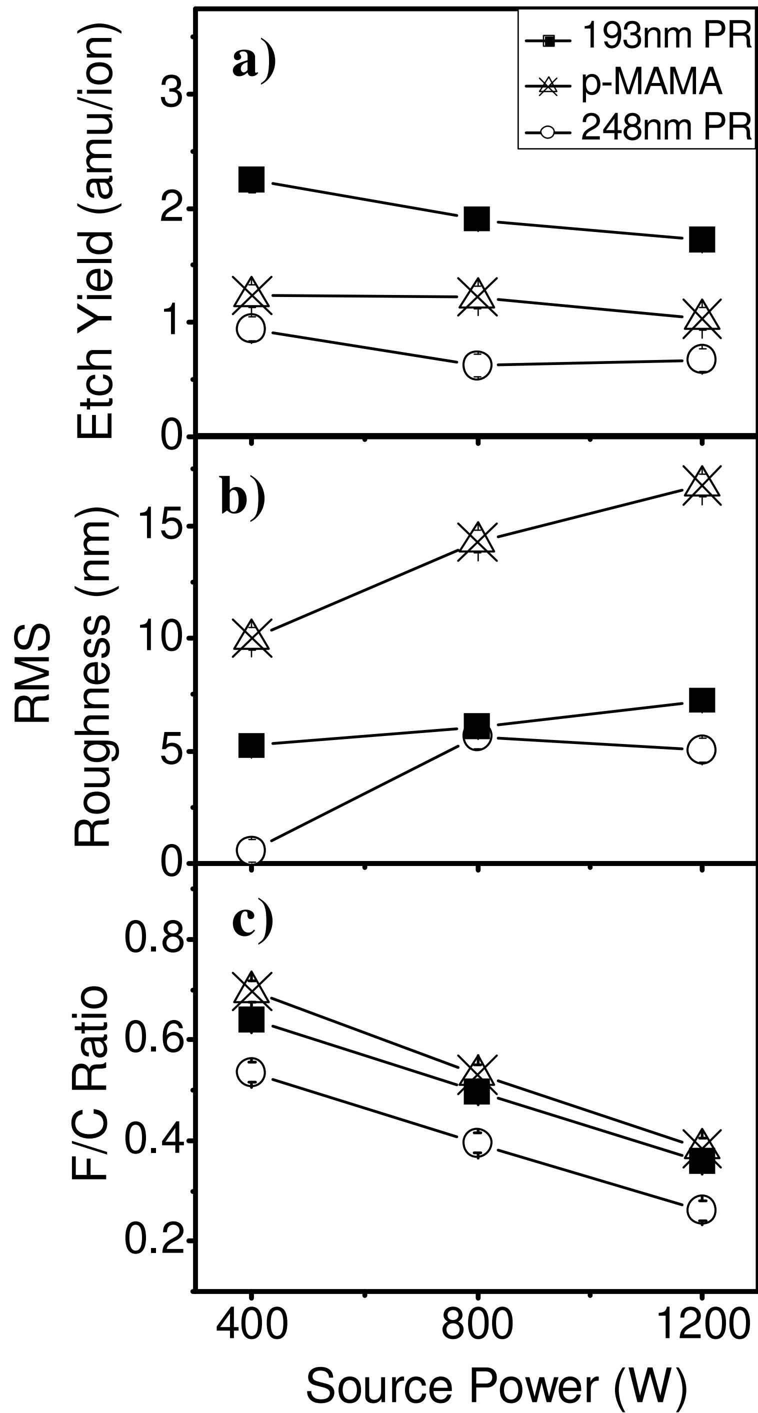

Figure 4.8 *Etch rates, RMS roughness and F/C ratios as a function of source power in a C_4F_8/90% Ar plasma.*

Figure 4.8b) shows clearly that increasing source power leads to a strong increase of surface roughness. The roughness trend for the three different materials is independent of source power.

The fluorination of the samples as reflected in the F/C ratio shows the opposite trend compared to the roughness evolution and is shown in Fig. 4.8c). Increasing the source power leads to decreased F/C ratios. This is consistent with a mechanism, where higher source power leads to increased mixing of the FC film with the PR underlayer because of higher ion flux and a more efficient fragmentation of the C_4F_8 molecule.

The results shown in Fig. 4.8 support the conclusion that the fluorocarbon interaction with the PR surface, in addition to Ar^+ ion bombardment, has important consequences. To study this mechanism further, we examined 193nm PR and 248nm PR at two different source power levels, while adding 0-10% C_4F_8 to the Ar discharge. Changing from pure Ar to a C_4F_8/90% Ar discharge decreases the percentage of Ar^+ ions of the total ion current to approximately 70%[4.7,4.8,4.11] and the total flux of Ar^+ ions at the sample surface changes little. The fluorination of the PR materials increases of course upon adding C_4F_8 to the Ar discharge. The measured etch yield and roughness data are displayed in Fig. 4.9. Pure Ar exposed samples show fairly high etch yields. Surprisingly, upon 2% C_4F_8 addition the etch yields drop to roughly half of the values measure for pure Ar, and then slowly increase as the C_4F_8 percentage is raised to 10%. It should be noted that these experiments were performed in a slightly modified chamber, where the substrate electrode and the quartz coupling window were protected from ion induced erosion in a pure Ar

plasma. Using this protection, contamination originating from the quartz window and silicon substrate could be reduced to an atomic percentage of less than 2 % for a pure Ar discharge. The etch yields for pure Ar agree in this case quantitatively to experiments performed with ion beam exposures.[4.17] The decrease of the PR etch yields seen here appears to be due to FC deposition on the PR surface caused by C_4F_8 addition to the Ar discharge.

An increase in the flux of depositing species results in a slight decrease in net etch yield. It can also be seen that pure Ar and C_4F_8/98% Ar lead to similar process results for different source powers, but the addition of 4 and 10% C_4F_8 to Ar leads to significant differences in both etch yields and roughness introduction for different applied source power levels. The etch yield results are consistent with the findings based on the measured F/C ratios (see Fig. 4.8). A higher source power also leads to continuously increasing roughness with C_4F_8 addition, while the roughness for the lower source power plasma etch stays fairly constant.

The F/C ratios of the samples as measured by the F(1s)/C(1s) ratio after processing are presented in Fig. 4.10a). Surface analysis reveals that an increase of the C_4F_8 percentage in the Ar discharge leads to increased fluorination, and plasma etching at lower source power result in higher surface F/C ratios. This is in agreement with the results shown in Fig 4.8. Consistently lower F/C ratios can be observed for 248nm PR than for 193nm PR for all conditions examined. Since differences in plasma source power affect C_4F_8 dissociation, a more detailed analysis of the fluorination of the samples was performed.

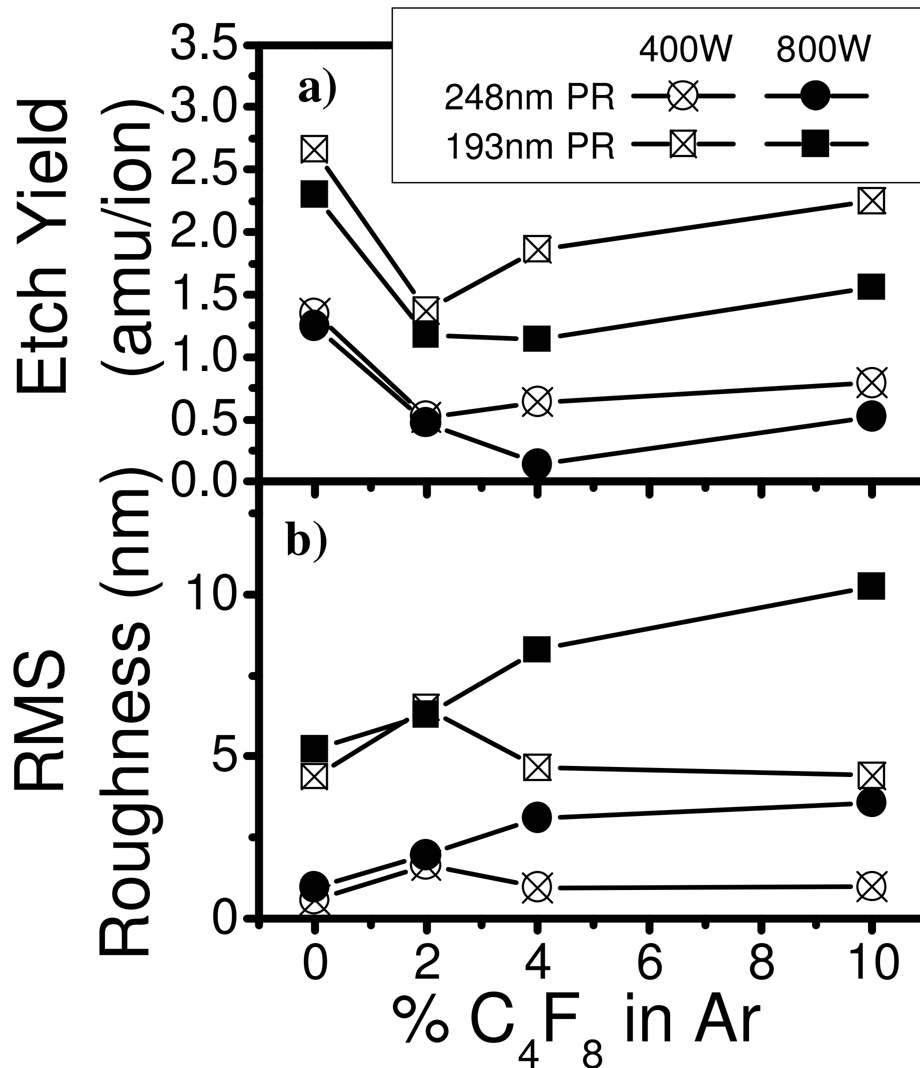

Figure 4.9: *Etch Yields and RMS roughness as a function of % C_4F_8 addition to an Ar discharge.*

X-ray photoelectron spectroscopy (XPS) offers two possibilities for depth profiling: The first technique is based on modifying the electron take-off angle for analysis.[4.1] For the present study, the energy-dependence of the electron inelastic mean free path was chosen for depth profiling.[4.18] Since the analyzer position is not changed during the acquisition, normalization of the signal using the C1s signal is not necessary. In XPS, the photoelectron kinetic energy depends on the binding energy of

the liberated electron according to $E_{kin} = h\nu - E_B$. Electrons with higher kinetic energy (lower binding energy) travel farther in the substrate before losing energy to inelastic collisions. Therefore photoelectrons detected at higher energy may originate from deeper regions within the sample. For our analysis, we analyzed the F 1s (E_{kin} ~790 eV) and F 2s (E_{kin} ~1450eV) regions in the binding energy scale as a measure for deeper (F2s) and shallower (F1s) fluorination of the sample. After measuring the peak areas, we normalized the emission intensities using the relative 1s and 2s photoemission cross-sections, and used the resulting intensity parameter F(2s)/F(1s) to characterize the fluorination profile. A ratio of 1 indicates that the same density of fluorine is present near the surface and deeper into the sample and represents uniform fluorination. A F(2s)/F(1s) ratio smaller than 1 indicates a decreased F density at larger depths, e.g. surface fluorination.

Measuring the surface F/C ratio of the polymer surface using the F(1s)/C(1s) ratio or the F(2s)/C(1s) ratio yielded the same trends (as seen in Fig. 4.10a for F(1s)/C(1s)). Analysis of the fluorination profile evolution as a function of C_4F_8/Ar composition is presented in Fig. 4.10b). All samples show a fairly uniform fluorine distribution for small C_4F_8 percentages, which gradually changes to surface fluorination (decreasing F(2s)/F(1s) ratio). We also observe that the F(2s)/F(1s) values for 800W plasma processing are consistently higher than corresponding plasma processing at 400W. Along with the information provided by the F/C ratio, this presents clear trends on the nature of surface fluorination at two different source power levels.

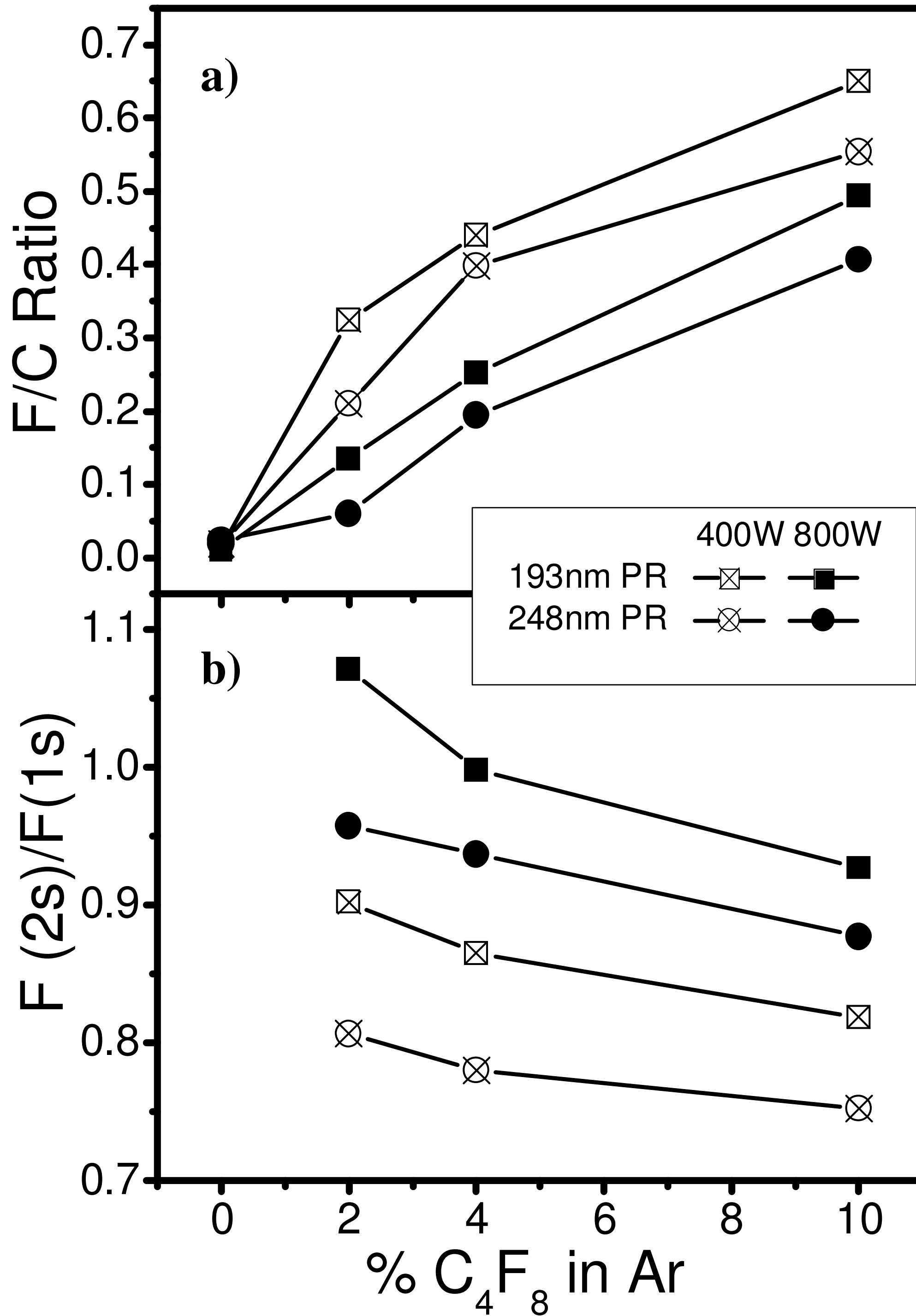

Figure 4.10: *F/C ratio (a)) and F(2s)/F(1s) ratio(b)) as a function of % C_4F_8 addition to an Ar discharge.*

While plasma etch at 800W produces a deep, uniform fluorination, 400W plasma etching results in a highly fluorinated top surface, where the fluorine sharply decreases as one moves deeper into the sample. In addition, 248nm PR after plasma etching always showed lower F(2s)/F(1s) ratios than similarly processed polymers containing the adamantyl structure. This indicates that a plasma-deposited FC layer on top of a 248nm PR does not easily mix with the polymer, creating a sharp interface. This characteristic appears consistent with the highly etch-resistant nature of the styrene molecule and the styrene derivatives used in 248nm PR materials. If we compare these fluorination results to the roughness data after processing, we see that higher F(2s)/F(1s) ratios typically coincide with high surface roughness values, whereas lower F(2s)/F(1s) values represent smoother surfaces. All observations are consistent with the idea that control of the fluorination of PR materials during plasma etch has a major impact on the level of post etch surface roughness measured. While mixing of the plasma FC film and the photoresist underlayers results in rough surfaces, a layer-like deposition of the fluorocarbon film onto the photoresist substrate produces smoother surfaces.

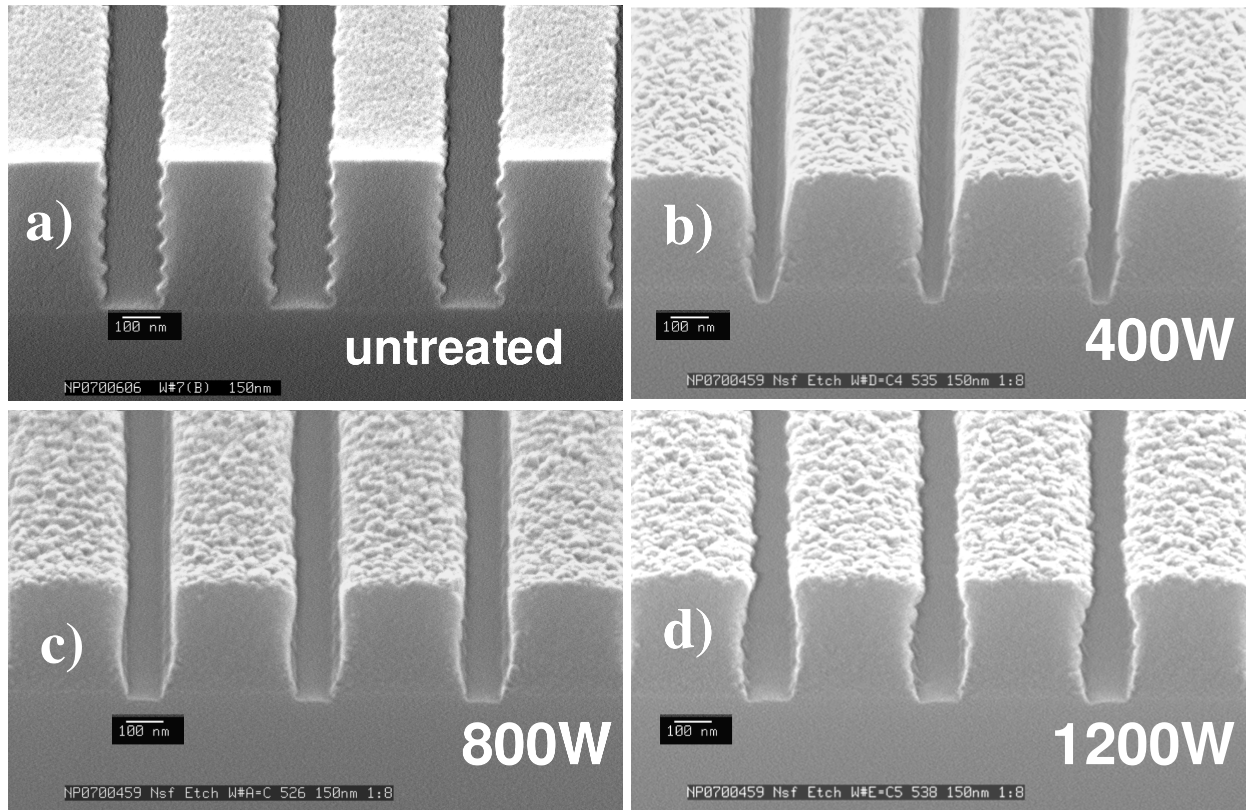

Figure 4.11: *SEM micrographs of unexposed (a)) and exposed trench structures after processing in a C_4F_8/90% Ar plasma with for a source power of 400W (b)), 800W (c)) and 1200W (d)).*

The impact of plasma source power on the profile evolution of patterned trenches is shown in Fig. 4.11 (SEM images) and Fig. 4.12 (SEM image analysis). As for processing of blanket PR films, the plasma etch time was adjusted so the samples received the same ion fluence. While the 400W sample shows a fairly uniform fluorination, increasing the source power lead to increased bowing of the sidewalls (increase of the middle CD, Fig. 4.12a)). It is also apparent that the 400W plasma etch exhibits fairly thick, uniform sidewall coverage. A significant reduction of the original CD was measured at 400W. The plasma etch at 400 W also led to significantly reduced values in LER and LWR, possibly due to deposition of a

protecting FC layer. Increasing the source power resulted in worse LER and LWR values (Fig. 4.12b)). The explanation of this effect is related to the nature of the FC radicals present during processing, and will be discussed in section 4.4.3.

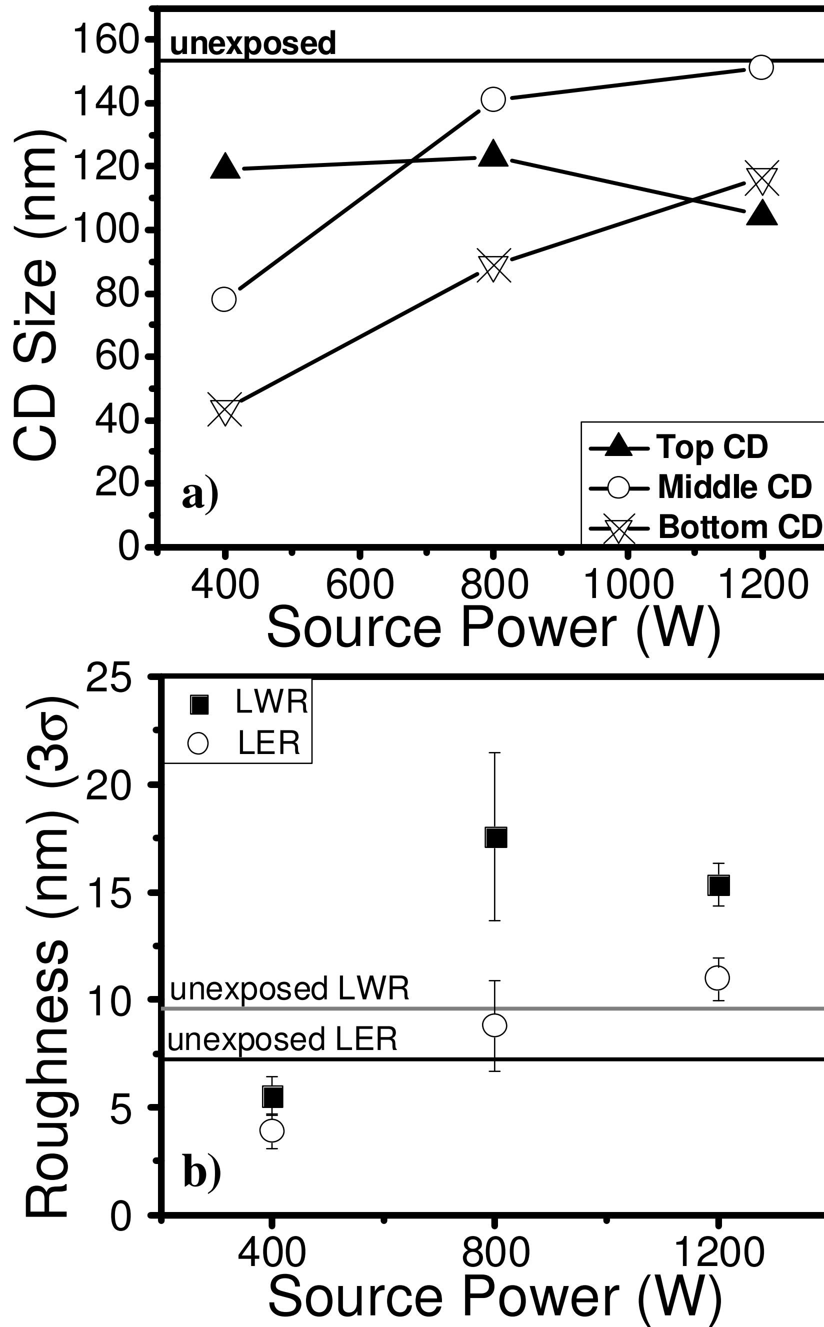

Figure 4.12: *CD measurements (a)) and LER/LWR values (b)) of trenches before and after plasma etch as a function of source power.*

4.3.2 Role of surface fluorine in roughening of PR materials

Previously, we examined modifications of different PR-related materials using the same plasma process conditions, and we observed a clear correlation of surface roughness and surface fluorination (F/C ratio).[4.1] Our results of the current study also show a connection between surface roughness and surface fluorination. A possible relationship between the roughness and the surface F/C ratio generated by different plasma conditions is examined in Fig. 4.13. When comparing surface roughness of different materials for all conditions examined in Section 4.3.1, we find higher F/C ratios for samples with greater surface roughness after processing, consistent with our previous findings.[4.1] On the other hand, when comparing results for a given material obtained by varying bias power, source power and pressure, we find the opposite trend. In that case, higher F/C ratios correspond to lower roughness. Figure 4.13 also indicates that most data points for a given material fall into a certain area to be characteristic of the particular polymer material. This is in agreement with the data reported in Fig. 4.10, where conditions which show a low F/C ratio usually contain a deeply fluorinated mixed layer of plasma damaged polymer and fluorocarbon species (high F2s/F1s ratio). On the other hand, high F/C ratios are an indication that the fluorine was deposited in a separate layer with a sharp interface to the photoresist material. It can be seen that through process adjustments significant variations of the process results can be obtained. Overall, we find that the surface F/C ratio provides an indication of the FC deposition mechanism, and relates to the observed surface

roughness. A dependence of the resist degradation on post exposure F/C ratios that is consistent with our data has previously been postulated by Negishi et al..[4.13]

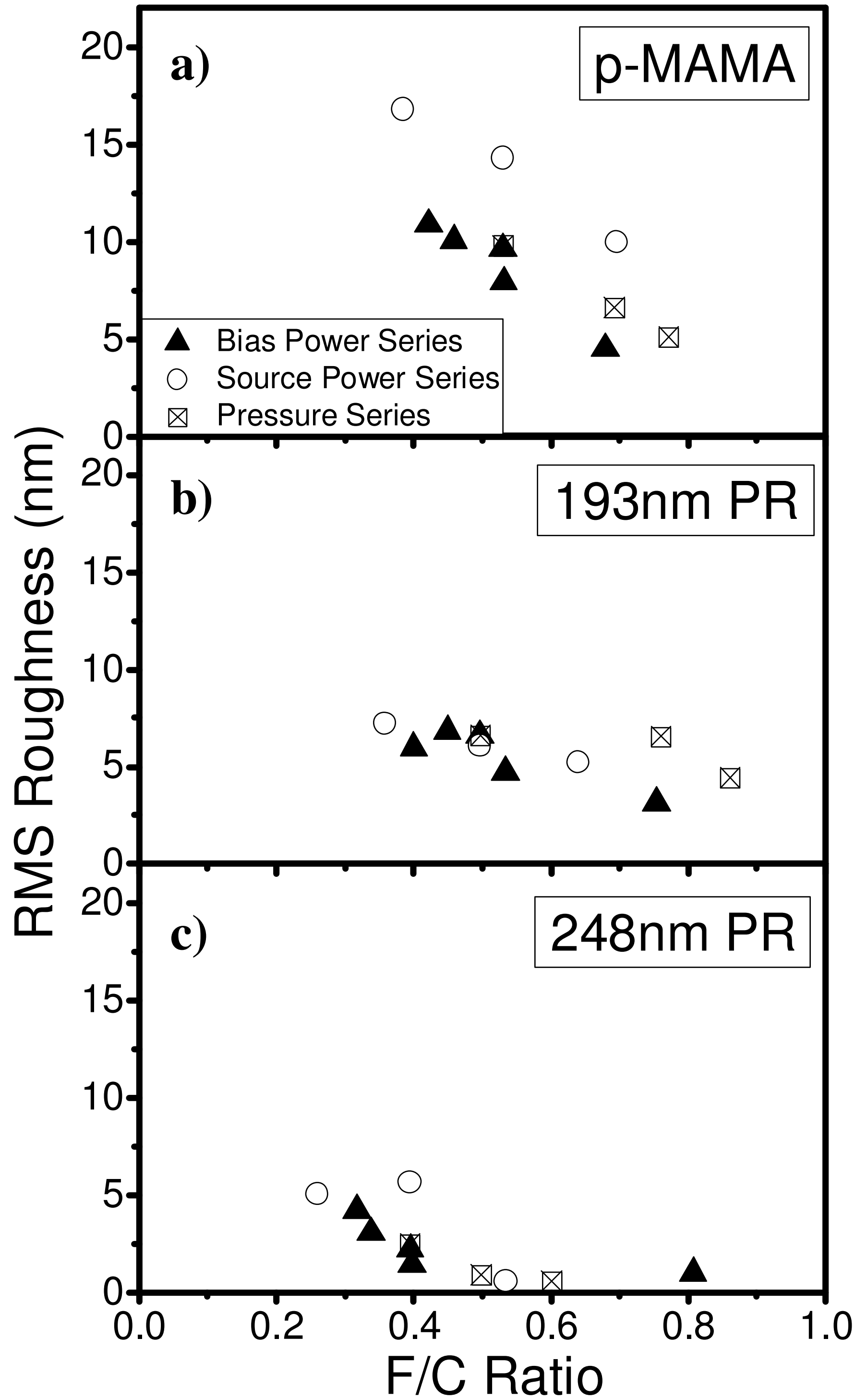

Figure 4.13: *Roughness as a function of the F/C ratio for C_4F_8/90% Ar exposures.*

We also monitored the evolution of 248nm PR, 193nm PR, RADA and EAMA under conditions examined in Figs. 4.9 and 4.10, for which the ion currents to the sample are comparable, but the surface fluorination changes. RADA and EAMA are molecular compounds of 193nm PR polymers that were examined in our previous publication.[4.1] Although the molecular structure of 193nm PR, EAMA and RADA are very similar, characteristic differences in roughening for these materials could be established in that work. A more fragile leaving group polymer in the EAMA polymer lead to higher surface roughness as compared to 193nm PR. Slightly lower roughness values than for 193nm PR due to reduced etching rates were found for the RADA polymer and attributed to increased crosslinking.

If fluorination determined surface roughness of the samples, we would expect that surface roughness increases as C_4F_8 is added. Additionally, one might expect that at least the differences in the process results for EAMA, RADA and 193nm PR should be similar for pure Ar exposures and by adding C_4F_8 these differences would increase. In contrast, Fig. 4.14 shows that the characteristic differences in the roughening behavior of different materials persist for all conditions. If fluorination would indeed be the dominant factor that causes surface roughening, RADA, EAMA and 193nm PR should show the same roughening rates in pure Ar. The results of Fig. 4.14 indicate that ion bombardment along with other interactions causes the roughening differences seen for plasma processing. The presence of fluorine at the surfaces of the polymers increases surface roughening rates for these materials, but it does not change the different characteristic material responses that reflect differences in molecular structure and monomer composition.

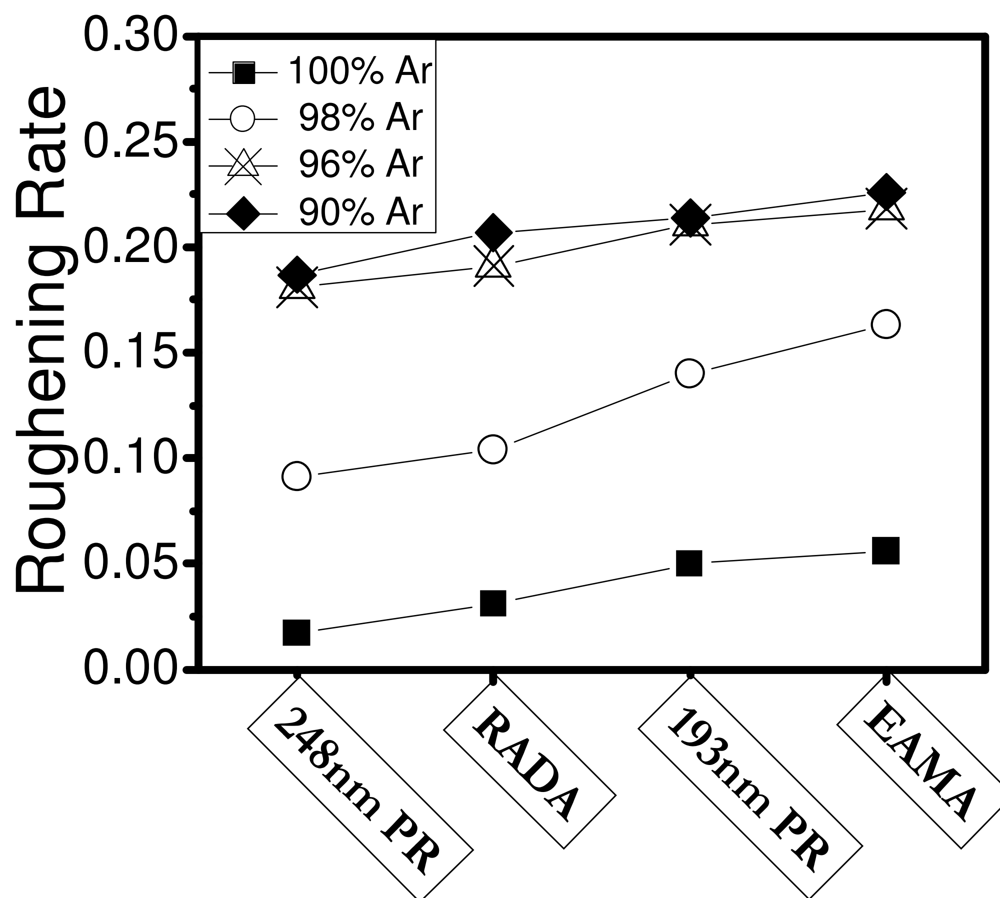

Figure 4.14: *Roughening rates of 248nm PR, RADA, EAMA and 193nm PR for pure Ar and C_4F_8/Ar mixtures.*

4.3.3 *Impact of plasma radicals*

4.3.3.1 Interactions with sidewalls

The data obtained as a function of source power were tested with respect to the change in surface fluorination. By exposing Si samples using a gap structure,[4.19] we found that increasing the source power increased the sticking coefficient of FC radicals. By examining contact hole profiles as a function of source power, the impact of increased radical sticking coefficient on sidewall profile, was evident. For low source power, the low sticking coefficient FC radicals are able to penetrate the contact hole completely, and by depositing, smooth the original standing wave patterns at the sidewalls (Fig. 4.15). When increasing source power, an increased sticking of the radicals on the top neck of the contact hole can be observed, whereas the bottom of the contact holes is not modified by FC radical deposition. The standing wave patterns remain after processing. The change in radical speciation for our discharge conditions is in qualitative agreement with simulations of fluorocarbon processes in our reactors performed by Vasenkov et al..[4.9]

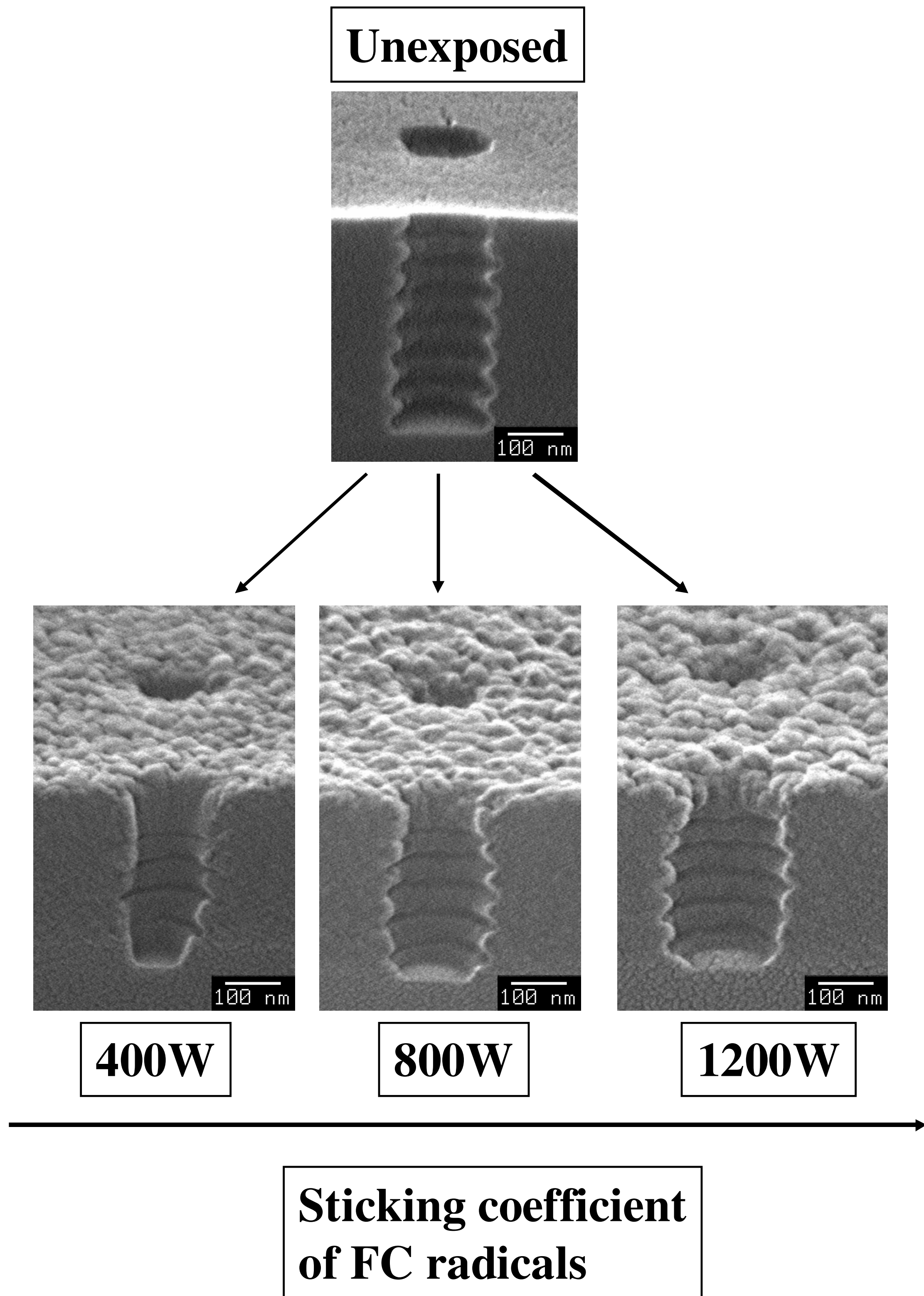

Figure 4.15: *Evolution of contact hole samples as exposed to different source power levels.*

4.3.3.2 Interactions of radicals with nanoscale geometries

The importance of the dimensionality of geometrical features of etched structures on process performance is shown in Fig. 4.16. Line features and contact holes were etched using the same discharge conditions (C_4F_8/90% Ar). The plasma etched lines (Fig. 4.16b)) show complete FC film coverage of the resist sidewalls (evident from the disappearance of the standing wave patterns present in the original structure). The contact holes (Fig. 4.16a)) only show limited FC film sidewall coverage (standing wave patterns remain visible after processing). Both structures started out with a CD of 150nm before etch, but the top CD of the processed trenches was measured as 129nm, whereas the top CD for the contact holes was measured as 136nm. In figure 4.15 we demonstrated that radical deposition plays an important role for profile shapes of nanoscale features. The more open structure of the trench reduces the neutral shading, increasing the smoothing sidewall deposition of FC polymer and decreasing the CD, relative to the contact hole.

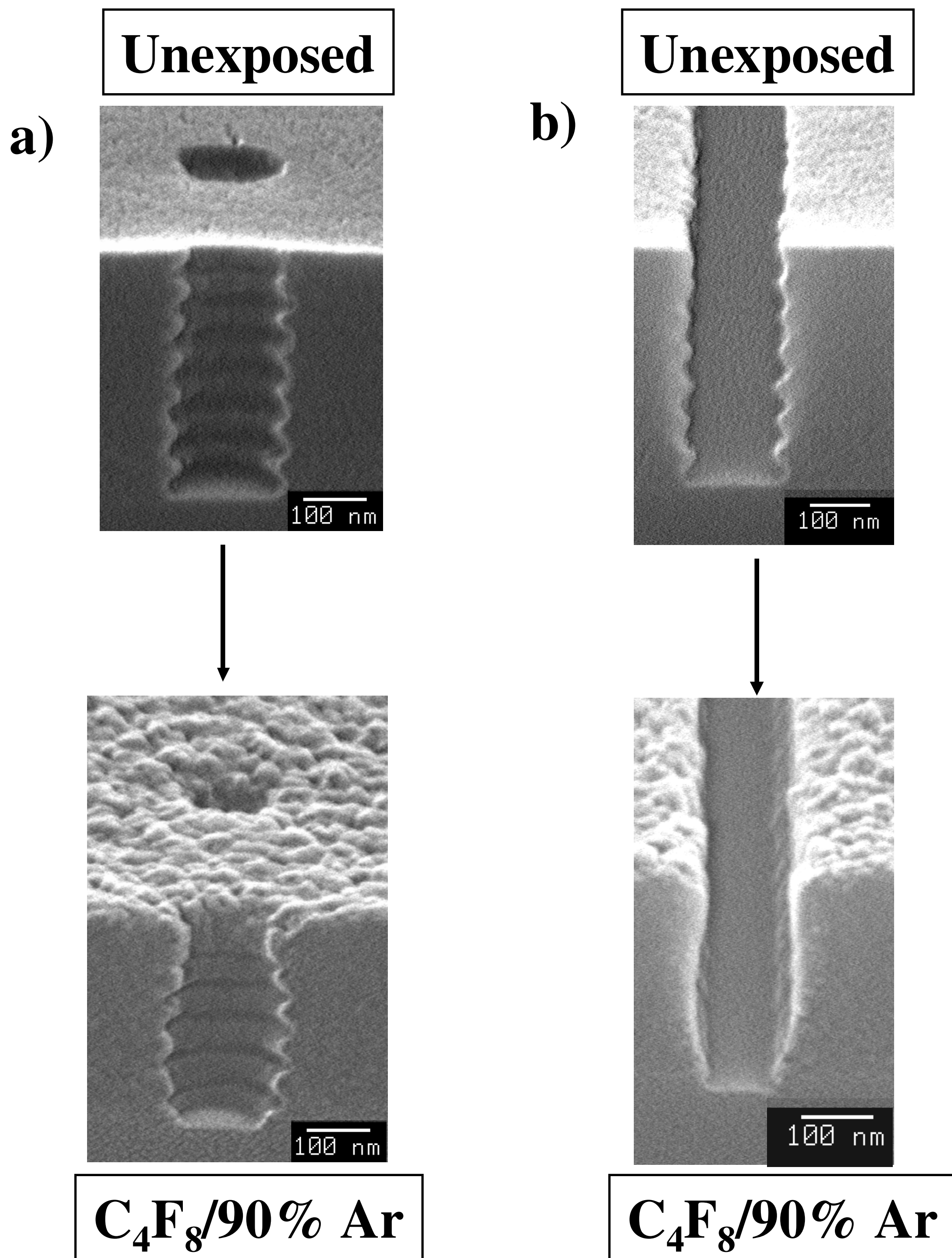

Figure 4.16: *Evolution of contact hole samples (a)) and trenches (b)) as exposed to the same discharge condition (C_4F_8/90% Ar).*

4.4 DISCUSSION

We divide this discussion into three sections. First we present a roughening model, which provides a description of the surface roughening behavior seen for all plasma parameters examined in this work. This is followed by a discussion of the PR surface roughness mechanism and the relationship between surface roughness and line edge roughness evolution during processing. We also address the effects of different FC plasma species and how changes in the FC species composition of the incident flux will influence process results.

4.4.1 Dependence of surface roughness on deposited energy density

It is well understood that roughness of 193nm PR materials may be introduced into the photoresist material during the lithographic exposure and/or plasma etch, followed by transfer into underlying materials.[4.3,4.20-4.24] Roughness formation during lithographic exposure has been related to unstable resist formulations,[4.25-4.30] and/or phase separation of unexposed and exposed polymer at the image definition area.[4.30-4.35] The impact of plasma etch on PR roughness evolution is much less understood. For certain process conditions smoothing of rough sidewalls can actually be achieved by the plasma etch process.[4.22,4.23,4.36] Most roughness studies are limited to variations in either resist materials[4.2,4.26,4.37] or discharge chemistries.[4.12,4.13] Thus a general model of PR roughening, including effects of materials and plasma process

parameters is missing. A model based on the experiments described in section 4.3 is presented in the following.

By evaluating the influence of plasma parameters on the surface roughness introduced, we found that the surface roughness as a result of processing originated from two mechanisms: In the bias power and pressure experiments we found that the surface roughness evolution can be linked to an ion induced transfer mechanism, i.e. amplification of the surface profile due to ion bombardment. The samples processed at different source power levels did not seem to follow the same mechanism. We developed a model combining all these observations to describe the roughness evolution seen in plasma processing.

Sumiya et al.[4.38] showed that PR materials undergo severe damage within the first seconds of plasma processing, where characteristic roughness length scales form on the PR surface based on plasma condition and PR material. After the characteristic length scales are formed, roughness increase is mostly attributed to an increase of the amplitude of the roughness features.[4.38] A roughness introduction mechanism was postulated based on spatially non-uniform removal of the PR during etch (see Fig. 15[4.38]).

We believe that in addition to this mechanism, roughness is introduced into the PR material based on the energy density ε deposited at the surface during processing.

$$\varepsilon = \frac{E_i}{v_i E Y} \tag{1}$$

As schematically depicted in Fig. 4.17, the ion bombardment of the PR surface generates an energy flux into the PR material during processing. For ion-assisted etching, a PR surface volume element v_i receives a characteristic mean energy E before it is volatilized. If the etch yield EY during processing differs strongly for two process conditions, the same material will require different energy densities ε for volatilization in each condition.

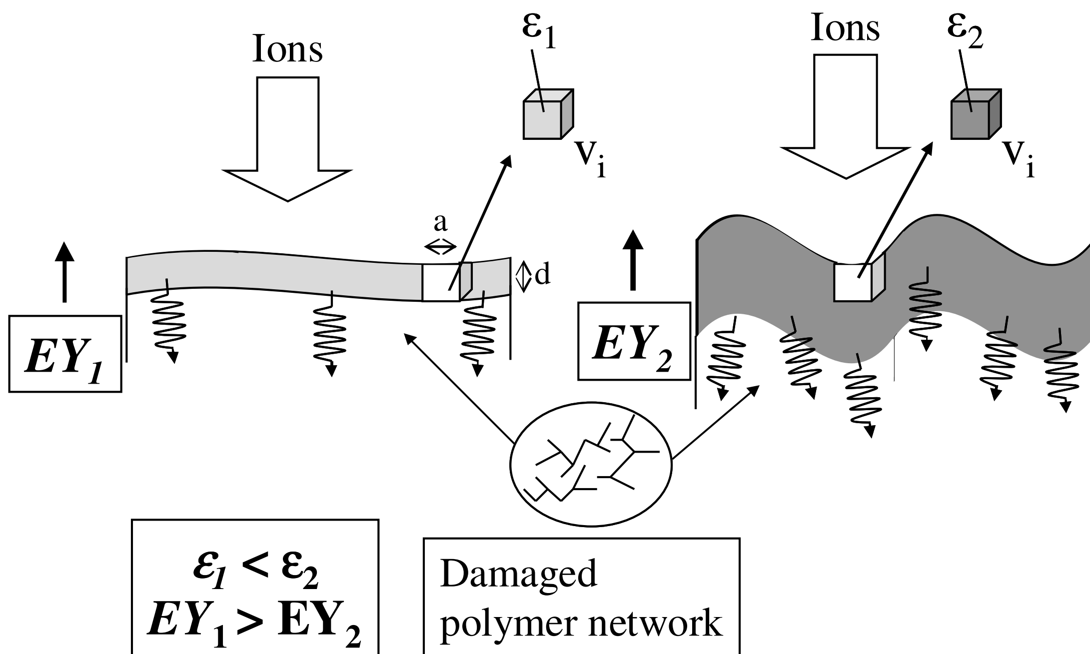

Figure 4.17: *Schematic surface conditions for etching at low or high energy densities during processing. For processing at high energy densities, more energy is transferred into the deeper regions of the surface leading to characteristic roughening of the surface.*

This is illustrated schematically in Fig. 4.17. With EY_1 being high, the time Δt the surface element v_i receives the energy input is short and a small energy density ε_1 is deposited at the PR surface during processing. In contrast to this situation is one characterized by a low etching yield EY_2. Since the energy required to volatilize the

surface element v_i is higher in this case, a higher energy density ε_2 is deposited at the surface. However the critical energy required to volatilize a volume element is a fairly fixed characteristic of the material, therefore the higher energy density ε_2 represents an excess of deposited energy beyond that needed for etching. Therefore a significant amount of the energy is transferred from the surface to the deeper PR layers and can induce damage in the polymer structure. The damage and spatial reorganization of the PR polymer material, induced by the energy transfer from the plasma, may be responsible for the formation of the characteristic surface roughness features. Such roughness features, once established, could serve as the starting point for the ion-based transfer and roughness amplification.[4.38]

The characteristic energy density ε deposited during processing can be found by the energy E carried to a surface element a during time Δt:

$$E = P_a a \Delta t \,, \tag{2}$$

where P_a is the power density (energy per unit area). This can be rewritten as

$$E = \Gamma_i E_i a \Delta t \,, \tag{3}$$

where Γ_i is the ion flux incident on the substrate and E_i the average energy of the ions incident on the substrate.

We define the etch yield EY (probability that an ion induces etch) as

$$EY = \frac{N_s}{N_i} \tag{4}$$

where N_s is the number of sputtered substrate atoms and N_i is the number of incident ions on the substrate, both expressed per unit area. The ion induced etching rate ER can be rewritten as

$$ER = v_i EY\Gamma_i \tag{5}$$

where v_i is the volume of substrate material removed per etch-inducing ion. If we assume that a layer with thickness d is removed during a time interval Δt, we have

$$d = ER\Delta t = v_i EY\Gamma_i \Delta t \tag{6}$$

or

$$\Delta t = \frac{d}{ER} = \frac{d}{v_i EY\Gamma_i}. \tag{7}$$

The energy that is deposited in the volume ad while etching the layer of thickness d becomes

$$E = \Gamma_i E_i a\Delta t = \frac{\Gamma_i E_i ad}{v_i EY\Gamma_i} \tag{8}$$

The energy deposited per unit volume ε is

$$\varepsilon = \frac{E}{ad} = \frac{E_i}{v_i EY}. \tag{9}$$

By examination of our data, we found that ε in concert with polymer structure plays a key role in polymer surface roughening. To see this, we rearranged our results from section 4.3.1 according to the above parameters. E_i was determined from the self-bias voltage V_{dc} to which the plasma potential V_p (20eV) was added.[4.10] The values for EY were obtained from the etch rate and the ion flux as stated in Eq. 4. As a measure for the roughness introduction we will use the roughening rate RR instead of the RMS surface roughness. As discussed earlier, one important mechanism of roughness formation in PR materials is based on a transfer mechanism by ions, where locally non-uniform removal rates lead to amplification of existing surface roughness.

For longer process times, a large contribution to the *RMS* surface roughness originates from this mechanism. By normalizing the *RMS* surface roughness to the removed thickness using the roughening rate *RR* contributions of this ion based transfer mechanism can be minimized.

$$RR_m = \frac{SR_m}{ER_m t} \tag{10}$$

Our model (Fig. 4.17) depicts the energy density, which is normalized by the volume removed during processing, to be characteristic for the roughening behavior. It makes therefore also sense to normalize the roughness introduction to the volume removed as done by using RR_m instead of using the absolute surface roughness SR_m.

The dependence of the roughening rates *RR* of the materials on energy density ε is shown in Fig. 4.18. All materials show a linear dependence of roughening rate on the deposited energy per unit volume removed. Consistent with the high fragility of the adamantyl group, p-MAMA shows a stronger dependence of *RR* on ε than 248nm PR. Overall, we find that the roughening rate *RR* is a function of the energy density and can be written as

$$RR_m(\varepsilon) = C_m \varepsilon(E_i, v_i, EY), \tag{11}$$

where C_m is a proportionality constant that reflects the molecular structure of the polymer. This proportionality constant C_m is a measure of how effectively deposited energy is converted into roughness by the polymer material. Linear Fits of the data (as shown in Fig. 4.18) yield values for C_m of adamantyl polymers as $3.6\text{x}10^{-6}$ nm^3/eV and of aromatic polymers as $7.9\text{x}10^{-7}$ nm^3/eV. A significantly higher roughening constant C_m was observed for the adamantyl containing polymers p-

MAMA and 193nm PR, which reflects the fragility of this polymeric structure. The constant C_m is related to the basic materials properties of the respective polymer material.

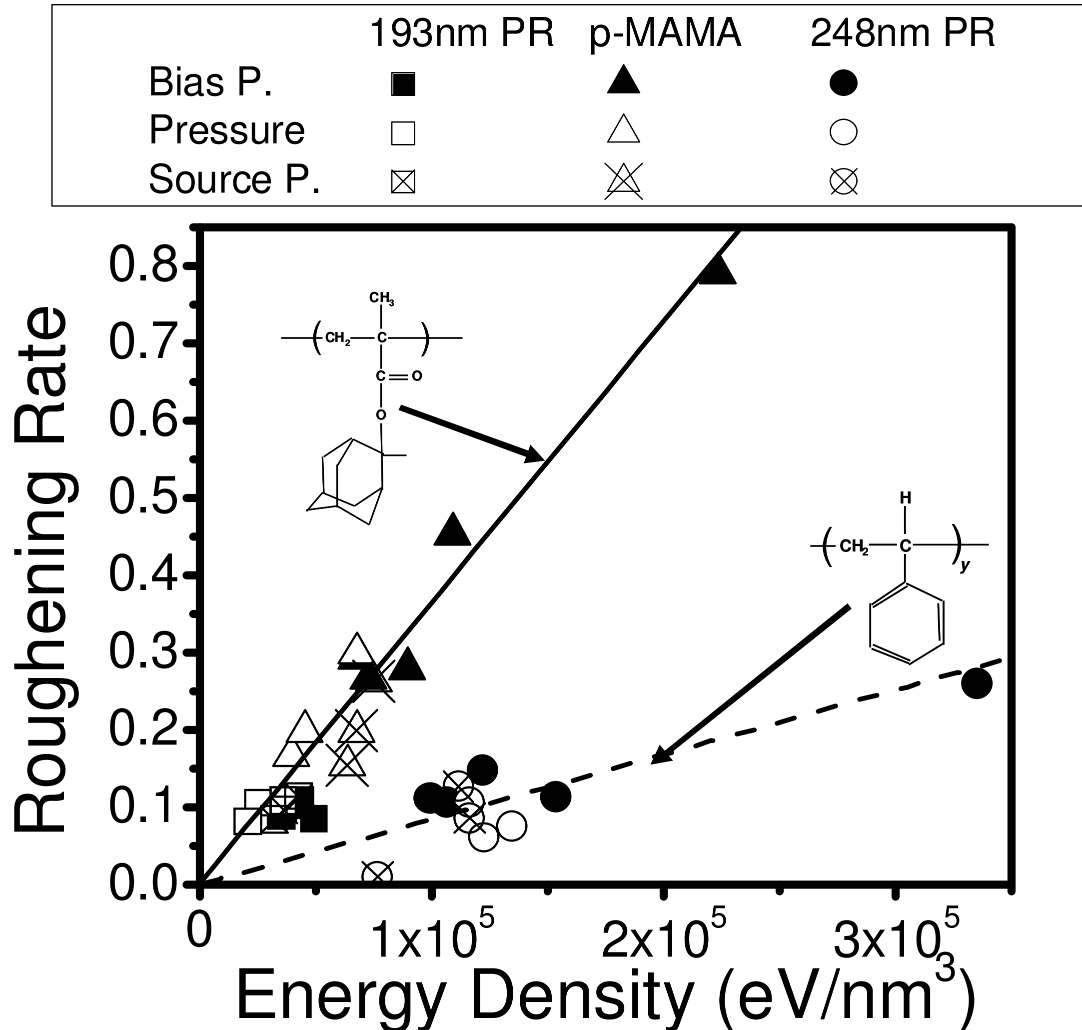

Figure 4.18: *Roughening rate vs. energy density for C_4F_8/90% Ar exposures.*

The high oxygen content of 193nm PR leads to high etch yields, and prevents the 193nm PR material from being exposed to high energy densities during processing. Because of this, the measured roughening rates *RR* for 193nm PR are

small, but still consistent with the fragility of the underlying adamantyl structure (p-MAMA). Since *absolute RMS surface roughness SR* is given by

$$SR_m = RR_m(\varepsilon)ER_m t\,, \tag{12}$$

the actual etch rate during the process impacts the absolute surface roughness. The high surface roughness values seen for 193nm PR are caused by a high removal rate in conjunction with large C_m values that are also characteristic of the adamantyl structure of p-MAMA. Roughening of 248nm PR is significantly lower due to a lower roughening constant C_m, which in conjunction with very low removal rates results in overall low absolute roughness values for 248nm PR. Very high C_m values are seen for p-MAMA. In our data there is no evidence that the roughening rates saturate at higher energy densities. Additional tests of this model, including a situation where the etch yield was significantly increased due to a fluorination of the PR material, can be found in a corresponding publication.[4.4]

4.4.2 Are line edge roughness and surface roughness correlated?

To examine if our surface roughness data obtained with blanket films are relevant to sidewall roughness evolution, we compared our results obtained with blanket films with data measured for plasma etched nanostructures. A general correlation of the observed top and sidewall roughness was found. For conditions where the surface energy density ε played a strong role for roughness formation, a strong correlation was found (see Fig. 4.19a), obtained for plasma etching at different source power levels). Different roughness levels based on the FC precursor

interaction with the damaged PR affected surface and sidewall roughness equally. The radical speciation, which is also linked to the FC film formation, was found to impact the profile evolution significantly (see Figs. 4.15 and 4.16). The roughness evolution for changing the RF bias shows a weaker correlation between surface roughness and sidewall characteristics (see Fig. 4.19b)), obtained for plasma etching at different self-bias voltages). Presumably, ion-induced transfer results in longer sidewall striations in this case, which does not impact the LWR/LER values on the top sidewall greatly.

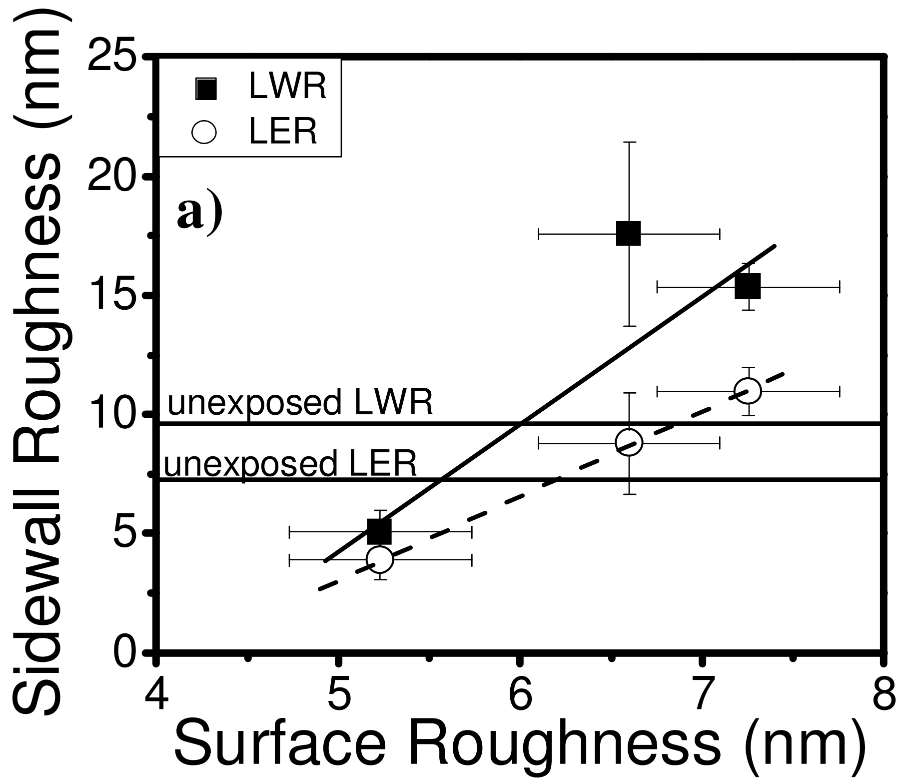

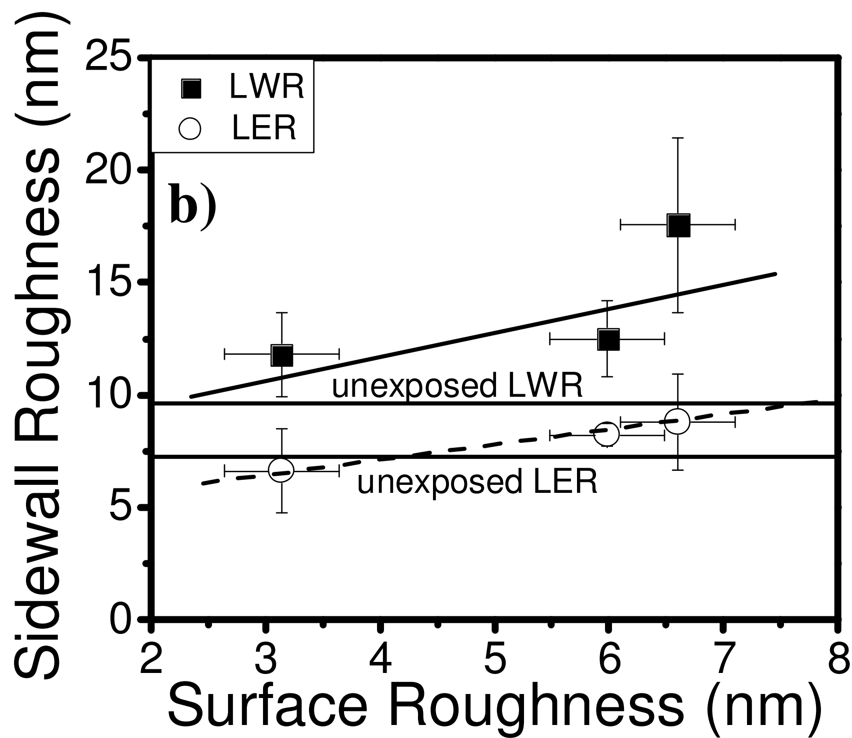

Figure 4.19: *LER and LWR roughness as a function of the RMS roughness for different source power levels (a)) and different ion energies (b)).*

4.4.3 Influence of plasma species

Our results showed, consistent with previous studies, that by increasing ion energy, both the material removal rate and polymer surface roughening increased.[4.39-4.42] On the other hand, increased ion energies produced better profiles (straighter sidewalls). Improved LER and LWR results can be mainly attributed to formation of protective FC films for low energy plasma etching, while high RF energy plasma etching showed pronounced ion-induced roughness formation and striation evolution. Similar trends for changing ion energies were obtained previously.[4.12,4.13,4.43,4.44] The inverted trend in F/C ratios for the -50V etch can be explained by the softness of the PR materials. Since the polymers only show very little etching for this process condition, the measured F/C ratio is mostly determined by the F/C ratio of the depositing FC film. The 248nm PR is based on a more stable polymer than 193nm PR and p-MAMA, and only little FC mixing with the PR takes place. The measured F/C ratios are similar to values for passively deposited FC films. The 193nm PR material and p-MAMA are chain scissioning polymers and FC radicals can diffuse into the PR material more easily, and the measured F/C ratios for these materials are lower.

Increasing process pressure resulted in an increase in etch yield together with increased surface fluorination, where 193nm PR showed a strong and 248nm PR a weaker dependence. A similar dependence was found for the F/C ratio with increasing pressure, where the increase in F/C ratio was significantly larger for 193nm PR than for 248nm PR. A possible connection between the two results was tested in Fig. 4.20, where we plotted results obtained for different self bias voltages,

source power settings and pressures. We notice that for most conditions the etch yield is fairly independent of the F/C ratio. A close correlation between F/C ratio and etch yield can however be noted for conditions with F/C >0.5. These data were measured for the pressure series, indicating that higher removal rates at higher pressure can be related to increased fluorination of these PR materials under those conditions. We also notice that 193nm PR shows the highest degree of fluorination of all materials, and the largest increase in etch yield. The high etch yields and F/C ratios of 193nm PR are consistent with the fact that chain scissioning of 193nm PR facilitates fluorination and removal of PR material. It is also a first indication of how the surface composition can be adjusted to change the process results, e.g. as examined in a separate publication.[4.4]

High ion to neutral ratios for low pressures resulted in high surface and sidewall roughness, but straight sidewall profiles. Conversely, a low ion to neutral ratio (high pressure) caused increased fluorination, which results in surface smoothing, and in some cases process complications such as etch stop or wiggling.[4.12,4.45] The improvements of LER and LWR after processing using high pressure discharges can be related to higher etch yield and corresponding lower energy densities ε, whereas the increased roughness observations for the high ion/neutral regime can be attributed to ion-induced transfer effects from the plasma process.

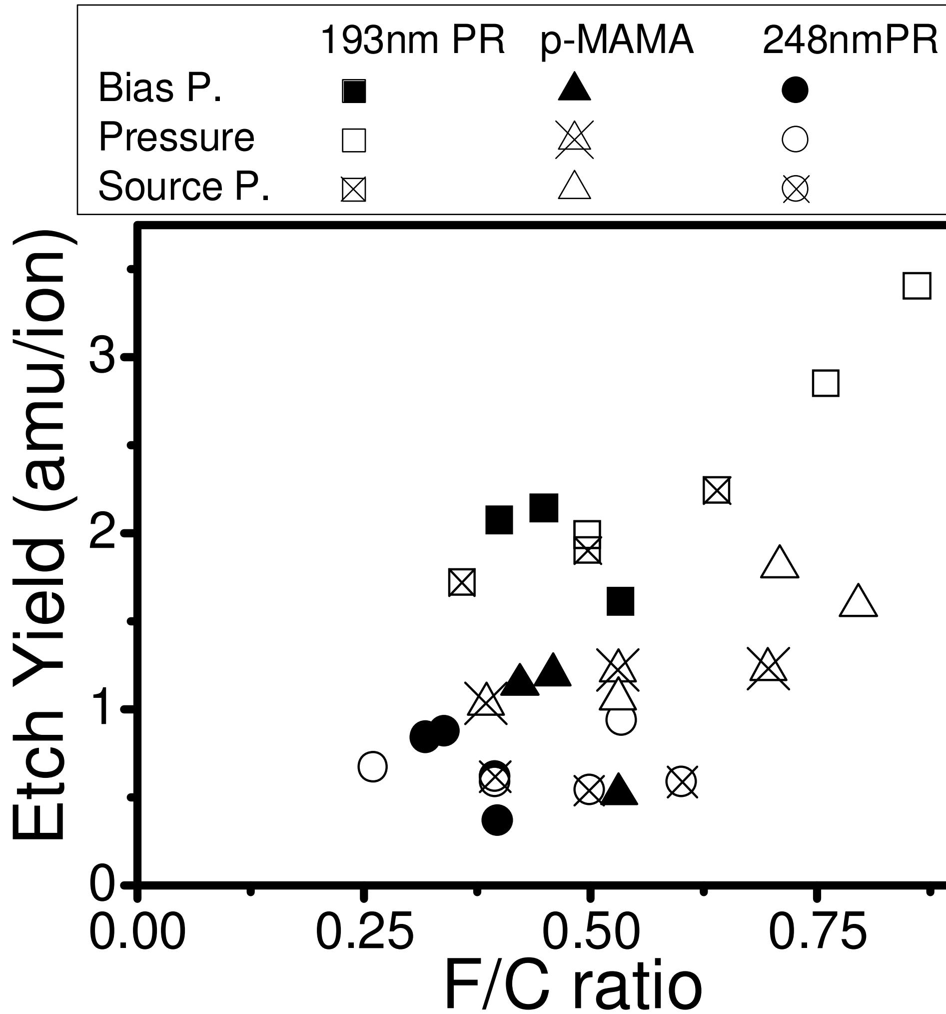

Figure 4.20: *Etch Yield vs. F/C ratio for C_4F_8/90% Ar exposures.*

The nature of the FC surface layers formed on the PR substrates is very characteristic of the roughening behavior due to plasma processing. Previous reports[4.41,4.46] found that thick FC films having low F/C ratios result in rough plasma etching, whereas thin, highly fluorinated films on top of 193nm PR material resulted in smooth plasma etched surfaces. The thin (smooth) steady state FC films accompany slightly higher PR etch yields, which is consistent with the model of etching through a fluorocarbon layer.[4.47]

Finally, the dependence of surface roughness introduction on the nature of the polymer material has been demonstrated. We found for all plasma process conditions, that the most stable polymer (248nm PR) showed less surface roughening than 193nm PR materials. The following observations provide some indications of the mechanisms that are responsible for these differences. One, a lower F(2s)/F(1s) ratio for 248nm PR points to the fact that fluorine and C_xF_y radicals are not able to penetrate 248nm PR very well, leading to only thin FC layers on top of the PR film. Two, p-MAMA displayed the highest surface roughening rates under all conditions. The fragility of this homo-polymer in FC etching plasmas has been observed before.[4.1] Additionally, the chain scissioning nature of 193nm PR and p-MAMA led to increased modification of the surfaces by plasma etching. The molecular structure of p-MAMA and 193nm PR also caused higher roughening rates, $RR(\varepsilon)$, pointing to the fact that the adamantyl structure is more susceptible to plasma damage than styrene polymers. Finally, the high oxygen content of 193nm PR prevents processing at high energy densities and enhances the roughness generation based on removal of the PR material.

4.5 CONCLUSIONS

We have examined the plasma surface interactions of advanced photoresist materials with C_4F_8/Ar discharges for a variety of plasma process conditions. We observed characteristic responses determined by polymer structure for all conditions tested. While ion energy and fluence primarily determine the removal rate of the PR

materials, enhanced removal rates due to surface fluorination of the PR materials during plasma etch were also observed. The surface roughening of the PR materials is based on two linked mechanisms. The relaxation of the near-surface polymer structure based on the excess energy deposited during processing determines the roughening behavior. A significantly different roughening constant C_m was found for adamantyl and aromatic polymers. Roughness introduced into surfaces during the early stages of the plasma-PR interaction are amplified based on spatially non-uniform ion-induced PR etching during processing. The high roughening constant C_m and high etch yields due to higher oxygen content are responsible for the poor etch results of *193nm PR*.

The fluorination of PR materials that accompanies FC-based transfer etch processes influences the overall roughening behavior of the PR materials. Roughening behavior was similar for pure Ar processing and for FC-based processes which produced thin FC films on top of the PR, whereas deposition of thicker FC films on the PR surfaces increased the overall roughening. The penetration of fluorination for *248nmPR* was found to be much shallower than for *193nm PR*, as indicated by significantly lower F2s/F1s XPS intensity ratios measured for *248nm PR* than for the other materials examined. Processing using F-rich FC radicals led to production of smoother surfaces and sidewalls, whereas conditions containing C-rich FC radicals increases the roughening on both surfaces and sidewalls. The effects of significantly different sticking coefficients of FC radicals, generated by different plasma conditions, were seen in the sidewall roughness and profile shapes of PR nanostructures after plasma processing. A general correlation between process-

induced polymer sidewall roughness and top surface roughness was found which suggests that the reported mechanisms for roughening of blanket films also apply to sidewall structures.

ACKNOWLEDGEMENTS

The authors gratefully acknowledge financial support of this work by the National Science Foundation under award No. DMR-0406120 and DMR-0705953. Florian Weilnböck, Brian Smith, Yilin Liu, Dr. D.Y. Lee and Dr. M. Moravej are thanked for help and contributions to parts of this work.

Chapter 5

Controlling photoresist surface modifications during plasma-based pattern transfer by choice of feedgas composition: Comparison of C_4F_8- and CF_4-based discharges

To be submitted to J. Vac. Sci. Technol. B, (2008)

S. Engelmann, R. L. Bruce, F. Weilnboeck, M. Sumiya, T. Kwon, R. Phaneuf,
G. S. Oehrlein, C. Andes, D. Graves and D. Nest and E. A. Hudson

ABSTRACT

We report a study of the impact of surface chemical factors on etch rates along with surface and line edge roughness introduction for prototypical photoresist (PR) materials and structures during plasma-based pattern transfer employing fluorocarbon (FC) discharges. For selected photoresist materials and model polymers (193nm PR, 248nm PR and poly-methyladamantyl methacrylate (p-MAMA)), the influence of bulk polymer properties on plasma durability was clarified by comparing etch rates, surface roughness introduction, and profile evolution of nano-structures. We studied the effects of both fluorocarbon fragment deposition and polymer surface fluorination by gas phase fluorine atoms on plasma etching resistance and surface roughness evolution of the organic materials by comparing discharges fed with C_4F_8/Ar or CF_4/Ar/H_2 gas mixtures. The spatial frequency distribution of surface roughness was obtained using fast Fourier transformation (FFT) of atomic force microscopy data. A graphitic layer was formed for Ar containing discharges on the polymer surfaces.

Fluorocarbon deposition on the damaged photoresist affected roughening in two opposing ways: Ion-induced mixing with the damaged polymer layer increased surface roughening, whereas for simple FC precursor deposition a reduction of surface roughness was seen. The latter effect was especially important during profile evolution of three-dimensional structures. Fluorination of the photoresist surfaces by fluorine-rich plasma increased polymer etching yields, and for highly fluorinated surfaces inhibited the formation of the graphitic surface layer. The destruction of the adamantyl structure is usually found in fluorocarbon/argon discharges and is a major origin of roughness evolution for 193nm PR materials. Process conditions having high etch yields were found to improve the roughness results of 193nm PR after etch. The fluorination of the photoresist materials prevented the formation of characteristic small scale roughness features at the cost of large scale roughness introduction. Use of low energy density process conditions prevented the introduction of large scale roughness, and can be explained by suppression of surface roughness growth by an ion induced transfer mechanism. Alternatively, CF_4/H_2 processing also showed improved roughness results due to a separate layer deposition of the fluorocarbon film on top of the photoresist material. The etch results for all process conditions can be combined in a surface roughening model where the roughening behavior of the film scales linearly with the energy density delivered to the polymer surface during processing. Even for a range of feedgas chemistries, adamantly-containing polymers show enhanced roughening rates, suggesting that the instability of the adamantyl structure used in 193nm PR polymers is the performance limiting factor for processing these PR materials.

5.1 INTRODUCTION

One reoccurring issue in nanoscale fabrication is roughness introduction in polymeric materials as a result of plasma processing. While studies addressing issues of either photoresist (PR) materials[5.1-5.3] or discharge conditions[5.4,5.5] on PR degradation have been published, a combined study of both, PR material and plasma conditions has been missing.

We studied *193nm PR*, *248nm PR* and poly-methyladamantyl methacrylate (*p-MAMA*) under different processing conditions. Briefly, the *193nm* and *248nm* PR materials frequently used in nanoscale manufacturing differ significantly in their polymer structure. Importantly, *193nm PR* has a higher oxygen content due to presence of lactone than *248nm PR* and additionally, their polymer structures differ (adamantyl vs. aromatic).[5.6] We previously reported that photoresist (PR) materials undergo rapid surface transformations including oxygen and hydrogen loss when exposed to plasmas or ion beams, which coincides with initially high materials etching and surface roughening rates.[5.6] A modified PR surface layer develops as a result of the interaction with the ions, photons and radicals of the plasma, which also reflects the materials characteristics of the original PR polymer. Steady state etch conditions are established after a time of 15 s or less for our process conditions.[5.6] We characterized roughness of PR films by determining the root mean square (RMS) value of the surface profile after processing. Smooth PR surfaces were seen for plasma process conditions that produced a fluorine rich, thin, separated fluorocarbon

(FC) layer on top of the modified PR layer, whereas rough PR surfaces show C-rich FC films that are highly mixed with the damaged PR.[5.7]

The roughening of PR materials could be described by a model where the energy density deposited during processing scales with the roughening rate of the process.[5.7] For adamantyl polymers, the deposited energy was much more efficiently converted into roughening than at comparable conditions for aromatic polymers.[5.7] The roughening behavior in conjunction with a non-uniform removal rate determined the surface roughness (SR) of the polymers.[5.7] For the examined conditions, a general correlation of PR surface and sidewall roughness was observed.[5.7]

The purpose of the present study is a more detailed analysis of the effect of fluorination of polymers on plasma durability of photoresist materials. It is known that discharges fed with C_4F_8/Ar produce a high amount of FC film deposition with little atomic fluorine in the discharge,[5.8-5.10] whereas use of CF_4/Ar/H_2 gas mixtures results in F-rich to F-deficient plasmas (depending on the amount of H_2 used), that exhibit much lower FC film deposition rates than C_4F_8/Ar discharges.[5.11-5.16] By employing FC discharges fed with either C_4F_8/Ar or CF_4/Ar/H_2 gas mixtures, we were able to distinguish the influence of *fluorocarbon fragment deposition* from *polymer surface fluorination by gas phase fluorine atoms* on plasma etching resistance and surface roughness evolution of organic materials. The role of the polymer backbone in plasma durability was established by comparing prototypical photoresist materials and a model polymer (193nm PR, 248nm PR and p-MAMA).

We start this article with the results of processing of these materials using five representative plasma process conditions.[5.17,5.18] This is followed by a detailed

examination of FC-radical rich to Ar-rich discharges (C_4F_8/Ar) and F-rich to Ar-rich discharges (CF_4/Ar). The results section will finish with a detailed compositional analysis of the conditions examined. The discussion section will review the effects of plasma speciation on etch rate, roughening behavior and 3d profile evolution in detail.

5.2 EXPERIMENTAL

5.2.1 Description of materials

The polymer materials in this study were provided by Rohm and Haas Electronic Materials and a detailed description of their properties has been presented in a previous publication.[5.6,5.7] Briefly, we employed a 248nm PR consisting of co-polymerized polystyrene, polyhydroxystyrene and ter-butylacrylate to study the effects of an aromatic ring containing polymer with low oxygen concentration. The second polymer is 193nm PR, consisting of co-polymerized methyl adamantyl methacrylate, α-gamma butyrolactone methacrylate and R-functionalized adamantyl methacrylate. In addition, a poly-methyladamantylmethacrylate (p-MAMA) polymer was selected to emphasize the influences of the fragile adamantyl group. While acrylate polymers (i.e. 248nm PR) undergo cross linking upon ionizing radiation, methacrylate polymers (i.e. 193nm PR and p-MAMA) tend to favor chain scission.[5.19,5.20] This allows the examination of the plasma etch behavior of the adamantyl structure at a similar oxygen content as used for the 248nm PR, which is lower than the oxygen content typically present in 193nm PR materials[5.6,5.7]. By

comparing these three materials, the effects of oxygen content and polymer structure on plasma durability and surface morphology evolution can be clarified. The preparation of the blanket and patterned samples was performed according to the protocol described in an earlier publication.[5.7] Due to the missing bottom anti reflection (BARC) coating, standing wave patterns were observed on the exposed contact holes and trenches, each having critical dimensions (CD) of 150nm before etch.

5.2.2 Plasma processing

The materials were processed in a plasma etch reactor described in a previous publication.[5.21] A 13.56 MHz inductively coupled plasma (ICP) source (0-2kW) controls the plasma density, while a 13.56 MHz (0-1kW) capacitively coupled RF bias enables independent control of the substrate ion energy. The temperature of the substrate electrode was kept at 10°C using an electrode chiller, while the chamber walls were kept at 50°C using heating straps. The gas flow into the chamber was fixed at 50sccm. Before each run, the chamber was dry cleaned using an O_2 plasma followed by a 1 min seasoning discharge applying the conditions for the next experiment. Operating pressures of 10mTorr during all experiments were controlled using a throttle valve in the exhaust line. The source power was set to 800W for all experiments described in this article. The bias power was adjusted for the different discharges to maintain a constant selfbias voltage of -100V. The process time for all experiments was 1 min.

In order to distinguish the effects of fluorocarbon and fluorine radicals on photoresist processing, c-C_4F_8 and CF_4 feedgases were selected.[5.22-5.24] A C_4F_8/90% Ar plasma etching process achieves a low photoresist etch rate because of FC film deposition and low gas phase fluorine radical density.[5.9,5.10,5.25-5.27] In comparison, a CF_4 plasma etching process is characterized by little FC film deposition and a high gas phase fluorine radical density and results in high PR etching rates[5.9,5.17,5.28,5.29]. To examine the effect of Ar addition on PR surface properties, we also plasma etched PR materials using CF_4/90% Ar. The influence of fluorocarbon gas on the process result was clarified further by varying the Ar percentage in C_4F_8/Ar percentage or CF_4/Ar. Since H_2 addition to CF_4 reduces the gas phase fluorine atom density[5.12,5.13,5.28], and also has been shown to reduce PR damage,[5.18] a CF_4/40% H_2 and CF_4/H_2/Ar discharges were also employed.

5.2.3 Post plasma process characterization

Average photoresist etching rates were determined using a single wavelength ellipsometer (632.8nm) to measure the PR thickness before and after plasma etching. For the analysis of the ellipsometric data we assumed a homogeneous PR layer. The surface profiles of blanket PR films were measured using atomic force microscopy (AFM). The root mean square (RMS) values of 2x2 μm^2 surface profiles are reported as a measure of surface roughness (SR). The Fast Fourier-Transform (FFT) signatures of the surface profiles were obtained according to the protocol described by Sumiya et al..[5.8] The surface chemical composition of the processed PR samples was analyzed

using x-ray photoelectron spectroscopy (XPS). A detailed description of the XPS analysis procedures was given in earlier publications.[5.6,5.7] The measured oxygen concentrations were found to be fairly low (O/C < 0.1) for all conditions and are not shown explicitly in this paper. As patterned and plasma etched PR nanostructures were examined using scanning electron microscopy (SEM). The SEM images were numerically analyzed in the same fashion as reported earlier.[5.7] Critical dimension (CD) analysis at the top, middle and bottom of the trench and contact hole samples was used to characterize the profile shape of the 3d structures after plasma processing. Line Edge Roughness (LER) and Line Width Roughness (LWR) were measured at the top of the trench and indicated transformations of the sidewall roughness as a result of plasma processing.

5.3 RESULTS

5.3.1 Polymer modifications for five fluorocarbon discharge conditions

Process results for the three polymers examined in this work for five characteristic fluorocarbon plasma etching conditions are shown in Fig. 5.1. Panel a) shows etching rates. For most processes, 248nm PR shows the lowest etch rate, followed by p-MAMA and 193nm PR. When changing from C_4F_8/90% Ar to

CF_4/90% Ar, the etching rate increases for all materials. A thinner FC layer is formed on the polymer surfaces in CF_4/90% Ar and provides less protection of the polymer against ion attack. Pure CF_4 plasma etching produces significantly increased etch rates for all materials, and can be explained by the high atomic fluorine concentration formed in the gas phase for these conditions. Finally, when using CF_4/40% H_2 and CF_4/40% H_2/40% Ar gas discharges, etching rates very similar to those measured for C_4F_8/90% Ar are seen.

In panel b) RMS surface roughness data are shown. A general RMS roughness trend is seen as a function of polymer material for all FC discharge conditions, which is consistent with earlier data reported by our group for C_4F_8/90% Ar. Polymers with more likelihood of cross-linking (e.g. 248nm PR) have a lower the surface roughness introduction rate.[5.6] CF_4/90% Ar discharges led to slightly reduced roughness compared to C_4F_8/90% Ar. CF_4/H_2 showed etch rates similar to C_4F_8/90% Ar, but maintained much smoother surfaces. Using CF_4/H_2, we obtained a very smooth surface even for p-MAMA . When adding Ar to the CF_4/H_2 discharge, this effect seems to vanish as CF_4/40% H_2/40% Ar shows roughnesses comparable to CF_4/90% Ar.

The F/C ratios shown in panel 5.1c) were obtained from peak fitting the C1s spectra, and provide information on the PR surface composition after processing. Minimal surface fluorination can be noted for CF_4/90% Ar and CF_4/40% H_2/40% Ar. Very high surface fluorination is seen for pure CF_4, CF_4/40% H_2, and C_4F_8/90% Ar.

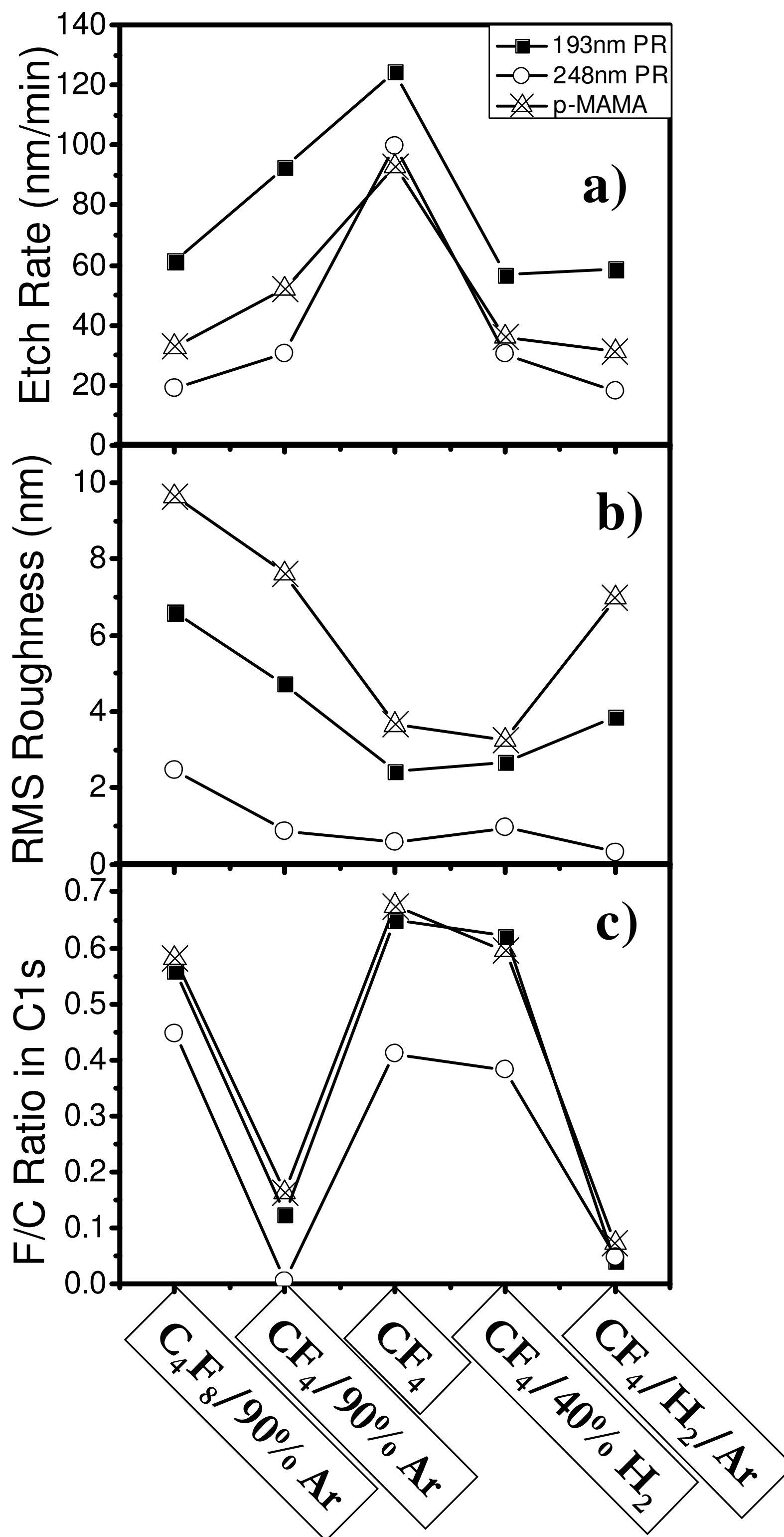

Figure 5.1: *Etch rates (a)), RMS roughness (b)) and F/C ratio (c)) after processing for five plasma process conditions.*

The material specific F/C ratios seen here for each plasma etch condition are consistent with the behavior seen previously for different model polymers plasma etched using C_4F_8/90% Ar, i.e. the greater the cross linking nature of the polymer, the less fluorinated the polymer.[5.6] A low F/C ratio was found to correlate to smooth surfaces after plasma processing.[5.6] For CF_4/40% H_2, p-MAMA, which typically displays the highest F/C ratio, also had a very low F/C ratio, consistent with improved surface roughness seen for this process condition.

Figures 5.2 (SEM images) and 5.3 (image analysis) show the evolution of patterned PR structures for these process conditions. The unprocessed samples exhibit significant sidewall roughness due to a missing bottom anti reflection coating (Fig. 5.2a)). C_4F_8/90% Ar shows a fairly straight profile, with large surface and sidewall roughness visible after processing. Significant FC deposition on the sidewalls of the trench features during plasma etching is indicated by the smoothing of the standing wave patterns and the reduction in critical dimension (CD) after processing. CF_4/90% Ar and CF_4/40% H_2/40% Ar (Figs. 5.2c) and 5.2f)) show bowed out etch profiles which are dominated by ion bombardment while having only thin FC overlayers. Indications for this are the mid CD having the highest value (Fig. 5.3a)) and increased LER/LWR values (Fig. 5.3b)). CF_4 displays a tapered profile (top CD greater than original CD) with near identical LER/LWR values compared to the original sidewalls. The PR samples etched in CF_4/40% H_2 seem to have near optimal dimensions after processing. With the top CD being almost the same as the original image and also the mid CD similar, a near perfect profile shape has been obtained (Fig. 5.3a)). Also the hydrogenated fluorocarbon (FCH) polymer deposited from the plasma under this

condition seems to have an effect on the roughness, as a decrease in both LER and LWR was achieved for this condition (Fig. 5.3b)).

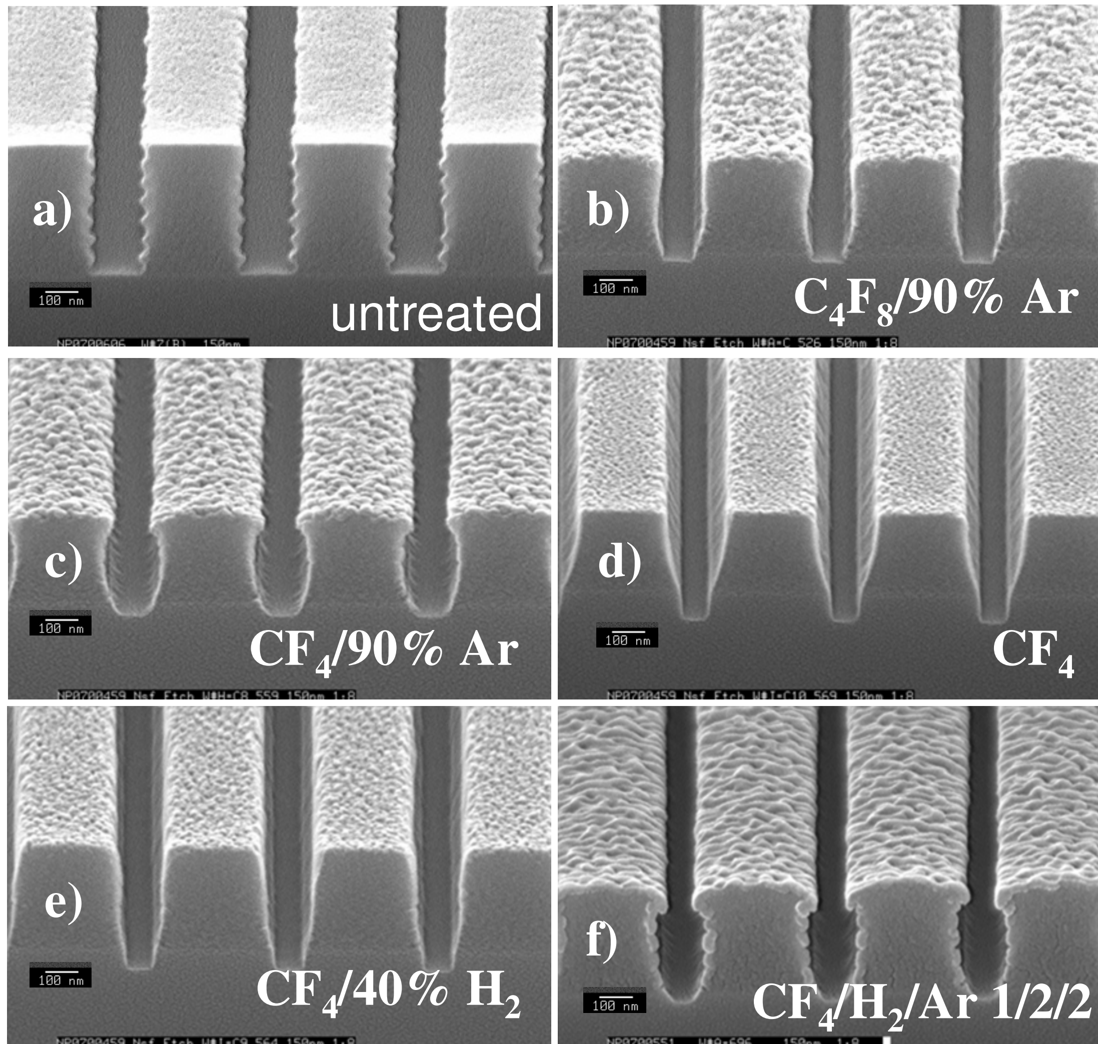

Figure 5.2: *SEM micrographs of trench samples before (a)) and after plasma processing using C_4F_8/90% Ar (b)), CF_4/90% Ar (c)), CF_4 (d)), CF_4/40% H_2 (e)) and CF_4/40% H_2/40% Ar (f)).*

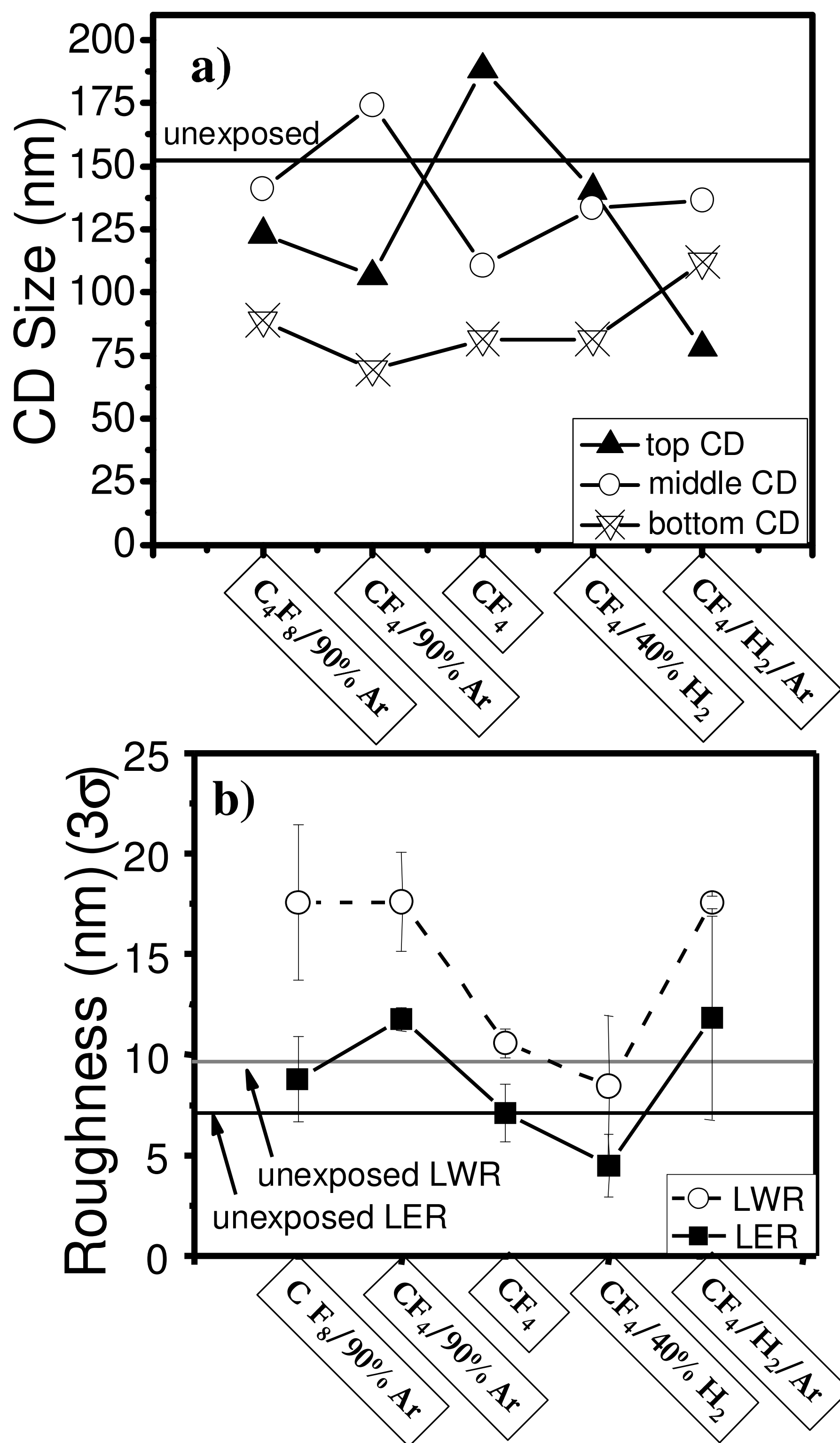

Figure 5.3: *CD measurements (a)) and LER/LWR values of trenches (b)) before and after plasma etching using five discharge conditions.*

The effect of the discharge chemistry on the PR evolution during etch was further studied by etching contact holes employing the same process conditions. Due to their reduced dimensionality and the need for multiple collisions for species to arrive at the bottom of contact holes, profile shapes of contact holes are highly sensitive to differences in sticking coefficients of plasma species at sidewalls.[5.7] Etched profiles of contact holes are shown in Fig. 5.4. The LER roughness measured on the processed trench samples was analyzed and a characteristic correlation length of the roughness features was found. We arranged the etched contact hole samples according to this trench parameter in Fig. 5.4. Process conditions with the shortest roughness correlation length for trench LER showed the deepest radical penetration for contact holes. These results suggest that low-sticking coefficient FC precursors tend to smooth the sidewalls during processing.

For conditions know to have FC precursors with higher sticking coefficients[5.30], e.g. C_4F_8/90% Ar, very shallow sidewall coverage was observed as expected. The evidence for this is the fact that the standing wave patterns are still visible after processing. Even though the radical speciation seems to relate to the contact hole profile evolution, significant differences in the appearance of the surface roughness after processing are clearly visible, which cannot be explained based on the radical speciation only. In particular, the CF_4 and the CF_4/Ar process seemed to produce much finer roughness than the other plasma conditions. To understand this, a detailed investigation of the C_4F_8/Ar and the CF_4/Ar etch regime was undertaken.

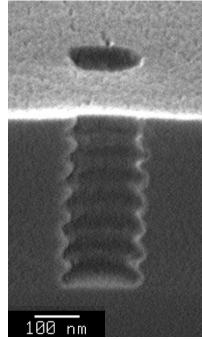

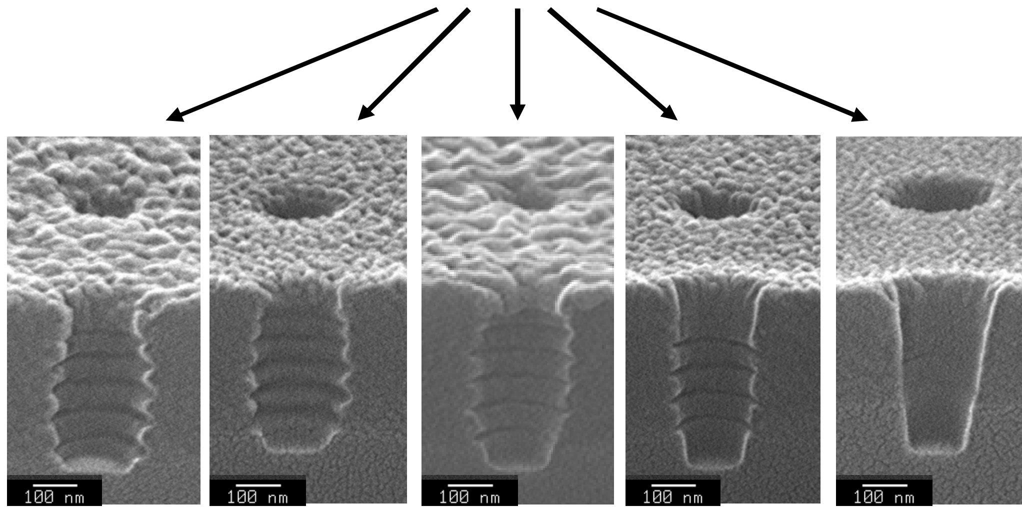

Figure 5.4: *Profile evolution of contact hole samples after plasma etching using five typical discharge conditions.*

5.3.2 Effect of fluorocarbon gas addition to Ar discharges

5.3.2.1 C_4F_8/Ar discharges

C_4F_8/Ar discharges are widely used for highly selective plasma etching of dielectrics.[5.12,5.18,5.27,5.31] While the process conditions are adjusted to achieve satisfactory etching results for the dielectric materials, the impact of these adjustments on the PR material and feature profile are often not clear.

Etch rates and surface roughness data obtained with the three polymer materials in C_4F_8/Ar discharges are displayed in Fig. 5.5 as a function of feedgas composition. For pure Ar processing, the highest etch rates were measured. Upon addition of only a few % C_4F_8, the etch rates decrease strongly. This can be explained by the formation of a thin fluorocarbon layer on top of the PR and a slight drop in the ion flux at the surface. When increasing the percentage of C_4F_8 further to up to 20%, a small increase in polymer ER is seen for all materials (Fig. 5.5a)). This may be attributed to an increase in fluorine availability at the polymer surface, since surface analytical studies have shown that the steady state FC film thickness changes little in this regime.[5.32] Increasing the flow of fluorocarbon growth precursors further leads to strongly increased FC deposition rates on the polymer substrates, which lowers the net etching rate further and ultimately causes a switch-over to net FC film deposition at 80% C_4F_8. Figure 5.5a) also shows data for pure C_4F_8. Due to the large flux of FC radicals for this condition we increased the RF bias power to maintain a self bias voltage of -150V. By doing this, deposition and etching rates were balanced, and no net change in film thickness took place. Overall, the behavior illustrated in Fig. 5.5a)

is consistent with the general understanding of fluorocarbon discharges, where for highly polymerizing plasma chemistries high ion bombardment energies are required to achieve net etching.[5.11]

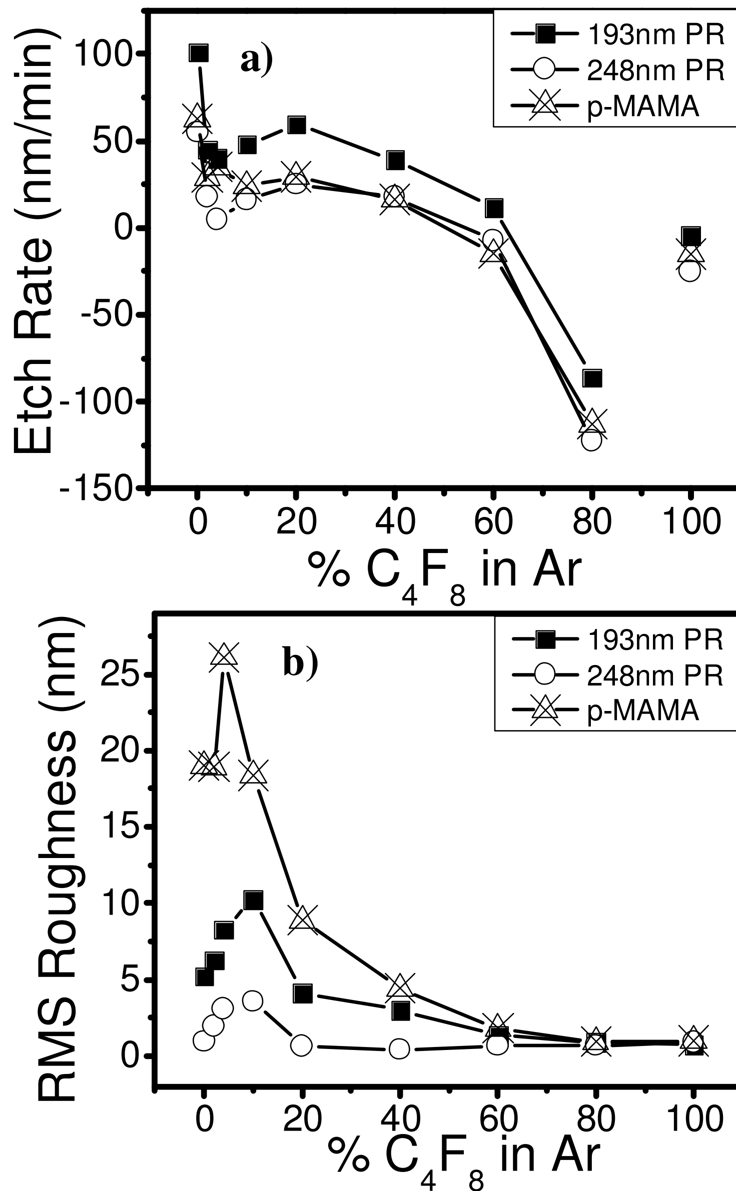

Figure 5.5: *Etch rates (a)) and RMS roughness (b)) as a function of C_4F_8/Ar percentage.*

A difference in the etch rates of 248nm PR and p-MAMA is measured only for the ion-dominated plasma regime (less than 20% C_4F_8). Previous studies employing different materials in highly polymerizing discharges have shown that, by increasing the deposition flux, the influence of the substrate material can be decreased.[5.33] The 193nm PR still displays slightly higher etching rates, possibly due to its higher oxygen content than for the other materials.

The evolution of surface roughness of the PR materials as a function of feedgas composition is shown in Fig. 5.5b). While clear differences for the three materials tested are present in an ion dominated plasma (less than 20% C_4F_8), these differences diminish for increasing C_4F_8 content. For C_4F_8-rich discharges (more than 60% C_4F_8), smooth surfaces may be maintained for all materials. This is consistent with the lack of substrate etching for process conditions with high surface polymerization rates.

Figures 5.6 (SEM images) and 5.7 (image analysis) present corresponding results for patterned 193 nm PR samples plasma processed using the same conditions. The sample processed using pure Ar discharge shows the highest amount of PR damage and surface roughness. Increasing the percentage of C_4F_8 in C_4F_8/Ar results in smoother surfaces. For plasma etching conditions employing a high percentage of C_4F_8, fluorocarbon film growth induced by the plasma fills the nanostructured features. Quantitative analysis of the etched structures (Fig. 5.7a)) show significant changes in the CDs after processing. Samples processed in pure Ar condition display a profile very similar to those in Figs. 5.2c) and 5.2f), where the middle CD is much wider (mid CD is larger than top CD).

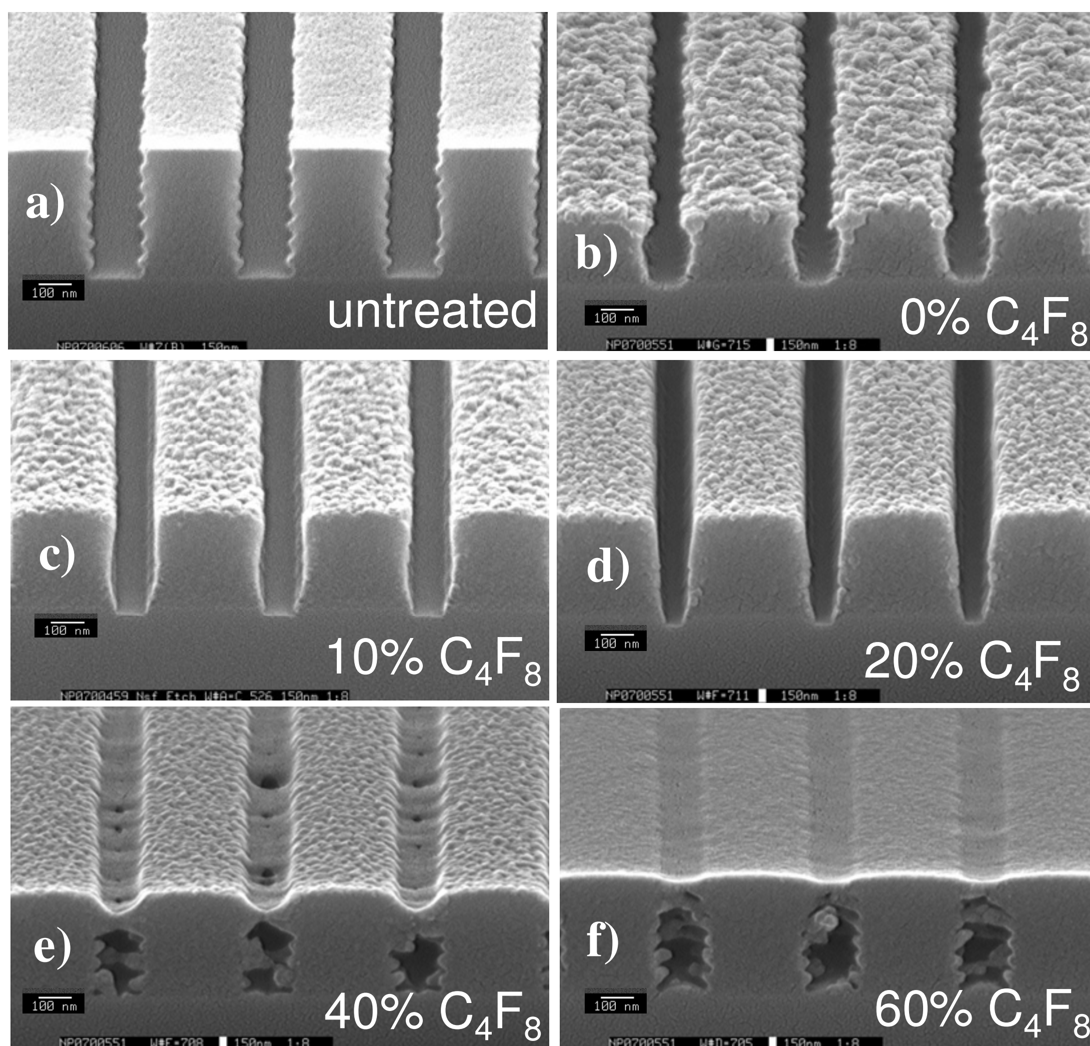

Figure 5.6: *SEM micrographs of trench sample before (a)) and after processing in pure Ar (b)), C_4F_8/90% Ar (c)) C_4F_8/80% Ar (d)), C_4F_8/60% Ar (e)) and C_4F_8/40% Ar (f)).*

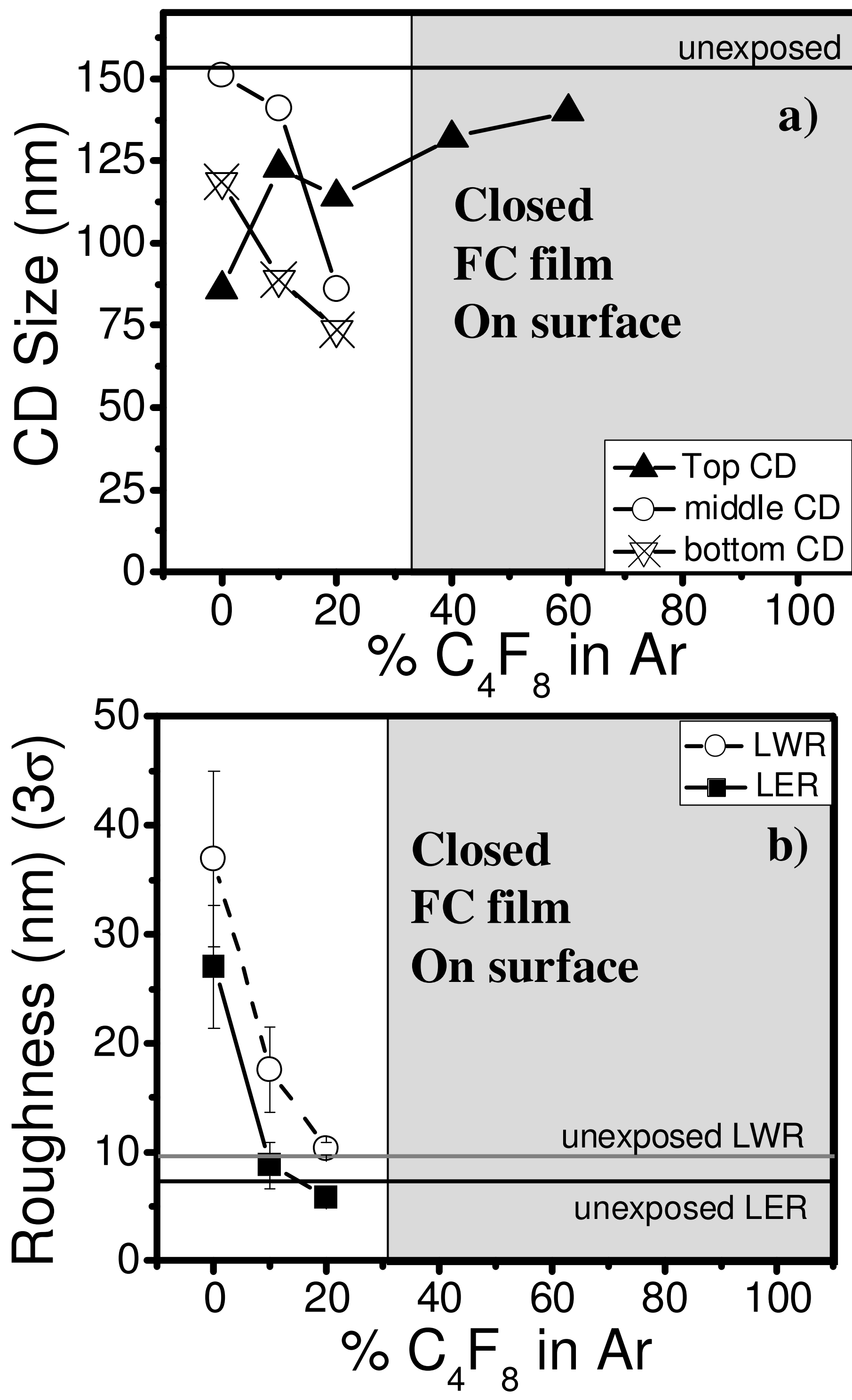

Figure 5.7: *CD measurements (a)) and LER/LWR values of trenches (b)) before and after processing as a function of C_4F_8/Ar percentage.*

By increasing the C_4F_8 percentage we can reduce the mid CD through increased FC deposition. C_4F_8 due to its highly polymerizing nature only leaves a small process window for successful pattern transfer, and for process conditions employing 40% C_4F_8 or greater, thick FC films grow on top of the photoresist obscuring the original pattern. By increasing the C_4F_8 percentage, both LER and LWR can be reduced, as shown in Fig. 5.7b).

5.3.2.2 CF_4/Ar discharges

In CF_4/Ar discharges, polymer etching rates are generally quite high and little etching selectivity to PR etching masks can be achieved. For this fluorine-rich gas mixture, FC films with high fluorine content are formed on PR substrates. These films etch quickly when ion bombarded, and only very thin steady state FC films remain on the substrates (see also Figs. 5.8,5.11,5.12).[5.34] Process results obtained with CF_4/Ar discharges are displayed in Fig 5.8. Similar to the C_4F_8/Ar series, we observe a drop in etch rates when adding CF_4 to pure Ar (Fig. 5.8a)). Increasing the CF_4 percentage in CF_4/Ar further, produces the opposite trend as compared to the C_4F_8/Ar series: As we raise the percentage of CF_4, the etch rates increase, and for percentages with more than 60% CF_4, a saturation of the etch rates can be observed. For discharges having only small percentages of Ar, no significant difference in etch rates between 248nm PR and p-MAMA is seen, while the 193nm PR shows higher removal rates, which may be related to the higher oxygen content in the polymer matrix and the destruction of the lactone group.

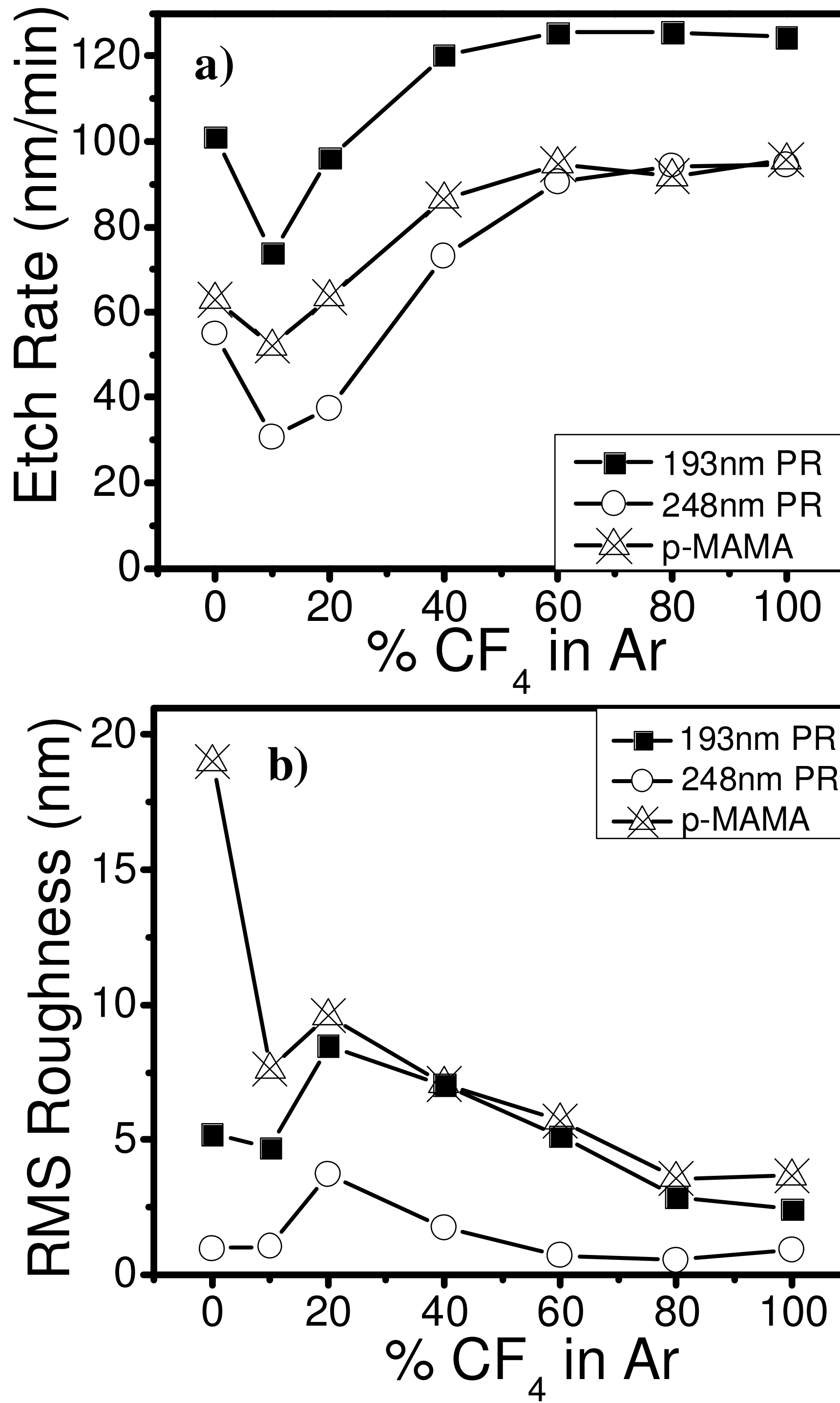

Figure 5.8: *Etch rates (a)) and RMS roughness (b)) as a function of CF_4 percentage in an Ar discharge.*

The surface roughness evolution shows that while small amounts of CF_4 increase surface roughening, smoother surfaces are produced as more CF_4 is added to the CF_4/Ar discharge. For process conditions with up to 20% CF_4, clear differences in roughness can be observed for the different polymer materials, whereas for higher amounts of CF_4 these differences diminish.

Figures 5.9 (SEM images) and 5.10 (image analysis) show the transformations seen for patterned 193 nm structures when processed using CF_4/Ar discharges. A transition from a bowed profile (as seen for 90% Ar, Fig. 5.9c)) to increasingly smooth, but tapered profiles for CF_4 rich conditions (see Fig. 5.9f)) is observed. A characteristic feature of the bowed profile is that the mid CD is largest, whereas the tapered profile has a top CD larger than the original CD (Fig. 5.10a)). At the process conditions closest to the transition between these profiles, i.e. CF_4/80% Ar, a nearly vertical etch profile shape is obtained. In addition to specimens etched in pure Ar, samples etched using CF_4/80% Ar also show very high sidewall roughness (Fig. 5.10b)). The evolution of the LER/LWR for exposed trenches shows that no improvement of the LER/LWR compared to the original values was obtained under any condition using CF_4/Ar discharges.

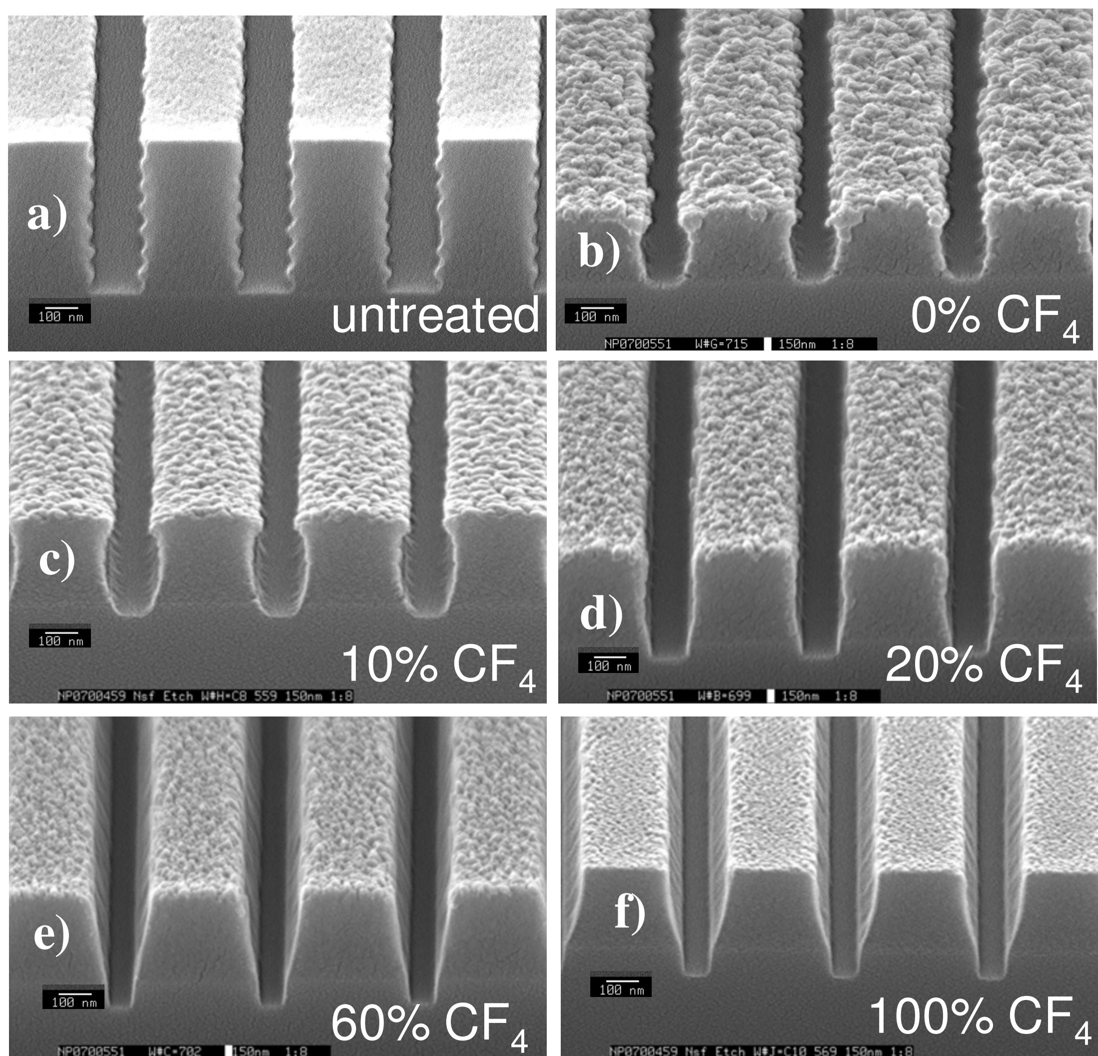

Figure 5.9: *SEM micrographs of trench sample before (a)) and after processing in pure Ar (b)), CF_4/90% Ar (c)), CF_4/80% Ar (d)), CF_4/40% Ar (e)) and CF_4 (f)).*

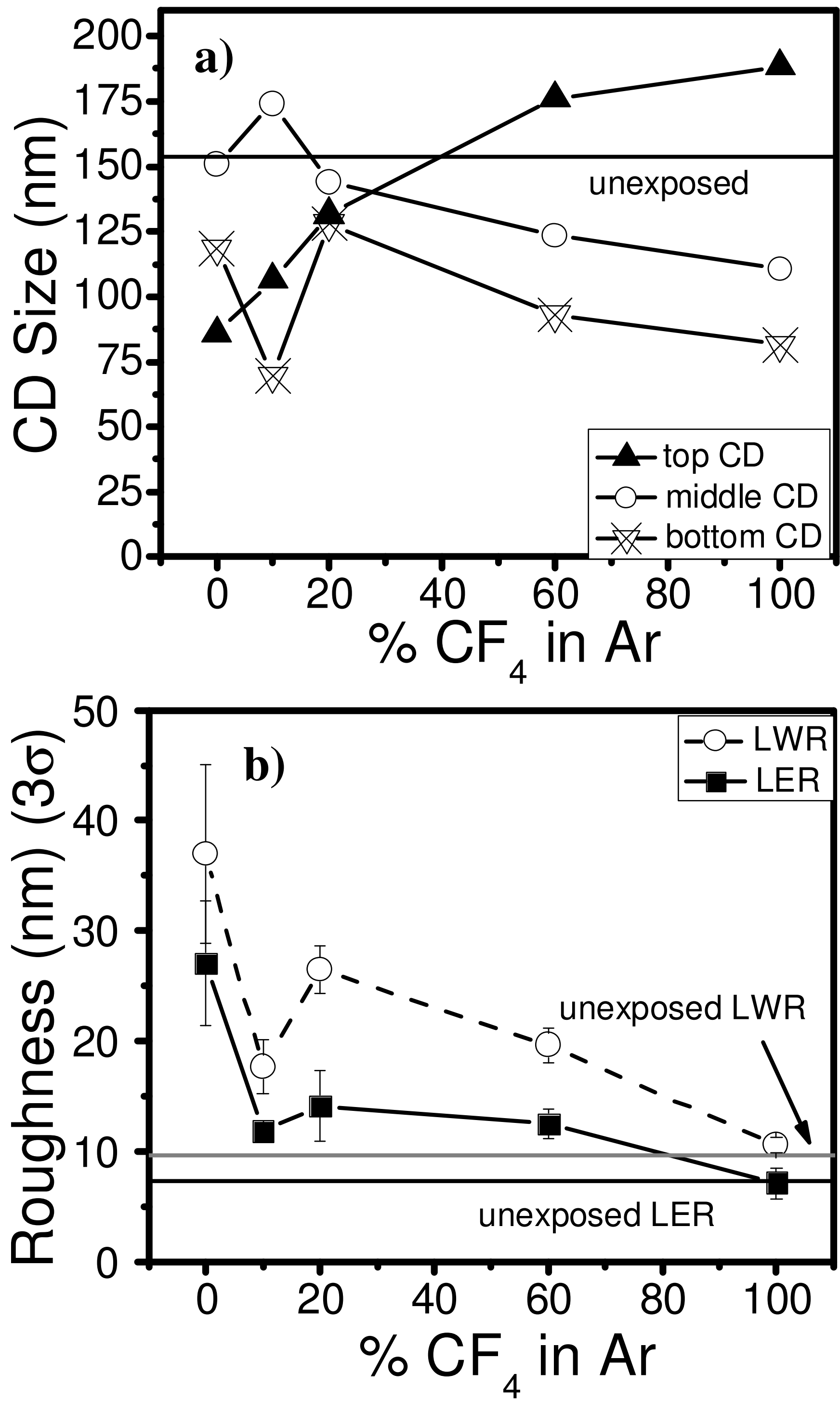

Figure 5.10: *CD measurements (a)) and LER/LWR values of trenches (b)) before and after processing as a function of CF_4/Ar percentage.*

5.3.3 Surface compositional analysis by XPS

The fluorocarbon interaction with the PR substrate was found to impact the roughness of the processed samples significantly. In particular, the mode in which a FC layer was produced on the polymer substrates, i.e. a clearly separate FC layer on top of the polymer versus a highly mixed layer, is correlated with the observed surface roughness.[5.7] For plasma etched PR samples, strong elemental gradients have been observed by XPS. To understand the origin of these findings, a detailed analysis of the XPS data was performed.

Table 5.1[5.35] lists the sampling depths of the Al-Kα source as a function of both electron energy and analyzer angle. From examination of this table one can understand that XPS offers the possibility of depth profiling by changing either the kinetic energy of the emitted photoelectrons or by changing the escape angle for which photoelectrons are detected. Table 5.1 also shows that the F(1s) and C(1s) sampling depths differ significantly. For C_4F_8 based chemistries, the F/C ratios were calculated by normalizing the integrated areas of the F(1s) and C(1s) core level peaks using adjustment and sensitivity factors. Another frequently used approach to calculate F/C ratios is by curve fitting the fine structure of the C1s spectrum and using the equation[5.36]

$$\frac{F}{C} = \frac{I_{CF} + 2xI_{CF_2} + 3xI_{CF_3}}{\sum I} \qquad (1)$$

where I_{CFx} refer to the peak areas obtained by fitting C(1s) spectra, where increasing numbers of fluorine neighbors induce chemical binding energy shifts, and ΣI sums all individual C-peak component areas. A uniform F and C elemental

distribution as a function of depth will result in the calculated F(1s)/C(1s) ratio and the F/C ratio extracted from C1s fine structure yielding the same elemental ratio. Figure 5.11a) shows that this is the case for all polymers etched using C_4F_8/90% Ar. By plotting the F(1s)/C(1s) vs. the F/C ratio, we can detect a fluorination gradient within the sample.

Core Level	***BE (eV)***	***10°***	***45°***	***90°***
F 1s	***686***	***1.1***	***4.5***	***6.3***
O 1s	***531***	***1.3***	***5.2***	***7.3***
N 1s	***402***	***1.4***	***5.7***	***8***
C 1s	***287***	***1.5***	***6.2***	***8.7***
Si 2p	***102***	***1.7***	***6.9***	***9.7***

Table 5.1: *Sampling depths of Al Kα source in [nm] (from D. Briggs)*[5.35]

The data obtained using CF_4/90%Ar can be better understood when looking at all examined CF_4/Ar chemistries (Fig. 5.11b)). While for high CF_4 percentages the data are close to the line through the origin, the data deviate more from the line as more Ar is added to the discharge. It is likely that for CF_4/90% Ar the fluorination depth becomes comparable to the probing depth of the XPS. Consistent with this is the observation that XPS data acquired at 20° relative to the sample surface did not show this deviation (not displayed for the sake of brevity). When probing shallower depths using 20° angle data, the data for all samples show F 1s/C 1s ratios that are equal to the F/C ratios obtained from the C1s fine structure. We can interpret this as

being due to CF_4/Ar plasma etched polymers showing uniform surface fluorination with depth, and additionally that for small amounts of CF_4 in Ar, fluorination depths are very shallow. For the CF_4/H_2 plasma, we can identify conditions where the fluorine is predominantly on the top surface (small offset of F/C ratios towards F(1s)/C(1s)). This is very similar to the influence of plasma source power on the nature of the FC layer formed on polymers reported previously.[5.7] In that work we observed a thin, separated FC layer that was characterized by a high F/C ratio and a steep fluorination gradient for low source power (small F2s/F1s ratio), whereas for high source power a mixed FC layer was obtained characterized by a lower F/C ratios and uniform fluorination as a function of depth (F2s/F1s ratio ≈ 1) [the ratio of deep (F2s) and shallow (F1s) fluorine signals was used to quantify the nature of the deposited FC layer].[5.7] Very low F/C ratios were seen for polymers processed using CF_4/H_2/Ar and CF_4/90% Ar. In a similar fashion, a very thin FC layer was found for processing with CF_4/H_2/Ar, but the fluorination depth in CF_4/90% Ar was comparable to the XPS probing depth. Overall, we found that FC film formation and depth of F penetration of the polymer materials aren't always coupled and might influence the discharge properties additionally.

The fluorination of the PR in C_4F_8/Ar and CF_4/Ar discharges was also examined. The results of the surface compositional analysis using XPS are shown in Fig. 12. The F/C ratio monotonically increases when raising the % of C_4F_8 (Figure 12a)). For all conditions, the ratios for the three polymer materials tested follow an order where p-MAMA shows the highest F/C ratio, followed by 193nm PR and 248nm PR. In C_4F_8/Ar discharges, the fluorination could be easily estimated from the

F (1s) over C (1s) ratio. The same measurement was found to be contradictive for the CF_4/Ar conditions (see also Fig. 11b)).

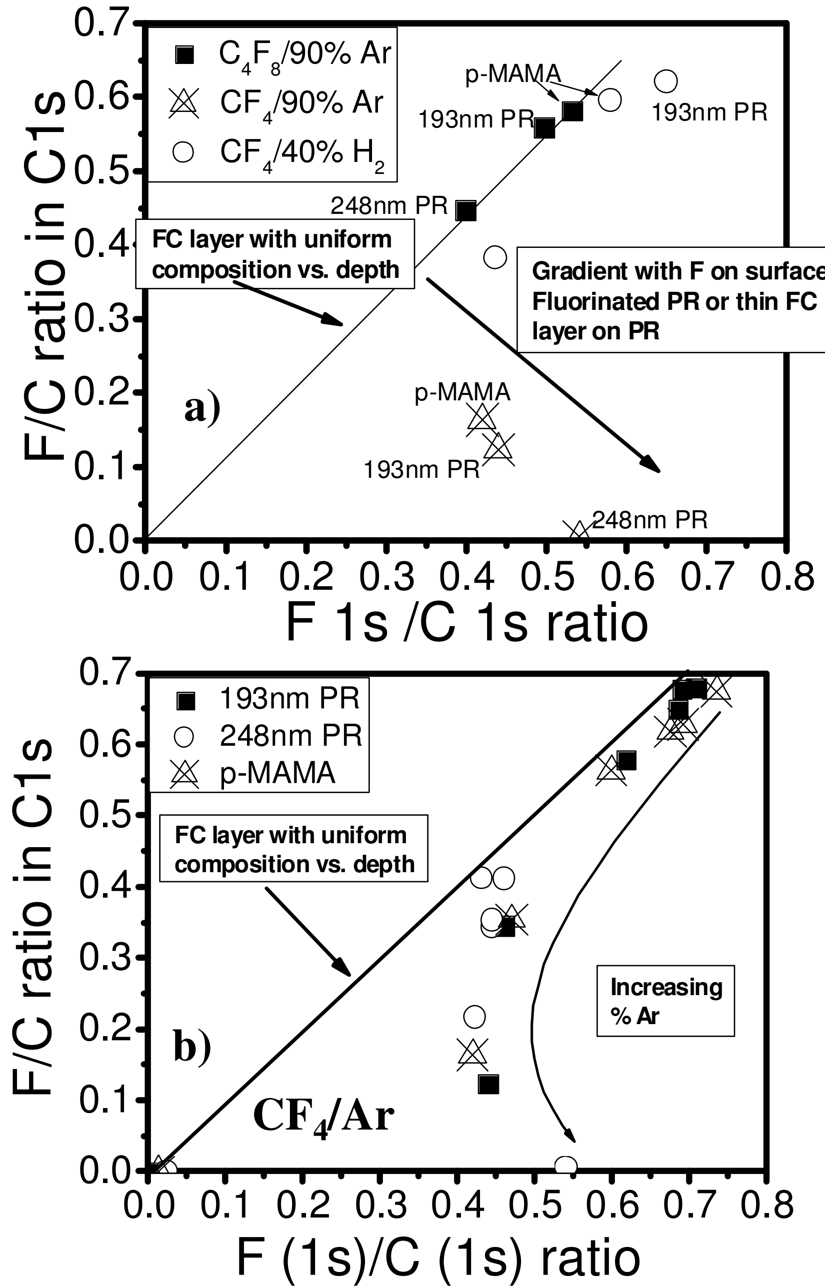

Figure 5.11: *F/C ratio vs. F/C ratio measured in the C1s spectrum for C_4F_8/90% Ar, CF_4/90% Ar and CF_4/40% H_2 (a)) and all conditions tested in CF_4/Ar discharges at 90 deg emission angle (b)).*

A better estimate of the F/C ratio at the polymer surfaces processed in CF_4/Ar discharges was obtained when the F/C ratios were obtained from measurement of the C1s spectra alone since in this case the difference in sensitivity depths is not present. (see discussion/results above). The general trend for increasing surface fluorination (greater F/C ratios) of polymer materials processed in CF_4/Ar discharges is similar to the behavior seen for C_4F_8/Ar discharges, i.e. increasing fluorination for increasing CF_4 percentages (see Fig. 5.12b)). Differences are reflected in the fact that Ar/CF_4 generates lower F/C ratios than Ar/C_4F_8 for the same % of Ar in the discharge. Lower F/C ratios were found to be characteristic for mixing of the FC layer with the PR substrate.[5.7] A higher degree of mixing between the FC film and the damaged PR is therefore indicated for processing of polymers in CF_4/Ar.

We determined the nature of the FC films deposited on Si substrates without applying a RF bias and also measured the deposition rates (see Fig. 5.13). Overall much lower FC film deposition rates are seen for CF_4/Ar than for C_4F_8/Ar discharges. We also find that the deposition rate reaches a maximum at 20% CF_4/80% Ar. As mentioned before, the FC films deposited with a high percentage of CF_4 in Ar are very fluorine rich and cannot withstand ion bombardment. Since we found that the FC deposition is uniform with depth for all CF_4/Ar conditions (see Fig. 5.11b)), the maximum of the surface roughness in CF_4/80% Ar (Fig. 5.8a)) might affected by this FC deposition rate maximum. Adding more C_4F_8 to the discharge resulted in continuously increased thickness of the FC film thickness. Most of the process results seen in Figs. 5.5-5.7 can be related to this effect.

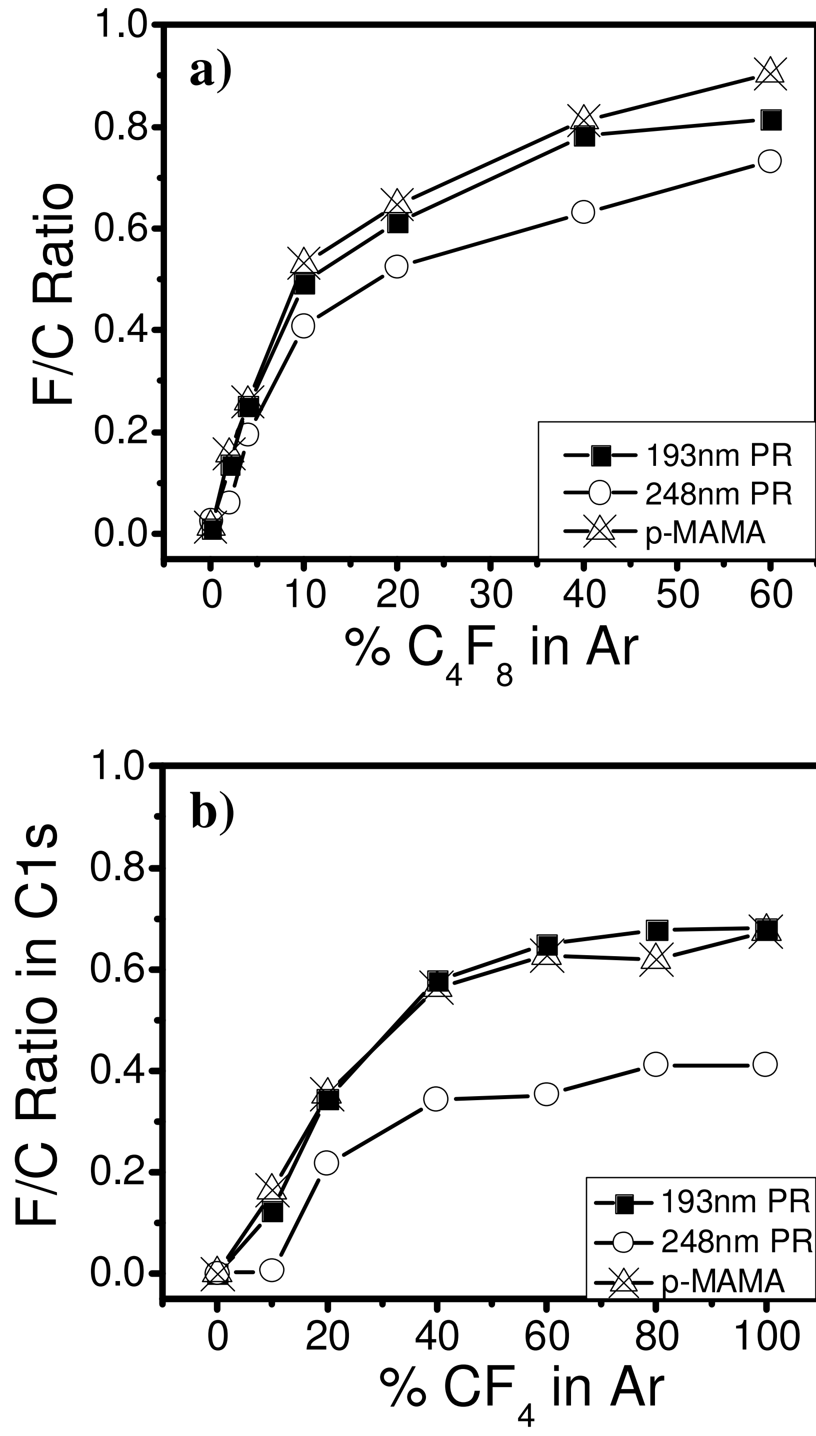

Figure 5.12: *F/C ratios after processing as a function of Ar percentage in a C_4F_8 discharge (a)) and F/C ratio obtained from the C1s spectrum as a function of percent CF_4 in an Ar discharge (b)).*

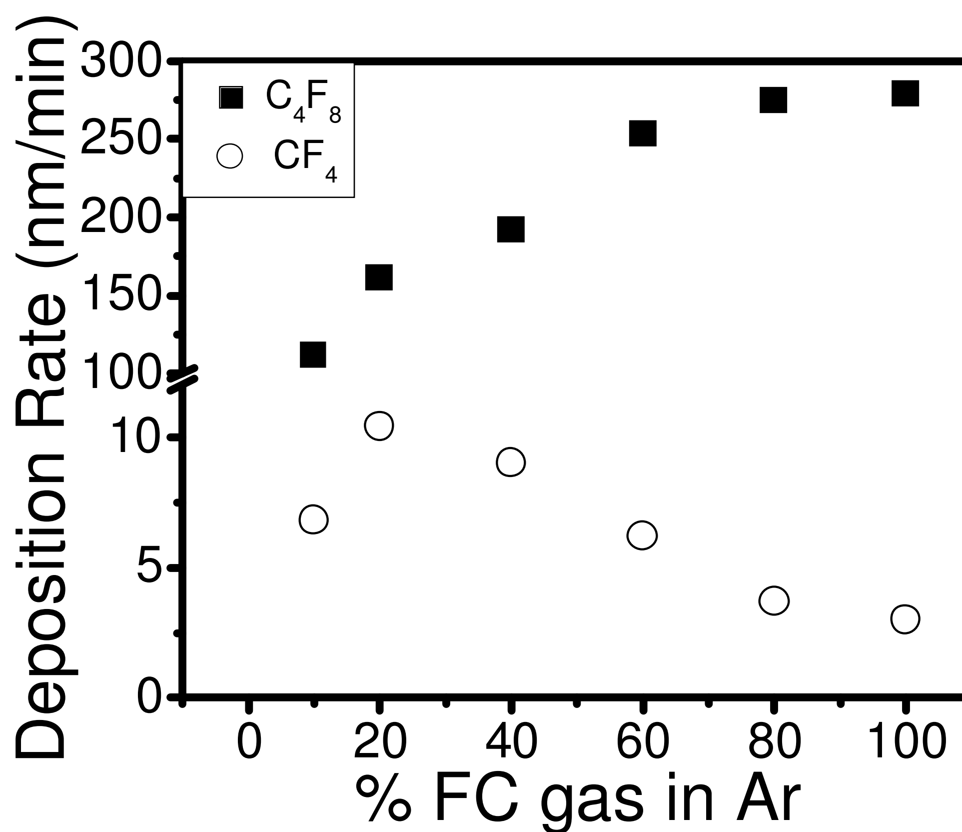

Figure 5.13: *Deposition rate vs. percentage of Ar in CF_4 and C_4F_8 discharges.*

5.4 DISCUSSION

5.4.1 Influence of surface composition on polymer etching rate

We examined the impact of five prototypical fluorocarbon etch conditions on polymer etch rates and roughness evolution for three representative PR materials. The C_4F_8/90% Ar chemistry has been extensively studied in previous publications of this group[5.6,5.7] and is popular for pattern transfer of PR masks into dielectric

materials.[5.3,5.18] The combination of high flux of polymerizing species, sidewall coverage by FC deposition and energetic Ar^+ ion bombardment enables the selective etching of silicon oxide and generation of high aspect ratio structures. Discharges based on CF_4 were also studied in our work, since this enables the examination of polymer modifications due to the attack by elemental fluorine, as opposed to deposition of C_xF_y radicals. Plasma etching processes based on CF_4 as compared to C_4F_8 show higher F concentrations[5.9,5.12,5.14], since the latter is primarily dissociated into CF_2 and CF_3.[5.26,5.37,5.38] When using less polymerizing fluorocarbon gases, e.g. CF_4, only thin steady state FC films are present on surfaces contacted by the plasma. CF_4/90% Ar was studied to examine the effects of the CF_4 gas for conditions for which the feedgas percentage of Ar was identical to the C_4F_8/90% Ar discharges. Discharges fed with CF_4/H_2 were also studied, since addition of H_2 to the CF_4 discharge reduces the fluorine density.[5.13,5.15,5.39] The study of H_2 was also motivated by a prior study that had shown reduced PR roughening for CF_4/H_2 discharges.[5.18] We also studied Ar addition to CF_4/H_2 discharges, to investigate the effect of Ar^+ ion bombardment in conjunction with the CF_4/H_2 chemistry.

For all of our experiments a constant selfbias voltage of -100V was employed. The use of a constant mean ion energy makes it easier to interpret results in terms of the contribution of surface chemistry changes only. In Fig. 5.1, we saw similar polymer etch rates for C_4F_8/90% Ar, CF_4/H_2 and CF_4/H_2/Ar, whereas for CF_4/90% Ar and CF_4 much greater etching rates were measured. One possible explanation is that for C_4F_8/90% Ar, CF_4/H_2 and CF_4/H_2/Ar, the polymer etch rate is controlled by ion bombardment, whereas for CF_4/90% Ar and CF_4 the etch rates is increased by

chemical modification of the polymer material by fluorine attack. Consistent with this notion, discharges based on different CF_4/Ar compositions exhibited a clear etch rate increase with increasing CF_4 content (see Fig. 5.8a)). This observation led to a more detailed examination of the etch mechanism in CF_4/Ar plasma chemistries.

Most polymer etch models focus on the effect of the polymer stoichiometry and their effect on etch rate.[5.40-5.46] One common observation is that the more carbon a polymer contains per monomer, the more etch resistant the polymer. This idea has been expressed in polymer etching models, although the actual calculation of the characteristic model parameter is often complicated, and may require information that is not easily available.[5.44-5.46] The effect of the plasma etching conditions on polymer etch behavior has been studied using a number of models, but they are typically restricted for the particular discharge properties employed in those studies.[5.47-5.51]

Based on the measured etching rates, compositional information and surface chemistry determination, we developed a simple etching model which can explain the observed etch behavior. In our approach, we present a very basic and simple etch model, which captures basic trends in removal. Deviations from this model can be used to indicate the importance of additional effects for these plasma processes.

For an oxygen or fluorine containing polymer, the plasma etching rate *ER* consists of the contribution of physical sputtering and an ion enhanced etching component, e.g. for carbon bonded to oxygen or fluorine atoms, and can be written as

$$ER = ER_{PS} + ER_{IE}. \qquad (2)$$

Following Mayer and Barker,[5.52-5.54] the ion enhanced etching rate ER_{IE} is proportional to the fractional neutral (oxygen and fluorine) coverage Θ. In our case, we assume that the neutral coverage is given by

$$\Theta=(n_O+n_F)/n \tag{3}$$

where n_O and n_F are the number of surface sites occupied by oxygen and fluorine respectively and n relates to the total number of surface sites.

We can express ER_{IE} as

$$ER_{IE} = v_i \Theta Y_{IE} \Gamma_i \tag{4}$$

where v_i is the volume of substrate material removed per etch inducing ion, $Y_{IE}(E_i)$ is the energy dependent etch yield of the process and Γ_i represents the ion flux. The total ER becomes

$$ER = ER_{PS} + ER_{IE} = v_{PS}(1-\Theta)Y_{PS}\Gamma_i + v_i \Theta Y_{IE}\Gamma_i \tag{5}$$

or

$$ER = v_{PS}(\frac{n-n_O-n_F}{n})Y_{PS}\Gamma_i + [v_{iO}\frac{n_O}{n}Y_{IEO} + v_{iF}\frac{n_F}{n}Y_{IEF}]\Gamma_i . \tag{6}$$

To simplify, we assume

$$v_{PS} \approx v_{iO} \approx v_{iF} = v \ . \tag{7}$$

Also, since Ar^+ ions dominate the ion flux, we ignore the contribution of ions on the chemical modification of the polymer materials. We then obtain

$$ER = vY_{PS}\Gamma_i + [\frac{n_O}{n}(Y_{IEO} - Y_{PS}) + \frac{n_F}{n}(Y_{IEF} - Y_{PS})]v\Gamma_i \tag{8}$$

If we assume $Y_{IEO} = Y_{IEF} = Y_{IE}$, we can simplify (7) to get

$$ER \approx ER_0 + (\frac{n_O + n_F}{n})(Y_{IE} - Y_{PS})v\Gamma_i \tag{9}$$

or

$$\frac{ER - ER_0}{v\Gamma_i} = \Delta EY \approx (\frac{n_O + n_F}{n})(Y_{IE} - Y_{PS}) \qquad (10)$$

In Fig. 5.14, we plotted the observed etch yield for C_4F_8/Ar etching chemistries vs. $\frac{n_F + n_O}{n}$ as measured by XPS at 20° emission angle of the electron detector relative to the sample surface. Since the etching reactions take place at the very top surface, this measure of the surface composition should be very close to the actual surface sites participating in the etch process. The etching yield solely based on physical sputtering can be found with the data for pure Ar processing (see Fig. 5.14a)) and is indicated by the line. Since for pure Ar processing, only the initial oxygen content of the polymer impacts the surface composition, and a fairly linear relationship is seen.

By adding F to the surface by C_4F_8 addition, the results become a lot more complex. The slope of this plot should be related to $(Y_{IE} - Y_{PS})$ and gives an indication to what degree enhanced etching takes place. Figure 5.14a) shows that for C_4F_8 addition, a strong deviation from this line occurs. The fluorine that is deposited in the form of FC precursors on the PR material produces a etching-resistant FC layer that builds up on the PR surface and does not contribute to an etch increase. A shift away from the original line depending on the amount of FC in the discharge can be noted. An increase of fluorine in the PR material, which was related to increased etch yields was found for raising the operating pressure from 10-80mTorr.[5.7]

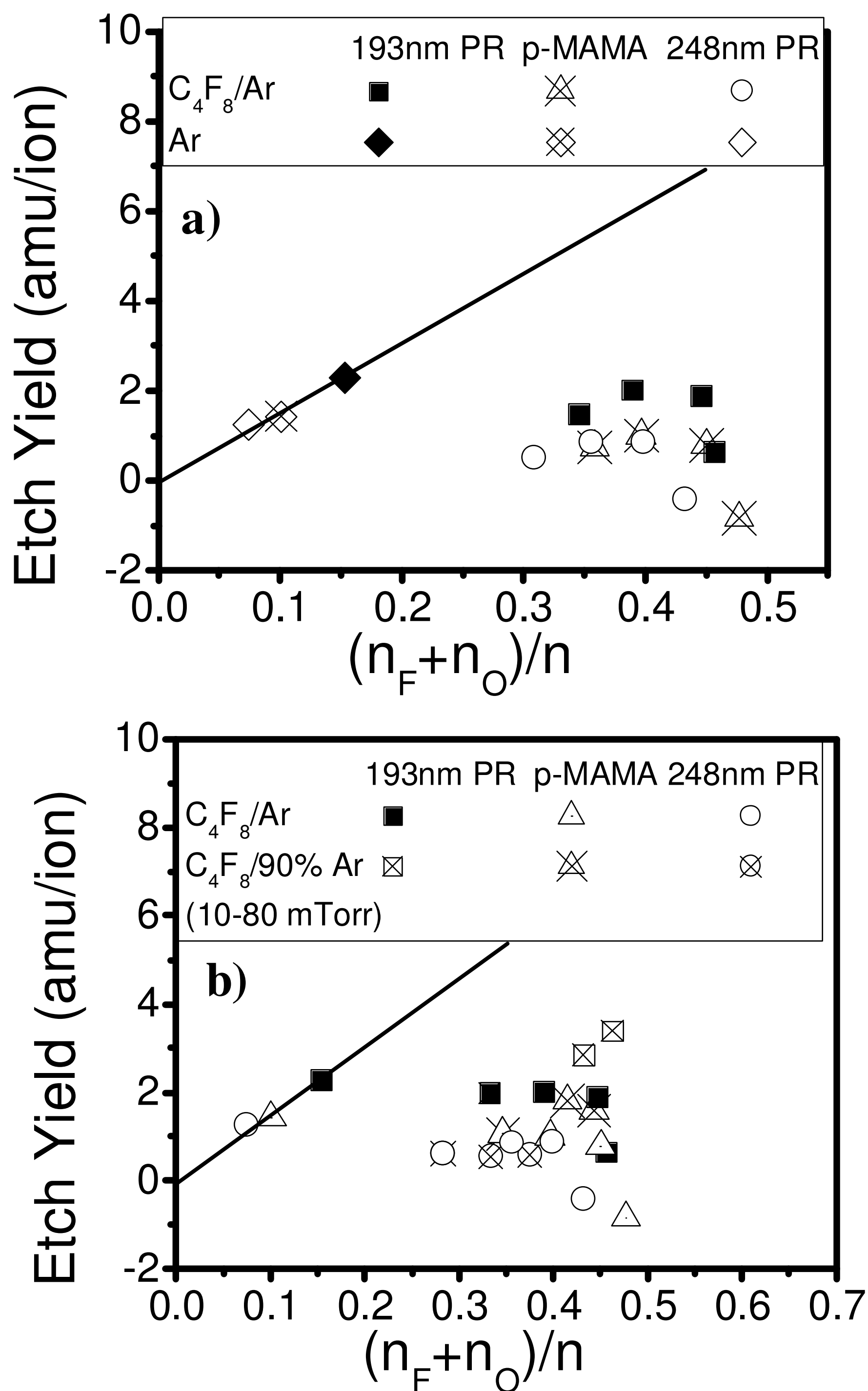

Figure 5.14: *Etching yields vs. neutral coverage of PR materials in pure Ar and C_4F_8/Ar discharges (a)). The data for C_4F_8/Ar are compared with data obtained in C_4F_8/90% Ar at different operating pressures (b)). (From [5.7])*

We see that for 193nm PR, which shows the largest dependence on this effect, the data points are parallel to the line given by pure Ar sputtering (see Fig. 5.14b)). For C_4F_8/Ar chemistries, we find that for fluorine deposited in a FC film (e.g. as seen in Fig. 5.14a)) the deviation is larger when more FC is present at the surface. If the fluorine is activated (e.g. as seen in Fig. 5.14b)) an increase in etch yields depending on the surface coverage can be noted.

A look at the data for CF_4/Ar shows that the same deviations are significantly smaller (Fig. 5.15a)). The thick FC layers for C_4F_8 chemistries cause a large offset, whereas the thin FC layers in CF_4 chemistries do not change the etch behavior significantly compared to pure Ar sputtering. We can clearly see that two distinct regions exist for processing of PR materials in CF_4/Ar discharges. The surface composition for our polymers is mostly determined by the fluorine atoms at the surface, since essentially all surface oxygen is removed during the first seconds of processing.[5.6] When smaller amounts of fluorine are added to the surface by plasma processing, the slow increase in etch yield can be related to the increased fluorine content in the surface. For higher amounts of fluorine, a substantially higher increase in etch yield can be noted. We interpret this behavior that for higher fluorine concentrations, the formation of the graphitic layer at the top surface is inhibited due to bulk fluorination and enhanced removal. Due to the rapidly moving etch boundary, the graphitic layer does not have time to establish and so elevated etch rates remain.[5.55,5.56] A chemically enhanced removal character for high CF_4 conditions might be responsible for tapered profile evolution seen in Figs. 5.9e) and 5.9f). Fig. 5.15b)) also shows the data for the missing CF_4/H_2 and CF_4/H_2/Ar conditions.

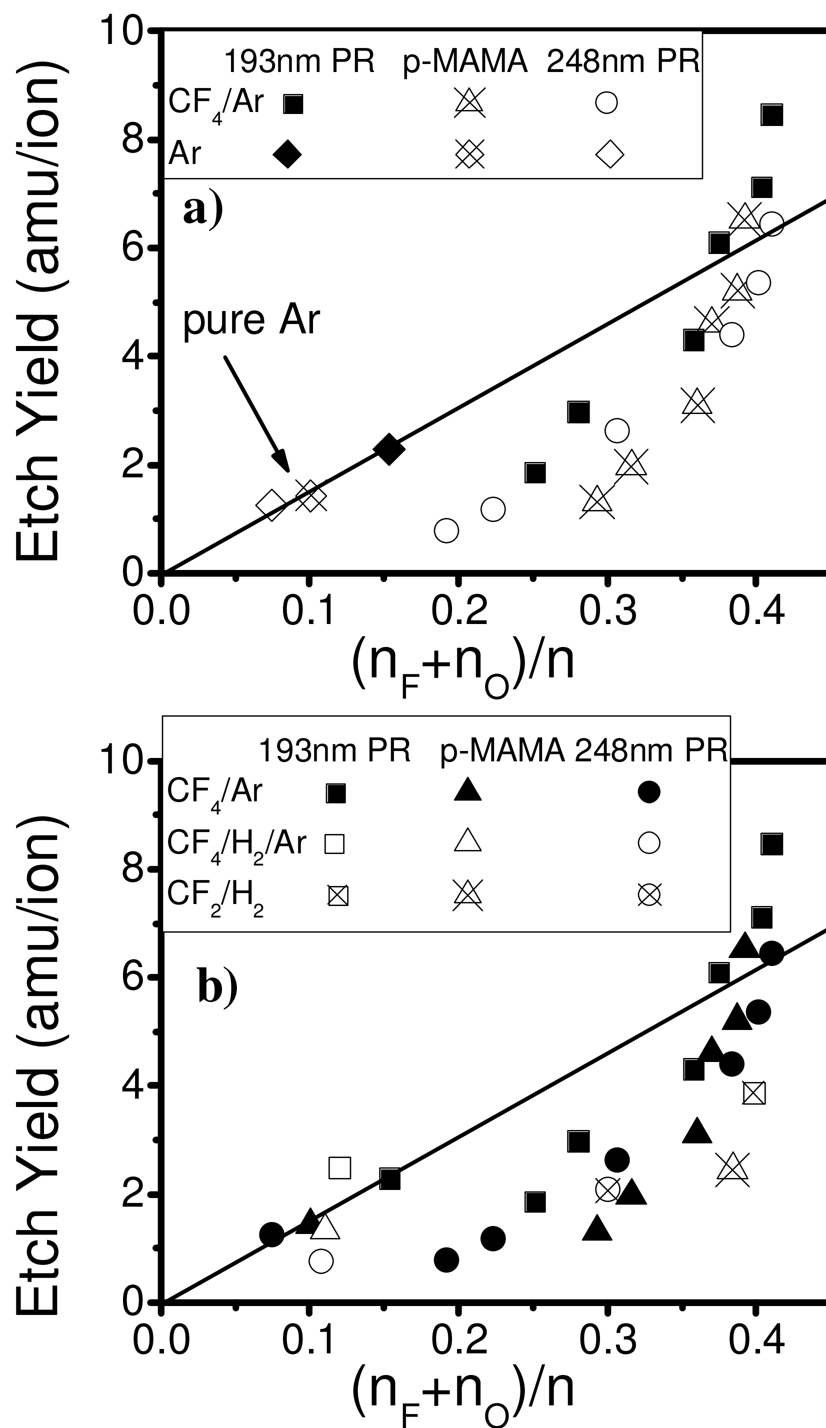

Figure 5.15: *Etching yields vs. neutral coverage of PR materials in pure Ar and CF_4/Ar discharges (a)). CF_4/Ar, CF_4/H_2 and CF_4/H_2/Ar conditions are compared in (b)).*

The material removal for $CF_4/H_2/Ar$ is very close to the pure Ar data, suggesting that the impact of the FC film and the F penetration on the etch behavior are negligible. The data for CF_4/H_2 fall on the data for the CF_4/Ar data, suggesting that the same etch mechanism is valid under this condition. The fact that the same CF_4 percentage yields smaller etch yields for CF_4/H_2 can be attributed to the fact that H_2 scavenges F from the discharge and so less fluorine is deposited into the PR and lower etch yields result.

We examined the etch behavior of polymer surfaces based on their oxygen and fluorine content. While for oxygen incorporation a simple linear dependence on the etch yield was found, a significantly more complex behavior was found for fluorine incorporation in the surface. The fact that all materials follow a similar trend suggests that the essential response of the polymer materials can be captured by this simple model based on experimentally determined surface stoichiometry and ion enhanced etching. The qualitative differences of C_4F_8/Ar and CF_4/Ar mixtures point to the fact that the FC films on the surface impact etch behavior significantly, indicating that the complexity of the actual mechanism goes beyond simple ion enhanced etching. Additional effects, such as cross linking abilities of the polymer materials can of course not be captured by this model and have been omitted for the sake of simplicity. The inability to measure hydrogen using XPS might be an additional reason for deviation of the data.

5.4.2 *Influence of surface composition on surface energy density and roughening*

In our prior work we have described the roughening behavior of polymers in fluorocarbon plasmas using a surface energy density model, where the roughening rate scales linear with the energy density required to remove a unit volume of material.[5.7] The PR material dependent roughening rate RR_m was defined as the RMS roughness introduced as a result of plasma processing divided by the depth of material removed due to processing. We found that the energy density deposited at the polymer surface during processing was very characteristic of the process condition used. The energy density density ε was defined as:

$$\varepsilon = \frac{E_i}{v_i EY}. \tag{11}$$

Here ε (eV/nm^3) is the energy density deposited by the plasma per unit volume removed, E_i (eV) is the average ion energy of the bombarding ions, v_i (nm^3) is the volume of substrate material removed per etch-inducing ion and EY is the etch yield (probability that an ion induces etch) of the material for the particular discharge conditions. A linear relationship of the roughening rate RR_m on the energy density ε was found as:

$$RR_m(\varepsilon) = C_m \varepsilon(E_i, v_i, EY) \tag{12}$$

where C_m is a PR materials constant that describes how effectively surface energy input by the plasma is converted into surface roughening. This material dependent roughening constant might be ultimately related to the stiffness of the examined

polymers. The 248nm PR material based on an aromatic polymer showed a much lower roughening constant C_m (7.9×10^{-7} nm^3/eV) than 193nm PR and p-MAMA materials (3.6×10^{-6} nm^3/eV), which are based on the more fragile adamantyl polymer structure.

The absolute *RMS surface roughness* SR_m that is introduced in the PR materials is determined by

$$SR_m = RR_m(\varepsilon)ER_m t\,. \tag{13}$$

The surface energy density deposited during plasma etching determines the polymer dependent roughening rate RR_m. Additionally, roughness is amplified on the PR surface by locally non-uniform removal based on the material dependent etch rate ER_m.[5.57] We also showed that sidewall roughness evolution during processing could be related to this surface roughening mechanism[5.7]. In our prior work we presented initial observations on the influence of surface fluorination of polymers on resulting surface roughness.[5.7] Through surface fluorination the etching yields of polymers increased and a reduction in energy density at the polymer surface during processing resulted. A reduction of the absolute *SR* was observed, which is consistent with Eq. (1) and (2). Similar process results have been obtained elsewhere.[5.17,5.58] This mechanism lead to the idea that the performance of *193nm PR* could be improved by conditions with low energy densities (i.e. high etch yields). Alternatively, separate FC deposition on the PR substrate has shown a beneficial impact on the roughening behavior.[5.7] In the following we will show how these mechanisms are reflected in our data.

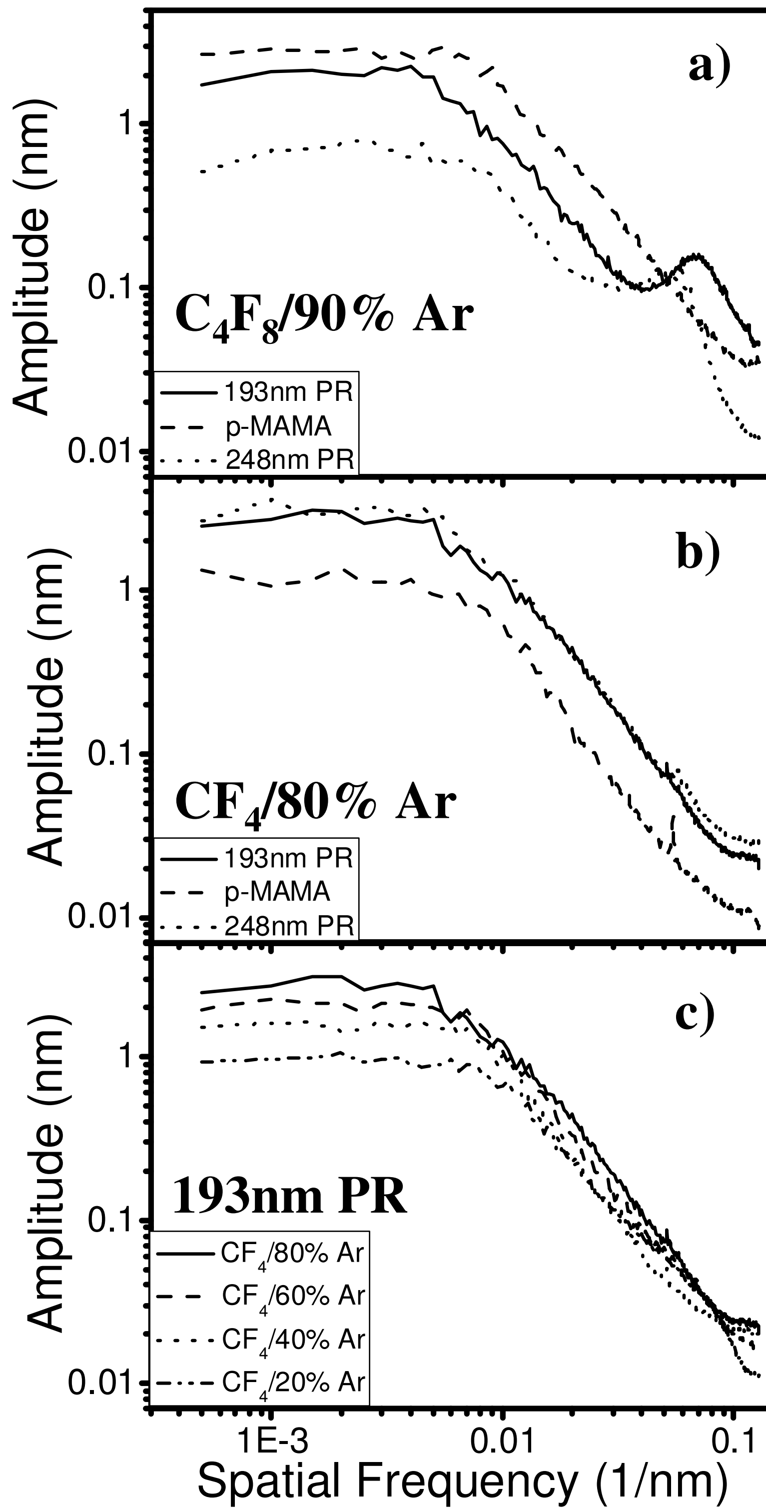

Figure 5.16: *Amplitude vs. spatial frequency of FT-AFM line scans for C_4F_8/ 90% Ar (a)), CF_4/80% Ar (b)) and 193nm PR in CF_4/Ar discharges (c)).*

The effect of fluorine on roughness evolution was analyzed in further detail. We used the FFT of AFM line scans to visualize the size distribution of the RMS roughness features on the PR surface (see Fig. 5.16). A detailed examination of FFT data obtained with RMS roughness scans for different process conditions can be found in a separate publication from our group.[5.8] The amplitude of height variation is plotted against spatial frequency, so the largest distances covered by our scan (2 μm) can be seen in the left side of the plot, whereas the smallest distances between measurement points (distance between the 512 scan points) are on the right.[5.59] Previous studies have shown that polymers show a characteristic peak in the high spatial frequency region (right side) which builds due to the polymer cross linking ability in the specific plasma condition.[5.8] Ion induced transfer of surface roughness – vertical growth of features - is reflected in these data by a gradual increase in the amplitude of the roughness features, whereas the spatial distribution does not change.[5.8] For samples processed in C_4F_8/90% Ar (Fig. 5.16a)), we find the material specific characteristic high spatial frequency features similar to the ones seen before by Sumiya et al..[5.8] The overall higher amplitudes can be attributed to the longer processing times (1 minute) for these samples. We see that 248nm PR shows a characteristic peak around 0.04 nm^{-1}, whereas 193nm PR shows a characteristic peak around 0.08 nm^{-1}. These characteristic peaks are consistent with the expected cross linking behavior of the PR materials and are likely responsible for the characteristic roughness features in the AFM surface images. Results are very different for CF_4/80% Ar (Fig. 5.16b)). The material characteristic broad high frequency peaks are eliminated, and only a very narrow, small peak is visible at 0.05 nm^{-1}. As opposed to

C_4F_8/90% Ar, this peak seems to have the same position for each material. The increase in CF_4 percentage reduced the amplitude of all spatial frequency values (Fig. 5.16c)). Our data also indicate that small roughness features can be easily suppressed by F-rich etch conditions, whereas large scale roughness features are much harder to reduce. This is consistent with findings reported by T. Wallow et al.[5.60]

Eqn. 12 predicts a proportional relationship between roughening rate and energy density deposited at the surface. The data for the adamantyl and aromatic polymer materials are plotted in Figure 5.17a), and roughly follow the expected proportionality. Linear regressions are also plotted to compare the data to the model found for processing using C_4F_8/90% Ar conditons.[5.7] The data for different C_4F_8/Ar chemistries are also shown in Fig. 5.17a). We can see that, as reported previously,[5.7] 193nm PR and p-MAMA have the same roughening constant C_m, but 193nm PR shows a significantly lower energy density due to a higher etch rate.[5.7] 248nm PR has a lower roughening constant than 193nm PR and p-MAMA.

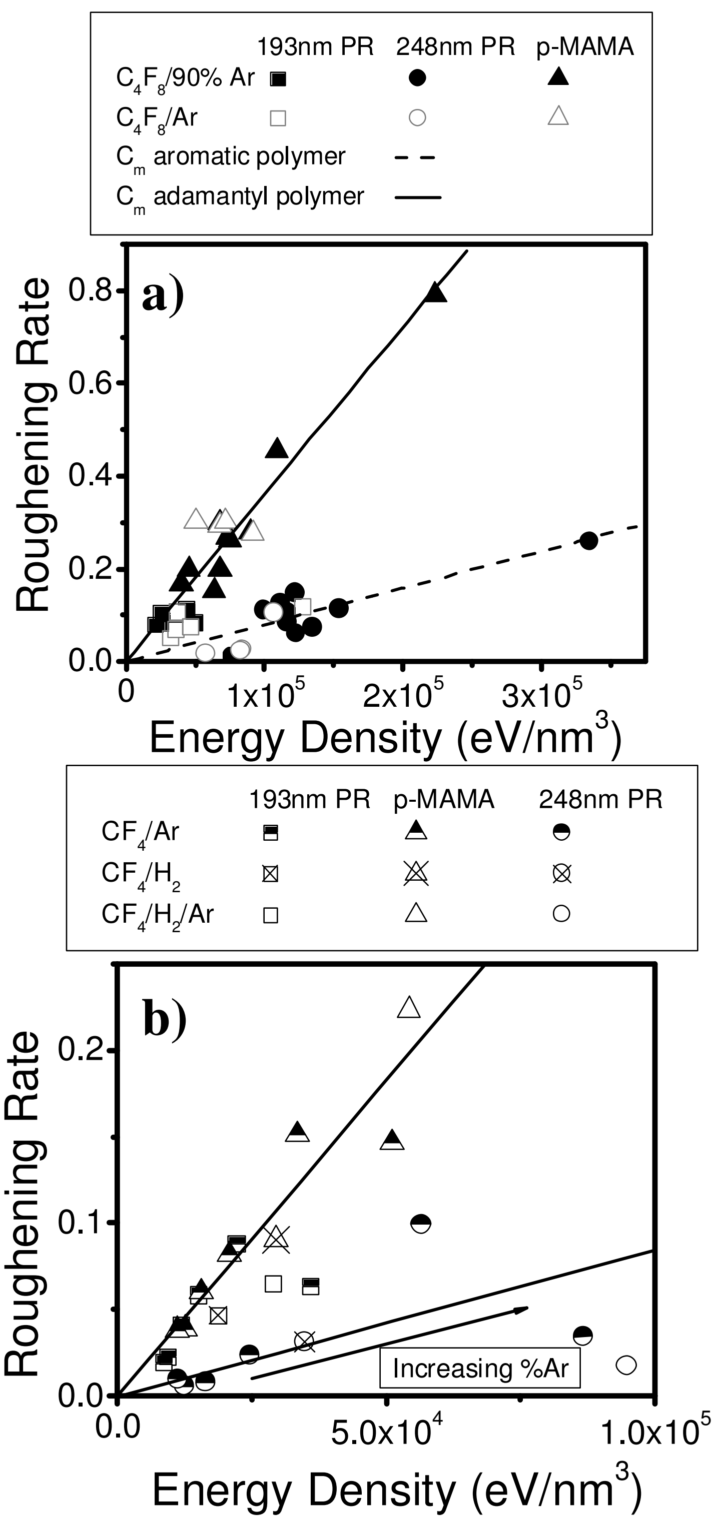

Figure 5.17: *Roughening rate vs. energy density as shown in[5.7] and for C_4F_8/Ar (a)) and for CF_4/Ar, CF_4/H_2 and CF4/Ar/H_2 discharge conditions(b)).*

One data point for 193nm PR does not follow the model. The high flux of fluorocarbon species in C_4F_8/40% Ar caused very little net removal for 193nm PR, but net deposition for 248nm PR and p-MAMA (see Fig. 5.5a)). The data for deposition have been omitted for simplicity sake. The very low etch rate of 193nm PR in C_4F_8/40% Ar allowed a fairly high energy density (1.3×10^5 eV/nm^3), much higher than typically seen for 193nm PR. The roughening rate seen for this condition is significantly lower than expected for adamantyl polymers at this energy density and actually more similar to the values for 248nm PR. We know from Fig. 5.13 that very large FC fluxes arrive at the surface under this condition and so the roughening rates might actually more reflect the roughening behavior of the FC film as opposed to the polymer material. We furthermore believe that it is an indication that thick, discrete FC surface films could potentially reduce polymer roughening without increasing polymer loss rate. In the case of C_4F_8/40% Ar however, this process fails, since deposition inside the 3d structures covers up the original pattern (see Fig. 5.6f)).

Figure 5.17b) shows that the energy densities in CF_4/Ar chemistries can be significantly reduced for all materials. The linear regression fits (obtained for C_4F_8/90% Ar conditions) for the materials constants C_m were inserted as a guide for the eye. While energy densities for the conditions examined in our previous publication were limited to about $5*10^4$ eV/nm^3, significant reductions in energy density were achieved through increased etch yields for CF_4/Ar plasma etch conditions. We can clearly identify a mechanism where high surface fluorination causes high etch yields (Fig. 5.15a)), which in turn results in small energy densities at the surface and with that minimal roughening rates. For CF_4 rich etch conditions,

selective material removal by ion bombardment and associated surface roughness amplification could be suppressed. As mentioned when discussing Fig. 5.12, FC mixing with the PR material can be expected for CF_4/Ar chemistries due to the relatively low F/C ratios.

We mentioned earlier that a roughening model was presented earlier,[5.7] where the energy density present during processing was proportional to the roughening rates. Roughening constants C_m have been obtained based on the polymer included in the specific PR resin. We see in Fig 5.17b) that the thickness of the FC films seems to be reflected in the deviations from proportionality for the roughening constants C_m. The process conditions that produced thick surface FC films (CF_4/80% Ar) show slightly enhanced roughening rates. The slightly reduced roughening rates for the CF_4/90 % Ar condition might be based on the fact that only a very shallow region is fluorinated in this case (Fig. 5.11b)). The data in Fig. 5.17b) also show that the data for CF_4/H_2 and CF_4/H_2/Ar can be captured by the energy density model. The validity of our model for different discharge chemistries is therefore confirmed further. Very low energy density conditions in CF_4/H_2 result in very small roughening rates, similar to CF_4 rich etch conditions. The stabilization of the adamantyl polymer due to interaction hydrogen may be reflected in the fact that the roughening rates for both, 193nm PR and p-MAMA are slightly lower than expected by the roughening constant for adamantyl polymers. The layer like deposition of the FCH film under this condition (Fig. 5.11a)) might also be responsible for this effect.

Data obtained for process conditions employing $CF_4/H_2/Ar$ show that Ar addition to CF_4/H_2 increases the energy densities significantly. We also see that 248nm PR shows a lower roughening rate than predicted by our model, whereas the roughening rates for p-MAMA and 193nm PR follow the model. This is in contrast to the finding for CF_4/90% Ar, where a reduced fluorination seemed responsible for reduced roughening rates. One possible explanation is that for $CF_4/H_2/Ar$, cross-linking of the 248nm PR prevents deeper fluorine penetration from the plasma, whereas the chain scissioning behavior of p-MAMA and 193nm PR allows fluorination and with that increased roughening rates.

The different appearance of the FFT data for different plasma conditions albeit similar surface roughness values is now much better understood. We showed that high surface roughness as a result of plasma processing is possible for low energy density process conditions when a high amount of surface roughness amplification due to non-uniform removal takes place (high etching rate), e.g. as seen for CF_4/80% Ar. Alternatively, introduction of high surface roughness is possible for processing at high energy densities even when only moderate amount of non-uniform surface amplification takes place (low etching rate), e.g. C_4F_8/90% Ar. We also find that roughening for surfaces and sidewalls is influenced by fluorocarbon interaction with the PR substrate. The tapered profile for CF_4 rich conditions might be a result of the removal mechanism being increasingly dependent on surface stoichiometry rather than just physical sputtering. For CF_4/Ar discharges, we never observed smoothing of the original sidewall standing-wave roughness. In CF_4/H_2 smoothing may have occurred due to a separate FC film deposition on the PR substrate (Fig. 5.11a)),

similar to conditions achieved by low source power processing in C_4F_8/90% Ar.[5.7] The FC film deposition can smooth out initial sidewall roughness by a deposition of a highly stable film on the PR material. Fluorine scavenging in CF_4/H_2 might be responsible for the gradual improvement in the etch profile, which reduced tapering.

The evolution of the contact hole profile shapes shown in Fig. 5.4 can be understood based on these considerations. The high F/C ratio seen for PR materials processed using CF_4 and CF_4/H_2 process conditions shows that both process conditions contain F-rich radicals, which are able to penetrate contact hole structures deeply.[5.7] The smooth appearance of the CF_4, CF_4/H_2 and CF_4/90% Ar condition can be attributed to higher etch yields and the suppression of characteristic roughness features due to F-addition. The severe surface damage for all discharge conditions for which Ar was present could be attributed to the high energy density, ε, which usually results when Ar is added to the discharge. Plasma-induced VUV photon bombardment, in conjunction with plasma ion bombardment,[5.61] might be responsible for characteristic cross link and chain scission reactions within the PR material, which could reduce or enhance the fluorine penetration of the PR materials.

5.4.3 Correlation of surface and sidewall roughness

The introduction of feature sidewall roughness during processing is important since it may be transferred into the underlying material. We tested how well surface roughness correlates to sidewall roughness formation for identical plasma process conditions. Figure 5.18 shows a roughly linear correlation for CF_4/Ar plasmas. The FC film thickness evolution (Fig. 5.13) is related to the evolution of sidewall roughness (Fig. 5.10b)) and surface roughness (Fig. 5.8b)). Similar results were found for the other process conditions. This shows that the mechanisms for blanket films, which can be explained very well, also relate to sidewall evolution, which is technologically more important.

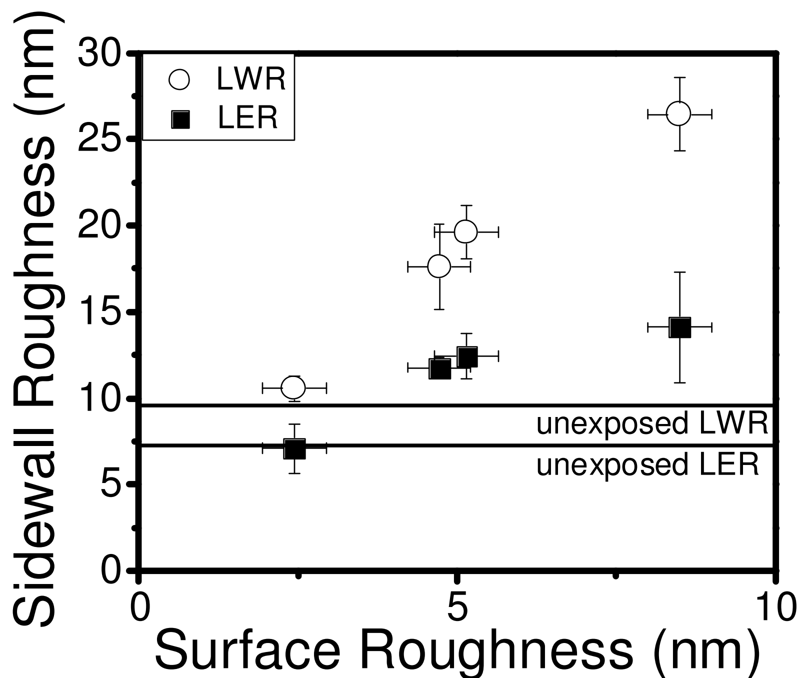

Figure 5.18: *Sidewall roughness vs. surface roughness in CF_4/Ar discharge conditions.*

5.5 CONCLUSIONS

We presented a study of plasma etching of prototypical photoresist materials and structures using fluorocarbon discharges fed with C_4F_8/Ar or CF_4/Ar/H_2 gas mixtures. FC addition in C_4F_8/Ar plasmas decreased etch rates, whereas F-incorporation into the polymer for CF_4/Ar plasmas increased the removal rate. The formation of a well-defined FC layer on top of the PR materials minimizes surface roughness and is able to smooth out rough sidewall edges. In contrast, strongly mixed FC layers at PR surfaces formed in plasma etching environments characterized by intensive ion bombardment. FC radicals with a large sticking coefficient enhance the roughening behavior on surfaces and sidewalls. The fluorination of PR material surface sites during steady state etching was found to impact the chemical removal during etching, and increased etch yields. This was captured in an ion enhanced etching model that included the surface fluorination of the PR surfaces.

The spatial frequency distribution of surface roughness obtained from AFM data showed that surface fluorination of the PR surfaces prevented the formation of small scale roughness features at the cost of large scale roughness. The large scale roughness evolution could effectively be suppressed by low surface energy density conditions, where high etch yields dominated the polymer response to the plasma conditions. Hydrogen addition during processing showed improved roughening behavior for the adamantyl structure. Finally, a model where the surface roughening rate varies proportionally with the energy density deposited at polymer surfaces during processing was introduced. The validity of our model for different discharge

and surface chemistries points to the fact that roughening and removal mechanisms for PR materials are coupled.

The general tradeoff between low etch rates or improved roughness for processing of PR materials was confirmed, suggesting that etch rates and surface roughness evolution are strongly coupled. The sidewall roughness evolution has additionally shown a stronger influence on radical speciation, where low sticking radicals leading to separate layer deposition may be able to reduce sidewall roughness. Depending on the plasma condition, highly resistant FC layers can be grown on the PR materials, in our case even leading to a smoothing of initially very rough sidewalls.

ACKNOWLEDGEMENTS

The authors gratefully acknowledge financial support of this work by the National Science Foundation under award No. DMR-0406120 and DMR-0705953. Dr. M. Moravej is thanked for help and contributions to parts of this work.

Chapter 6:

Overall Conclusions

The focus of this work was aimed at improving the understanding of plasma-photoresist surface interactions as they are of crucial importance in nano-patterning of substrates using photoresist (PR) polymers in plasma-based pattern transfer processes. Etch resistance and roughness evolution as a function of time, polymer material, operating parameters or discharge chemistry were studied. Resist loss rates and surface (blanket materials) and line edge (patterned substrates) roughening trends of representative polymers during realistic fluorocarbon-Ar based plasma etching processes were characterized. The impact of the plasma conditions on PR removal rates and surface roughening rates was discussed. Based on the observations, a roughening model for photoresist polymers in plasma environments was developed. Although the focus of this study were advanced photoresist systems as they are used in 193nm PR lithography, our findings provide important insights for plasma-polymer interactions for other materials used in plasma processing of materials.

In chapter 2 we reported results of the study of the time dependence of plasma surface interactions for several advanced PR materials and model polymers. Within the first seconds of plasma exposure of polymers, its structure is destroyed in the surface region, accompanied by H and O loss. During this period, increased PR erosion rates and increased roughening rates are seen, and explained by the H and O content of the PR. The fluorination of the near-surface region of the PR/polymer materials that takes place for FC plasmas used for pattern transfer also reaches

saturation within the same time period. Increased surface roughening is caused by interactions of the damaged top layer and the FC layer formed by interaction with the plasma on the polymer substrate surface. In particular, the effect of ions, radicals, metastables and photons influence damage layer formation greatly and contribute to the roughening behavior. After this initial PR surface transformation, steady-state etch conditions and surface properties have been established, which, as the initial transient, reflect the plasma properties. The amount of surface roughness introduced per PR layer thickness removed approaches zero during the steady state period, indicating that changes in surface roughness during this period is coupled to the material removal. The surface roughness generated during the initial PR transformation period grows by non-uniform ion-induced etching during the steady-state etching period.

In chapter 2 we also describe studies of the influence of polymer structure and composition on the results of the plasma-surface interactions. While a very rough estimate of the PR erosion rate based on polymer stoichiometry is possible, small, but definite discrepancies were observed and reflect different cross-linking tendencies of the polymers. The chain scission behavior of methacrylate adamantyl polymers was reduced by inserting acrylate groups. This change resulted in smaller polymer erosion rates and reduced surface roughness introduction. The surface roughening behavior of the polymers was found to be even more influenced by the side chain chemistry. By changing the functional groups of the polymer matrix from methyladamantyl to ethyladamantyl, a characteristic increase of the surface roughening resulted. This increase was still present when normalizing the surface roughness to the removed

thickness during processing. The functional additives typically added to PR polymers to make the resin photoactive were found to have no measurable impact on the roughening and etch behavior. One interesting observation was that the measured surface fluorination and surface roughness were directly correlated, and also mirrored the relative softness of the polymers and tendencies for fluorination in the plasma environment.

In chapter 3, several key comparisons of our newly developed surface roughening model are presented. By summarizing all results reported in chapters 2-5, we found that the surface energy density during processing is predictive of the surface roughening rates. Process conditions requiring a high surface energy density to remove polymer material from the surface showed high surface roughening rates, whereas process conditions with low energy densities show very low roughening rates. This observation reflects the effective polymer etching yields, with high etching yields yielding smoother surfaces than low etching yield processing. Surface roughness introduction is thus linked to ion bombardment related energy flux to the surface which causes both removal of the PR materials, and by damaging the surface polymer structure and polymer relaxation, surface roughness introduction. By increasing the etch yield, e.g. using CF_4 rich process conditions, a suppression of surface roughness introduction can be achieved.

A clear dependence of the surface roughening rates on both polymer material structure and surface energy density was found. Although by modification of the polymer surface composition in different FC discharge chemistries, etching of polymers at different surface energy densities takes place, the overall surface

roughness behavior is for all conditions controlled by the polymer structure itself. Overall, a tradeoff has been observed, where the surface roughening can be reduced by selecting discharge conditions resulting in high etching rates or lower polymer etching rates can be achieved at the cost of increasing the roughening rate of the polymers.

In chapter 4, a detailed survey of the influence of plasma operating parameters on PR etching rate and surface roughening is presented. Increasing ion energies caused increased polymer etching rates for all materials. When reducing the ion/neutral ratios by increasing operating pressure, etch yields increased and are explained by greater fluorination of the polymer materials. The fluorination of 193nm PR was greater, which may suggest that the lactone group of the 193nm PR is easily fluorinated. The variation of the polymer etching rate as a function of plasma source power was found to be dominated by changes in the thickness of the FC material formed on the polymers during steady-state etching. The changes in surface roughness were dominated by ion-induced erosion effects when RF bias power or pressure were changed. The polymer surface roughening behavior was significantly changed as a function of source power, and reflected both surface energy density and molecular dissociation of the FC feedgas. Fluorine-rich, thin FC polymer deposits were formed at low source power, and resulted in fairly smooth polymer films. Carbon-rich, thick FC films were produced a high source power levels and yielded very rough polymer films or etched structures. Generally, increasing the surface energy density through use of higher source power levels and/or increasing selfbias voltage and changing ion energy increased the overall roughening behavior of the PR

materials. By comparing the model compounds at different C_4F_8 percentages in Ar (while maintaining >70% of the ion flux as Ar^+) we found that the fluorination due to plasma processing can affect the overall roughening behavior of the PR materials (as also seen for different source power levels). Characteristic nanoscale differences between the surface roughness introduced in the polymer compounds were present for all conditions, and suggest that the plasma species (radicals, metastables, photons and ions) modify in a characteristic fashion the polymer materals and generate the cross linking and chain scissioning behavior for each material. The degree of surface fluorination was found to be characteristic of the measured surface roughness for each material. Fluorine-rich surface conditions typically resulted in smoother polymer surfaces, whereas C-rich surfaces showed a higher level of surface roughness introduction as a result of plasma processing. By comparing results of blanket materials and patterned nanostructures, we showed that surface and sidewall roughness generally correlated well to each other. The nature of the FC radicals formed in the discharges was found to have a big impact on the sidewall coverage of the nanostructures. A difference in fluorination of trenches and contact holes based on the radical sticking was also found. Increased sticking of the FC radicals was seen for contact hole structures than for trenches. Even though 193nm PR contains oxygen, thicker FC films are typically observed for 193 nm PR than for 248nm PR after equivalent plasma processing.

A new surface roughening model was presented. The energy density required to remove a unit volume of material at the surface during processing controls surface roughening of the PR materials, in combination with the molecular structure of the

polymer being processed. This surface energy and material structure dependent surface roughening is followed by roughness amplification due to laterally non-uniform ion-induced polymer removal during the steady state etch regime.

The effect of different plasma gas chemistries on polymer plasma etching resistance was examined in chapter 5 employing C_4F_8/Ar or CF_4/Ar/H_2 gas mixtures. In all cases the transition from ion-flux dominated to a neutral-flux dominated discharge condition resulted in more fluorine-rich surface conditions and substantially smoother polymer films. For high C_4F_8 percentages when employing C_4F_8/Ar, high FC film deposition rates on the polymers resulted in reduced removal rates and smoother films. For high CF_4 percentages when using CF_4/Ar/H_2 gas mixtures, smoother films were generated, even though the PR removal rates increased due to interaction with atomic fluorine. Generally, the plasma-induced fluorination of the PR materials was found to be directly linked to the polymer removal rates, since the etching yields reflected the fluorine surface coverage during plasma processing. When processing patterned structures, increased surface fluorination for CF_4 rich conditions lead to increasingly tapered profiles. This could be counter-acted by the addition of H_2 to the CF_4 discharge. One important effect appeared to be the stabilization of the adamantyl group of 193 nm PR by the addition of H_2 to the plasma. The addition of Ar to a CF_4/H_2 discharge resulted in highly damaged PR structures and films, to a significant extent due to insufficient FC film coverage of the PR materials and increased ion bombardment. The roughening model presented in chapter 4 was found to be applicable to a description of the surface roughening results obtained with different polymers in diverse gas chemistries.

Our examination of plasma-induced modifications of model polymers for 193nm PR lithography showed that plasma-induced polymer degradations reflect the energy dissipated in the surface region during processing in a fashion which is universal for adamantyl based polymers. For 248 nm PR materials, the ability to cross link is a crucial step in improving plasma etch performance. Although for 193 nm PR materials the fluorination of the surface region improves surface roughening behavior, the presence of fluorine reduces the etch resistance even further. These initial insights on the effect of surface fluorination on polymer surface roughening during plasma processing is expected to be of great importance for immersion lithography which involves fluorinated PR materials.

Chapter 7:

Future work and directions

The experiments presented in chapters 2-5 yielded valuable insights into plasma-surface interactions of advanced photoresist (PR) materials. We discussed the effects of different PR polymers for plasma processing and also were able to identify major factors controlling the removal of the PR and polymer films. The roughness evolution of blanket films samples was explained by two linked mechanisms, roughening of the PR materials based on the energy density present during processing followed by roughness amplification based on localized non-uniform removal rates. For processing of 3diensional structures, similar trends for the sidewall as well as the surface roughness evolution were found. However, there are additional factors that need to be considered for 3dimensional structures, and the examination of the significance of the blanket roughening model for evolution of line edge roughness and CD control needs to be improved. In the following, we will present a few further experiments that should clarify or confirm some of the remaining questions raised by this work.

A study of discharge chemistries other than fluorocarbon/Ar discharges would test how our results hold true even in processes used for significantly different applications. Discharge conditions often investigated include, but are not limited to oxygen, nitrogen chlorine or hydrogen bromide discharges.[7.1,7.2] The latter processes have recently gained interest due to induction of an altered degradation scheme.[7.3] A hydrogen bromide discharge as pre-treatment step is often used to reduce roughness

issues with 193nm PR. It would be useful to test how our roughness model applies to these discharge chemistries and how it applies to pre-treated polymer surfaces. An extension of our experimental studies to discharge reactors of significantly different geometric and plasma heating configurations would also be useful to test the validity of the roughening model under those conditions.

A better understanding of the relation of the blanket film mechanisms to the sidewall evolution is also desirable. While the blanket film evolution can be explained very well by our studies, many questions remain open with regard to 3d structures. While smoothing was seen on sidewalls for plasma conditions having low-sticking coefficient FC radicals (see Figs. 4.12, 5.3), moderate roughening was still observed on the blanket films (see Figs. 4.8, 5.1). For etch conditions with a higher degree of ion-induced etching and isotropic etching effects, the sidewall roughness did not change significantly compared to the sidewall roughness after the lithography process (see Fig. 5.10). The driving forces for this resist sidewall smoothing based on FC deposition are not well understood at this point. The 3d samples processed in chapters 4 and 5 all had standing wave patterns due to the lithographic exposure. Processing of samples with the same dimensions without these standing waves (by applying a bottom anti-reflection coating on the Si surface) will clarify findings that might be skewed by these. The control of the CDs of the PR structures by plasma processing can also be further investigated. While initial results were obtained by our studies, effects on the CD due to FC films should be clarified. An improvement in the smoothness of the sidewalls was usually accompanied by a CD decrease. Etch conditions with a higher degree of isotropic etch (i.e. CF_4 rich Ar discharges) showed

a significant increase in CD. The mid and bottom CD were mostly related to the radical species types present in the discharge. Resist smoothing processes[7.4] typically relying on FC deposition onto PR could also be explained by these effects. A model incorporating these findings could be developed to design plasma etch processes suitable for various CDs and profile shapes.

Other aspects of the plasma-surface interactions that can still be improved is the sample metrology. Further investigation of the plasma processed surfaces by new methodologies and techniques should lead to further insights and understanding of the process results. While the composition of the blanket thin films could be related to process trends very well, a detailed understanding of the spatial distribution of compositional differences seems important in a couple aspects. The roughness amplification mechanism postulated by Sumiya et al.[7.5] was based on the fact that a variation of the FC film thickness might result in a localized difference in etch rate. This in turn then leads to the growth of hills and valleys on the PR surface resulting in the characteristic roughness features seen for PR processing. By using a compositional technique that has high spatial resolution, a much better understanding of this issue could be obtained. Electron energy loss spectroscopy (EELS)[7.6-7.8] might be used to examine SEM images of exposed and rough PR surfaces. By having very high spatial resolution, compositional differences (C/O/F analogue to XPS) of the regions with high and low ER could be examined. The graphite content of the different phases might be estimated using EELS. Special attention would have to be directed to the stability of the polymer materials under these high energy electron beams. In a similar way, high resolution images of the top surfaces of the samples

could be obtained by transmission electron microscopy (TEM).[7.6-7.10] Phase contrast images might be able to estimate the graphite content of the films and improve the understanding of the density fluctuations of the PR films and their impact on the index measurement by ellipsometry (see chapter 2). An improved understanding of the fluorine profile could result from a successful investigation. Challenges for the use of TEM include the time consuming sample preparation or the high energy bombardment and resulting damage of the polymer samples.

Additional information on the transformation of the polymer materials could be deducted from complimentary Fourier-transform infrared (FTIR) and Raman spectroscopy. Characteristic peaks corresponding to polymer moieties in the main or side chain can be used to identify transitions of the polymer material as a function of PR polymer or plasma condition. Raman Spectroscopy might be able to estimate the relative graphite contents of the PR films depending on the energy density present during processing (see chapter 5). Since both, FTIR and Raman, are able to detect $C-H_x$ bonds, a better understanding of the hydrogen loss processes of the PR materials could be studied. Since the significant transitions of the PR material might be only limited to the top 10nm of the sample, special care has to be taken to make sure enough surface sensitivity is given by these techniques. Internal reflection spectroscopy (IRS), also called attenuated total reflectance (ATR) would have to be used to provide sufficient surface sensitivity for the FTIR technique.[7.11] Surface-enhanced Raman scattering (SERS)[7.12] might be able to provide enough surface sensitivity to study the polymer films by means of Raman scattering. A collection of possible approaches can be found here.[7.13]

Further investigation of the polymer materials by secondary ion mass spectroscopy[7.6,7.7] might also gain additional insights. A detailed investigation of the PR polymers with slightly differing polymer composition (see chapter 2) might lead to a better understanding of the chain scissioning/cross linking effects seen by plasma processing. By examining different plasma process conditions, the stability of the lactone group in 193nm PRs could be clarified.

The application of our improved understanding of plasma-surface interactions could also be extended to the field of surface wettability.[7.7,7.14] The surface properties can easily be tailored using different polymer materials and generating different surface morphologies based on the energy density of the process.

Direct implications for future PR materials design can already be learned from our data. Immersion photoresist material resists, which are essentially fluorinated 193nm PR resists to prevent leaking out of PAG,[7.15,7.16] higher etch yields can be expected due to the fluorine content. Along with this behavior, these immersion resists should also maintain smoother surfaces, as the energy density on the surface is reduced by the increased etch yield. Similar trends have in fact already been reported.[7.1] Sumiya et al.[7.5] suggested that one reason for the instability of 193nm is that the oxygen is only found in the side chain polymer, whereas plasma fluorination usually equally affects the main chain polymer and the side chain. The synthesis of many differing fluorinated PR systems has been demonstrated and can therefore be used for a detailed investigation of the impact of fluorine in the side chain vs. the main chain. Future imprint lithography resists systems based on the stable 248nm PR[7.17] could be improved further based on the insights gained by the roughening

model (chapters 3,4 and 5). A collaborative effort to investigate plasma-surface interaction of immersion resists is currently being investigated by the GOALI team under NSF-GOALI DMR-0705953.

References:

Chapter 1:

1.1 S.M. Sze, *Semiconductor Devices Physics and Technology* (J. Wiley & Sons, Inc., New York, 2002)

1.2 G. Cao, *Nanostructures & Nanomaterials – Synthesis, Properties & Application* (Imperial College Press, London, 2004)

1.3 G.E. Moore, Electronics, Vol. **38**, (1965); G.E. Moore, IEEE IEDM Tech Digest, 11 (1975)

1.4 L. Sivitz, Science News **158**, 350 (2000)

1.5 International Technology Roadmap for Semiconductors, 2007 edition

1.6 M.S. Liang, IEDM Tech. Dig, 313 (2004),

1.7 P. Bai, et al., IEDM Tech. Dig., 657 (2004)

1.8 S.Wolf, R.N. Tauber, *Silicon processing for the VLSI era –Volume 1: Process Technology* (Lattice Press, Sunset Beach, 1986)

1.9 P. Singer, Semicond. Int. **20**, 79 (1997)

1.10 H. Ito, Adv. Polym. Sci. **172**, 37 (2005)

1.11 J.M. Shaw, J.D. Gelorme, N.C. LaBianca, W.E. Conley, S.J. Holmes, IBM J. Res. Dev. **41**, 81 (1997)

1.12 H. Ito, IBM J. Res. Dev. **45**, 683 (2001)

1.13 R.D. Allen, G.M. Wallraff, D.C. Hofer, R.R. Kunz, IBM Journal of Research and Development **41**, 95 (1997)

1.14 T. Kajita, Y. Nishimura, M. Yamamoto, H. Ishii, A. Soyano, A. Kataoka, M. Slezak, M. Shimizu, P.R. Varansi, G. Jordahamo, M.C. Lawson, R. Chen, W.R. Brunsvold, W.Li, R.D. Allen, H. Ito, H. Truong and T. Wallow, Proc. SPIE **4345**, 712 (2001)

1.15 H. Ito, G.M. Wallraff, N. Fender, P.J. Brock, W.D. Hinsberg, A. Mahorowala, C.E. Larson, H.D. Truong, G. Breyta and R.D. Allen, J. Vac. Sci. Technol. B **19**, 2678 (2001)

1.16 Y. Uetani and H. Fujishima, Proc. SPIE **3999**, 974 (2000)

1.17 E.A. Hudson, Z. Dai, Z. Li. S. Kang, S. Lee, W. Chen and R. Sadjadi, Proc. Of International Symposium on Dry Process, Tokyo, Institute of Electrical Engineers of Japan, 253 (2003)

1.18 J. Kon, K. Nozaki, T. Namiki and E. Yano, Proc. SPIE **3999**, 1207 (2000)

1.19 H. Gokan, S.Esho and Y. Ohnishi, J. Electrochem. Soc. **130** , 143 (1983)

1.20 L. Ling, X. Hua, X. Li, G.S. Oehrlein, E.A. Hudson, P. Lazzeri and M. Anderle, J. Vac. Sci. Technol. B **22**, 2594 (2004)

1.21 X. Hua, S. Engelmann, G.S. Oehrlein, P. Jiang, P. Lazzeri, E. Iacob and M. Anderle, J. Vac. Sci. Technol. B **24**, 1850 (2006)

1.22 Y.C. Bae, C. Andes (unpublished)

1.23 J.W. Coburn, H.F. Winters, J. Appl. Phys. **50,** 1960 (1979)

1.24 X. Li, X. Hua, L. Ling, G.S. Oehrlein, M. Barela, H.M. Anderson, J. Vac. Sci. Technol. A **20**, 2052 (2002)

1.25 X. Li, X. Hua, L. Ling, G.S. Oehrlein, M. Barela, H.M. Anderson, J. Vac. Sci. Technol. A **21**, 284 (2003)

1.26 D.Y. Kim, J.H. Ko, M.S. Park, N.E. Lee, Thin Solid Films **516**, 3512 (2008)

1.27 Y. Wang, L. Luo, J. Vac. Sci. Technol. A **16**, 1582 (1998)

1.28 J.P. Chang, J.W. Coburn, J. Vac. Sci. Technol. A **21**, S145 (2003)

1.29 D. Perret, C.E. Andes, K.S. Cheon, M. Sobhian, C.R. Szmanda, G.G. Barclay, P. Trefonas III, Proc. SPIE **6519** (2007), 651912

1.30 H. Biedermann, *Plasma polymer films* (Imperial College Press, London, 2004)

1.31 R.J. Woods, A. K. Pikaev, *Applied Radiation Chemistry – Radiation processing* (John Wiley & Sons, Inc., New York, 1994)

1.32 F. H. Attix, *Introduction to radiological physics and radiation dosimetry* (Wiley-VCH Verlag GmbH & Co. KGaA, Weinheim, 2004)

1.33 M.R. Wertheimer, A.C. Fozza, A. Holländer, Nuclear Instruments and Methods in Physics Research B. **151**, 65 (1999)

1.34 B. Chapman, *Glow discharge processes – Sputtering and plasma etching* (John Wiley & Sons, Inc., New York, 1980)

1.35 M.A. Lieberman, A.J. Lichtenberg, *Principles of plasma discharges and materials processing* (John Wiley & Sons, Hoboken, 2005)

1.36 D.M. Manos, D.L. Flamm, *Plasma Etching* (Academic, San Diego, 1990)

1.37 R. D'Agostino, F. Cramarossa, F. Fracassi, F. Illuzzi, *Plasma Deposition, Treatment and Etching of Polymers* (Academic, San Diego, 1990)

1.38 F. Jansen, *Plasma-enhanced chemical vapor deposition* (American Vacuum Society, New York, 1997)

1.39 R.K. Waits, *Thin film deposition and patterning* (American Vacuum Society, New York, 1998)

1.40 R. d'Agostiono, P. Favia, F. Fracassi, *Plasma processing of polymers* (Kluwer Academic Publishers, Dordrecht, 1997)

1.41 O.A. Popov, *High density plasma sources – Design, physics and performance* (Noyes Publications, Park Ridge, 1995)

1.42 M. Sugawara, *Plasma etching – Fundamentals and applications* (Oxford University Press, New York, 1998)

1.43 T.E.F.M. Standaert, C. Hedlund, E.A. Joseph, G.S. Oehrlein, T.J. Dalton, J.Vac.Sci.Technol. A **22**, 53 (2004)

1.44 H.G. Tompkins, W.A. McGahan, *Spectroscopic ellipsometry and reflectometry – a user's guide* (John Wiley & Sons, Inc., New York, 1999)

1.45 D. Briggs, *Surface analysis of polymers by XPS and static SIMS* (Cambridge University Press, Cambridge, 1998)

1.46 D. Briggs, M.P. Seah, *Practical surface analysis by Auger and x-ray photoelectron spectroscopy* (John Wiley & Sons Ltd., Chichester, 1983)

1.47 P.E.J. Flewitt, R.K. Wild, *Physical Methods for Materials Characterisation* (Institute of Physics Publishing, Bristol, 1994)

1.48 D.G. Nest, PhD Thesis, Department of Chemical Engineering, UC Berkeley, Berkeley, CA

1.49 X. Hua, PhD Thesis, Department of Physics, University of Maryland, College Park, MD (2006)

1.50 G.S. Selwyn, *Optical Diagnostic Techniques for Plasma Processing* (American Vacuum Society, New York, 1993)

1.51 G.S. Oehrlein, X. Hua, C. Stolz and P. Jiang, J. Vac. Sci. Technol. B **24**, 279 (2006)

Chapter 2:

2.1 International Technology Roadmap for Semiconductors, 2005 edition

2.2 H. Ito, G.M. Wallraff, N. Fender, P.J. Brock, W.D. Hinsberg, A. Mahorowala, C.E. Larson, H.D. Truong, G. Breyta and R.D. Allen, J. Vac. Sci. Technol. B **19**, 2678 (2001)

2.3 T. Kajita, Y. Nishimura, M. Yamamoto, H. Ishii, A. Soyano, A. Kataoka, M. Slezak, M. Shimizu, P.R. Varansi, G. Jordahamo, M.C. Lawson, R. Chen, W.R. Brunsvold, W.Li, R.D. Allen, H. Ito, H. Truong and T. Wallow, Proc. SPIE **4345**, 712 (2001)

2.4 H. Ito, IBM J. Res. Dev. **45**, 683 (2001)

2.5 M. Schaepkens, R.C.M. Bosch, T. Standaert, G.S. Oehrlein and J. Cook, J. Vac. Sci. Technol. A **16**, 2099 (1998)

2.6 M. Schaepkens and G.S. Oehrlein, J. Electrochem. Soc. **148**, C211 (2001)

2.7 D. Eon, V. Raballand, G. Carty, M.C. Peignon-Fernandez and C. Cardinaud, Eur. Phys. J. Appl. Phys. **28**, 331 (2004)

2.8 E.A. Hudson, Z. Dai, Z. Li. S. Kang, S. Lee, W. Chen and R. Sadjadi, Proc. Of International Symposium on Dry Process, Tokyo, Institute of Electrical Engineers of Japan, 253 (2003)

2.9 L. Ling, X. Hua, X. Li, G.S. Oehrlein, E.A. Hudson, P. Lazzeri and M. Anderle, J. Vac. Sci. Technol. B **22**, 2594 (2004)

2.10 X. Hua, S. Engelmann, G.S. Oehrlein, P. Jiang, P. Lazzeri, E. Iacob and M. Anderle, J. Vac. Sci. Technol. B **24**, 1850 (2006)

2.11 Y. Uetani and H. Fujishima, Proc. SPIE **3999**, 974 (2000)

2.12 Y. Kaimoto, K. Nozaki, S. Takechi and N. Abe, Proc. SPIE **1672**, 66 (1992)

2.13 J. Kon, K. Nozaki, T. Namiki and E. Yano, Proc. SPIE **3999**, 1207 (2000)

2.14 P.R. Varasani, R.W. Kwong, M. Khojasteh, K. Patel, K-J. Chen, W. Li, M.C. Lawson, R.D.Allen, R. Sooriyakumaran, P. Brock, L.K. Sundberg, M. Slezak, G.Dabbagh, Z. Liu, Y. Nishiimura, T. Chiba and T. Shimokawa, J. Photopolym. Sci. Tech. **18**, 381 (2005)

2.15 T. Fedynshyn, R.R. Kunz, R.F. Sinta, R.B. Goodman and S.P.Doran, J. Vac. Sci. Technol. B **18**, 3332 (2000)

2.16 W. Dawes and L.C. Glover, In: J.E. Mark, Editor, "*Physical Properties of Polymers Handbook*" (American Institute of Physics Press, Woodbury, NY, 1996) (chapter 41)

2.17 K. Harada, J. Appl. Pol. Sci. **26**, 3395 (1981)

2.18 G.S. Oehrlein, X. Hua, C. Stolz and P. Jiang, J. Vac. Sci. Technol. B **24**, 279 (2006)

2.19 H. Ito, IBM J. Res. Dev. **41**, 69 (1997)

2.20 G. Pohlers, G. Barclay, A. Razvi, C. Stafford, T. Barbieri and J. Cameron, Proc. SPIE v **5376**, 79 (2004)

2.21 E. Reichmanis, O. Nalamasu and F.M. Houlihan, Acc. Chem. Res. **32**, 659 (1999)

2.22 Y.C. Bae and C. Andes (unpublished, 2005)

2.23 X. Hua, X. Wang, D. Fuentevilla, G.S. Oehrlein, F.G. Celii and K.H.R. Kirmse, J. Vac. Sci. Technol. A **21**, 1708 (2003)

2.24 V. Krastev, I. Reid, C. Galassi, G. Hughes and E. McGlynn, J.Mat.Sci. **16**, 541 (2005)

2.25 D. Humbird and D.B. Graves, J.Appl.Phys. **96**, 65 (2004)

2.26 B. Ji, S.A. Motika, P.R. Badowski, S. Dheandhanoo, J.R. Stets and E.J. Karwacki, Solid State Technol. **48**, 45 (2005)

2.27 N. Negishi, H. Takesue, M. Sumiya, T. Yoshida, Y. Momonoi and M. Izawa, J. Vac. Sci. Technol. B **23**, 217 (2005)

2.28 M.J. May, B. Mortini, C. Sourd, D. Perret, D.W. Chung, G. Barclay, C. Brochon and G. Hadziioannou, Proc. SPIE **6153**, 61530P (2006)

2.29 X. Li, X. Hua, L. Ling, G.S, Oehrlein, M. Barela and H.M. Anderson, J. Vac. Sci. Technol. A **20**, 2052 (2002)

2.30 X. Li, L. Ling, X. Hua, M. Fukasawa, G.S. Oehrlein, M. Barela and H.M. Anderson, J. Vac. Sci. Technol. **A 21**, 284 (2003)

2.31 A. V. Vasenkov, Xi Li, G. S. Oehrlein, and M. J. Kushner, J. Vac. Sci. Technol. **A 22**, 511 (2004)

2.32 X. Li, L. Ling, X. Hua and G. S. Oehrlein, Y. Wang, A. V. Vasenkov and M. J. Kushner, J. Vac. Sci. Technol. **A 22**, 500 (2004)

2.33 X. Hua, C. Stolz, G.S. Oehrlein, P. Lazzeri, N. Coghe, M. Anderle, C.K. Inoki, T.S. Kuan and P. Jiang, J.Vac.Sci.Technol. A **23**, 151 (2005)

2.34 X. Li, L. Ling, X. Hua, G.S. Oehrlein, Y. Wang and H.M. Anserson, J.Vac Sci.Technol. A **21**, 1955 (2003)

2.35 T.E.F.M. Standaert, M.Schaepkens, N.R. Rueger, P.G.M. Sebel, G.S. Oehrlein and J.M. Cook, J.Vac Sci.Technol. A **16**, 239 (1998)

2.36 S. Ben Amor, G. Baud, M. Jaquet, G. Nansé, P. Fioux and M. Nardin, Appl. Surf. Sci. **153**, 172 (2000)

2.37 H.Gokan, S.Esho and Y. Ohnishi, J. Electrochem. Soc. **130** , 143 (1983)

2.38 T. Wallow, P. Brock, R. DiPietro, R. Allen, J. Opitz, R. Sooriyakumaran, D. Hofer, A.M. Mewherter, Y. Cui, W. Yan, G. Worth, W. Moreau, J. Meute, J. Byers, G.K. Rich, M. McCallum, S. Jayaraman, R. Vicari, J. Cagle, S. Sun and K. Hullihen, Proc. SPIE **v 3678**, 26 (1999)

2.39 T.E.F.M. Standaert, P.J. Matsuo, X. Li, G.S. Oehrlein, T.M. Lu, R. Gutmann, C.T. Rosenmayer, J.W. Bartz, J.G. Langan and W.R. Entley, J. Vac. Sci. Technol. A **19**, 435 (2001)

2.40 H. Biedermann, "*Plasma Polymer Films*" (Imperial College Press, London, 2004)

2.41 C.E. Foerster, I.T.S. Garcia, F.C. Zawislak, F.C. Serbena, C.M. Lepienski, W.H. Schreiner and M. Abbate, Thin Film Solids **411**, 256 (2002)

2.42 K.J. Orvek and C. Huffman, Nuc. Instr. Meth. Physi.Res. **B7/8**, 501 (1985)

2.43 Y. Okuyama, T. Hashimoto and T. Koguchi, J. Electrochem. Soc. **125**, 1293 (1978)

2.44 M.F. Doemling, B. Lin, N.R. Rueger, G.S. Oehrlein, R.A. Haring and Y.H. Lee, J. Vac. Sci. Technol. A **18**, 232 (2000)

2.45 C. Steinbruechel, Appl. Phys. Lett. **55**, 1960 (1989)

2.46 D. Nest, E. Pargon and D.B. Graves (in preparation)

2.47 P. Martens, S. Yamamoto, K. Edamatsu, Y. Uetani, L. Pain, R. Palla, M. Ross and W. Livesay, Proc. SPIE **v4345**, 138 (2001)

Chapter 3:

3.1 E. A. Hudson, Z. Dai, Z. Li, S. Kang, S. Lee, W. L. Chen, and R. Sadjadi, Proceedings of the Dry Process Int. Symp., 2003 (unpublished), Vol. 3, p.253;

3.2 N. Negishi, H. Takesue, M. Sumiya, T. Yoshida, Y. Momonoi, and M. Izawa, *J. Vac. Sci. Technol. B*. **23**, 217 (2005).

3.3 D. Goldfarb, A. Mahorowala, G. Gallatin, K. Petrillo, S. Rasgon, H. Sawin, S. Allen, M. Lawson, R. Kwong, J. Vac. Sci. Technol. B **22**, 647 (2004)

3.4 T. Wallow, A. Acheta, Y. Ma, A. Pawloski, S. Bell, B. Ward, C. Tabery, B. La Fontaine, R.H. Kim, S. McGowan, H.J. Levinson, Proc. SPIE **6519**, 651919 (2007)

3.5 H. Namatsu, M. Nagase, T. Yamaguchi, K. Yamazaki, K. Kurihira, J. Vac. Sci. Technol. B **16**, 3315 (1998)

3.6 T. Yamaguchi, H. Namatsu, M. Nagase, K. Yamazaki, K. Kurihira, Appl. Phys. Lett. **71**, 2388 (1997)

3.7 E.K. Lin, C.L. Soles, D.L. Goldfarb,B.C. Trinque, S.D. Burns, R.L. Jones, J.L. Lenhart, M. Angelopoulos, C.G. Willson, S.K. Satija, W.L. Wu, Science **297**, 372 (2002)

3.8 M.J. May, B. Mortini, C. Sourd, D. Perret, D.W. Chung, G. Barclay, C. Brochon and G. Hadziioannou, Proc. SPIE **6153**, 61530P (2006)

3.9 S. Engelmann, R.L. Bruce, T. Kwon, R. Phaneuf, G.S. Oehrlein, Y.C. Bae, C. Andes, D. Graves, D. Nest, E.A. Hudson, P. Lazzeri, E. Iacob and M. Anderle, J. Vac. Sci. Technol. B **25**, 1353 (2007)

3.10 S. Engelmann, R.L. Bruce, M. Sumiya, T. Kwon, R. Phaneuf, G.S. Oehrlein, C. Andes, D. Graves, D. Nest, E.A. Hudson, submitting to J. Vac. Sci. Technol. B

3.11 S. Engelmann, R.L. Bruce, F. Weilnboeck, M. Sumiya, T. Kwon, R. Phaneuf, G.S. Oehrlein, C. Andes, D. Graves, D. Nest, E.A. Hudson, submitting to J. Vac. Sci. Technol. B

3.12 D. Nest, D.B. Graves, S. Engelmann, R.L. Bruce, F. Weilnboeck, G.S. Oehrlein, C. Andes, E.A. Hudson, Appl. Phys. Lett. **92**, 153113 (2008)

3.13 J.J. Vegh, D. Nest, D.B. Graves, R. Bruce, S. Engelmann, T. Kwon, R.J. Phaneuf, G.S. Oehrlein, B.K. Long, C.G. Willson, Appl. Phys. Lett. **91**, 233113 (2007)

3.14 X. Hua, S. Engelmann, G.S. Oehrlein, P. Jiang, P. Lazzeri, E. Iacob and M. Anderle, J. Vac. Sci. Technol. B **24**, 1850 (2006)

3.15 M. Sumiya, R. Bruce, S. Engelmann, F. Weilnboeck, G.S. Oehrlein, submitted to J. Vac. Sci. Technol. B

3.16 M. Schapkens, T.E.F.M. Standaert, N.R. Rueger, P.G.M. Sebel, G.S. Oehrlein, J.M. Cook, J. Vac. Sci. Technol. A **17**, 26 (1999)

Chapter 4:

4.1 S. Engelmann, R.L. Bruce, T. Kwon, R. Phaneuf, G.S. Oehrlein, Y.C. Bae, C. Andes, D. Graves, D. Nest, E.A. Hudson, P. Lazzeri, E. Iacob and M. Anderle, J. Vac. Sci. Technol. B **25**, 1353 (2007)

4.2 X. Hua, S. Engelmann, G.S. Oehrlein, P. Jiang, P. Lazzeri, E. Iacob and M. Anderle, J. Vac. Sci. Technol. B **24**, 1850 (2006)

4.3 D. Goldfarb, A. Mahorowala, G. Gallatin, K. Petrillo, S. Rasgon, H. Sawin, S. Allen, M. Lawson, R. Kwong, J. Vac. Sci. Technol. B **22**, 647 (2004)

4.4 S. Engelmann, R.L. Bruce, F. Weilnboeck, M. Sumiya, T. Kwon, R. Phaneuf, G.S. Oehrlein, C. Andes, D. Graves, D. Nest, E.A. Hudson, *submitted to* J. Vac. Sci. Technol. B

4.5 T. Fedynshyn, R.R. Kunz, R.F. Sinta, R.B. Goodman, S.P.Doran, J. Vac. Sci. Technol. B **18**, 3332 (2000)

4.6 X. Hua, X. Wang, D. Fuentevilla, G.S. Oehrlein, F.G. Celii, K.H.R. Kirmse, J. Vac. Sci. Technol. A **21**, 1708 (2003)

4.7 X. Li, X. Hua, L. Ling, G.S, Oehrlein, M. Barela, H.M. Anderson, J. Vac. Sci. Technol. A **20**, 2052 (2002)

4.8 X. Li, L. Ling, X. Hua, M. Fukasawa, G.S. Oehrlein, M. Barela, H.M. Anderson, J. Vac. Sci. Technol. A **21**, 284 (2003)

4.9 A. V. Vasenkov, Xi Li, G. S. Oehrlein, M. J. Kushner, J. Vac. Sci. Technol. A **22**, 511 (2004)

4.10 X. Li, L. Ling, X. Hua, G. S. Oehrlein, Y. Wang, A. V. Vasenkov, M. J. Kushner, J. Vac. Sci. Technol. A **22**, 500 (2004)

4.11 X. Hua, C. Stolz, G.S. Oehrlein, P. Lazzeri, N. Coghe, M. Anderle, C.K. Inoki, T.S. Kuan, P. Jiang, J.Vac.Sci.Technol. A **23**, 151 (2005)

4.12 E.A. Hudson, Z. Dai, Z. Li. S. Kang, S. Lee, W. Chen and R. Sadjadi, Proc. Of International Symposium on Dry Processes, 253 (2003)

4.13 N. Negishi, H. Takesue, M. Sumiya, T. Yoshida, Y. Momonoi, M. Izawa, J. Vac. Sci. Technol. B **23,** 217 (2005)

4.14 T.E.F.M. Standaert, C. Hedlund, E.A. Joseph, G.S. Oehrlein, T.J. Dalton, J.Vac.Sci.Technol. A **22**, 53 (2004)

4.15 Y. Zhang, G.S. Oehrlein, E. Defresarte, J.W. Corbett, J.Vac.Sci.Technol. A **11**, 2492 (1993)

4.16 S. Engelmann, G.S. Oehrlein (unpublished) (2005)

4.17 S. Engelmann, D.G. Nest, D.B. Graves, G.S. Oehrlein (unpublished) (2006)

4.18 D.T. Clark, W.J. Feast, W.K.R. Musgrave, I. Ritchie, J. Polym. Sci. **13**, 857 (1975)

4.19 L. Zheng, L. Ling, X. Hua, G.S. Oehrlein, E.A. Hudson, J.Vac.Sci.Technol. B **23**, 634 (2005)

4.20 B. Bosch, J. LaCara, Solid State Technology **47**, 126 (2004)

4.21 S. Lassig, E. Hudson, Solid State Technology **45**, 47 (2002)

4.22 T. Wallow, A. Acheta, Y. Ma, A. Pawloski, S. Bell, B. Ward, C. Tabery, B. La Fontaine, R.H. Kim, S. McGowan, H.J. Levinson, Proc. SPIE **6519**, 651919 (2007)

4.23 H. Namatsu, M. Nagase, T. Yamaguchi, K. Yamazaki, K. Kurihira, J. Vac. Sci. Technol. B **16**, 3315 (1998)

4.24 K.P. Larsen, D.H. Petersen, O. Hansen, Journal of The Electrochemical Society **153**, G1051 (2006)

4.25 C. Hohle, N. Heckmann, M. Sebald, M. Markert, N. Stepanenko, F. Houlihan, A. Romano, R. Sakamuri, D. Rentkiewicz, R.R. Dammel, J. Microlith., Microfab., Microsyst. **4**, 043009 (2005)

4.26 Y.C. Bae, G.G. Barclay, P.J. Bolton, R.J. Kavanagh, L. Bu, T. Kobayashi, T. Adams, N. Pugliano, J.W. Thackeray, Proc. SPIE **5039**, 665 (2003)

4.27 H.W. Kim, J.Y. Lee, J. Shin, S.G. Woo, H.K. Cho, J.T. Moon, IEEE Transactions on Electron Devices **51**, 1984 (2004)

4.28 T. Yamaguchi, H. Namatsu, M. Nagase, K. Yamazaki, K. Kurihira, Appl. Phys. Lett. **71**, 2388 (1997)

4.29 H. Namatsu, M. Nagase, T. Yamaguchi, K. Yamazaki, K. Kurihira, J. Vac. Sci. Technol. B **16**, 3315 (1998)

4.30 Q. Lin, R. Sooriyakumaran, W. Huang, Proc. SPIE **3999**, 230 (2000)

4.31 B.D. Vogt, S. Kang, V.M. Prabhu, A. Rao, E.K. Lin, S.K. Satija, K. Turnquest, W. Wu, Proc. SPIE **6153**, 615316 (2006)

4.32 M.D. Smith, Proc. SPIE **6153**, 6153X (2006)

4.33 S. Yasin, M.N. Khalid, D.G. Hasko, S. Sarfraz, Microelectronic Engineering **78-79**, 484 (2005)

4.34 E.K. Lin, C.L. Soles, D.L. Goldfarb,B.C. Trinque, S.D. Burns, R.L. Jones, J.L. Lenhart, M. Angelopoulos, C.G. Willson, S.K. Satija, W.L. Wu, Science **297**, 372 (2002)

4.35 T. Sakamizu, H. Shiraishi, Microelectron. Eng. **61-62**, 763 (2002)

4.36 F. Ren, S.J. Pearton, J.R. Lothian, C.R. Abernathy, W.S. Hobson, J. Vac. Sci. Technol. B **24**, 1386 (2006)

4.37 M.J. May, B. Mortini, C. Sourd, D. Perret, D.W. Chung, G. Barclay, C. Brochon and G. Hadziioannou, Proc. SPIE **6153**, 61530P (2006)

4.38 M. Sumiya, R. Bruce, S. Engelmann, F. Weilnboeck, G.S. Oehrlein, submitted to J. Vac. Sci. Technol. B

4.39 K. Takechi, M.A. Lieberman, J. Appl. Phys. **89**, 5318 (2001)

4.40 C.H. Lee, D.H. Kim, N.E. Lee, G.C. Kwon, J. Vac. Sci. Technol. A **24**, 1386 (2006)

4.41 D.H. Kim, C.H. Lee, S.H. Cho, N.E. Lee, G.C. Kwon, J. Vac. Sci. Technol. B **23**, 2203 (2005)

4.42 D.H. Kim, S.H. Cho, N.E. Lee, K.C. Kwon, Jpn. J. Appl. Phys. **44**, 5856 (2005)

4.43 J. Kim, Y. Chae, W. Lee, J. Shon, C. Kang, W. Han, J. Moon, J. Vac. Sci. Technol. B **21**, 790 (2003)

4.44 P. Bhatnagar, S. Panda, N.L. Edleman, S.D. Allen, R. Wise, A. Marorowala, Appl. Phys.Lett. **88**, 231501 (2006)

4.45 K.S. Patel, V. Pham, W. Li, M. Khojasteh, P.R. Varanasi, Proc. SPIE **6153**, 6153Q (2006)

4.46 M. Kim, K. Bai, C. Kang, H. Cho, J. Vac. Sci. Technol. B **24**, 2231 (2006)

4.47 T.E.F.M. Standaert, M. Schaepkens, N.R. Rueger, P.G.M. Sebel, G.S. Oehrlein, J.Vac.Sci.Technol. A **16**, 239 (1998)

Chapter 5:

5.1 X. Hua, S. Engelmann, G.S. Oehrlein, P. Jiang, P. Lazzeri, E. Iacob and M. Anderle, J. Vac. Sci. Technol. B **24**, 1850 (2006)

5.2 Y.C. Bae, G.G. Barclay, P.J. Bolton, R.J. Kavanagh, L. Bu, T. Kobayashi, T. Adams, N. Pugliano, J.W. Thackeray, Proc. SPIE **5039**, 665 (2003)

5.3 M.J. May, B. Mortini, C. Sourd, D. Perret, D.W. Chung, G. Barclay, C. Brochon and G. Hadziioannou, Proc. SPIE **6153**, 61530P (2006)

5.4 E.A. Hudson, Z. Dai, Z. Li. S. Kang, S. Lee, W. Chen and R. Sadjadi, Proc. Of International Symposium on Dry Processes, 253 (2003)

5.5. N. Negishi, H. Takesue, M. Sumiya, T. Yoshida, Y. Momonoi, M. Izawa, J. Vac. Sci. Technol. B **23,** 217 (2005)

5.6 S. Engelmann, R.L. Bruce, T. Kwon, R. Phaneuf, G.S. Oehrlein, Y.C. Bae, C. Andes, D. Graves, D. Nest, E.A. Hudson, P. Lazzeri, E. Iacob and M. Anderle, J. Vac. Sci. Technol. B **25**, 1353 (2007)

5.7 S. Engelmann, R.L. Bruce, M. Sumiya, T. Kwon, R. Phaneuf, G.S. Oehrlein, C. Andes, D. Graves, D. Nest, E.A. Hudson, submitting to J. Vac. Sci. Technol. B

5.8 J.H. Min, G.R. Lee, J.K. Lee, S.H. Moon, J.Vac.Sci. Technol. B **22**, 2580 (2004)

5.9 V. Krastev, I. Reid, C. Galassi, G. Hughes, E. McGlynn, J.Mat.Sci:Mat. In Elec. **16**, 541 (2005)

5.10 M. Schaepkens, I. Martini, E.A.Sanjuan, X. Li, G.S. Oehrlein, W.L. Perry, H.M. Anderon, J.Vac.Sci. Technol. A **19**, 2946 (2001)

5.11 H.H. Doh, J.H. Kim, S.H. Lee, K.W. Whang, J.Va.Sci. Technol. A **14**, 2827 (1996)

5.12 L.M. Ephrath, J.Electrochem.Soc.**126**, 1419 (1979)

5.13 Y. Zhang, G.S. Oehrlein, F.H. Bell, J.Vac.Sci. Technol. A **14**, 2127 (1996)

5.14 G.S. Oehrlein, H.L. Williams, J.Appl.Phys. **62**, 662 (1987)

5.15 N. Takada, T. Iida, K. Shibagaki, K. Sasaki, J.Vac.Sci. Technol. A **22**, 413 (2004)

5.16 G.S. Oehrlein, Y. Zhang, D. Vender, M. Haverlag, J.Vac.Sci.Technol. A **12**, 323 (1994)

5.17 C. Hohle, N. Heckmann, M. Sebald, M. Markert, N. Stepanenko, F. Houlihan, A. Romano, R. Sakamuri, D. Rentkiewicz, R.R. Dammel, J. Microlith., Microfab., Microsyst. **4**, 043009 (2005)

5.18 K. Yonekura, K. Yoshikawa, Y. Fujiwara, S. Sakamori, N. Fujiwara, T. Kosaka, M. Ohkuni, K. Tateiwa, Thin Solid Films **515**, 5012 (2007)

5.19 T. Fedynshyn, R.R. Kunz, R.F. Sinta, R.B. Goodman and S.P.Doran, J. Vac. Sci. Technol. B **18**, 3332 (2000)

5.20 A.A. Miller, E.J. Lawton, J.S. Balwit, J. Polym. Sci **14**, 503 (1954)

5.21 X. Hua, X. Wang, D. Fuentevilla, G.S. Oehrlein, F.G. Celii, K.H.R. Kirmse, J. Vac. Sci. Technol. A **21**, 1708 (2003)

5.22 S. Nakamura, M. Itano, H. Aoyama, K. Shibahara, S. Yokoyama, M. Hirose, Jpn.J.Apl.Phys. **42**, 5759 (2003)

5.23 W.T. Tsai, H.P. Chen, W.Y. Hsien, J.Loss.Prev.Proc.Ind. **15**, 65 (2002)

5.24 N. Takada, H. Toyoda, I. Murakami, H. Sugai, J.Appl.Phys. **97**, 013534 (2005)

5.25 M.J. May, B. Mortini, M. Heitzmann, P. Gautier, C. Sourd, C. Brochon, G. Hadziioannou, Microelectronic Engineering **83**, 1098 (2006)

5.26 X. Li, X. Hua, L. Ling, G.S. Oehrlein, M. Barela, H.M. Anderson, J.Vac.Sci.Technol. A **20**, 2052 (2002)

5.27 H.H. Doh, J.H. Kim, K.W. Whang, S.H. Lee, J.Vac.Sci.Technol. A **14**, 1088 (1996)

5.28 C.J. Choi, O.S. Kwon, Y.S. Seol, Y.W. Kim, I.H. Choi, J.Vac.Sci.Technol. B **18**, 811 (2000)

5.29 G.S. Oehrlein, Y. Zhang, D. Vender, O. Joubert, J.Vac.Sci.Technol. A **12**, 333 (1994)

5.30 M. Izawa, N. Negishi, K. Yokogawa, Y. Momonoi, Jpn. J.Appl.Phys. **46**, 7870 (2007)

5.31 B. Ji, S.A. Motika, P.R. Badowski, S. Dheandhanoo, J.R. Stets and E.J. Karwacki, Solid State Technol. **48**, 45 (2005)

5.32 X. Li, L.Ling, X. Hua, G.S. Oehrlein, Y. Wang, A.V. Vasenkov, M.J. Kushner, J.Vac.Sci.Technol. A **22**, 500 (2004)

5.33 X. Hua, C. Stolz, G.S. Oehrlein, P. Lazzeri, N. Coghe, M. Anderle, C.K. Inoki, T.S. Kuan, P. Jiang, J.Vac.Sci.Technol. A **23**, 151 (2005)

5.34 S. Engelmann, G.S. Oehrlein (unpublished)

5.35 S. Briggs, *Surface Analysis of polymers by XPS and static SIMS* (Cambridge University Press, Cambridge, 1998)

5.36 M. Schaepkens, T.E.F.M. Standaert, N.R. Rueger, P.G.M. Sebel, G.S. Oehrlein, J.M. Cook, J.Vac.Sci.Technol. A **17**, 26 (1999)

5.37 X. Li, L. Ling, X. Hua, G.S, Oehrlein, Y. Wang, H.M. Anderson, J. Vac. Sci. Technol. A **21**, 1955 (2003)

5.38 X. Li, L. Ling, X. Hua, M. Fukasawa, G.S. Oehrlein, M. Barela, H.M. Anderson, J.Vac.Sci.Technol. A **21**, 284 (2003)

5.39 F.H. Bell, O. Joubert, G.S. Oehrlein, Y. Zhang, D. Vender, J.Vac.Sci.Technol. A **12**, 3095 (1994)

5.40 H. Gokan, S.Esho, Y. Onishi, J. Electrochem. Soc.**130 (1)**, 143 (1983)

5.41 R.R. Kunz, S.C. Palmateer, A.R. Forte, R.D. Allen, G.M. Wallraff, R.A. DiPietro, D.C. Hofer, Proc. SPIE **2724**, 365 (1995)

5.42 S. Kishimura, M. Endo, M. Sasogo, Proc. SPIE **4690**, 200 (2002)

5.43 K.S. Patel, V. Pham, W. Li, M. Khojasteh, P.R. Varasani, Proc. SPIE **6153**, 6153Q (2006)

5.44 T.I. Wallow, P.J. Brock, R.A. DiPietro, R.D. Allen, J. Opitz, R. Sooriyakumaran, D.C. Hofer, A.M. Mewherter, Y. Cui, W. Yan, G. Worth, W.M. Moreau, J. Meute, J.D. Byers, G.K. Rich, M. McCallum, S. Jayaraman, R. Vicari, J. Cagle, S. Sun, K.A. Hullihen, Proc. SPIE **3678**, 26 (1999)

5.45 T. Yu, P. Ching, C.K. Ober, S.V. Deshpande, R. Puligadda, Proc. SPIE **4345**, 945 (2001)

5.46 D. Perret, C.E. Andes, K.S. Cheon, M. Sobhian, C.R. Szmanda, G.G. Barclay, P. Trefonas III, Proc. SPIE **6159**, 651912 (2007)

5.47 C.W. Jurgensen, A. Shugard, N. Dudash, E. Reichmanis, M.J. Vasile, J.Vac.Sci.Technol. A **6**, 2938 (1988)

5.48 J.Ding, J.S. Jenq, G.H. Kim, H.L. Maynard, J.S. Hamers, N. Hershkowitz, J.W. Taylor, J.Vac.Sci.Technol. A **11**, 1283 (1993)

5.49 T.E.F.M. Standaert, P.J. Matsuo, X. Li, G.S. Oehrlein, T.M. Lu, R.Gutmann, C.T. Rosenmayer, J.W. Bartz, J.G. Langan, W.R. Entley, J.Vac.Sci.Technol. A **19**, 435 (2001)

5.50 O. Joubert, J. Pelletier, Y. Arnal, J.Appl.Phys. **65**, 5096

5.51 C.W. Jurgensen, A. Rammelsberg, J.Vac.Sci.Technol. A **7**, 3317 (1989)

5.52 T.M. Mayer, R.A. Barker, J.Vac.Sci.Technol. **21**, 757 (1982)

5.53 T.M. Mayer, R.A. Barker, J. Electrochem. Soc. **129**, 585 (1982)

5.54 T.M. Mayer, R.A. Barker, L.J. Whitman, J.Vac.Sci.Technol. **18**, 349 (1981)

5.55 J.J. Vegh, D. Nest, D.B. Graves, R. Bruce, S. Engelmann, T. Kwon, R.J. Phaneuf, G.S. Oehrlein, B.K. Long, C.G. Willson, Appl. Phys. Lett. **91**, 233113 (2007)

5.56 J.J. Vegh, D. Nest, D.B. Graves, R. Bruce, S. Engelmann, T. Kwon, R.J. Phaneuf, G.S. Oehrlein, B.K. Long, C.G. Willson, submitted to J. Appl. Phys.

5.57 M.Sumiya, R. Bruce, S. Engelmann, F. Weilnboeck, G.S. Oehrlein, submitted to J. Vac. Sci. Technol. B

5.58 B.J. Orf, S.G. Walton, D. Leonhardt, G.S. Oehrlein, J.Vac.Sci.Technol. B **25**, 779 (2007)

5.59 J.M. Elson, J.M. Bennett, Appl. Opt. **34**, 201 (1995)

5.60 T. Wallow, A. Acheta, Y. Ma, A. Pawloski, S. Bell, B. Ward, C. Tabery, B. La Fontaine, R. Kim, S. McGowan, H.J. Levinson, Proc. SPIE **6519**, 651919 (2007)

5.61 D. Nest, D.B. Graves, S. Engelmann, R.L. Bruce, F. Weilnboeck, G.S. Oehrlein, C. Andes, E.A. Hudson, Appl. Phys. Lett. **92**, 153113 (2008)

Chapter 7:

7.1 C. Hohle, N. Heckmann, M. Sebald, M. Markert, N. Stepanenko, F. Houlihan, A. Romano, R. Sakamuri, D. Rentkiewicz, R.R. Dammel, J. Microlith., Microfab., Microsyst. **4**, 043009 (2005)

7.2 E. Pargon, O. Joubert, N. Posseme, L. Vallier, J.Vac.Sci.Technol. B **22**, 1858 (2004)

7.3 H. Kawahira, N. Matsuzawa, E. Matsui, A. Ando, K. Salam, M. Yadhida, Y. Yamaguchi, K. Kugimiya, T. Tatsumi, H. Nakano, T. Iwai, and M. Irie, Proc. SPIE **6153**, 615319 (2006)

7.4 Y. Inatomi, T. Kawasaki, M. Iwashita, Proc. SPIE **6153**, 61533X (2006)

7.5 M. Sumiya, R. Bruce, S. Engelmann, F. Weilnboeck, G.S. Oehrlein, submitted to J. Vac. Sci. Technol. B

7.6 M. Ohring, *The Materials Science of Thin Films* (Academic Press, San Diego, 1992)

7.7 F. Garbassi, M. Morra, E. Occhiello, *Polymer Surfaces – From Physics to Technology* (John Wiley & Sons, Chichester, 1994)

7.8 L.C. Sawyer, D.T. Grubb, *Polymer Microscopy* (Chapman and Hall Ltd, New York, 1987)

7.9 G. Cao, Nanostructures & Nanomaterials – Synthesis, Properties & Application (Imperial College Press, London, 2004)

7.10 D.B. Williams, C.B. Carter, *Transmission Electron Microscopy – A Textbook for Materials Science* (Plenum Press, New York, 1996)

7.11 A.W. Czaderna, *Methods of Surface Analysis*, (Elsevier, Amsterdam, 1975)

7.12 K.L. Mittal, *Physiochemical Aspects of Polymers*, (Plenum Press, New York, 1983)

7.13 R.J.H. Clark, R.E. Hester, *Spectroscopy of Surfaces* (John Wiley & Sons, Chichester, 1988)

7.14 R.R. Deshmukh, A.R. Shetty, J.Appl.Polym.Sci. **107**, 3707 (2008)

7.15 B.J. Lin, Microelectronic Engineering **83**, 604 (2006)

7.16 Y. Takebe, T. Sasaki, N. Shirota, O. Yokokoji, Microelectronic Engineering **83**, 1091 (2006)

7.17 B.K. Long, K. Keitz, C.G. Willson, J. Mater. Chem. **17**, 3575 (2007)